HETEROGENEOUS MIXTURES FOR SYNTHETIC ANTENNA SUBSTRATES

by

CHINWE CHRISTIANA NJOKU

A Doctoral Thesis

Submitted in partial fulfilment of the requirements

for the award of

PhD in Electrical, Electronics & Systems Engineering

of Loughborough University

April, 2013

SUMMARY

Heterogeneous mixtures have the potential to be used as synthetic substrates for antenna applications giving the antenna designer new degrees of freedom to control the permittivity and/or permeability in three dimensions such as by a smooth variation of the density of the inclusions, the height of the substrate and the manufacture the whole antenna system in one process. Electromagnetic, fabrication, environmental, time and cost advantages are potential especially when combined with nano-fabrication techniques. Readily available and cheap materials such as Polyethylene and Copper can be used in creating these heterogeneous materials. These advantages have been further explained in this thesis.

In this thesis, the research presented is on canonical, numerical and measurement analysis on heterogeneous mixtures that can be used as substrates for microwave applications. It is hypothesised that heterogeneous mixtures can be used to design bespoke artificial dielectric substrates for say, patch antennas.

The canonical equations from published literature describing the effective permittivity, ε_{eff} and effective permeability, μ_{eff} of heterogeneous mixtures have been extensively examined and compared with each other. Several simulations of homogenous and heterogeneous media have been carried out and an extraction/inversion algorithm applied to find their ε_{eff} and μ_{eff}. Parametric studies have been presented to show how the different variables of the equations and the simulations affect the accuracy of the results. The extracted results from the inversion process showed very good agreement with the known values of the homogenous media. Numerically and canonically computed values of ε_{eff} and μ_{eff} of various heterogeneous media were shown to have good agreement.

The fabrication techniques used in creating the samples used in this research were examined, along with the different measurement methods used in characterising their electromagnetic properties via simulations and measurements. The challenges faced with these measurement methods were explained including the possible sources of error. Patch antennas were used to investigate how the performance of an antenna may be affected by heterogeneous media with metallic inclusions. The performance of the patch antenna was not inhibited by the presence of the metallic inclusions in close proximity. The patch measurement was also used as a measurement technique in determining the ε_{eff} of the samples.

ACKNOWLEDGEMENTS

I tell everyone who cares to listen that I have the best supervisors ever. I am yet to meet a PhD student with my kind of supervisors – Dr William G. Whittow and Professor Yiannis C. Vardaxoglou. It does not get any better than these. Thank you both very much for being amazing, helpful and guiding me through these 3+ years as a PhD student at Loughborough University.

To my colleagues, friends and members of staff within the School: Emma, Ajit, Shiyu, Dr Alford Chauraya, Dr Chinthana Panagamuwa, Mr Rob Seager, Prof. Jonathan Chambers, Mrs Julie Allen, the workshop and IT staff, thank you for making these 3 years easier.

Now, I have great friends to make the average man green with jealousy. I love you guys to bits and you know. I promised Damilola Ogunniyi and Osarieme Osakue their names will be fully spelt out in this thesis. You have been AMAZING! I love you girls! I sincerely appreciate Vera, Jumoke, James, Samson, Tunde, Gbemiga, Fred, Segun, Seun, Tola, Sunkanmi, Oyinkan, Kunbi, Ugonna, Jeff, TJ, Tolu, Herbert, Simi, Funlola, Nenny, Akpovi, Suji, Toyosi, Kemi, Ozak, Funmi, Tosin, Sola A., big thanks to you all for making my Loughborough experience one to always brag about, and allowing me live a purposeful life. Aliu, Sola O., Folarin, Obitayo, Yinka, Eniola, Funke and Kemi, thank you for being available. Special thanks to Pastors Joe, Akin, Eno, Keme and Kingsley and Uncles Austin and Tmak for taking care of the non-academic sides of my life. God bless you all.

Did I ever say my family IS the BEST? Indeed!! To my dad and mum, Engr. & Mrs S. N. Njoku, to my sister: Nneka and my brothers: Nnaji, Chike and Jethro, here is a massive, heartfelt thank you for walking these 3+ years totally by my side, supporting me with your love and prayers, calls and texts and monies. We will always remain together, God help us!! Very special thanks to Onyedikachi Enebechi aka MOG – your impact on my life will definitely go beyond this generation, thank you indeed.

DEDICATION

This thesis in its entirety is totally dedicated to the GOD of the Bible, my Father and Friend.

LIST OF PUBLICATIONS

Journals:

[1] C. C. Njoku, W. G. Whittow, and J. C. Vardaxoglou, "Simulation Methodology for Synthesis of Antenna Substrates with Micro-scale Inclusions," IEEE Trans Antennas and Propagation, vol. 60, no. 5, pp. 2194–2202, 2012.

[2] C. C. Njoku, W. G. Whittow, and Y. C. Vardaxoglou, "Effective permittivity of heterogeneous substrates with cubes in a 3D lattice," IEEE Antennas and Wireless Propagation Letters (Special Issue on Metamaterials), vol. 10, pp. 1480–1483, 2011.

Peer Reviewed Conference Papers:

[3] C. C. Njoku, J. C. Vardaxoglou, and W. G. Whittow, "Complementary frequency selective surfaces for waveguide dielectric measurements," to be presented at the IEEE APS/USNC-URSI Meeting, July 2013.

[4] W. G. Whittow, C. C. Njoku, and J. C. Vardaxoglou, "Fine scale simulations of patch antennas with heterogeneous substrates," to be presented at the IEEE APS/USNC-URSI Meeting, July 2013

[5] C. C. Njoku, W. G. Whittow, and J. C. Vardaxoglou, "Antennas on Quasi Synthetic Media," in the 4th International Conference on Metamaterials, Photonic Crystals and Plasmonics, META'13, 2013.

[6] W. G. Whittow, C. C. Njoku, and J. C. Vardaxoglou, "Review of Artificial Dielectrics Containing Small Scale Inclusions," in IEEE International Workshop on Antenna Technology (IWAT), 2013.

[7] C. C. Njoku, J. C. Vardaxoglou, and W. G. Whittow, "Complementary frequency selective surfaces in a waveguide simulator," to be presented at the 7th European Conference on Antennas and Propagation (EuCAP), April 2013 (Accepted).

[8] J. C. Vardaxoglou, C. C. Njoku, and W. G. Whittow, "EM Properties of Synthetic Media," to be presented at the 7th European Conference on Antennas and Propagation (EuCAP), April 2013 (Accepted).

[9] W. G. Whittow, C. C. Njoku, J. C. Vardaxoglou, and J. Joubert, “Designing Multi-Band and High Bandwidth Antennas with Heterogeneous Substrates,” in IEEE Tropical Conference on Antennas and Propagation in Wireless Communications (APWC), 2012

[10] W. G. Whittow, C. C. Njoku, and J. C. Vardaxoglou, “Patch Antennas with Heterogeneous Substrates and Reduced Material Consumption Enabled by Additive Manufacturing Techniques,” in 2012 IEEE International Symposium on Antennas and Propagation and USNC-URSI National Radio Science Meeting, 2012

[11] C. C. Njoku, W. G. Whittow, and J. C. Vardaxoglou, “Designing Microwave Patch Antennas Using Heterogeneous Substrates,” in European Conference on Antennas and Propagation (EuCAP), 2012.

[12] C. C. Njoku, W. G. Whittow, and J. C. Vardaxoglou, “Antenna performance on quasi synthetic media,” in IEEE International Workshop on Antenna Technology (IWAT), 2012.

[13] C. C. Njoku, W. G. Whittow, and J. C. Vardaxoglou, “Microstrip Patch Antennas on Substrates with Metallic Inclusions,” in Loughborough Antennas & Propagation Conference (LAPC), 2012.

[14] C. C. Njoku, W. G. Whittow, and J. C. Vardaxoglou, “Microwave antennas and heterogeneous substrates using nanomaterial fabrication techniques (Invited Paper),” in IEEE Tropical Conference on Antennas and Propagation in Wireless Communications (APWC 11), 2011.

[15] C. C. Njoku, W. G. Whittow, J. C. Vardaxoglou, C. Topraxoglu, and K.-A. T. Thoma, “Metallic inclusions in a non-uniform lattice,” in 2011 Loughborough Antennas & Propagation Conference (LAPC), 2011.

[16] C. C. Njoku, W. G. Whittow, and J. C. Vardaxoglou, “Study on the variation in dielectric properties of heterogeneous substrates composed of nanomaterials,” in European Conference on Antennas and Propagation (EuCAP), 2011.

[17] C. C. Njoku, W. G. Whittow, and J. C. Vardaxoglou, “Comparative study of nanomaterials’ effective properties using canonical formulations,” in 2010 Loughborough Antennas & Propagation Conference (LAPC), 2010.

[18] C. C. Njoku, W. G. Whittow, and J. C. Vardaxoglou, “An analytical approach to modifying the properties of dielectric substrates composed of nanomaterials,” in 2010 Loughborough Research Student Conference, 2010.

[19] C. C. Njoku, W. G. Whittow, and C. Panagamuwa, “Printable Windscreen Quad-band GSM Antenna,” in 2009 Loughborough Antennas & Propagation Conference (LAPC), 2009, pp. 781–784.

LIST OF ACRONYMS & ABBREVIATIONS

2D	Two dimensional
3D	Three dimensional
ABC	Absorbing Boundary Conditions
BCC	Body Centred Cubic
BIE	Boundary Integral Equation
CFSS	Complementary Frequency Selective Surfaces
C-M	Clausius-Mossotti
CNTs	Carbon Nano-Tubes
dB	decibels
EBG	Electromagnetic Band Gap
EM	Electromagnetic
EuCAP	European Conference on Antennas and Propagation
FCC	Face Centred Cubic
FDTD	Finite-Difference Time-Domain
FSS	Frequency Selective Surfaces
G*n*SG	*n* double-sided copper etched GTS® laminates with plain GTS® dielectric on either side
M-G	Maxwell-Garnett
MRR	Microstrip Ring Resonator
MSL	Microstrip Line
MUT	Material under test
NRW	Nicholson-Ross-Weir
PEC	Perfect Electric Conductor
PMC	Perfect Magnetic Conductor

PML	Perfectly Matched Layers
PW	Plane Wave
RF	Radio Frequency
RWG	Rectangular Waveguide
SC	Simple Cubic
SPDR	Split-Post Dielectric Resonator
TE	Transverse Electric
TM	Transverse Magnetic
TEM	Transverse Electromagnetic
TRL	Through-Reflect-Line
UV	Ultra Violet
VNA	Vector Network Analyser

LIST OF SYMBOLS

ε_o	Permittivity of free space, F/m
μ_o	Permeability of free space, H/m
ε_r, μ_r	Relative permittivity and permeability
ε_1, μ_1	Relative permittivity and permeability of host medium
ε_2, μ_2	Relative permittivity and permeability of inclusions
ε_p, μ_p	Effective relative permittivity and permeability of inclusions
$\varepsilon_{eff}, \mu_{eff}$	Effective relative permittivity and permeability of homogenous or heterogeneous medium
$\varepsilon', \varepsilon''$	Real and imaginary parts of ε_r
tan δ	Loss tangent delta
σ	Conductivity, S/m
λ, λ_g	Free space and guided wavelength, m
$k = 2\pi/\lambda$	Wave number, m^{-1}
f	Frequency, Hz
f_r	Resonant frequency, Hz
p	Volume fraction of inclusions
r	Radius of disc, m
t	Thickness of disc, m
a	Radius of spherical inclusions, m
l	Length of cubic inclusions, m
s	Centre-to-centre spacing between inclusions, m
V	Volume of inclusions, m^3
d	Thickness of structure under test, m

d_1	Distance from Port 1 to edge of medium under test, m
d_2	Distance from Port 2 to edge of medium under test, m
S_{11}, S_{21}	Scattering (S-) parameters
φ_1, φ_2	Phase of S_{11} and S_{21} in degrees or radians
$\varphi_{1c}, \varphi_{2c}$	Corrected phase of S_{11} and S_{21} in degrees or radians
$\Delta\varphi_r$	Rectified phase of medium under test, degrees or radians
$\Delta\phi_d$	Phase of medium under test, radians
n	Refractive index
η	Wave impedance, Ω
ω	Angular frequency, radians/s
E	Electric field, V/m
H	Magnetic field, A/m
P	Net polarisation vector, C/m^2
M	Net magnetisation vector, A/m
χ_e, χ_m	Electric and Magnetic susceptibility
α_1, β_1	Electric and Magnetic dipole polarisability
a_m, b_m	m^{th} electric and magnetic scattering coefficient
C	Interaction constant
N	Number density of inclusions
$\overline{\boldsymbol{p}}$	Dipole moment
c	Speed of light in air, m/s
Γ, T	Reflection, transmission coefficients
τ_g	Group delay
d_m	Mean diameter of ring, m

w or w_o, w_s	Width of transmission line and substrate
W_p, L_p	Width and length of patch antenna
l_o	Depth of inset/recessed feed for patch antenna

TABLE OF CONTENTS

Chapter 1. Introduction

In this chapter, Section 1.1 gives the hypothesis while Section 1.2 states the novel contributions of this thesis. Section 1.3 introduces the concept of artificial dielectrics and the proposed final artificial dielectric structure is discussed in Section 1.4. The electromagnetic advantages of using these structures are highlighted in Section 1.5 with an example application to patch antennas. A few of the available nanomaterial fabrication techniques are briefly described in Section 1.6 while the defining properties of materials are introduced in Section 1.7. A summary of the research so far on heterogeneous media is given in Section 1.8, with an overview of this thesis in Section 1.9.

1.1 Hypothesis

The permittivity and permeability of a macroscopically homogeneous medium can be altered by inserting inclusions of various shapes and sizes. It is hypothesised that heterogeneous mixtures can be used to design bespoke artificial dielectric substrates for different microwave antennas such as the patch antenna (as it quite commonly used). It is postulated that electromagnetic, fabricational and environmental advantages can be realised by manufacturing such mixtures from emerging and futuristic nanotechnology processes. Note, this thesis will only investigate the electromagnetic behaviour of such mixtures and it is beyond the scope of this work to create nanomaterial samples.

1.2 Novel Contributions of this Thesis

The novel contributions of this thesis are

1) Different analytical equations for heterogeneous mixtures have been critically analysed and compared;
2) The effective properties of mixtures and the ability to control the effective permittivity and permeability has been studied with a range of parameters on the micro-scale;
3) A robust simulation methodology to extract the effective permittivity and permeability has been extended and validated with canonical equations for spherical and cubic inclusions;
4) Metallic inclusions with a range of geometries have been examined;

5) Scaled samples have been fabricated and the properties have been examined using a range of techniques;
6) The effective loss tangents have been investigated;
7) The efficiency and radiation patterns of patch antennas with heterogeneous substrates has been measured;
8) Anisotropy and diamagnetism of various samples has been analysed and can be controlled.

Note, the word ‘particle’ or ‘obstacle’ as used in this thesis refers to a generic inserted object or an inclusion and can therefore mean either a nanoparticle, a micro- or millimetre sized particle or a micro/millimetre-sized cluster of nanoparticles. In addition, the permittivity and permeability values used and given in this thesis are their values relative to those of free space, ε_o and μ_o, where $\varepsilon_o = 8.854 \times 10^{-12}$ F/m and $\mu_o = 4\pi \times 10^{-7}$ H/m.

1.3 Introduction to Artificial Dielectrics

Wireless communication is vital to the modern-day information-seeking lifestyles. It is challenging to continuously improve antennas in terms of efficiency, bandwidth and reduced size. This thesis investigates the idea of creating artificial dielectrics out of heterogeneous structures as a mechanism to improve the electromagnetic (EM) performance of antenna systems.

The long term aim of this research work is to study the possibility of designing and fabricating new antenna systems with heterogeneous segments by using nano- or micro-scale inclusions made up of nanomaterials via additive manufacturing processes [1], [2], the bottom-up approach instead of the currently used destructive processes. These destructive processes, for example, in the manufacture of conventional patch antennas, involve the use of costly and environmentally damaging chemicals to etch away selected or unwanted parts of the metal layers. Several iterative processes might be needed to create the final desired antenna system. With the rising material and labour costs, it can be expected that the costs involved in these destructive processes will become even more significant. However, various nanotechnology fabrication techniques such as self-assembly, electro deposition and lithography [3–6] which are additive processes, already exist and could be used in the manufacture of heterogeneous substrates. These characteristics have led to the industry becoming a multi-trillion dollar one with the technology developing very quickly [7]. Thus it is expected that we will soon have the technology to control the small-scale geometry and thus the properties of our materials without being limited to naturally-occurring materials. As the costs of nanotechnology decreases, these techniques of manufacturing antenna systems may become more cost effective, environmentally friendlier [8], and faster than conventional methods. Furthermore they can lead to EM advantages and may enable the manufacture of high permittivity substrates which are often very expensive. In addition, manufactured substrates and/or antenna systems may then have fewer variations in physical size and EM properties for batch productions.

This potential to manipulate materials has prompted extensive research [9–19] into the creation of these artificial materials that provide the EM properties, losses and other parameters pre-required for the EM system. Typically, small-size material inclusions having a higher permittivity and/or permeability can be added to a low dielectric, homogenous host to increase the effective EM properties of the end mixture. This has been proven both

theoretically and via measurements to give rise to materials of different EM characteristics. Synthesized materials can be formed from homogenous materials within which are embedded inclusions of different sizes and in (any) different lattice arrangements. The sizes and arrangement of these inserted inclusions are dependent on the specific requirements, and may be either micro- or nano-sized individual particles or micro-sized clusters of nanoparticles. Therefore, by enabling heterogeneous substrates, the antenna designer will have two new degrees of freedom compared to conventional substrates: 1) the substrate height and 2) the EM properties and these can be used to design bespoke substrates for antenna systems that often must be incorporated into increasingly compact packaging.

Heterogeneous mixtures are mixtures made up by embedding inclusions whose bulk materials can have either the same or different EM properties (of equal or varying sizes), within a homogenous medium. These inclusions can be either dielectric or metallic depending on the desired effective properties; typically, the host medium is dielectric. The two main EM properties of interest when examining heterogeneous mixtures are typically the effective relative permittivity (or dielectric constant), ε_{eff}, and effective relative permeability, μ_{eff}, of these mixtures, as these are the primary factors which determine how the final structure behaves when illuminated by EM fields. The permittivity indicates the "charge (energy) storage capabilities" of the dielectric material [20]. Thus the amount of interaction, typically by scattering between the particles will determine to a large extent, the effective permittivity of the mixture [9]. The permeability shows the susceptibility of the material to aid or oppose impinging magnetic fields. As permeability values for most naturally existing materials are typically very close to 1, the effective permeability of heterogeneous mixtures will generally not significantly vary from 1, except in cases where the bulk properties of the inclusions are ferromagnetic or ferrimagnetic, having relative permeabilities much greater than unity [20]. It should be noted that these effective properties, as with naturally occurring materials, typically vary with frequency and can be complex [20]. In this thesis, negative permittivity and permeability values are not being researched.

From the literature reviewed, Lord Rayleigh [10] was the first to examine how the EM properties of a medium are affected when obstacles are placed in it. However, more commonly cited and used for related problems is the analysis carried out by Lewin in [9]. The study shown in [9] forms a strong foundation for this work being carried out on using small-scale particles to build antenna structures without having to deal with the restrictive nature of

already existing materials but ‘creating’ new materials that can provide the constitutive parameters, control and/or reduce losses and other characteristics pre-determined for the whole antenna system. A related area of research to artificial dielectrics is on metamaterials whose properties are due to the geometry of the structure and not the materials themselves. They are often used to create negative ε_{eff} and negative μ_{eff} for stop bands [21–23]. This work however deals with creating positive values of ε_{eff}. “There is restriction to achieve a desired permeability value at a frequency of interest, specially, in the microwave and optical ranges” [23]. Artificial magnetism which may be achieved using loop circuits, split-ring resonators (SRRs) [24], [25], [26] is more difficult to deal with than electric polarisation. Thus, if this work could create low loss magnetic materials, novel structures can be made which could provide a better, easier to fabricate alternative to the use of loops for artificial magnetism.

In this thesis, the effective dielectric properties will be examined using various canonical equations and finite-difference, time-domain (FDTD) EM simulations. Host media of existing EM characteristics when they have particles of known and existing EM properties embedded in them, will be examined and analysed via these canonical and simulation models.

1.4 The Proposed Structure

There are potentially several advantages that will result from the use of nanotechnology in the fabrication of future antenna systems. These systems might in the future be built using the bottom-up approach by accurately positioning metallic and non-metallic inclusions of pre-determined geometric characteristics, in pre-designed positions. Figure 1.1 is a sketch of the vision of the future for the intended antenna structure and not what has been achieved already. Here, all the components of the antenna system – including the substrate and metallic sections are made from smaller particles, or clusters of nanoparticles. For example, a scratch resistance radome with increased physical durability could be incorporated into the same fabrication process. Other RF components including the feed and the balun can be envisioned and added to the manufacturing process as depicted in Figure 1.1.

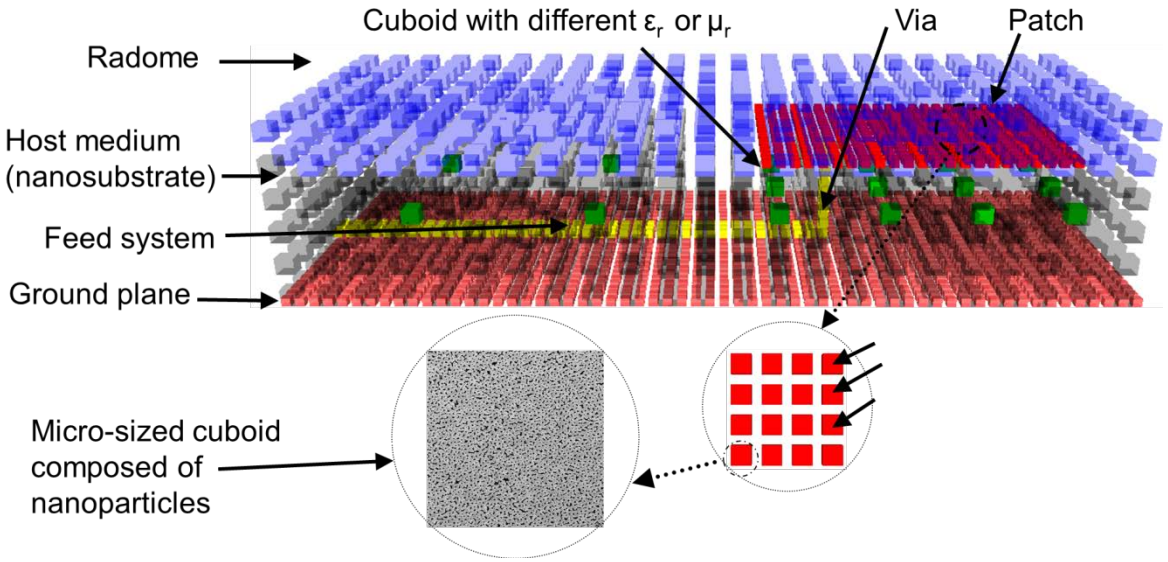

Figure 1.1: A sketch of a futuristic antenna system where the radiating element, substrate, vias and radome can be integrated into one manufacturing process

1.5 Electromagnetic Advantages

The use of nanofabrication processes in the manufacture of antenna systems, complete, or partial, has several potential advantages including electromagnetic ones. These include being able to control the dielectric and possibly the magnetic properties, thus allowing the creation of novel substrates with pre-determined characteristics. EM advantages relative to bandwidth, size and efficiency can be achieved as a by-product of being able to control the material's EM properties.

Substrates with bespoke dielectric properties and height can be considered giving additional degrees of freedom during antenna design, an example of which is given in Section 1.5.1. These degrees of freedom include being able to control the permittivity and permeability of microwave substrates in three dimensions and the ability to potentially manufacture the whole antenna system in one process. More consistent substrates will reduce the EM variations between identically manufactured products. In previous work, it has been shown that a highly efficient, compact antenna with a large bandwidth can be designed with a thus far unrealisable substrate which has equality of permittivity and permeability [27]. Such materials may become possible by using artificial dielectrics. Also, double negative materials are possible. Macroscopically homogenous metamaterials can also be made possible using artificial dielectrics.

1.5.1 Example Application to Patch Antennas

It is well known that the distribution of the electric fields for a radiating patch antenna is not distributed evenly over the radiating area. In addition, it has been shown in published literature [9], [10], [15], that the effective permittivity of a material can be altered by adding inclusions of different EM properties to the material. By mapping the permittivity of the substrate to the intensity of the electric field, it is expected that the overall performance of the patch will be altered compared to when it is on a continuously homogenous substrate. This can be exploited to achieve EM advantages. Figure 1.2 gives an example of how the distribution of these inclusions can be varied in a substrate in order to dictate the local effective permittivity; these structures are not examined in this thesis but further information can be found in [28].

An interesting method of improving antenna performance is by using textured dielectrics [29–32]. The key idea here is to distribute the concentration of the antenna's electric fields by

creating heterogeneous substrates such that the volumes of high permittivities are matched to areas on the antenna where the electric fields are small. These papers used discrete heterogeneous substrates and it was hypothesized that the electromagnetic performance could be further improved by varying the permittivity smoothly. Such structures are currently difficult to make with existing fabrication processes as typically objects of higher permittivity need to be physically located within a lower permittivity host substrate. It is expected that the use of small scale inclusions brought about by advances in nanotechnology will help to solve these manufacturing difficulties while still allowing the control of the EM performance.

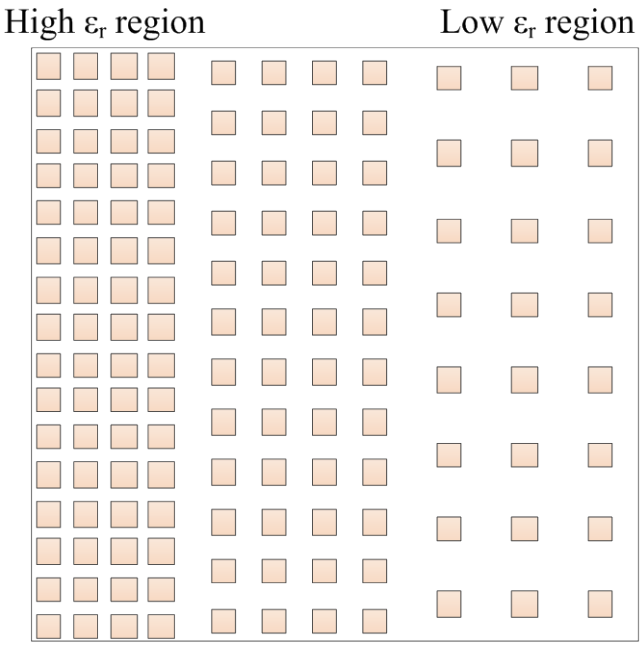

Figure 1.2: A sketch showing how the permittivity can be varied within the substrate by changing the spacing of the inclusions (not to scale)

.

1.6 Nanomaterial and Fabrication Techniques

Nanomaterials are in a general sense, described as a class of materials in which at least one of the dimensions of the constitutive particles in the material is in the nano-scale range typically less than 1000 nm. The definition of 'Nanomaterials' tends to vary from country to country [33], [34], however in the UK, they have been defined as "those which have structured components with at least one dimension less than 100 nm [35]." Nanomaterials have been of great interest over the past decades and find various applications in different industries [36], [37], so that there are probably more than 100 nano-related conferences [38]. A word search for "nanomaterials" in IEEE yields over a thousand articles published over the last two decades. Increased interests can be attributed to nanomaterials having innate advantages because of their high surface area to volume ratio, which includes increased hardness, improved physical strength and electrical conductivity [1], [2], [35]. The properties of these materials tend to differ from the bulk properties which can be due to increased surface areas and quantum effects [9], [35]. These material advantages have led to a multibillion dollar industry where the technology and possible structures are developing at a rapid rate due to increased funding and interest from stakeholders –governments, public and private bodies [36]. This new technology can potentially control the placement of individual dielectric and metallic particles (or conducting carbon nanotubes (CNTs)) which can be used to design new antenna systems. The ability to pre-determine the particles' volume ratio allows for the creation of novel and custom-made substrates [35] with high permittivity values using low-cost and/or readily available materials which will provide antenna and material engineers with a variety of substrates.

With the intensive interest in nanotechnology, several techniques have been developed for the manufacture of nano-based materials or systems over the years [6], and have been improved upon over the years to accommodate various specifications. A few of these techniques are mentioned and briefly discussed in this section. Nanofabrication processes are typically additive techniques and give the designer more control over the final geometry of the structure. Some of these nanofabrication techniques can be generally classed under one or more of these categories including: deposition, self-assembly, lithography, and etching and their many variants [39]. The costs and complexities of using any of these, in addition to the area and thickness of the sample to be manufactured, play an important role in deciding which one to use [40]. These methods have been used for different applications and provide a wide range of dimensions of the inclusions. These techniques are beyond the scope of this

thesis as this thesis focuses on finding the EM properties of artificial dielectrics. However, a brief summary has been provided.

1.6.1 Deposition:

This is an additive process in which a sample of required thickness is built up by depositing particles, typically in the nano-scale onto a substrate. The deposit grows to form the final structure and is controllable [39]. Deposition techniques involve the use of a precursor material that aids in the depositing of the particles – metallic or non-metallic materials in the nano-scale. Variants of deposition include electron-beam-induced deposition [41], advanced thin-film and atomic layer deposition [42], localised-electro deposition [43], [44], chemical and physical vapour depositions [35], [45], [46] and ion deposition [47]. Demerits are that it can be time-consuming [48] and may include impurities in the final structure [41]. An example of the electro deposition process is shown in Figure 1.3 (a).

1.6.2 Self-assembly:

Self-assembly describes a method whereby particles in a disordered arrangement (tend to) organise themselves into structures as a result of the interactions between the particles themselves, without external influence. Where external force is applied to hasten the process, this is referred to as directed self-assembly [35]. With regards to nanotechnology, the desired final structure is based on the geometric and other properties of the particles used in the process [49], [50]. Self-assembly is used in various forms [5], [44] such as self-assembled monolayers [51] and can be incorporated into other nanofabrication methods.

1.6.3 Lithography:

This is the “process of transferring a pattern into a reactive polymer film, termed as resist, which will subsequently be used to replicate that pattern into an underlying thin film or substrate” [39], and has been used to create structures as small as 40 nm [35]. It can generally be classed as either micro- or nano-lithography. Variants of lithography include photolithography [51], electron-beam lithography [48], optical or X-ray lithography [52], [53], soft lithography [51] and nano-imprint lithography [3], [54], [55]. An example of the photo-lithography process is shown in Figure 1.3 (b). This process is similar to that used in the etching process for creating the multi-layered sample used in this thesis as discussed in Chapter 5.

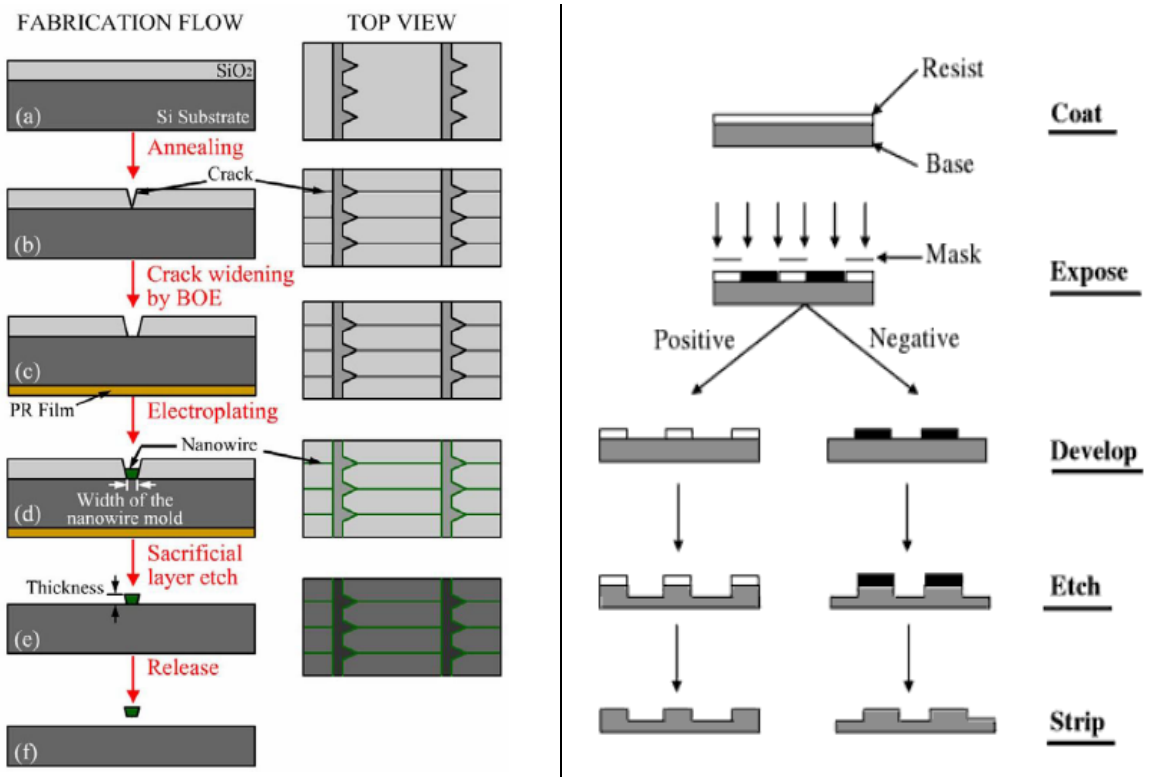

Figure 1.3: Schematic diagram of (a) the photolithographic process showing the different sequences. (Image from [39]) and (b) an example of eletro-deposition (Image from [44]).

Other nanomaterial fabrication techniques from another collaborator[1] on this project are: electrochemistry plus metal evaporation (nano-perforated metallic film on dielectric substrate), electrochemistry with chemical deposition (porous material made up of parallel cylindrical pores filled with nanoparticles, in a metal oxide matrix) and casting or spin-coating (polymer film containing dispersed nanoparticles).

1.6.4 Facilities at Loughborough University, UK[2]

The Photovoltaics Group at the Centre for Renewable Energy Systems Technology (CREST) at Loughborough University has the capability of generating nano-patterns of requisite dimensions from metals or dielectric particles. The following methods that can be processed at CREST were proposed for this project. However these methods were not used for this thesis as they were expensive and the priority here was to build a solid foundation for any

[1] Information provided by Professor Chris Toprakcioglu, Department of Physics, University of Patras, Greece
[2] Information provided by Professor Hari Upadhyaya, now at School of Engineering and Physical Sciences, Heriot-Watt University, Edinburgh, UK

future work in this area and because it is difficult to get thick enough samples with a high volume fraction of inclusions.

Low cost non-vacuum methods:

1. Dispersal of metal nanoparticles of different dimensions in an insulator or thermoplastic polymer matrix, in non-aqueous solution phase. Using this method, free standing flexible films or films on glass substrates of thicknesses ranging from a few microns to a few 100 microns can be produced.
2. The homogeneous solution of metal/ insulator, carbon nanotube, nano composites can be made using spin coating techniques as well. The thin films as thin as 100nm can be obtained using this technique on glass substrates.
3. It is also possible to generate mesoporous interpenetrating nano composites of TiO_2 (metal oxides) and metal particle composites, using screen printing or spin coating methods. The particle size from 10 – 100 nm can be varied to get a range of distributions. This metal–insulating matrix follows a distribution in three dimensions. CREST has a good expertise in developing such structures.
4. Nano-templating of metal/polymer using network of block copolymers could be another method that can be explored with CREST's facilities.

Vacuum based methods:

1. The metals can be deposited precisely of known thicknesses using vacuum deposition methods such as sputtering or evaporation performed at CREST.
2. Another approach could be the use of laser scribers available at CREST to create the patterns with the spacing as close as 50 microns.
3. Patterns on deposited metal layers could also be created using ion beam microtoming facility at Loughborough Materials Characterisation Centre (LMCC) at the Department of Materials. However, it may be difficult to generate the structure over an area of a few square centimetres.

One of the challenges of these fabrication processes is their limitation in the height of the substrate that can be created and how uniform the inclusions will be distributed in/on them.

1.7 Fundamental Electrical Properties of Materials

Understanding the reaction of the constituents of a material including the atoms, electrons, and protons, to applied EM fields, is fundamental in understanding how the physical and electrical properties of a material are affected by these fields. An atom of a material is made up of a nucleus containing protons (positively charged particles) and neutrons (neutral particles), around which electrons (negatively charged particles) orbit. Reference [20] examines the behaviour of the atoms of different materials, when subjected to external fields.

Dielectrics are "materials whose dominant charges in atoms and molecules are bound negative and positive charges that are held in place by atomic and molecular forces, and they are not free to travel" [20]. When external electric fields are applied to them, polarisation occurs, creating a net electric polarisation vector, $\boldsymbol{P}$ that increases the electric flux density. This gives rise to a *permittivity* (ε) that defines the dielectric, and varies from material to material [20], [56]. The relative permittivity, ε_r of a material is the ratio of its absolute permittivity, ε to the absolute permittivity of free space, ε_o.

Magnetic materials "exhibit magnetic polarisation when they are subjected to an applied magnetic field" [20]. This is a phenomenon that can only be exactly represented by quantum theory, but can be analysed using small electric current loops. A net magnetisation vector, $\boldsymbol{M}$ results that increases the magnetic flux density, related to the magnetic field intensity by the *permeability* (μ) of the material. The direction of $\boldsymbol{M}$ relative to that of the applied magnetic field defines the form of the material. The relative permeability, μ_r of a material is the ratio of its absolute permeability, μ to the absolute permeability of free space, μ_o.

Conductors are "materials whose prominent characteristic is the motion of electric charges and the creation of current flow" [20]. They possess loosely held free (valence) electrons that move to the surface of the conductor when an electric field is applied, resulting in a *conductivity* (σ) value, which is a function of the electron drift velocity and charge density of the material. For a conductor, $\sigma \gg j\omega\varepsilon$, where ω is the angular frequency.

When these materials are subjected to varying EM fields, these defining properties (ε, μ, σ) typically become lossy as they are not just real values but complex, where the imaginary parts indicates the loss of the material [56]. Applied fields alternating in polarity affect the polarization and magnetisation vectors, $\boldsymbol{P}$ and $\boldsymbol{M}$, and thus the permittivities and permeabilities which are therefore functions of frequency.

1.8 Heterogeneous Mixtures

Heterogeneous mixtures are mixtures made up of a homogenous media within which particles of equal or different sizes and different EM properties, in any lattice arrangement are embedded. A more commonly used configuration is spherical particles of equal radii in a(n) (in/semi-)finite simple cubic lattice for simpler analysis [9]. These mixtures have been extensively studied as they allow the existence of 'new' materials which do not occur naturally and have controllable EM properties by their inherent geometry.

The theories established in [9] form the general basis for the study of heterogeneous substrates/artificial dielectrics, although the earliest study is in [10]. The Clausius-Mossotti equation is used in [12–17] for describing the effective EM properties of a heterogeneous material. However, this equation is represented differently in the literature as some exclude the EM properties of the host [13]; only examine the static case, that is, no frequency terms [15], [16]; differentiate the particles' densities and polarisabilities in electric and magnetic modes [17] or do not distinguish between the inclusion's EM properties on a small or bulk scale [16]. They are similar in that their analyses are based on an infinite or semi-infinite heterogeneous medium. In general, an expression for the effective EM properties of a heterogeneous medium is given in [12] as

$$K_{\text{eff}} = K_1 \frac{[(K_2 + 2K_1)(K_1 - K_2)^{-1}] - 2p + C(K_1, K_2, p)}{[(K_2 + 2K_1)(K_1 - K_2)^{-1}] + p + C(K_1, K_2, p)}$$

where K_1, K_2 and K_{eff} are the appropriate EM parameters of the host material, the inclusions and the mixture respectively; p is the volume fraction of the inclusions, which is based on the local unit cell of the medium. $C(K_1, K_2, p)$ represents corrections for higher-order multipole terms as a result of the scattered fields [9], [57]. These canonical equations are extensively reviewed in Chapter 2 of this thesis.

1.8.1 Other Related Studies

Due to the amount of research gone into the study of heterogeneous media, a number of developments and applications have been carried out to examine how heterogeneous structures can be used in practice. Related research has been in the areas of metamaterials [13], [58], lens research [15], artificial dielectrics or materials [15], [59], single [60] or double negative materials [17], [18], [23], [61], and materials with equal permittivity and permeability [62], [63].

1.9 Overview of this Thesis

This chapter has given a general introduction to the research area for this thesis. The subsequent chapters deal with the different areas covered during the research. In Chapter 2, an extensive analysis of the canonical equations from different researchers in the field of artificial dielectrics is given. The different parameters that define what the effective EM properties of the heterogeneous structures will have are analysed individually using these equations. Graphical results are presented from these analyses. The variations between these equations have also been discussed and a conclusion given on which of them is robust enough to cover different heterogeneous structures. Chapter 3 explains the FDTD EM simulation process in order to generate a plane wave and thus the scattering (S-) parameters of homogenous and heterogeneous structures. This is necessary as the inversion algorithm used to obtain ε_{eff} and μ_{eff} requires these S-parameters along with the thickness of the samples. The inversion algorithm has also been explained in detail. In Chapter 4, comparisons are made between the results from the canonical equations and the simulation-inversion process, in order to give confidence that the inversion process works correctly and that the canonical equations can be used to quickly get an estimate of the ε_{eff} and μ_{eff} of a heterogeneous medium is. An example of designing a heterogeneous medium with pre-determined ε_{eff} using dielectric or metallic spherical or cubic inclusions have been given in this chapter.

Brief descriptions of the fabrication methods used in creating the samples used in this research are given in Chapter 5. Different measurement techniques used in measuring the permittivity and permeability of the samples has been explained; the measured and simulated results have also been discussed and compared. These different measurement techniques were done in order to determine which gave results agreeing more with those from the canonical equations and EM simulations. In Chapter 6, the simulated and measured performance of patch antennas on homogenous and heterogeneous substrates are examined and compared to understand how the samples impact the antenna performance. A summary of the key results and conclusions from this thesis along with the possible implications for industry and recommendations for future work are given in Chapter 7. The appendix containing relevant background information used in this thesis is given at the end.

1.10 References

[1] "YouTube - Nano, the next dimension (Film produced for European Commission)." [Online]. Available: http://www.youtube.com/watch?v=eCpkq_AeX50. [Accessed: 21-Jun-2011].

[2] "YouTube - IBM Self Assembly Technology Creates Airgap Microprocessors." [Online]. Available: http://www.youtube.com/watch?v=T8p8_zZNJEU. [Accessed: 21-Jun-2011].

[3] C.-C. Hsu and Y.-C. Lee, "Fabrication of flexible nano-wired polarizer by contact-transferred and mask embedded lithography and polyurethane acrylate mold," in *5th IEEE International Conference on Nano/Micro Engineered and Molecular Systems (NEMS)*, 2010, pp. 893–897.

[4] F. Juillerat, H. H. Solak, P. Bowen, and H. Hofmann, "Fabrication of large-area ordered arrays of nanoparticles on patterned substrates," *Nanotechnology*, vol. 16, no. 8, pp. 1311–1316, Aug. 2005.

[5] Y. H. Seo, D.-S. Choi, and K.-H. Whang, "A new fabrication method of nano-fluidic filters using self-Assembly of nano-spheres and surface tension," in *19th IEEE International Conference on Micro Electro Mechanical Systems*, 2006, pp. 306–309.

[6] H. I. Smith and H. G. Craighead, "Nanofabrication," *Physics Today*, vol. 43, no. 2, pp. 24–30, 1990.

[7] C. C. Njoku, W. G. Whittow, and J. C. Vardaxoglou, "Microwave antennas and heterogeneous substrates using nanomaterial fabrication techniques," in *IEEE Tropical Conference on Antennas and Propagation in Wireless Communications*, 2011, pp. 843–846.

[8] K. Banerjee, H. Li, C. Xu, Y. Khatami, H. F. Dadgour, and D. Sarkar, "Prospects of carbon nanomaterials for next-generation green electronics," in *10th IEEE International Conference on Nanotechnology*, 2010, pp. 56–61.

[9] L. Lewin, "The electrical constants of a material loaded with spherical particles," *IEE-Part III: Radio Comm. Eng.*, vol. 94, no. 27, pp. 65–68, 1947.

[10] Lord Rayleigh, "On the influence of obstacles arranged in rectangular order upon the properties of a medium," *Philosophical Magazine*, vol. 34, pp. 481–502, 1892.

[11] J. Brown, "Artificial dielectrics having refractive indices less than unity," *Proceedings of the IEE - Part IV: Institution Monographs*, vol. 100, no. 5, pp. 51–62, 1953.

[12] W. T. Doyle, "The Clausius-Mossotti problem for cubic arrays of spheres," *Journal of Applied Physics*, vol. 49, no. 2, pp. 795–797, 1978.

[13] X. Cai, R. Zhu, and G. Hu, "Experimental study for metamaterials based on dielectric resonators and wire frame," *Metamaterials*, vol. 2, no. 4, pp. 220–226, 2008.

[14] W. T. Doyle, “Optical properties of a suspension of metal spheres,” *Physical Review B*, vol. 39, no. 14, pp. 9852–9858, 1989.

[15] R. E. Collin, *Field Theory of Guided Waves*. New York: IEEE Press, 1991.

[16] A. Sihvola, *Electromagnetic Mixing Formulas and Applications*. London: IET, 1999.

[17] I. A. Kolmakov, L. Jylha, S. A. Tretyakov, and S. Maslovki, “Lattice of dielectric particles with double negative response,” in *28th Gen. Ass. Int. Union Radio Sci. (URSI)*, 2005.

[18] C. L. Holloway, E. F. Kuester, J. Baker-Jarvis, and P. Kabos, “A double negative (DNG) composite medium composed of magnetodielectric spherical particles embedded in a matrix,” *Antennas and Propagation, IEEE Transactions on*, vol. 51, no. 10, pp. 2596–2603, 2003.

[19] W. Whittow and J. Vardaxoglou, “Modifying conventional microwave antenna designs using fine scale structures and nanomaterials,” in *Loughborough Antennas & Propagation Conference*, 2009, pp. 749–752.

[20] C. A. Balanis, *Advanced Engineering Electromagnetics*, 2nd ed. New York: Chichester: Wiley, 1989.

[21] V. Yannopapas, “Artificial magnetism and negative refractive index in three-dimensional metamaterials of spherical particles at near-infrared and visible frequencies,” *Applied Physics A*, vol. 87, no. 2, pp. 259–264, Jan. 2007.

[22] O. F. Siddiqui, S. J. Erickson, G. V. Eleftheriades, and M. Mojahedi, “Time-domain measurement of negative group delay in negative-refractive-index transmission-line metamaterials,” *IEEE Transactions on Microwave Theory and Techniques*, vol. 52, no. 5, pp. 1449–1454, May 2004.

[23] A. Ahmadi and H. Mosallaei, “All-dielectric metamaterials: double negative behavior and bandwidth-loss improvement,” *IEEE Antennas and Propagation International Symposium*, pp. 5527–5530, Jun. 2007.

[24] J. B. Pendry, A. J. Holden, D. J. Robbins, and W. J. Stewart, “Magnetism from conductors and enhanced nonlinear phenomena,” *IEEE Transactions on Microwave Theory and Techniques*, vol. 47, no. 11, pp. 2075–2084, 1999.

[25] K. Buell, H. Mosallaei, and K. Sarabandi, “Embedded-circuit magnetic metamaterial substrate performance for patch antennas,” in *IEEE Antennas and Propagation Society International Symposium*, 2004, vol. 2, pp. 1415–1418.

[26] B. Tellini and M. Bologna, “Magnetic composite materials and arbitrary B-H relationships,” *IEEE Transactions on Magnetics*, vol. 46, no. 12, pp. 3967–3972, 2010.

[27] M. I. Kitra, C. J. Panagamuwa, P. McEvoy, J. (Yiannis) C. Vardaxoglou, and J. R. James, “Low SAR ferrite handset antenna design,” *IEEE Transactions on Antennas and Propagation*, vol. 55, no. 4, pp. 1155–1164, Apr. 2007.

[28] C. C. Njoku, W. G. Whittow, and Y. C. Vardaxoglou, “Designing microwave patch antennas using heterogeneous substrates,” in *European Conference on Antennas and Propagation (EuCAP)*, 2012, pp. 886–888.

[29] G. Kiziltas, D. Psychoudakis, J. L. Volakis, and N. Kikuchi, “Topology design optimization of dielectric substrates for bandwidth improvement of a patch antenna,” *IEEE Transactions on Antennas and Propagation*, vol. 51, no. 10, pp. 2732–2743, Oct. 2003.

[30] C.-C. Chen and J. L. Volakis, “Bandwidth broadening of patch antennas using nonuniform substrates,” *Microwave and Optical Technology Letters*, vol. 47, no. 5, pp. 421–423, Dec. 2005.

[31] D. Psychoudakis, Y.-H. Koh, J. L. Volakis, and J. H. Halloran, “Design method for aperture-coupled microstrip patch antennas on textured dielectric substrates,” *IEEE Transactions on Antennas and Propagation*, vol. 52, no. 10, pp. 2763–2765, Oct. 2004.

[32] D. Psychoudakis, J. L. Volakis, Z. N. Wing, S. K. Pillai, and J. W. Halloran, “Enhancing UHF antenna functionality through dielectric inclusions and texturization,” *IEEE Transactions on Antennas and Propagation*, vol. 54, no. 2, pp. 317–329, Feb. 2006.

[33] G. Lövestam, H. Rauscher, G. Roebben, B. S. Klüttgen, N. Gibson, J. Putaud, and H. Stamm, “Considerations on a Definition of Nanomaterial for Regulatory Purposes,” 2010.

[34] The Australian Government, “NICNAS Information Sheet,” *Industrial Chemicals Notification and Assessment Scheme*, Sydney, 2006.

[35] The Royal Society and the Royal Academy of Engineering, “Nanoscience and nanotechnologies : opportunities and uncertainties,” *Nanoscience and nanotechnologies*, London, Jul-2004.

[36] K. Hickman, “Nanomaterials: It’s a Small, Small World,” *CSA Discovery Guides*, 2002. [Online]. Available: http://www.csa.com/discoveryguides/nano/overview.php. [Accessed: 11-Jul-2011].

[37] J. Kim and C.-S. Han, “Nanomaterials for applications,” in *10th IEEE International Conference on Nanotechnology*, 2010, pp. 490–492.

[38] “NanoMaterials 2011 - Inspiring Commercial Success of Nanotechnology in Europe,” 2011. [Online]. Available: http://www.nanomaterials-conference.com/home.aspx. [Accessed: 11-Jul-2011].

[39] G. Cao, *Nanostructures & Nanomaterials: Synthesis, Properties & Applications*. Imperial College Press, 2004.

[40] J. Rao, H. Zou, R. R. A. Syms, E. Cheng, and C. Liu, “Fabrication of 2D silicon nano-mold based on sidewall transfer,” *Micro & Nano Letters*, vol. 6, no. 1, pp. 29–33, 2011.

[41] A. Botman, J. J. L. Mulders, and C. W. Hagen, “Creating pure nanostructures from electron-beam-induced deposition using purification techniques: a technology perspective,” *Nanotechnology*, vol. 20, no. 37, Sep. 2009.

[42] K. Hyungjun, L. Han-Bo-Ram, K. Woo-Hee, P. Sang-Joon, and C. H. In, “Nanomaterials fabrication using advanced thin film deposition and nanohybrid process,” in *IEEE Nanotechnology Materials and Devices Conference*, 2009, pp. 3–4.

[43] R. A. Said, “Localized electro-deposition (LED): the march toward process development,” *Nanotechnology*, vol. 15, no. 10, pp. S649–S659, Oct. 2004.

[44] O. Sardan, A. D. Yalcinkaya, and B. E. Alaca, “Batch fabrication of self-assembled Nickel-Iron nanowires by electrodeposition,” in *1st IEEE International Conference on Nano/Micro Engineered and Molecular Systems*, 2006, pp. 1101–1104.

[45] R. Yang, J. Zheng, W. Li, J. Qu, and X. Li, “Plasma-enhanced chemical vapour deposition of inorganic nanomaterials using a chloride precursor,” *Journal of Physics D: Applied Physics*, vol. 44, no. 17, pp. 1–6, May 2011.

[46] S. Matsui, *Three-Dimensional Nanostructure Fabrication by Focused Ion Beam Chemical Vapor Deposition*. Berlin, Heidelberg: Springer Berlin Heidelberg, 2010, pp. 211–229.

[47] M. S. Schmidt, A. Boisen, and J. Hubner, “Towards easily reproducible nano-structured SERS substrates,” in *IEEE Sensors*, 2009, pp. 1763–1767.

[48] K. Yamazaki and H. Namatsu, “Three-dimensional nanofabrication (3D-NANO) down to 10-nm order using electron-beam lithography,” in *7th IEEE International Conference on Micro Electro Mechanical Systems*, 2004, pp. 609–612.

[49] J. Zhang, Z.-I. Wang, J. Liu, S. Chen, and G. Liu, *Self-Assembled Nanostructures*. New York: Kluwer Academic Publishers, 2004.

[50] K. Bullis, “Self-Assembling Nanostructures,” *MIT Technology Review*, 2007. [Online]. Available: http://www.technologyreview.com/news/408313/self-assembling-nanostructures/. [Accessed: 20-Nov-2012].

[51] Y. Xia and G. M. Whitesides, “Soft Lithography,” *Annual Review of Materials Science*, vol. 28, pp. 153–184, Aug. 1998.

[52] M. Rothschild, T. M. Bloomstein, T. H. Fedynyshyn, R. R. Kunz, V. Liberman, M. Switkes, N. N. Efremow, S. T. Palmacci, J. H. C. Sedlacek, D. E. Hardy, and A. Grenville, “Recent trends in optical lithography,” *Lincoln Laboratory Journal*, vol. 14, no. 2, pp. 221–236, 2003.

[53] J. H. Bruning, “Optical lithography below 100 nm,” *Solid State Technology*, vol. 44, no. 11, Nov. 1998.

[54] D. J. Wagner, “Nanoimprint lithography: Review of aspects and applications,” *Proceedings of SPIE*, vol. 6002, p. 60020R, 2005.

[55] C. Wang, Q. Xia, W.-D. Li, Z. Fu, K. J. Morton, and S. Y. Chou, “Fabrication of a 60-nm-diameter perfectly round metal-dot array over a large area on a plastic substrate using nanoimprint lithography and self-perfection by liquefaction.,” *Wiley InterScience*, vol. 6, no. 11, pp. 1242–1247, Jun. 2010.

[56] A. R. von Hippel, *Dielectric Materials and Applications*. Artech House, 1954.

[57] J. A. Stratton, *Electromagnetic Theory*. New York: McGraw-Hill Book Inc, 1941.

[58] H. Cory, Y. J. Lee, Y. Hao, and C. G. Parini, “Use of conjugate dielectric and metamaterial slabs as radomes,” *IET Microwaves, Antennas & Propagation*, vol. 1, no. 1, pp. 137–143, 2007.

[59] D. R. Smith, J. B. Pendry, and M. C. K. Wiltshire, “Metamaterials and negative refractive index,” *Science*, vol. 305, pp. 788–792, Aug. 2004.

[60] P. N. Melezchik, A. Y. Poyedinchuk, Y. A. Tuchkin, and N. P. Yashina, “Periodic surface of materials with single and double negative parameters: absorption resonances,” in *The Fifth International Kharkov Symposium on Physics and Engineering of Microwaves, Millimeter, and Submillimeter Waves*, 2004, vol. 1, pp. 311–313.

[61] S. Sudhakaran, Y. Hao, and C. G. Parini, “An enhanced prediction of negative refraction from EBG-like structures,” *Microwave and Optical Technology Letters*, vol. 41, no. 4, pp. 258–261, May 2004.

[62] L. B. Kong, Z. W. Li, G. Q. Lin, and Y. B. Gan, “Ni-Zn ferrites composites with almost equal values of permeability and permittivity for low-frequency antenna design,” *IEEE Transactions on Magnetics*, vol. 43, no. 1, pp. 6–10, Jan. 2007.

[63] A. Thakur, A. Chevalier, J.-L. Mattei, and P. Queffélec, “Low-loss spinel nanoferrite with matching permeability and permittivity in the ultrahigh frequency range,” *Journal of Applied Physics*, vol. 108, no. 1, p. 014301, Jul. 2010.

Chapter 2. Dielectric Properties of Heterogeneous Mixtures with Inclusions of Different Shapes – Canonical Analysis

2.1 Introduction

An overview of the background research in this thesis has been given in Chapter 1. This chapter examines the electromagnetic (EM) properties of heterogeneous mixtures with emphasis on those with spherical and cubic inclusions. This will be done based on existing canonical equations found in published literature. It is essential to test these equations rigorously as they form the foundation of the simulations and measurements to follow, and are the basis of this thesis and any follow-on future research. This chapter introduces the analytical aspect of this thesis and the concepts explored here will be applied in the subsequent chapters, emphasizing the need for a well-rounded understanding of the effective EM properties of the heterogeneous media with various kinds of inclusions.

Interests in artificial dielectrics composed of small scale inclusions have existed as early as the late 19th century by Lord Rayleigh in [1]. The inclusions in these dielectrics can typically be in the nano- or micro-scale size or can be micro-sized clusters of nanoparticles. The inclusions can be dielectric [2–6], metallic/conducting [7–12] or ferrites [13–17] and there can be different lattice arrangements of these particles within the homogenous media depending upon requirements. The typical arrangement is the simple cubic (SC) lattice in which the particles are equi-distant from each other in all three dimensions (axes) only. Other cubic lattice arrangements include face-centred cubic (FCC), body-centred cubic (BCC), [18], which allow for greater volume fraction of spherical inclusions (see Figure 2.1). The FCC increases the total volume that the particles occupy from that of the SC by almost 50% for the most densely packed scenario [19]. In addition, there are other non-cubic lattice arrangements [20] such as monoclinic, triclinic and hexagonal lattices [21]. These arrangements may also be simple, face-, body- or base-centred. In this research, simple cubic lattices were primarily investigated because of their symmetry, simplicity and ease of reproduction. Spherical and cuboidal shaped inclusions [22–24] were considered. Depending on the lattice arrangement and the EM properties selected for these inclusions and their host media, different materials with a different effective permittivity, ε_{eff} and permeability, μ_{eff}

(and other EM properties) result. These mixtures typically have an ε_{eff} and μ_{eff} lying between the ε and μ of the host medium and that of the inclusions, as sometimes negative permittivity and/or permeability may occur over frequencies in the GHz to THz range and dependent on the modes of excitation [25–27]. These 'effective' EM properties can be defined as the EM properties the heterogeneous medium has when considered as a homogenous/bulk material.

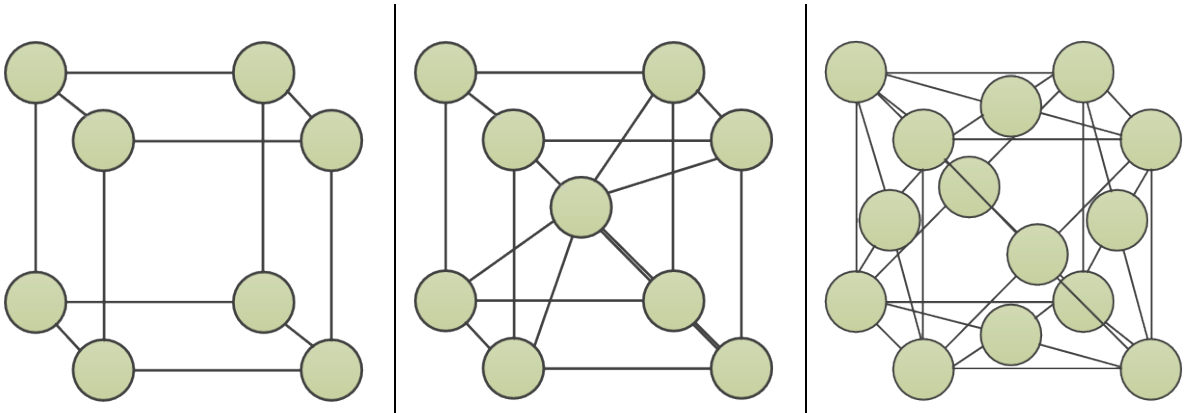

(a) (b) (c)

Figure 2.1: 3-D representation of the (a) simple cubic, (b) body-centred cubic and (c) face-centred cubic lattices.

Throughout this thesis, (ε_1, μ_1) and (ε_2, μ_2) are the permittivity and permeability of the host medium and the inclusions respectively, while *p* is the total volume fraction of the inclusions. The permittivity and permeability values are relative ε_0 and μ_0. It should be noted that the spacing of the particles is measured centre-to-centre or edge-to-edge throughout this research as shown in Figure 2.2 (a). These spacings also represent the unit cell size for an SC lattice arrangement where the spacing is equal in all 3 dimensions, as shown in Figure 2.2 (b), which shows the 2-D view. In the SC lattice, the inclusions are placed at each corner of an imaginary cube of size, *s*. This size is also known as the lattice constant.

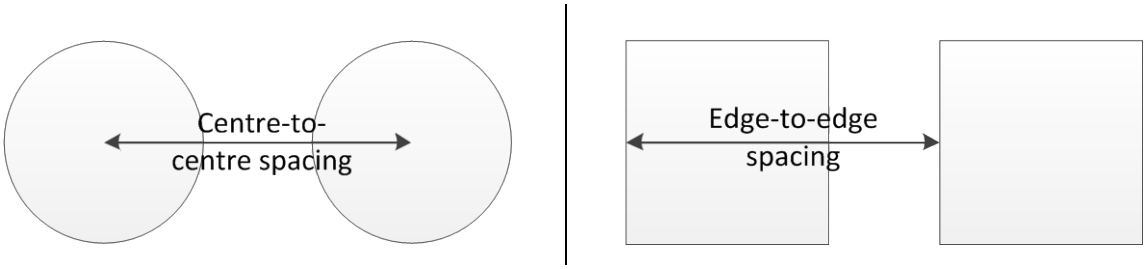

(a)

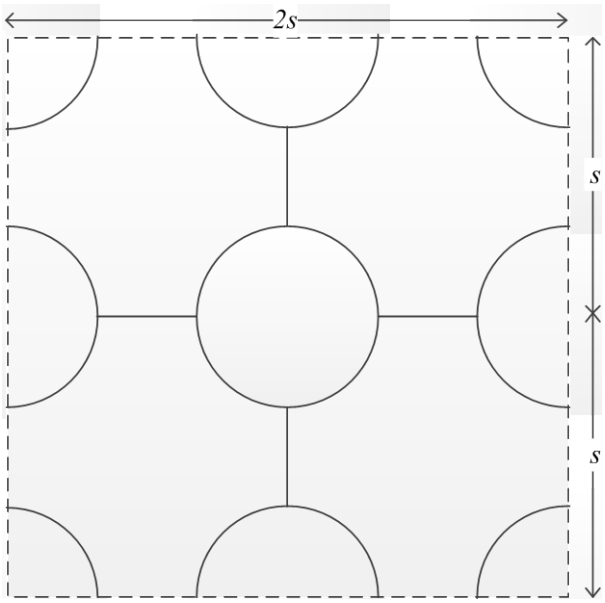

(b)

Figure 2.2: Diagrams showing (a) the different spacing definitions and (b) a unit cell of size, *s*, in a simple cubic lattice as used in this thesis

Previous papers on heterogeneous mixtures for EM applications were analysed and reviewed in-depth in Section 2.2. This formed the foundation of this thesis and gave insight on the expected values of the EM properties of the heterogeneous mixtures. Section 2.3 compares the different canonical equations and how they affect the ε_{eff} and μ_{eff} of the heterogeneous mixtures. Parametric studies of the different variables in the canonical equations are presented in Section 2.4 in order to understand/show how they affect the effective permittivity (ε_{eff}) and permeability (μ_{eff}) of the heterogeneous mixtures, while Section 2.5 examines heterogeneous mixtures with non-spherical inclusions. The conclusions are given in Section 2.6.

2.2 Literature Review of Canonical Equations

Several authors have developed analytical equations for the effective permittivity of mixtures; these will be discussed in detail in this section and compared to each other in Section 2.3. Generally, more emphasis was placed on finding the effective permittivity, ε_{eff} first and then deriving the μ_{eff} as an analogue of the equations for the ε_{eff}. This may be due to the fact that there are more materials likely to have the same permeability as that of free space.

2.2.1 Lewin's Analysis

In [3], Lewin studied a dielectric homogenous medium which had in it an array of spherical particles from a different bulk material, with uniform spacing, *s* and radius, *a*, in order to determine the effective permittivity (ε_{eff}) and permeability (μ_{eff}) of the mixture. His arrangement was infinite in two axes, *x* and *y*, and semi-infinite in the third, *z*, from z = 0 to z = $+\infty$. The validity of his study is stated as being restricted to frequencies where the sizes of the particles are small, less than a tenth of the wavelength ($\leq \lambda/10$), so that the particles themselves do not resonate at the operating frequencies. Another restriction was that the particles should not be too densely packed as the formula may break down when the "electrical contact between the particles interferes with the normal behaviour of the binder" or host medium [3]. However, as will be seen in Chapter 4, these equations agree with the results from simulations for mixtures with closely packed inclusions. His analysis assumed that the particles were arranged in an SC lattice as shown in Figure 2.3.

An EM plane wave propagates through the mixture in the positive *z*-direction; the electric (*E*) and magnetic (*H*) fields are orthogonal and linearly polarised: E_x and H_y respectively. At the $z = 0$ boundary, part of this wave is reflected while part is transmitted through the mixture, as the refractive index on either side of the boundary differs. Each particle in the mixture is influenced by two fields: the incident field and the "mutual" field. The "mutual" field is the sum of all the fields due to the reflections and transmissions from all the other particles. The incident and 'mutual' field within the medium forms the transmitted field. For a particle at position, say (x_1, y_1, z_1), let the sum of the fields at that particle be E_{x1} and H_{y1}. All the particles on the plane $z = z_1$ are affected the same way, so the fields at each of these particles are functions of z_1 only. Since the total field varies in a complex exponential form: e^{-jkz_1} (where k is the propagation constant in the medium) and the inclusions are spherical, the

problem may be reduced to the scattering of a plane wave by a spherical object as fully described in [28].

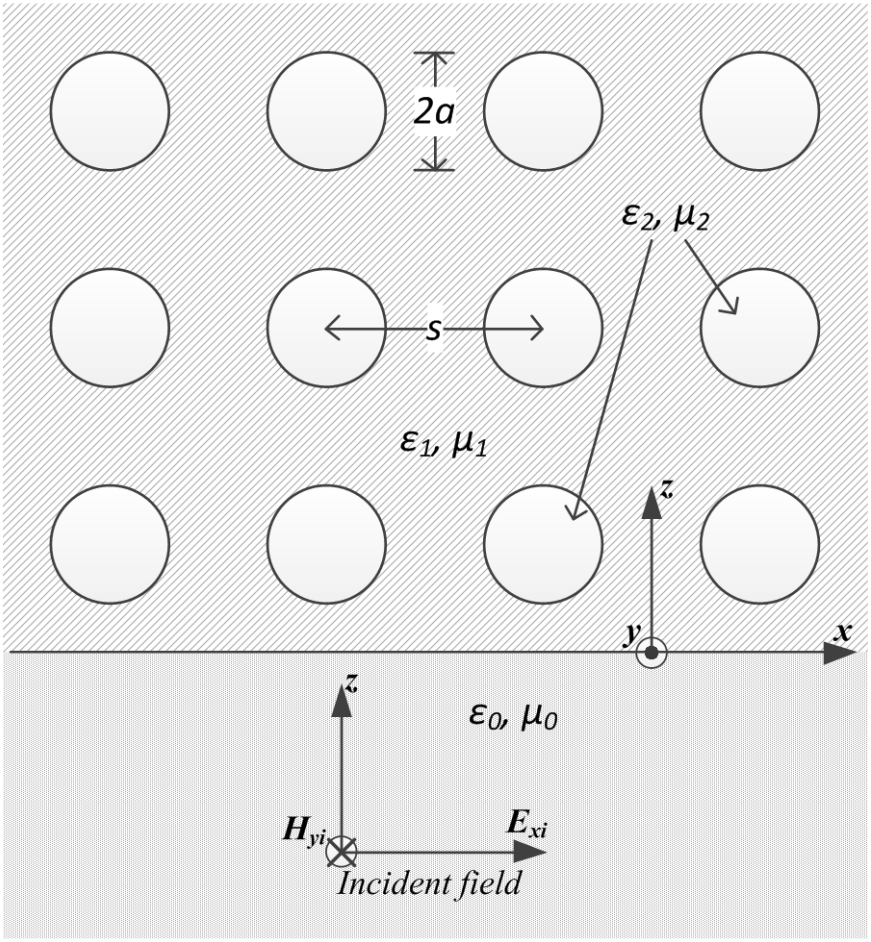

Figure 2.3: EM plane wave incident on a cubic lattice of spheres in a homogenous medium (image adapted from [3])

Equations for the scattered E and H fields from these spherical inclusions were obtained by assuming $a \ll \lambda/\sqrt{\varepsilon_1 \mu_1}$ in order to reduce the solution given Stratton in [28] by retaining only the first term of the series of vector wave functions. This inequality also serves as a rule of thumb for differentiating a heterogeneous medium when it can be seen as macroscopically homogenous from when it is distinctively heterogeneous. The magnetic and electric scattering coefficients are also reduced to simple forms by using the above inequality. The mutual E and H fields were derived as a summation of the individual E and H scattered fields through further approximations and simplifications. The total field is the sum of the incident and 'mutual' fields. The equation for the total field is used to calculate the reflected field at the boundary, $z = 0$, and at the reference position (x_1, y_1, z_1) and two simultaneous equations

in terms of ε_{eff} and μ_{eff} are obtained. Following this, expressions for the bulk constants of the mixture were obtained as functions of the effective ε and μ of the particles, the ε and μ of the host medium and the volume fraction of the particles, as shown in equation (2-1) [3].

$$\varepsilon_{eff} = \varepsilon_1\left(1 + \frac{3p}{\frac{\varepsilon_p + 2\varepsilon_1}{\varepsilon_p - \varepsilon_1} - p}\right); \qquad \mu_{eff} = \mu_1\left(1 + \frac{3p}{\frac{\mu_p + 2\mu_1}{\mu_p - \mu_1} - p}\right); \tag{2-1}$$

where $(\varepsilon_{eff}, \mu_{eff})$ and (ε_p, μ_p) are the effective permittivity and permeability of the mixture and the particles respectively; (ε_1, μ_1) is the permittivity and permeability of the host; $p = \frac{4}{3}\pi\, a^3/s^3$ is the ratio of the total particle volume to the total volume of the mixture. The volume fraction can alternatively be calculated from the number and geometric shape of the inclusions when they are known especially in the case of non-uniform distribution [2].

Lewin differentiates between the effective permittivity of the particle at a much smaller physical size, typical $\ll \lambda/10$ and that of the bulk form of the particle material. That is, if the permittivity and permeability of the bulk material of the particle is given by (ε_2, μ_2), the effective EM parameters of the particle (ε_p, μ_p), is given by equation (2-2) [3].

$$\frac{\varepsilon_p}{\varepsilon_2} = \frac{\mu_p}{\mu_2} = \frac{2(sin\theta - \theta cos\theta)}{(\theta^2 - 1)sin\theta + \theta cos\theta} = F(\theta) \tag{2-2}$$

where the argument, $\theta = ka\sqrt{\mu_2\varepsilon_2}$; $k = 2\pi/\lambda$; $\lambda =$ operating wavelength and a is the radius of the spherical inclusions. Note: the derivation or source of $F(\theta)$ has not been given in [3]. ε_p and μ_p are "the values of the constants ε_2 and μ_2 which very small particles would have to possess (as in the static case) in order to produce the same electrical effect" [3]. As (ε_p, μ_p) are dependent on the wavelength and size of the particle, $F(\theta)$ approaches 1 when $a \ll \lambda$, as such $(\varepsilon_p, \mu_p) \cong (\varepsilon_2, \mu_2)$. In this case, that is, where θ is very small, $F(\theta)$ can be expanded using Taylor's series, as in equation (2-3), and the θ terms vanish, leaving $F(\theta) \approx 1$.

$$F(\theta) = 1 + \frac{\theta^2}{10} + \frac{9\theta^4}{100} + \cdots \tag{2-3}$$

Figure 2.4 shows the variation of ε_p with particle size, a, for constant frequency, $f = 10$ GHz, $\varepsilon_2 = 10$ and $\mu_2 = 1$. It can be seen from Figure 2.4 that $\varepsilon_p = \varepsilon_2$ until where $a \approx \lambda/10$. The spikes tend to occur when the denominator of equation (2-2) becomes very small and

goes through zero, but this is very likely a numeric effect given the choice of the equation for $F(\theta)$ – a periodic function, used to relate ε_2 to ε_p. The positions of these spikes are affected by the value of ε_2 and the frequency of operation, and occur at regular intervals as shown, when $a = 0.5n\lambda_g$, where $n = 0,\ 1,\ 2,\ 3,\ldots$, and $\lambda_g = \lambda/\sqrt{\mu_2\varepsilon_2}$, is the wavelength in the dielectric.

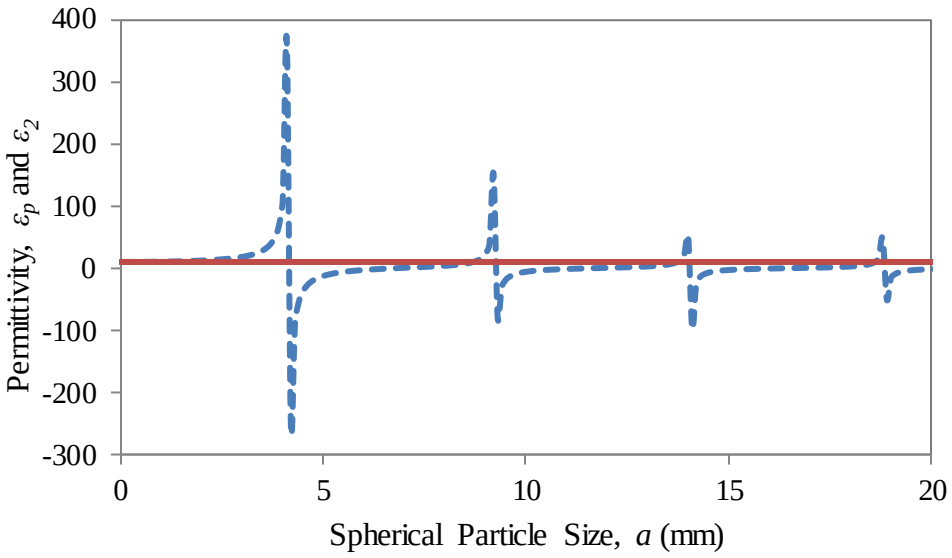

Figure 2.4: Variation of ε_p (– – –) and ε_2 (——) with particle size, a, at $f = 10$ GHz

On obtaining these equations in [3], the author examined the bulk constants of the mixture for different scenarios – a static case where the "field fully penetrates the particles", and when the particles were "small air bubbles", metal and non-magnetic materials. Lossy or complex effective permeability may result due to the heterogeneity of the mixture. The effect of the particle volume density (spheres/m^3) was examined to see how it affected the validity of the formulae derived. Lewin restricted the upper limit of the validity of his formula to being when $\lambda_g/|\sqrt{\varepsilon\mu}| > 10a$, as $\varepsilon_{eff} = \varepsilon_p$ when $p = 1$ (100% loading, theoretically), whereas ε_{eff} should equal ε_2 [3]. The structures used in this thesis satisfy this inequality, that is, $\lambda_g/|\sqrt{\varepsilon\mu}| > 10a$.

For dielectric inclusions, by extending the range of the frequencies to as much as 500 GHz, higher values of ε_{eff} as high as 110 occur, for say, an inclusion size of 110 μm. This is because the guided wavelength $\left(\lambda_g = \lambda_0/\sqrt{\varepsilon_2\mu_2}\right)$ approaches the size of the inclusions. However, for metallic inclusions, there is a cut-off frequency at about 46 GHz as the high

value of the imaginary part of ε_2, $Im(\varepsilon_2)$ creates a value of infinity in the arguments of the $\sin(\cdot)$ or $\cos(\cdot)$ (in the equations) which are used to find the ε_{eff} and μ_{eff}.

2.2.2 Sihvola's Analysis

Beginning with an analysis of the EM response of a sphere to an electric field, Sihvola in [2] also examined the case of a homogeneous medium with "spherical inclusions" and stated its effective permittivity as

$$\varepsilon_{eff} = \varepsilon_1 + \frac{N\alpha_1}{1 - \frac{N\alpha_1}{3\varepsilon_1}} \qquad \frac{\varepsilon_{eff} - \varepsilon_1}{\varepsilon_{eff} + 2\varepsilon_1} = \frac{N\alpha_1}{3\varepsilon_1} \tag{2-4}$$

where N = number density of the spheres (m^{-3}), that is, the number of spheres per unit volume, and α_1 is the electric dipole polarisability. Equation (2-4) is called the *Clausius-Mossotti (C-M) formula*. An expression for polarisability of a sphere was given as

$$\alpha_1 = V(\varepsilon_2 - \varepsilon_1)\frac{3\varepsilon_1}{\varepsilon_2 + 2\varepsilon_1} \tag{2-5}$$

where V is the volume of one sphere. Due to the inherent symmetry of the sphere, the polarisability is equal in all three dimensions. The polarisability of an inclusion is "the simplest measure of its response to an incident electric field" and it relates the dipole moment created to the external electric field in a linear relationship given by $\overline{\boldsymbol{p}} = \alpha\overline{\boldsymbol{E}}$ [2]. For other shapes, the expression will be different. Combining equations (2-4) and (2-5) give the *Rayleigh mixing formula*, also known as the *Maxwell Garnett (M-G) mixing formula*; they are usually written in slightly different forms distinguished only by simple algebraic manipulations. The M-G equation is given as:

$$\varepsilon_{eff} = \varepsilon_1 + 3p\varepsilon_1\frac{\varepsilon_2 - \varepsilon_1}{\varepsilon_2 + 2\varepsilon_1 - p(\varepsilon_2 - \varepsilon_1)} \tag{2-6}$$

where $p = NV$, is the "volume fraction of the inclusions in the mixture". Rearranging equation (2-6) gives an expression simlar to Lewin's equations [3] (equation (2-1)) as shown in equation (2-7):

$$\varepsilon_{eff} = \varepsilon_1 \left[1 + 3p \frac{1}{\frac{\varepsilon_2 + 2\varepsilon_1}{\varepsilon_2 - \varepsilon_1} - p} \right] \tag{2-7}$$

The use of the dipole moments in deriving the ε_{eff} and μ_{eff} presents an alternative to using the scattered fields by the inclusions used in [3] to extract the ε_{eff} and μ_{eff} of the heterogeneous medium. The results plotted in [2] show that the host and inclusion media are not contributing to the effective permittivity on a simple volume ratio basis. This is an important concept and the graphical representation of this phenomenon is also shown in Figure 2.5. This graph was derived by swapping the values of ε_1 and ε_2 with each other and shows the non-symmetric nature of the M-G equation. Data used: $\varepsilon_{1,2} = 1.04$ (tan $\delta =$ 0.00012) and 11.9 (tan $\delta = 0.02$), $\mu_1 = \mu_2 = 1$ (the values shown are absolute values).

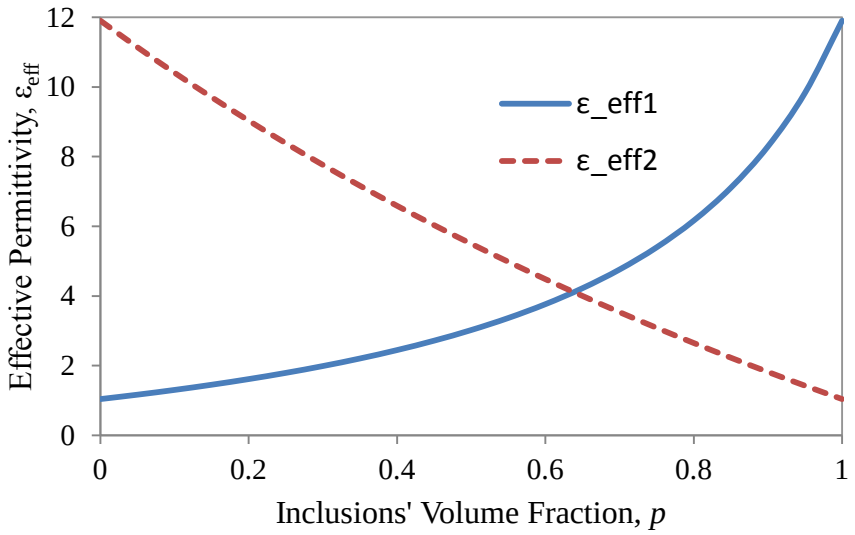

Figure 2.5: Variation of ε_{eff} with inclusions' volume fraction for complementary mixtures, where the continuous line represents the case where ε_1 = 1.04 (tan $\delta = 0.00012$) and ε_2 = 11.9 (tan $\delta = 0.02$), and the dashed line where these values are swapped.

If the host and inclusions' EM properties were contributing to the effective EM properties in equal proportion, the point at which the two ε_{eff} lines cross would be at the 0.5 volume fraction. Thus, a 50% volume ratio each from the host and from the inclusions does not imply that the ε_{eff} is halfway between ε_1 and ε_2 because the "geometric structure of the mixture is not symmetric" [2]. Figure 2.5 also shows that the host properties dominate the effective EM properties and thus to obtain a higher value of ε_{eff}, it may be better to have $\varepsilon_1 > \varepsilon_2$ for a

volume fraction below the point of intersection. The higher the dielectric contrast between ε_1 and ε_2, the further away this intersection point goes from 0.5. Therefore, if $\varepsilon_1 = \varepsilon_2$, this point of intersection will occur at 0.5, which can also be deduced logically. Figure 2.5 can also be derived using Lewin's equations for ε_{eff} and μ_{eff}.

Similar expressions can be written for the effective magnetic permeability by substituting the electric quantities with magnetic quantities. Using equation (2-7) for the μ_{eff} of a heterogeneous medium with $\mu_1 = \mu_2 = 1$ results in $\mu_{eff} = 1$, for any inclusion type due to the $(\mu_1 - \mu_2)$ term in the denominator, as shown in Figure 2.8 (b). These equations are limited to heterogeneous media with spherical inclusions and have been modified for inclusions with non-symmetric shapes such as ellipsoids, needles and discs by using their depolarisation factors. Equations for random orientation of inclusions have been derived such that the effective EM properties are primarily functions of the volume fraction of the inclusions and their polarisabilities, taking into account any symmetries or lack of. Lossy, inhomogeneous, anisotropic, nonlinear and dispersive mixtures were examined.

2.2.3 Cai's Analysis

The total scattering effect of the medium containing electrically small "obstacles" when an electromagnetic wave travels through it can be represented by the effective permittivity and permeability of that medium [29]. By initially examining the scattering properties represented by electric and magnetic scattering coefficients, of an isolated sphere on which an EM wave impinges, Cai et al states the *Clausius-Mossotti* equation for the effective properties, as

$$\varepsilon_{eff} = 1 + \frac{N\alpha_1}{1 - N\alpha_1/3} \qquad \mu_{eff} = 1 + \frac{N\beta_1}{1 - N\beta_1/3} \tag{2-8}$$

where N is the number of particles per unit volume given by $p = 4\pi N a^3/3$; a is the sphere radius; α_1, β_1 are the electric and magnetic dipole polarisabilities; $\alpha_1 = j6\pi a_1/k_0^3$, $\beta_1 = j6\pi b_1/k_0^3$; a_1, b_1 are the electric and magnetic scattering coefficients (their general expressions are given in equations (2-9) and (2-10)), and $k_0 = \omega/c$ is the wave vector in a vacuum. The m^{th} order electric scattering coefficient is given by:

$$a_m = \frac{n\psi_m(nx)\psi'_m(x) - \psi_m(x)\psi'_m(nx)}{n\psi_m(nx)\xi'_m(x) - \xi_m(x)\psi'_m(nx)} \tag{2-9}$$

while the m^{th} order magnetic scattering coefficient by:

$$b_m = \frac{\psi_m(nx)\psi'_m(x) - n\psi_m(x)\psi'_m(nx)}{\psi_m(nx)\xi'_m(x) - n\xi_m(x)\psi'_m(nx)} \tag{2-10}$$

where n is the refractive index of the particle, ψ_m and ξ_m are the Riccati-Bessel functions related to the spherical Bessel functions by $\psi_m(z) = zj_m(z)$ and $\xi_m(z) = zh_m^{(1)}(z)$ [11], [28], [29]. The prime ($'$) represents differentiation and is given by [30]:

$$\left(\frac{1}{z}\frac{d}{dz}\right)^m [z^{n+1}f_n(z)] = z^{n-m+1}f_{n-m}(z) \tag{2-11}$$

where $f_n(z)$ is any of the spherical Bessel functions on z. These coefficients are useful in calculating the electric and magnetic polarisabilities used in deriving ε_{eff} and μ_{eff}, and have been used in deriving equation (2-1) above in their reduced forms. Equations (2-9) and (2-10) are from the expansion of the incident, reflected and transmitted fields in vector spherical wave functions by analysing the boundary conditions for the diffraction of these fields by a single spherical object, as fully described in [28]. The Cartesian coordinate system was used in representing the electric and magnetic fields of the plane wave impinging on the sphere. The graphical result in [29] for a Polymer medium containing dielectric particles, was recalculated in this research over the same frequency range, and the real parts of the ε_{eff} and μ_{eff} are shown in Figure 2.6. Data used: $\varepsilon_1 = 1.05$, $\varepsilon_2 = 88.3$, $\mu_1 = \mu_2 = 1$, $f = 4.5 - 7.0$ GHz, $a = 2.7$ mm, $s = 6.7$ mm. Note that the real part of μ_{eff} is negative over a certain frequency band – due to magnetic resonance. This band spans between the frequency where the imaginary part of the magnetic scattering coefficient, b_1 goes through zero and where μ_{eff} goes through zero [29]. At the upper frequency, the size of the gaps between the spheres was greater than $\lambda/10$ of the operating frequency. By varying the permittivity and/or size of the inclusions, the bandwidth over which the negative μ_{eff} occurs can be altered which may be useful in the design of magnetic resonators. This initial analysis by the authors was used in designing a double negative medium by including wire frames in the structure in order to create a negative permittivity region, which coincided with where the negative permeability created by the spheres occurred. An explanation for this magnetic response has been given in Section 2.2.6. Cylindrical inclusions were also examined here by using a volume equivalence transformation process as will be discussed later in Chapter 4.

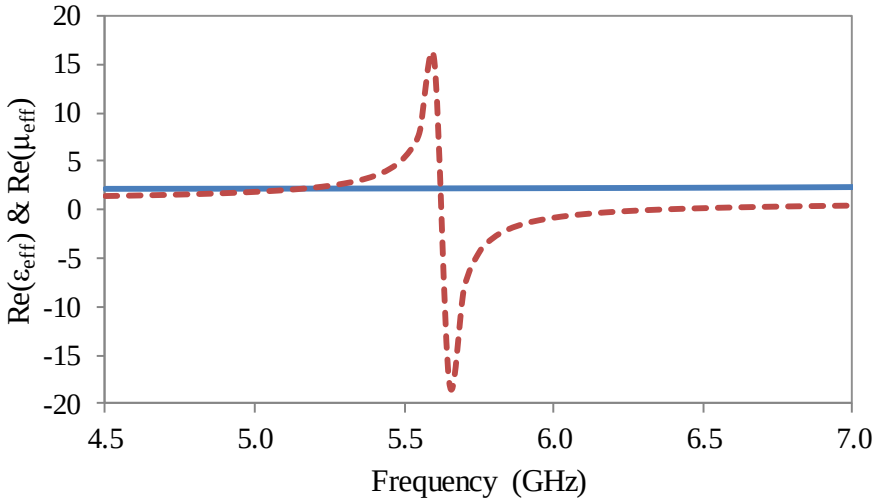

Figure 2.6: Variation of the real parts of ε_{eff} (continuous) and μ_{eff} (dashed) with frequency as shown in [29]

2.2.4 Doyle's Analysis

A general mathematical expression for the effective electric permittivity, magnetic permeability, electrical and thermal conductivities, and particle diffusivity for an isotropic heterogeneous medium is given in [31] as

$$K_{eff} = K_1 \frac{[(K_2 + 2K_1)(K_1 - K_2)^{-1}] - 2p + C(K_1, K_2, p)}{[(K_2 + 2K_1)(K_1 - K_2)^{-1}] + p + C(K_1, K_2, p)} \tag{2-12}$$

where K_1, K_2 and K_{eff} are the general constitutive parameters of the host medium, the spheres and the mixture respectively. These parameters can be the electric permittivity, magnetic permeability, conductivities or diffusivities (thermal motion of particles). $C(K_1, K_2, p)$ represents corrections for higher-order multipole terms [10], [31]. This correction term accounts for the higher inclusion densities and/or lattice types; different expressions for this term have been proposed [1], [31] and may be dependent on the lattice arrangement of the inclusions. Higher multipole terms vanish in a uniform field [2]. Equation (2-12) is partly based on the work by J. C. Maxwell in [32] and has been modified to include the correction terms.

In [31], the correction term is examined in order to come up with a more accurate expression for the effective parameters of the heterogeneous medium irrespective of volume ratios, because without it, equation (2-12) is limited in its validity to moderate or low particle densities, where the inclusions were much smaller than their spacing. Without this correction

term, and substituting with the symbols used in [3], an equation closely related to Lewin's equation (2-1) was obtained. The result of this algebraic manipulation is given in equation (2-13):

$$K_m = K_1\left[1 - \frac{3p}{\frac{K_2 + 2K_1}{K_1 - K_2} + p}\right] \tag{2-13}$$

In a later analysis by Doyle in [11], the ε_{eff} of the mixture is given as:

$$\varepsilon_{eff} = \varepsilon_1\left(1 + \frac{4\pi N\alpha_1}{1 - 4\pi\frac{N\alpha_1}{3}}\right) \qquad \alpha_1 = i\frac{3a^3}{2x^3}a_1 \tag{2-14}$$

where α_1 is the exact effective dipole polarisability; a is the particle radius; a_1 is the 1st order electric scattering coefficient (see equation (2-9)); x is a size parameter defined as $2\pi n_0 a/\lambda$; n_0 is the real refractive index of the host medium; and λ is the vacuum wavelength. Equation (2-14) by Doyle from [11] is valid for isolated spheres of any size. Although [11], [31] focused on deriving ε_{eff}, the equation for μ_{eff} can be obtained as being analogous to equation (2-14).

2.2.5 Collin's Analysis

The work carried out by Collin in [7] is similar to that done by Lewin in [3]. The main difference here is that Collin examined "identical conducting obstacles in a regular three-dimensional pattern", held by a lightweight material, and looked at the static case initially being simpler to analyse. Each obstacle when exposed to a propagating electric field mirrors the behaviour of a dielectric molecule by exhibiting a dipole moment, producing a net polarization, and thus an effective permittivity, ε_{eff}, greater than that of free space. Also, when the artificial dielectric is under the influence of a "high-frequency magnetic field", a net magnetic polarisation is produced, and this conducting obstacle exhibits a diamagnetic behaviour, that is, the magnetic field it produces is in opposition to the impinging magnetic field. The equation derived for the effective permittivity of the medium uses Lorentz Theory, assumes the obstacles have spherical symmetry in a cubical or random array, and considers only dipole interactions [7]. Thus it is valid only for cases where the dimensions of the inclusions are much smaller than their spacing. The effective properties of the artificial dielectric from this analysis are given in (2-15):

$$\varepsilon_{eff} = 1 + \frac{N\alpha_1}{1 - \alpha_1 C} \qquad \mu_{eff} = 1 + \frac{N\beta_1}{1 - \beta_1 C} \tag{2-15}$$

where α_1, β_1 are the inclusion's electric and magnetic polarisabilities; *N* is the density of the inclusions and *C* is the interaction constant, which depends primarily on particle shape and in some geometries, depends on the number of inclusions along each axis and can be defined as:

$$C = \frac{1.202}{\pi v^3} - \frac{8\pi}{v^3}\left[K_0\left(\frac{2\pi w}{v}\right) + K_0\left(\frac{2\pi u}{v}\right)\right] \tag{2-16}$$

where *u*, *v* and *w* are the spacings of the obstacles in the *x*, *y* and *z* directions respectively; $K_0(\cdot)$ is the zeroth order modified Bessel function of the second kind, and for small *r*, is given by

$K_0\left(\frac{2m\pi r}{v}\right) \approx -\left(\gamma + \ln\frac{m\pi r}{v}\right)$, and for large *r*, decays exponentially according to:

$$K_0\left(\frac{2m\pi r}{v}\right) \approx \left(\frac{v}{4mr}\right)^{1/2} e^{-2m\pi r/v} \tag{2-17}$$

where γ is Euler's constant, and $r = [(x - x_0)^2 + (y - y_0)^2 + (z - z_0)^2]^{1/2}$, is the vector between an obstacle at the origin (x_0, y_0, z_0) where $x = y = z = 0$, and one at (x, y, z). This Bessel function is readily computed in MATLAB using the function '*besselk*'. The approximation for small *r* is in closer agreement with the actual calculated value of $K_0\left(\frac{2m\pi r}{v}\right)$, and the actual decay is represented by the approximation for large *r*.

The interaction constant was derived from considering a three-dimensional array of unit dipoles polarised along the *y*-axis and extending to plus and minus infinity. By considering the effect of all other dipoles on a single one positioned at the origin, $x = y = z = 0$, the potential at the origin was derived. Further derivations were carried out using cylindrical coordinates. Although the limiting value of r in order to decide which of the equations in (2-17) to use in calculating $K_0(\cdot)$ is not stated, it can be taken from the definition of r to be related to the density of the inclusions in the host, that is, how closely packed they are within the lattice. More complex forms of equation (2-16) are given in [7] to take into account the number of inclusions along each axis. These derivations were carried out in the Cartesian coordinate system. More complicated versions of equation (2-16) were derived for different scenarios such as the unit dipoles within a waveguide.

If equations (2-15) – (2-17) are solved for spherical inclusions, a closed form equation similar to that in [3] is obtained as shown in equation (2-1), as will be discussed in Section 2.3.

2.2.6 Kolmakov's Analysis

Although the focus of the study in [4] was on arranging dielectric particles to obtain negative real parts of ε and μ, it first examined the ε_{eff} and μ_{eff} of the mixture by modifying the equations in [3] to include magnetic and electric resonance modes [25], [33] represented using resonating spheres of different sizes. The magnetic resonance mode accounted for the magnetic dipoles while the electric resonance mode was for the electric dipoles, and each mode was represented by small and large spheres respectively. This magnetic resonance was also examined in [34]. Graphical results in [4] show the effect of this modification over a specific frequency range and for selected physical and EM properties. The volume fraction and particle radius were different in each of these modes in order to take into account the effect of these different modes on the ε_{eff} and μ_{eff}. Using these different resonance modes created a slight frequency shift as it takes into account the "electrical contrast between the inclusions" and the host medium. In addition to spherical particles, [4] examines the case for an array of cylindrical particles as an analogue of the spherical particles.

Reference [4] also states the *Clausius-Mossotti* relation extended from [31] to include volume densities and polarisabilities in electric and magnetic resonance modes as:

$$\frac{\varepsilon_{eff}-\varepsilon_1}{\varepsilon_{eff}+2\varepsilon_1}=\frac{n_e\alpha_e}{3\varepsilon_1}+\frac{n_m\alpha_m}{3\varepsilon_1} \qquad \frac{\mu_{eff}-1}{\mu_{eff}+2}=\frac{n_m\beta_m}{3\mu_0} \tag{2-18}$$

where μ_0 is the permeability of the host material assuming it is non-magnetic; (n_m, n_e) and (α_m, α_e) are the volume densities and electric polarisabilities in magnetic and electric resonance modes respectively; and β_m is the magnetic polarisability in magnetic resonance. α_m accounts for "the remaining static electric polarisability of spheres in magnetic resonance modes" [4]. If $\alpha_m = 0$, reverts (2-18) to (2-4). Again the validity of the mixing theory here is limited to when the lattice constant (or particle spacing) is much smaller than the wavelength.

As two spheres of different sizes are used, the larger sphere resonates in the TM_{111} mode while the smaller sphere resonates in the TE_{111} mode over the same frequency band in order to create a double negative medium. The poles of Lewin's equation (2-1) for ε_{eff} and μ_{eff} occur at different points, therefore, by matching them up using different sphere sizes, the

electric and magnetic resonance modes occur over the same frequency band. “These modes are not strong eigenmodes of the spherical cavity resonator but can be specified to at frequencies close to the spherical cavity eigenfrequencies” [25]. This concept has been briefly mentioned in Section 4.2 and is shown in Figure 2.7. Data used: $a = 600$ µm, $s = 1300$ µm, f = 1-100 GHz, $\varepsilon_1 = 2.25$ (tan $\delta = 0.001$), $\varepsilon_1 = 10.2$ (tan $\delta = 0.0023$), $\mu_1 = \mu_2 = 1$. It can be seen that the electric and magnetic resonances occur at different frequencies for the same sized sphere. As the resonances are partially dependent on the size of the inclusions, by changing the size of some of the spherical inclusions, these resonances can be altered such that they occur at the same frequency.

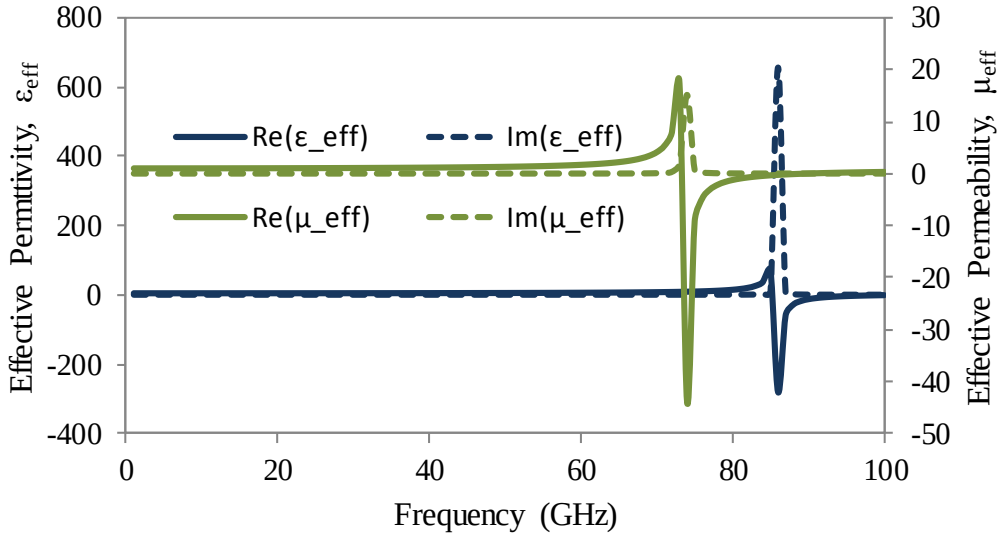

Figure 2.7: Variation of the real (continuous) and imaginary (dashed) parts of ε_{eff} (blue) and μ_{eff} (green)

The limitations of these equations are discussed next in Section 2.3 and summarised in Table 2-1. It should be noted that the permittivities and permeabilities in these equations examined in the preceding sections are not restricted to their real values only but can also be complex as will be seen in the following sections.

2.3 Comparison of these Effective Medium Theories

This section highlights the differences and similarities between the different effective medium theories examined in Section 2.2 in order to determine which of the theories were robust enough to cover the structures investigated in this research, and which ones were not suitable. Mathematical manipulations and applying other assumptions/conditions were carried out on some of the equations to show their similarities.

With respect to the assumptions in Lewin's study [3], because of the trigonometric functions in $F(\theta)$, when the values of θ are very large at high frequencies or big inclusions dependent on the geometry, divisions by zero occur in the calculations leading to 'NaN' ($= \infty$) results for ε_{eff}. The limit of the validity of formulas is that the volume fraction of the spherical inclusions should not approach its maximum. This is similar to that in [7] whose validity is based on the relationship between the obstacles' dimension and their spacing. By assuming conducting spheres in a cubic array and using algebraic manipulations, it is shown below that the equations (2-1) and (2-15) from [3] and [7] respectively are similar to each other. Using a spherical obstacle of radius a, [7] states that it has electric polarisability, $\alpha_1 = 4\pi a^3$ and magnetic polarisability, $\beta_1 = -2\pi a^3$.

Assuming uniform spacing in x, y, z directions, $u = v = w$, the interaction constant, C from (2-16) is given by: $= \frac{1}{\pi u^3}[1.202 - 16\pi^2 K_0(2\pi)]$, which reduces to $C = 1.06/\pi u^3$. Substituting this into equation (2-15) gives,

$$\varepsilon_{eff} = \frac{1 + 8.33\, a^3/u^3}{1 - 4.24\, a^3/u^3} \qquad \mu_{eff} = \frac{1 - 4.16\, a^3/u^3}{1 + 2.12\, a^3/u^3} \tag{2-19}$$

As discussed by Lewin in [3], for metal particles, ε_p is much greater than ε_1. Thus the expression for permittivity in equation (2-1) is reduced to

$$\varepsilon_{eff} = \varepsilon_1[1 + 3p/(1 - p)] \tag{2-20}$$

Substituting the expression for $p = 4\pi a^3/s^3$ and using the same notation by Collin in [7] reduces the expression in the square brackets above to $\frac{1+8.38a^3/u^3}{1-4.19a^3/u^3}$, which is very similar (± 0.05 difference in the multipliers of a^3/u^3) to the expression for ε_{eff} in (2-19) above. Since a "lightweight binder" like Polyfoam which has a dielectric constant of 1.05 [35] is used in the analysis in [7], ε_1 can be approximated to ε_0.

Also, using the approximation for μ_{eff}, if the particles are non-magnetic such that $\mu_p \to 0$, the expression for permeability in equation (2-1) is reduced to

$$\mu_{eff} = \mu_1(1 - 3p/2 + p) \tag{2-21}$$

Substituting for p and using the same notation in [7], reduces the expression in the bracket above to $\frac{1-4.19a^3/u^3}{1+2.09a^3/u^3}$, which is again similar to equation (2-19). Since the binder material is non-magnetic, $\mu_1 \approx \mu_0$.

From the foregoing calculations, the expressions for the ε_{eff} and μ_{eff} of a dielectric host containing spherical particles, obtained in [3] and [7] are almost the same assuming: uniform simple cubic spacing, non-magnetic spherical conducting inclusions and a host permittivity close to that of air, $\varepsilon_0 = 1$.

Furthermore, the expressions for the effective parameters by Collin [7] as shown in equation (2-15) is similar to that of Cai et al, in [29] as shown in equation (2-8). In [7], the interaction constant for equally-spaced spheres was obtained as $C = 1.06/\pi u^3$. In this case, the number of spheres per unit volume, $N = u^{-3}$, and therefore $C = N \times 1.06/\pi$. Since $\frac{1.06}{\pi} \cong 1/3$, substituting in (2-15) yields $\varepsilon_{eff} = 1 + \frac{N\alpha_1}{1-N\alpha_1/3}$, which is the same as Cai's equation in [29]. Collin's equations also suggest that they can be applied to mixtures with non-uniform spacings along the *x*, *y* and *z* axes.

Although [2], [7], [11], [29] have used polarisabilities in their determination of effective constitutive parameters, they have represented these expressions differently. As an example, the expression for polarisability in (2-8) [29] and that in (2-14) [11] yield very similar graphs as shown in Figure 2.8 of Section 2.4 when used to plot the ε_{eff} against frequency, even though they are mathematically not exactly equal. In addition, although there is a '4π' product difference in their equations for the effective properties appearing in the numerator and denominator of (2-14) [11], the 4π's cancel each other out. Another dissimilarity is in their expressions for polarisability given in [11] and [29] which is due to the presence of the host medium's refractive index value in the expression in [11].

Notable is the difference in the representation of the *Clausius-Mossotti* equation in (2-4) by Sihvola [2] from that used in (2-8) by Cai et al [29], by the presence of the 'ε_1' term in the

denominator. This is because equation (2-8) by Cai et al from [29] takes into account the EM properties of the inclusions but not those of the host or assumes the host has EM properties close to that of free space.

The difference between the *Maxwell-Garnett* equation and Lewin's formula from [3] is that while Lewin makes the particles exhibit an effective ε and μ due to their small size, *Maxwell Garnett* assumes that the smaller size particles have the same EM properties as when in their bulk forms. As the value of θ in equation (2-2) changes from being very small to being large and complex as the size-to-wavelength ratio increases, this variation in permittivity decreases. The value of the expression for θ in [3], [4], [26] differs with the size parameter, x in [11], [29] in that the effect of ε_2 and μ_2 are not accounted for. $\sqrt{\varepsilon_2\mu_2}$ in the expression for θ in equation (2-2) is equal to the refractive index of the material of the particle, say n_2, while *x* uses the refractive index of the host medium, n_0.

Kolmakov et al in [4] adopts the formula by Sihvola in [2] for mixtures with more than one size of spherical inclusions to write an expression for ε_{eff} and μ_{eff} of a heterogeneous medium with a single-size sphere but having two different frequency-dependent polarisabilities. It takes into account the fact that the radii, the polarisabilities, the volume fractions and volume densities of the spheres will vary in magnetic and electric resonance modes. This is the primary difference from Lewin's study in [3] where these variations are not taken into account. The spheres have different radii and were arranged in layers accordingly. In their study the particle spacing was taken to be much smaller than the wavelength. This is in line with the conditions for formulae validity in [3]. Numerical simulations were carried out on dielectric spherical and cylindrical particle arrays and it was found out that when the lattice constant was close to a wavelength, or even approximately half of the wavelength, the effective medium approach was not best suited for such mixtures [4]. This is explained as a situation in which "the particle interferes with the normal behaviour" of the host in [3]. A summary of this comparison is given in Table 2-1.

Other minor differences are that: the difference in the formulas for effective constitutive parameters in [3], [7] and [31] can be attributed to the fact that there is a product term difference of ε_o in their expressions for dipole moment, $\overline{\boldsymbol{p}}$.

More advanced studies are carried out in [2], [36] for mixtures that include two or more homogenous material particles of equal or different sizes. In this case, the effective permittivity is a function of summation terms where the volume fractions of each included material and their respective permittivities are examined separately. Inclusion shapes other than spherical, such as ellipsoidal, and inhomogeneous, anisotropic, bi-anisotropic and non-linear mixtures were also examined in [2]. A review of the extended M-G theories has been done in [37].

Even though the equations from the published literature reviewed above, appear to be different, on closer inspection and under certain assumptions, they can be shown to be quite similar to each other.

Table 2-1: Summary of comparative study on canonical equations

EQUATIONS	BASIS	LIMIT OF VALIDITY
Lewin [3]	SC lattice of spheres, semi-infinite medium	$a \ll \lambda/10$
Sihvola [2]	Regular & random lattices, symmetric & non-symmetric inclusions	
Cai et al [29]	SC lattice, plane wave	$\varepsilon_1 \approx 1$
Doyle [31]	SC lattice, spherical inclusions	$a \ll \lambda/10$
Collin [7]	Metallic inclusions	$\varepsilon_1 \approx 1; a \ll s$
Kolmakov et al [4]	Electric and magnetic resonance modes	$a \ll \lambda/10$

2.4 Parametric Studies using Canonical Equations

In this section, the different parameters in the equations for the effective EM properties of the heterogeneous media in Section 2.2 are examined individually to understand their impact on the ε_{eff} and μ_{eff}. As metallic particles were used for some of the analyses in the literature reviewed in Sections 2.2 and 2.3, the Drude model [38–40] was used to determine the EM properties of the metallic inclusions. All inclusions in this section are spherical and in an SC lattice. MATLAB was used to carry out these parametric studies on the equations presented in Section 2.2. Initially, numerical examples from some of the papers were replicated to ensure that their equations had been correctly entered into MATLAB. The values shown in the graphs below are the absolute values of the effective ε and μ, as such the loss tangents of these media are not presented here but are later examined in Section 4.4. The individual host and inclusion media examined in this section are assumed to be linear, homogenous, non-dispersive and isotropic. Speed of light in air, $c = 3 \times 10^8 m/s$.

2.4.1 The Drude Model

From [41], an equivalent to the Drude model beginning from first principles is discussed, by using the atomic parameters of a material: its electron density, the mass of its electrons and/or holes, and its electron and hole collision angular frequencies, to derive the equivalent permittivity and hence the conductivity of the material. The relative permittivity of a material can be expressed as:

$$eps(f, N_e) = \varepsilon_u - \left[\frac{\omega_e(N_e)}{(\omega(f))^2 + (\upsilon_e)^2} \cdot \left(1 + j\frac{\upsilon_e}{\omega(f)}\right) + \frac{\omega_h(N_e)}{(\omega(f))^2 + (\upsilon_h)^2} \cdot \left(1 + j\frac{\upsilon_h}{\omega(f)}\right)\right] \quad (2\text{-}22)$$

where $\omega_{e,h}\left(N_{e,h}\right) = \frac{N_{e,h} \cdot (q)^2}{\varepsilon_o . m_{e,h}}$ is the plasma frequency, q is the electron charge, ε_o is permittivity of free space, (m_e, m_h) is the effective mass of the material's electron and hole respectively, $N_{e,h}$ is the electron (hole) density, ε_u is the material's undisturbed dielectric constant, $\upsilon_{e,h}$ is the electron (hole) collision angular frequency, and f is frequency. This model is not only applicable to metals, but can be used for other classes of materials such as semiconductors.

2.4.2 Varying the Inclusion Size, *a*

In this section, the inclusion size was varied while the spacing and the frequency were kept constant. Fixing the frequency, *f* at 3 GHz, and the spacing, *s* at 200 µm, while varying the radius, *a*, of the particle from 1 to 100 µm, the effective ε and μ of a mixture with a dielectric host medium (Polyethylene, $\varepsilon_1 = 2.25$ (tan $\delta = 0.001$)) was obtained as shown in Figure 2.8. $\mu_1 = \mu_2 = 1$. When the particle has a radius of 100 µm, the particles are touching (in an SC lattice), and although Lewin's equations are stated as being limited to the case of not too densely packed media, this may give insight into what happens if the particles were touching. For this study, metal inclusions were used. Since the inclusions here are metallic, the heterogeneous medium approaches that of a continuous metal structure when the spheres are in contact. As such, the $\varepsilon_{eff} = 10$ value may not be valid in this case. This will be examined in further detail in Chapter 4. The permittivity of the metal (in this case, Copper) was obtained as $\varepsilon_2 = (1.2 - j103.5) \times 10^6$, from first principles using the Drude model using equation (2-22) over a 1–100 GHz frequency range. The conductivity determined from this permittivity value was very close to the well-known conductivity value of Copper, 5.76×10^7 S/m [42], [43]. Figure 2.8 shows the effective ε and μ of the mixture as obtained from the different equations from Section 2.2. As shown, the ε_{eff} increases while the μ_{eff} decreases as the spherical inclusions get bigger in size for a fixed unit cell size. It is expected that with denser packing such as with the BCC and FCC lattices, further increases and decreases in ε_{eff} and μ_{eff} respectively, will occur. The results from [7] and [29] agree with each other but do not agree with those from [2–4], [11] as [7] and [29] do not include the value of the host permittivity, ε_1 in their equations and so will only agree with the other equations when the host permittivity, $\varepsilon_1 \cong 1$.

Even though $\mu_1 = \mu_2 = 1$, the effective μ reduces with increase in the particle volume fraction because the inclusions are metallic and may create diamagnetism within the heterogeneous medium when illuminated by an external magnetic field. Diamagnetism occurs when an applied magnetic field on a material produces a net magnetisation vector oriented in such a way as to oppose the applied field, thereby resulting in a permeability less than unity [42]. But due to the structure of the equation in [2] (see equation (2-7)) with its denominator term, $\mu_2 - \mu_1 = 0$, this results in its $\mu_{eff} = 1$.

In Figure 2.8, the unit cell size is held constant and the particle size varied, but if the reverse case was studied where the particle size is held constant but the spacing varied, the same

graph will also be reproduced – the ε_{eff} increasing as the spacing reduces. Calculations have also shown that the equivalent results are obtained by varying the spacing of the inclusions instead.

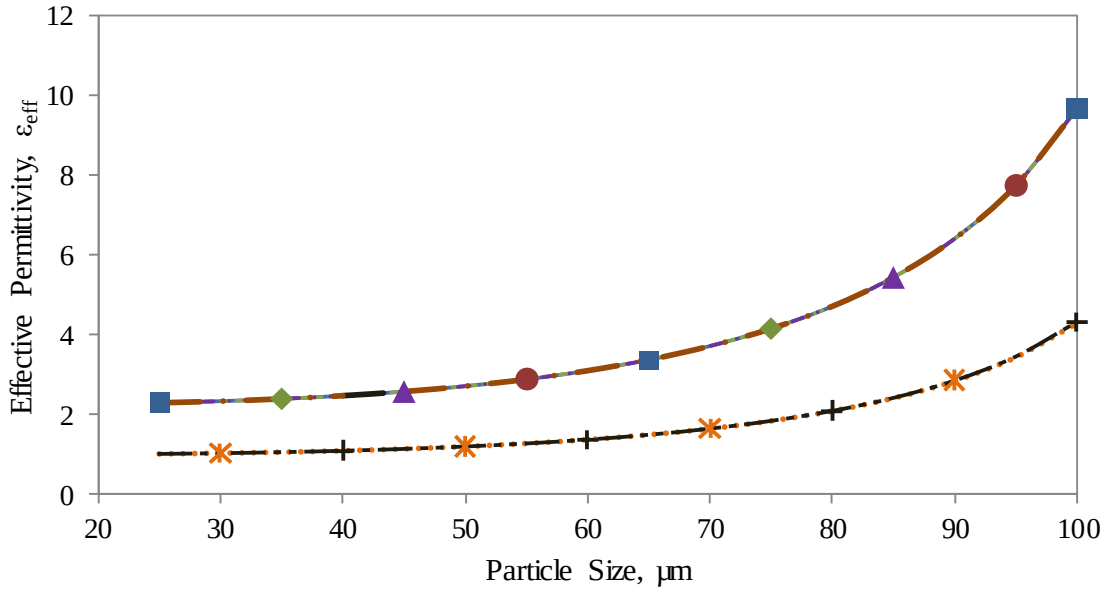

(a)

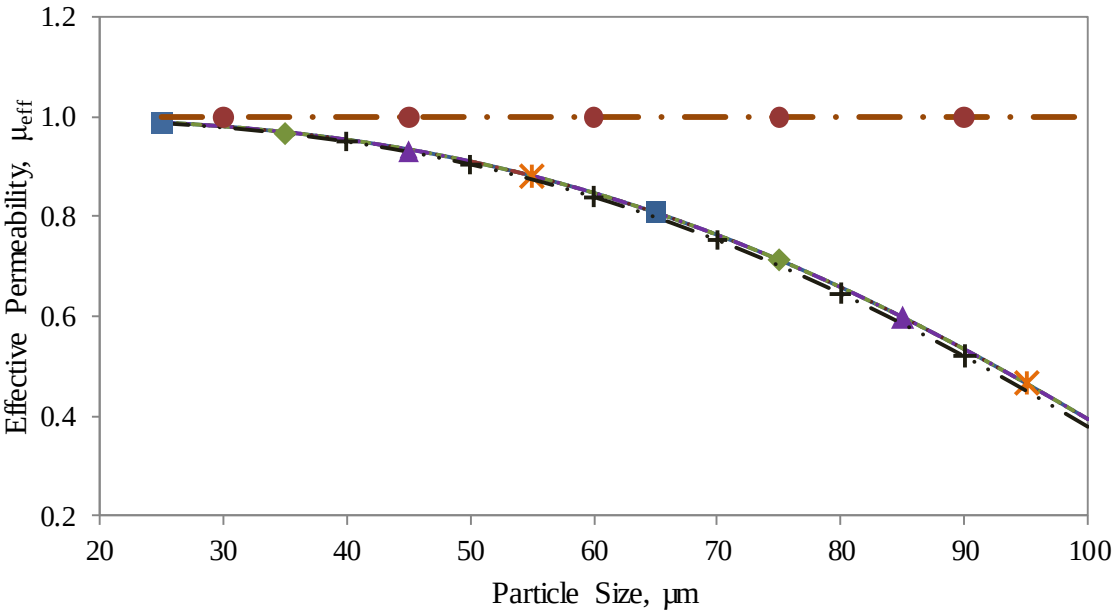

(b)

Figure 2.8: Variation of (a) ε_{eff} and (b) μ_{eff} with spherical inclusion size, a, from [2] (Sihvola, ═•═•●•═•═), [3] (Lewin, ▬■▬), [4] (Kolmakov, ▪▪▲▪▪), [7] (Collin, ─••+••─), [11] (Doyle, ─ ─♦─ ─) and [29] (Cai, ▬•✳•▬).

2.4.3 Varying the Operating Frequency, f

Formulations from [2], [7] do not have frequency terms, therefore only equations from [3], [4], [11], [29] are used to understand the effect of variation of the operating frequency with the EM properties of the heterogeneous mixture as shown in Figure 2.9. Here, it is assumed that the permittivities and permeabilities of the host and the inclusions are constant with frequency, that is, non-dispersive. However, this could be modified to accommodate variation with frequency, especially over large frequency ranges. This would allow dispersive materials to be considered. Here, the frequency, f is varied from 1 to 30 GHz; other data: $a = 100$ µm, $s = 220$ µm, $\mu_1 = \mu_2 = 1$, $\varepsilon_1 = 2.25$ (tan $\delta = 0.001$) (Polyethylene) and $\varepsilon_2 = (1.2 - j103.5) \times 10^6$ (metallic inclusions).

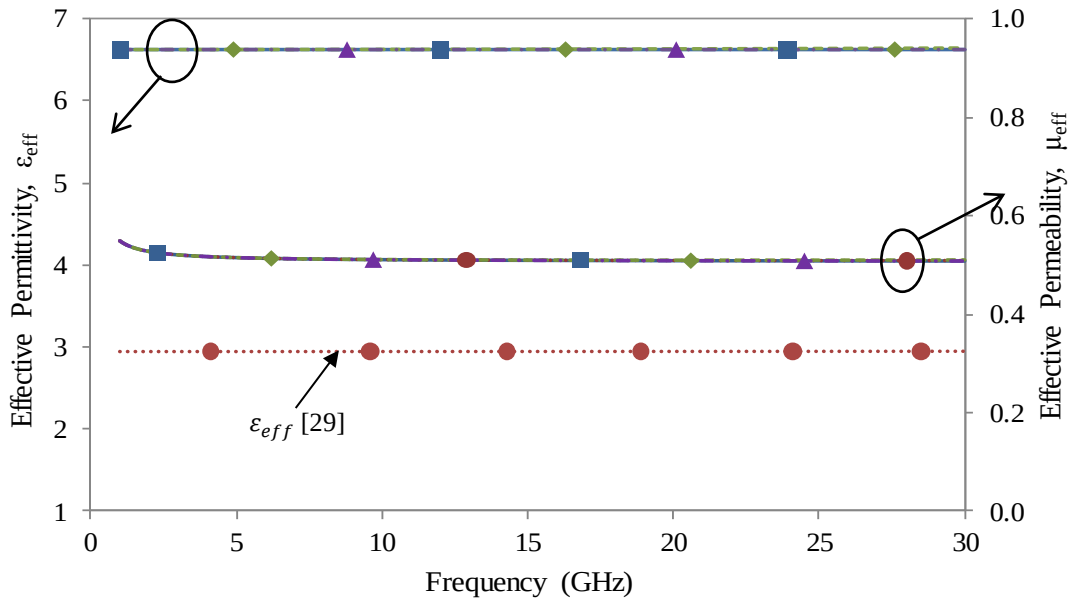

Figure 2.9: Variation of ε_{eff} and μ_{eff} with frequency from [3] (Lewin, —■—), [4] (Kolmakov, —•▲•—), [11] (Doyle, --♦--) and [29] (Cai, ▪▪●▪▪).

As shown in Figure 2.9, ε_{eff} from [29] differs significantly from the others because $\varepsilon_1 > 1$ which is not included in its equation for ε_{eff}. The other results agree over the frequency range considered. For the case of μ_{eff}, all the results from the equations agree with each other. As the frequency increases an initial reduction in the μ_{eff} from 1 is seen, and then μ_{eff} remains nearly constant at approximately 0.5 – the diamagnetic characteristic introduced by metallic inclusions as explained in Section 2.4.2.

2.4.4 Varying the Host Permittivity, ε_1

As [7], [29] do not account for the properties of the host medium, their equations were not used in this study. While [11] has ε_2 affecting both ε_{eff} and μ_{eff} of the mixture, ε_2 affects only the ε_{eff} in [2–4]. For the plot of μ_{eff}, only the results from [11] were used as only its μ_{eff} equation has ε_1 in it. The variation of ε_{eff} with ε_1 is shown in Figure 2.10. Data used: $\mu_1 = \mu_2 = 1$, $\varepsilon_2 = (1.2 - j103.5) \times 10^6$, f = 3 GHz, a = 100 µm, and s = 220 µm. the volume fraction, p = 39.34%. As shown in Figure 2.10, for the dimensions and EM parameters used in this example, the ε_{eff} and μ_{eff} of the mixture agree across the different equations used. It is worth noting that although the host permittivity, ε_1 increases to a value of ~10, the ε_{eff} of the mixture increases linearly in a straight line but does not reach the permittivity of the inclusions, remaining at about 3 times the value of the host. It can be deduced that the host's EM properties, ε_1 and μ_1, are dominant in deciding the ε_{eff} and μ_{eff} of the mixture as pointed out in the analysis in Section 2.2.2, despite the high level of the dielectric contrast between the EM properties of the host and inclusion material. Due to the assumption of non-dispersive media, the same variation shown in Figure 2.10 will be repeated for any other frequency, as far as the size and spacing of the inclusions are far less than the wavelength in the medium, that is, $a, s \ll \lambda/\sqrt{\varepsilon_1 \mu_1}$.

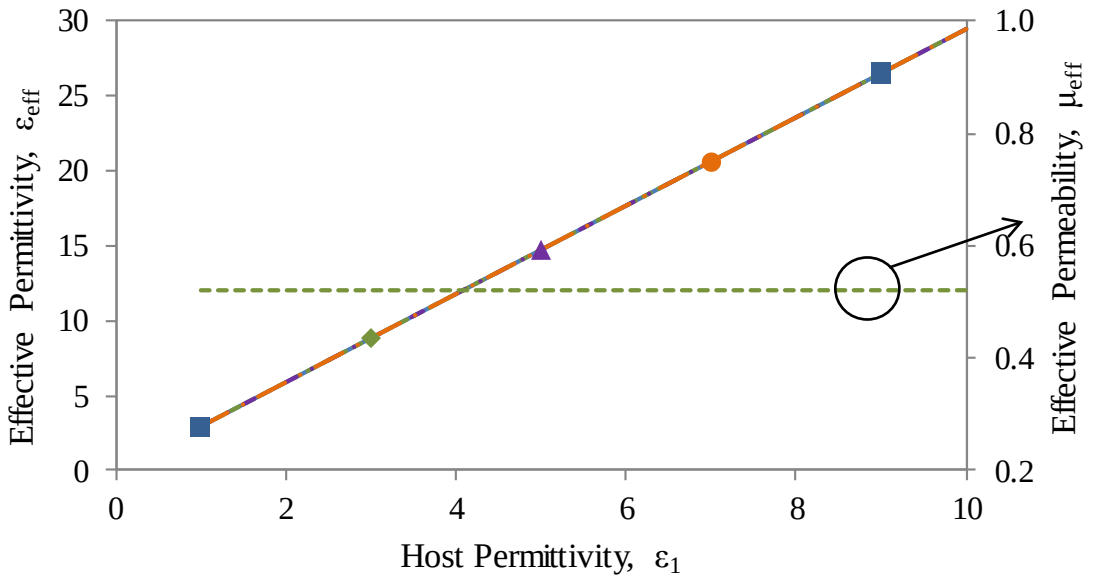

Figure 2.10: Variation of ε_{eff} and μ_{eff} with host permittivity, ε_1 from [2] (Sihvola, ▪●▪), [3] (Lewin, ▬■▬), [4] (Kolmakov, —•▲•—) and [11] (Doyle, — —♦— —) at f = 3 GHz.

2.4.5 Varying the Inclusion Permittivity, ε_2

The effect of changing the permittivity of the inclusion from 1 to 200, while keeping a = 100 µm, s = 220 µm, $\varepsilon_1 = 2.25$ (tan $\delta = 0.001$) and frequency at 3 GHz, is shown in Figure 2.9, using [2–4], [11], [29]. Reference [7] is not used as ε_2 is not present explicitly in its equations as it assumes metallic inclusions in its derivations.

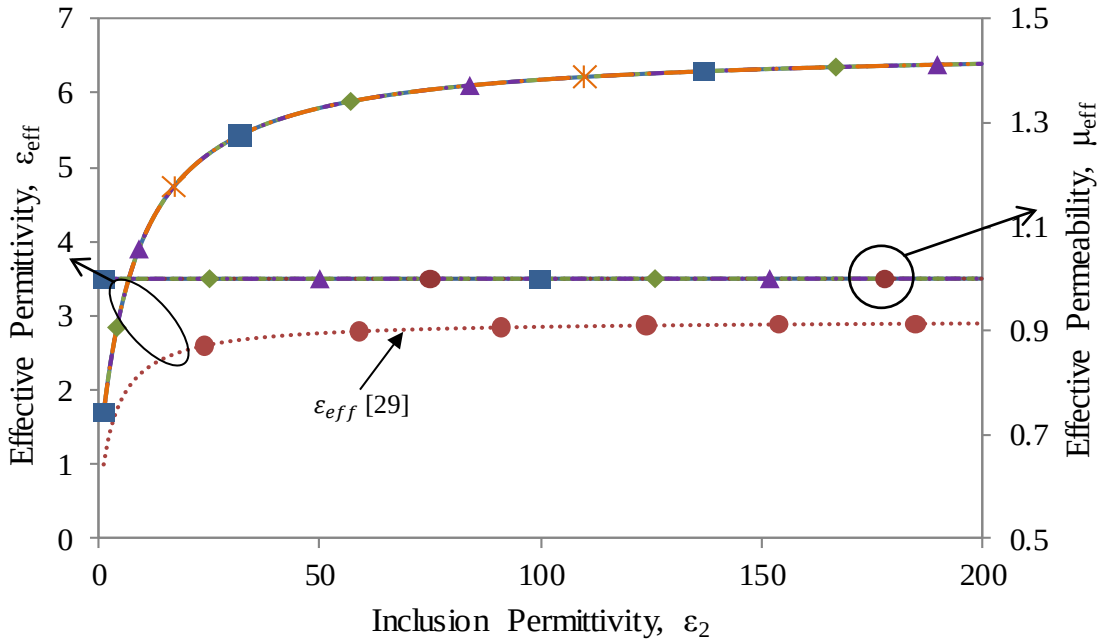

Figure 2.11: Variation of ε_{eff} and μ_{eff} with spherical inclusion permittivity, ε_2 from [2] (Sihvola, —x—), [3] (Lewin, —■—), [4] (Kolmakov, —•▲•—), [11] (Doyle, – —◆— –) and [29] (Cai, ▪▪●▪▪).

Results from [29] in Figure 2.11 differ significantly as ε_1 is not accounted for while the other models show good agreement. Although ε_2 is intricately part of the equations for μ_{eff} in [3], it is worth noting that the μ_{eff} of the mixture still remains very close to unity as with other models and μ_{eff} is therefore different compared with metallic inclusions. The ε_{eff} values remain the approximately the same irrespective of the frequency at which the ε_2 is varied. However, if the particle size is slightly increased from 100 µm to 110 µm, that is, to where the spheres are directly in contact, the effective ε increases to about 9.2. Also, even though the permittivity of the inclusions is quite high, the permittivity of the host medium seems to have a higher influence on the effective ε of the mixture. By a simple volume occupied to permittivity ratio, the ε_{eff} should be higher.

2.5 Effect of Non-Spherical Inclusions

As stated in Section 2.2, some of the authors reviewed examined the effect of having inclusions with shapes other than spherical in a homogenous host [2], [7]. These include discs, cubes, cylinders and ellipsoids, examples of which are as shown in Figure 2.12. This section examines a few of these shapes and their merits (or lack of) compared with spherical inclusions.

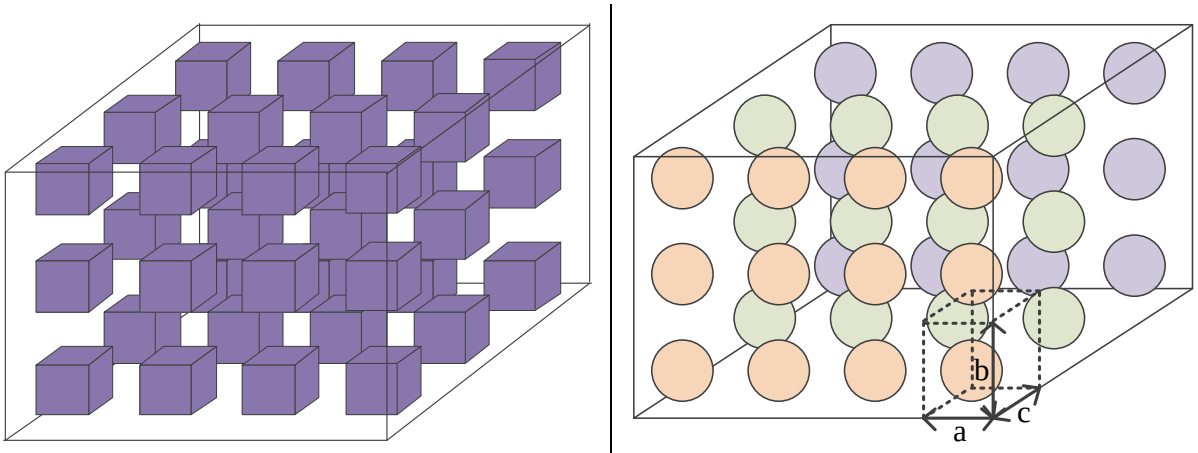

(a) (b)

Figure 2.12: 3-D diagrams of a cross-section of (a) cubes and (b) discs in a dielectric host

2.5.1 Cubes

Next in popularity to the spheres with respect to the shapes of the inclusions are cubes as shown in Figure 2.12 (a). Different methods have been used to calculate the ε_{eff} of a heterogeneous medium with cubic inclusions such as the Boundary Integral Equation (BIE) method [44] and the Clausius-Mossotti (C-M) equation [45] as stated in equation (2-4). The method used here is that in [45] which uses the polarisability of a cube which is different from that of a sphere. As explained in Chapter 1, the polarisability of a material determines its dielectric response to an applied electric field. Previous research has been carried out in determining the polarisability of a cube as published in [46], [47]. Thus, for a cube, the polarisability, α is best approximated in equation (2-23) [45]:

$$\alpha = V\varepsilon_1 \frac{(\tau - 1)(3.6438\tau^2 + 11.948\tau + 6.4945)}{\tau^3 + 6.4703\tau^2 + 10.651\tau + 3.9638} \tag{2-23}$$

where $\tau = \varepsilon_2/\varepsilon_1$ and V is the volume of the cube. As the C-M equation has no frequency term, Figure 2.13 shows the variation of the ε_{eff} of a mixture with 100 µm cubes spaced in

an SC lattice of 180 and 250 µm lattice constant. ε_1 varies from 1 to 10 ($\tan\delta = 0.002$), while ε_2 is fixed at 11.9 ($\tan\delta = 0.01$). Calculations were carried out in MATLAB.

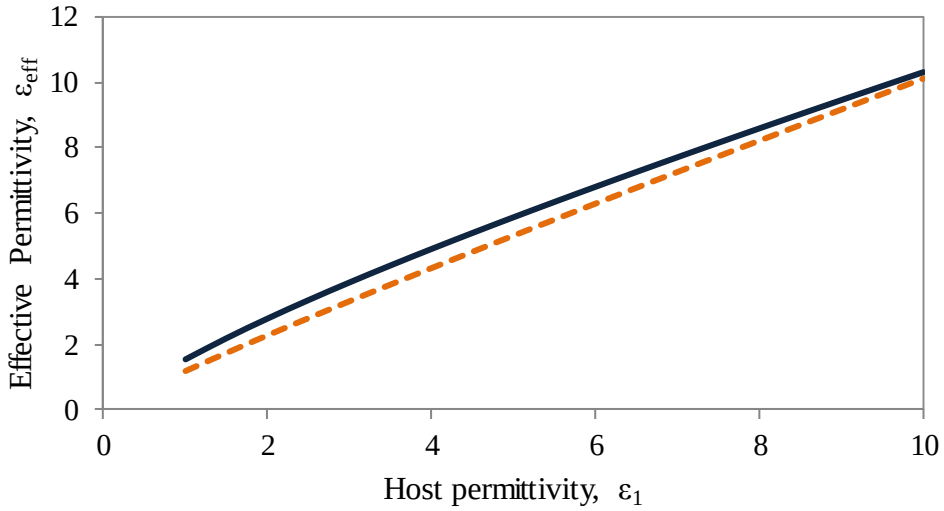

Figure 2.13: Variation of ε_{eff} with ε_1 for a heterogeneous medium of 100 µm cubes with 180 (▬) and 250 µm (– – –) spacing

The cubes allow the inclusions to take up more of the volume of the host medium thereby increasing the volume fraction to a maximum of 1. However, the heterogeneous mixture still retains the isotropic nature of the spheres. As shown in Figure 2.13, an increase in ε_1 results in increase in ε_{eff} as expected. Here, the volume fractions of the cubes are 17.1% and 6.4% for 180 and 250 µm spacings respectively. The volume fraction and the non-metallic nature of the cubes implies that $\varepsilon_{eff} \cong \varepsilon_1$ as seen in the graph. The two curves do not differ significantly from each other as the cubes are quite sparsely distributed within the host medium.

It should be noted that for C-M equations in [45], as the volume fraction of the heterogeneous mixtures approach 1, the accuracy of the ε_{eff} results significantly reduces, and as such does not agree with extracted results from simulations as will be discussed in Chapter 4.

2.5.2 Discs

Disc-shaped inclusions can also be used in heterogeneous mixtures as discussed in [2], [7], [9], [44] and as shown in Figure 2.10 (b). These discs can be dielectric [2] or conducting [7], [9], [48], and are usually assumed to be very thin when they are conducting [48]. Due to the inherent characteristic of the disc not being symmetrical along all 3 axes, it tends to produce anisotropic effective EM properties when used in heterogeneous mixtures as its polarisability varies in each axis [2], [44], [49], [50]. The non-uniformity of the disc's polarisability is derived from the fact that the 'depolarisation factor' along the *x*, *y* and *z*-axes are not equal as in the case of the sphere (which is $1/3$) [51]. For a disc, the depolarisation factors along the *x*, *y* and *z*-axes are given by $(N_x, N_y, N_z) = (0, 0, 1)$. The value '1' corresponds to the axis normal to the plane of the disc. Figure 2.14 shows the variation of the ε_{eff} with disc spacing. It has been assumed here that the impinging wave is a plane wave in which the electric and magnetic fields are in the plane of the discs. Thus, no magnetic polarisation is produced as the magnetic field is in this plane [7]. Data used: disc radius, $r = 100$ µm, disc thickness, $t = 10$ µm, disc spacing on the plane parallel to the disc surface, $s = 210 - 400$ µm, disc spacing normal to the plane of the disc surface, $h = 25$ µm, $\varepsilon_1 = 2.25$ (tan $\delta = 0.002$), $\varepsilon_2 = 11.9$ (tan $\delta = 0.01$), frequency, $f = 3$ GHz. Calculations were carried out in MATLAB using equations in [2], [7].

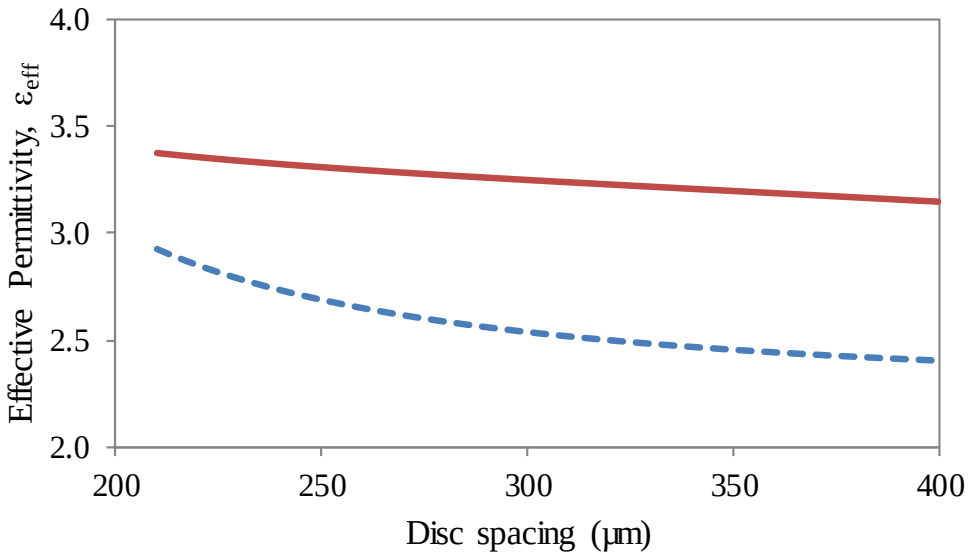

Figure 2.14: Variation of ε_{eff} with disc spacing (parallel to the surface of the disc) using [2] (continuous) and [7] (dashed)

From Figure 2.14, the ε_{eff} from [7] is higher than that from [2] by about 0.5. This is probably because the original equation for the ε_{eff} in [7] assumes the permittivity of the host to be air and deals with conducting discs. As such it was modified by multiplying the right-hand-side of equation (2-15) by ε_1. In addition, it does not account for the thickness of the disc. In [2], all these parameters are accounted for its equation (see equation (2-6)) and is based on dielectric inclusions. However, the shape/slope of these two plots agree with that shown in Figure 12.9 of [7]. As expected, the ε_{eff} of the heterogeneous mixture increases with a decrease in the disc spacing and tends towards the permittivity of the host.

A good grasp of thin discs in a dielectric host was important as in Chapter 5, the initial measurements were based on thin cuboids etched on a relatively thicker dielectric substrate and stacked up to achieve an overall thickness within the range of that typically available for microwave substrates. Due to the non-uniformity of the size of the discs along the 3 Cartesian coordinates, it is expected that the heterogeneous medium will show anisotropy as depolarisation factors of the disc are not equal along all three axes. Therefore, ε_{eff} and μ_{eff} will be represented by permittivity and permeability tensors instead. This will be further discussed in Chapter 5.

2.5.3 Cylinders

Cylindrical inclusions were used in [4], [7], [29], [52] and were either dielectric or conducting. By using an equal volume transformation between the cylinder and a sphere, the equations for the ε_{eff} and μ_{eff} of spherical inclusions in a dielectric host can be used, to obtain those for media with cylindrical inclusions. If the height of the cylinders are such that they are equal to the diameter of the sphere, the equivalent radius of the cylinder, r_c is given by $r_c = r_s\sqrt{2/3}$, where r_s is the radius of the sphere. Thus similar graphs to those given in Section 2.4 will be obtained. However, there will be slight differences because of "higher-order scattering at the edges of the cylindrical particles" [29] and the scattering equations may differ from that of a sphere given in [28]. Negative permittivity and permeability can also be obtained depending on the polarisation of the wave exciting the structure [34]. Refractive indices less than unity can also be obtained [53].

2.6 Conclusions

As with all research, it is important to understand the theory behind artificial dielectrics and heterogeneous mixtures. Different equations representing various effective medium theories have been reviewed in this chapter. Most of the equations examined here agree with each other to a good degree. For the equations with deviations, the reasons behind these deviations have been highlighted and discussed. From the review of the various models, the equations from Cai in [29] are valid only when the permittivity of the host is 1 and thus cannot be used where the host properties are not close to that of air. Sihvola and Collin in [2], [7] respectively do not have frequency terms in their expressions, and so cannot be used for frequency-dependent results or to detect electric and magnetic resonances in a heterogeneous medium. The equations by Lewin, Kolmakov and Doyle from [3], [4], [11] respectively have been deemed sufficient and robust enough for the further research presented in this thesis, with the latter two having more complicated forms. They have been used primarily when comparisons were to be made between the results from the canonical equations, EM simulations and measurements. This is because in addition to having terms representing frequency and the host's EM properties, they make use of the electric and magnetic scattering coefficients of the inclusions. A summary of this comparison has been given in Table 2-1.

Some of the graphical results given in the literature reviewed have been reproduced where possible and explained. Additional parametric studies on the different parameters constituting these canonical equations for the effective properties of the heterogeneous media, ε_{eff} and μ_{eff}, have also been carried out with the results presented. This step was important for understanding how these parameters individually affect the overall properties of the mixtures which would potentially be useful in the design of heterogeneous media with readily available materials.

In addition, heterogeneous media of non-spherical inclusions such as cubes, discs and cylinders, have been reviewed with graphical results. This was necessary because in the following chapters, non-spherical inclusions will also be used to create these heterogeneous media with the effective properties examined via simulations and compared with these equations. As it is probably easier to create these non-spherical shapes in practise, this emphasises the importance of understanding how these effective medium equations perform for non-spherical inclusions. Thus, the equations presented in this chapter will be used directly for some of the other results given in this thesis.

2.7 References

[1] Lord Rayleigh, "On the influence of obstacles arranged in rectangular order upon the properties of a medium," *Philosophical Magazine*, vol. 34, pp. 481–502, 1892.

[2] A. Sihvola, *Electromagnetic Mixing Formulas and Applications*. London: IET, 1999.

[3] L. Lewin, "The electrical constants of a material loaded with spherical particles," *IEE-Part III: Radio Comm. Eng.*, vol. 94, no. 27, pp. 65–68, 1947.

[4] I. A. Kolmakov, L. Jylha, S. A. Tretyakov, and S. Maslovki, "Lattice of dielectric particles with double negative response," in *28th Gen. Ass. Int. Union Radio Sci. (URSI)*, 2005.

[5] D. A. Boyarskii and V. V. Tikhonov, "Microwave effective permittivity model of media of dielectric particles and applications to dry and wet snow," *Geoscience and Remote Sensing, IEEE Transactions on*, vol. 4, pp. 2065–2067, 1994.

[6] H. Looyenga, "Dielectric constants of heterogeneous mixtures," *Physica*, vol. 31, no. 1, pp. 401–406, 1965.

[7] R. E. Collin, *Field Theory of Guided Waves*. New York: IEEE Press, 1991.

[8] C. A. Kyriazidou, H. F. Contopanagos, W. M. Merrill, and N. G. Alexopoulos, "Effective permittivity and permeability functions of metalo-dielectric photonic band gap materials," *IEEE Antennas and Propagation Society International Symposium*, vol. 3, pp. 1912–1915, 1999.

[9] N. G. Alexopoulos, C. A. Kyriazidou, and H. F. Contopanagos, "Effective parameters for metamorphic materials and metamaterials through a resonant inverse scattering approach," *IEEE Transactions on Microwave Theory and Techniques*, vol. 55, no. 2, pp. 254–267, 2007.

[10] W. T. Doyle and I. S. Jacobs, "Effective cluster model of dielectric enhancement in metal-insulator composites," *Physical Review B*, vol. 42, no. 15, pp. 9319–9329, 1990.

[11] W. T. Doyle, "Optical properties of a suspension of metal spheres," *Physical Review B*, vol. 39, no. 14, pp. 9852–9858, 1989.

[12] O. Rybin, "Enhancement of dielectric constant in metal-dielectric meta-materials," *African Physical Review*, vol. 3, pp. 49–55, 2009.

[13] N. N. Al-Moayed, M. N. Afsar, U. A. Khan, S. McCooey, and M. Obol, "Nano ferrites microwave complex permeability and permittivity measurements by T/R technique in waveguide," *IEEE Transactions on Magnetics*, vol. 44, no. 7, pp. 1768–1772, Jul. 2008.

[14] M. N. Afsar, A. M. Ayala, N. Al-Moayed, and M. Obol, “Microwave permittivity and permeability properties and microwave reflections of ferrite powders,” in *IEEE Instrumentation and Measurement Technology Conference*, 2009, pp. 274–278.

[15] L. B. Kong, Z. W. Li, G. Q. Lin, and Y. B. Gan, “Ni-Zn ferrites composites with almost equal values of permeability and permittivity for low-frequency antenna design,” *IEEE Transactions on Magnetics*, vol. 43, no. 1, pp. 6–10, Jan. 2007.

[16] P. Talbot, A. Konn, and C. Brosseau, “Electromagnetic characterization of fine-scale particulate composite materials,” *Journal of Magnetism and Magnetic Materials*, vol. 249, no. 3, pp. 481–485, Sep. 2002.

[17] A. Verma, A. K. Saxena, and D. C. Dube, “Microwave permittivity and permeability of ferrite–polymer thick films,” *Journal of Magnetism and Magnetic Materials*, vol. 263, pp. 228–234, Jul. 2003.

[18] I. Awai, O. Mizue, and A. K. Saha, “Artificial dielectric resonator made of spherical metal particles,” *IEICE Transactions on Electronics*, vol. E92–C, no. 1, pp. 72–76, 2009.

[19] B. Van Zeghbroeck, *Principles of Semiconductor Devices*. Boulder: ECEE, University of Colorado, 2004.

[20] N. W. Ashcroft and N. D. Mermin, *Solid State Physics*. New York: Holt, Rinehart and Winston, 1976.

[21] “Crystal Structure,” *Wikipedia*. [Online]. Available: http://en.wikipedia.org/wiki/Crystal_structure. [Accessed: 11-Nov-2012].

[22] C. C. Njoku, W. G. Whittow, and Y. C. Vardaxoglou, “Effective permittivity of heterogeneous substrates with cubes in a 3-D Lattice,” *IEEE Antennas and Wireless Propagation Letters (Special Issue on Metamaterials)*, vol. 10, pp. 1480–1483, 2011.

[23] C. C. Njoku, W. G. Whittow, and Y. C. Vardaxoglou, “Study on the variation in dielectric properties of heterogeneous substrates composed of nanomaterials,” in *European Conference on Antennas and Propagation (EuCAP)*, 2011, pp. 488–492.

[24] C. C. Njoku, W. G. Whittow, Y. C. Vardaxoglou, C. Toprakcioglu, and K. T. Thoma, “Metallic inclusions in a non-uniform lattice,” in *Loughborough Antennas & Propagation Conference (LAPC)*, 2011, pp. 1–4.

[25] I. Vendik, O. Vendik, I. Kolmakov, and M. Odit, “Modelling of isotropic double negative media for microwave applications,” *Opto-Electronics Review*, vol. 14, no. 3, pp. 179–186, Sep. 2006.

[26] C. L. Holloway, E. F. Kuester, J. Baker-Jarvis, and P. Kabos, “A double negative (DNG) composite medium composed of magnetodielectric spherical particles embedded in a matrix,” *Antennas and Propagation, IEEE Transactions on*, vol. 51, no. 10, pp. 2596–2603, 2003.

[27] K. Siakavara and C. Damianidis, “Microwave filtering in waveguides loaded with artificial single or double negative materials realized with dielectric spherical particles in resonance,” *Progress In Electromagnetics Research*, vol. 95, pp. 103–120, 2009.

[28] J. A. Stratton, *Electromagnetic Theory*. New York: McGraw-Hill Book Inc, 1941.

[29] X. Cai, R. Zhu, and G. Hu, “Experimental study for metamaterials based on dielectric resonators and wire frame,” *Metamaterials*, vol. 2, no. 4, pp. 220–226, 2008.

[30] M. Abramowitz and I. A. Stegun, *Handbook of Mathematical Functions*, 1st ed. New York: Dover Publications Inc, 1970.

[31] W. T. Doyle, “The Clausius-Mossotti problem for cubic arrays of spheres,” *Journal of Applied Physics*, vol. 49, no. 2, pp. 795–797, 1978.

[32] J. C. Maxwell, *A Treatise on Electricity and Magnetism*, 3rd ed. Oxford: Clarendon, 1891, p. 57.

[33] I. Vendik, M. Odit, and D. Kozlov, “3D Metamaterial based on a regular array of resonant dielectric inclusions,” in *Radioengineering*, 2009, vol. 18, no. 2, pp. 111–116.

[34] Q. Zhao, J. Zhou, F. Zhang, and D. Lippens, “Mie resonance-based dielectric metamaterials,” *Materials Today*, vol. 12, no. 12, pp. 60–69, Dec. 2009.

[35] R. Asmatulu, B. Geist, W. B. Spillman, and R. O. Claus, “Dielectric constant and breakdown field studies of electrostatic self-assembled materials,” *Smart Materials and Structures*, vol. 14, no. 6, pp. 1493–1500, Dec. 2005.

[36] W. M. Merrill, R. E. Diaz, M. M. LoRe, M. C. Squires, and N. G. Alexopoulos, “Effective medium theories for artificial materials composed of multiple sizes of spherical inclusions in a host continuum,” *IEEE Transactions on Antennas and Propagation*, vol. 47, no. 1, pp. 142–148, 1999.

[37] R. Ruppin, “Evaluation of extended Maxwell-Garnett theories,” *Optics Communications*, vol. 182, no. 4–6, pp. 273–279, Aug. 2000.

[38] M. A. Ordal, L. L. Long, R. J. Bell, S. E. Bell, R. R. Bell, R. W. Alexander, and C. a Ward, “Optical properties of the metals Al, Co, Cu, Au, Fe, Pb, Ni, Pd, Pt, Ag, Ti, and W in the infrared and far infrared,” *Applied Optics*, vol. 22, no. 7, pp. 1099–1120, Apr. 1983.

[39] H. Ehrenreich and H. R. Philipp, “Optical properties of Ag and Cu,” *Physical Review*, vol. 128, no. 4, pp. 1622–1629, 1962.

[40] P. B. Johnson and R. W. Christy, “Optical constants of the noble metals,” *Physical Review B*, vol. 6, no. 12, pp. 4370–4379, 1972.

[41] J. C. Vardaxoglou, “Optical switching of frequency selective surface bandpass response,” *Electronics Letters*, vol. 32, no. 25, pp. 2345–2346, 1996.

[42] C. A. Balanis, *Advanced Engineering Electromagnetics*, 2nd ed. New York: Chichester: Wiley, 1989.

[43] D. J. Griffiths, *Introduction to Electrodynamics*, 3rd ed. Upper Saddle River, N.J.: Prentice Hall, 1999.

[44] B. Sareni, L. Krahenbuhl, A. Beroual, and A. Nicolas, "A boundary integral equation method for the calculation of the effective permittivity of periodic composites," *IEEE Transactions on Magnetics*, vol. 3, no. 2, pp. 1580–1583, 1997.

[45] J. Avelin, A. Sihvola, R. Sharma, and I. Hanninen, "Modelling of dielectric materials with cubic inclusion shapes," in *29th European Microwave Conference*, 1999, pp. 36–39.

[46] D. Herrick and T. Senior, "The dipole moments of a dielectric cube," *IEEE Transactions on Antennas and Propagation*, vol. 25, no. 4, pp. 590–592, Jul. 1977.

[47] L. Eyges and P. Gianino, "Polarizabilities of rectangular dielectric cylinders and of a cube," *IEEE Transactions on Antennas and Propagation*, vol. 27, no. 4, pp. 557–560, 1979.

[48] J. Brown and W. Jackson, "The relative permittivity of tetragonal arrays of perfectly conducting thin discs," *Proceedings of the IEE - Part B: Radio and Electronic Engineering*, vol. 102, no. 1, pp. 37–42, 1955.

[49] A. H. Sihvola and J. A. Kong, "Effective permittivity of dielectric mixtures," *IEEE Transactions on Geoscience and Remote Sensing*, vol. 26, no. 4, pp. 420–429, Jul. 1988.

[50] J.-P. Huang and K. W. Yu, *New Nonlinear Optical Materials: Theoretical Research*. New York: Nova Science Publishers, 2007.

[51] J. A. Osborn, "Demagnetizing factors of the general ellipsoid," *Physical Review*, vol. 67, no. 11–12, pp. 351–357, 1945.

[52] S. O'Brien and J. B. Pendry, "Photonic band-gap effects and magnetic activity in dielectric composites," *Journal of Physics: Condensed Matter*, vol. 14, no. 15, pp. 4035–4044, Apr. 2002.

[53] J. Brown, "Artificial dielectrics having refractive indices less than unity," *Proceedings of the IEE - Part IV: Institution Monographs*, vol. 100, no. 5, pp. 51–62, 1953.

Chapter 3. Dielectric Properties of Heterogeneous Mixtures using Electromagnetic Simulations

3.1 Introduction

Chapter 2 developed an understanding of the canonical analysis of (semi-) infinite structures consisting of spherical and non-spherical particles embedded in a dielectric host medium and arranged in a simple cubic (SC) lattice, using formulations from several authors. In order to validate the canonical equations discussed in Chapter 2, simulations of these heterogeneous mixtures were carried out. This allowed the validation of the canonical results from the simulated results. This chapter explains the simulation process to extract the effective permittivity, ε_{eff} and permeability, μ_{eff} for heterogeneous mixtures with dielectric and metallic inclusions.

The process, methods and results of using electromagnetic (EM) simulations to find the effective EM properties of heterogeneous mixtures are discussed. Stated simply, the simulation process works by applying an EM plane wave to the heterogeneous medium and then extracting the scattering (S-) parameters, typically, S_{11} and S_{21}. An inversion algorithm is applied to these S-parameters in order to obtain the EM properties of the medium. Numerical simulations of these structures were carried out with an appropriate 3D Finite-difference-time-domain (FDTD) EM simulation software, Empire XCcel®.

Before the heterogeneous structures were simulated, it was important to determine that the choice of the extraction method used in obtaining the effective permittivity and permeability $(\varepsilon_{eff}$ and $\mu_{eff})$ of the medium from the simulation results were correct. The foundation for the effective-medium theory as discussed in Chapter 2 [1–6] was used here because the heterogeneous media could be homogenized on a macroscopic scale as the wavelengths considered were much larger than the lattice constants/periodicity and the size of the inclusions. Well-known inversion/extraction techniques exist such as the Nicholson-Ross-Weir (NRW) method [7], [8], the Resonant Inverse Scattering method [9], and other variants of the S-parameter inversion process [10–14]. These methods use the S-parameters and the thickness of the material to obtain the effective EM properties of the medium subjected to a plane wave or when the sample is placed in a waveguide.

On deciding on the extraction technique to be used as that described in [9], it was necessary to make sure that the technique was robust enough to be applied to other heterogeneous and homogenous materials and not only on the sample described in [9]. Therefore, dielectric slabs of known EM properties (ε and μ) and finite thicknesses were simulated using Empire XCcel®. In order to achieve infinite dimensions in the simulated structures (as used in the structures from the canonical equations in Chapter 2), perfect electric and magnetic conductors (PEC and PMC) were used as boundary conditions along two axes. Perfectly matched layers (PML) were used along the third axis.

In this chapter, an overview of the FDTD method and the boundary conditions is given in Section 3.2. Section 3.3 discusses the plane wave incidence and the expected response of the material and the simulation geometry of homogenous samples as a foundation for the heterogeneous ones. While Section 3.4 gives a detailed description of the inversion technique used here, Section 3.5 discusses the verification of the implementation of the technique with validating examples. A flowchart showing the whole process for the ε_{eff} and μ_{eff} extraction described in this chapter is given in Figure 3.1. The conclusions are given in Section 3.6.

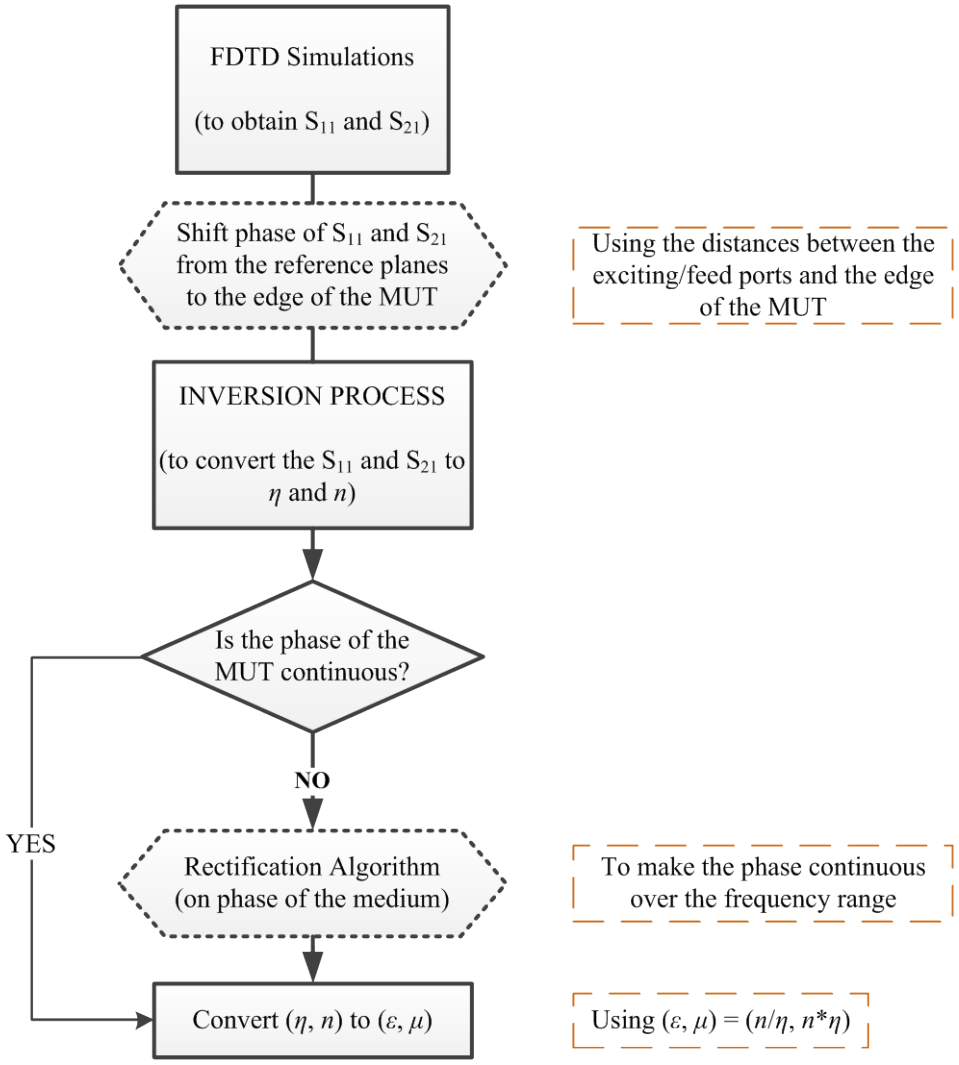

Figure 3.1: Flowchart of the Inversion Process to extract ε_{eff} and μ_{eff}. (MUT: material under test; η and n are the MUT's impedance and refractive index respectively)

3.2 Overview of FDTD Technique

The history and introduction of FDTD to solving electromagnetic problems is presented in [15]. The FDTD method is a numerical modelling technique that discretises the problem space into time and space, and uses the differential form of Maxwell's equations to provide the solution over time. FDTD was first described in [16] and it uses the Yee cell in which the three Cartesian components of the electric and magnetic fields are discretised to form a 3-D space lattice. The FDTD method works by dividing the problem space into smaller cells called Yee cells [16], of size $\Delta x, \Delta y$ and Δz, the differential equations are represented by their discretised forms. Further discussion on the FDTD method is given in Appendix 3.

FDTD is a discontinuous method and each Yee cell can be surrounded by materials having different electrical properties. This is particularly useful for this research as the artificial dielectrics to be designed are made up of at least two materials of different electrical properties. A significant characteristic of FDTD is that it requires the whole computational space to be discretised which may require large computational memory and thus long simulation times. Empire XCcel® FDTD software was used in this work. It uses grid or mesh lines to divide the problem space into Yee cells of different sizes depending on the resolution required.

3.2.1 Boundary Conditions in FDTD

Perfect Electric and Magnetic Conductors (PEC and PMC) can be used as boundary conditions in an FDTD simulation; they can also be used as symmetry planes [17]. A PEC boundary has an infinite conductivity and so forces the tangential electric field to zero at the outermost grid line of the problem space. This is particularly useful in the simulations in this research where the incident wave is a Transverse ElectroMagnetic (TEM) wave and so has no electric field component in the direction of wave travel, that is, parallel to the PEC boundaries. The PMC boundary also forces the tangential magnetic field to zero in the middle of the outermost cell. As the PEC and PMC boundaries serve as symmetry planes, they allow the replication of a structure to an infinite extent along the plane parallel to those boundaries. In Empire XCcel®, the PEC boundary lines lock to the edge of the problem space while the PMC boundary line locks to the middle of the outermost cell. An example of how these two boundary conditions are represented in Empire XCcel® is shown in Figure 3.2. In (a), the top blue line is the edge of the structure while the lower green line is the PMC boundary which is between the black and red grid/mesh lines at the right edge column; in (b) the top red line

with the ground symbol is the PEC boundary and as shown is locked to the edge of the structure/outermost grid line, which is blue in this case. The meshing at the PMC boundary of the structure in Empire XCcel® can be increased in the outermost cell manually to force the PMC to be at the edge of the structure. In this case, the blue and green lines in Figure 3.2 (a) will then coincide.

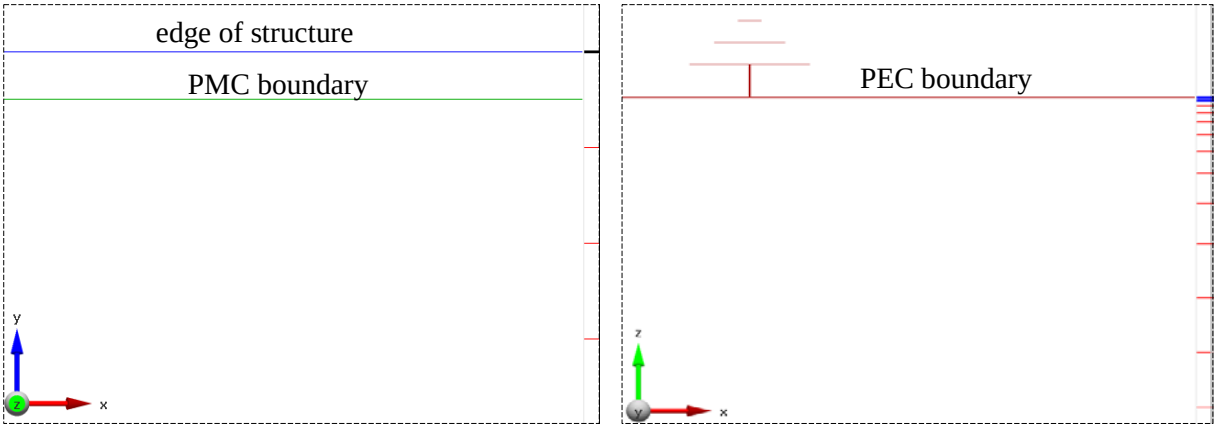

(a) (b)

Figure 3.2: Screenshots from Empire XCcel® to show (a) the PMC and (b) PEC boundaries

For the absorbing boundary conditions (ABC), their impedance is matched to the impedance of the free space and so in an ideal case, there are no reflections at these interfaces. ABC's contain lossy materials to absorb the incident wave. These ABC's are represented by perfectly match layers (PML) in Empire XCcel®. PML was introduced by Berenger [18] and reduced reflections to about 80dB, which effectively puts the material/sample in free space. In Empire XCcel®, the higher the number of these layers, the smaller the reflections and the more accurate the S-parameter results, but the slower the simulation speeds [17]. More details on the FDTD process can be found in [15], [19], [20].

3.3 Plane Wave Simulation Geometry

3.3.1 Plane Wave Incidence

The effect of a plane wave incident on a finitely thick material is briefly explained here. References [21], [22] give an explanation for the behaviour of a plane wave impinging on a flat surface. For simplicity here, a TEM plane wave is used in which the electric (E) and magnetic (H) fields are linearly polarised and tangential to the plane of incidence. The direction of propagation is perpendicular to this plane of incidence. This is shown in Figure 3.3.

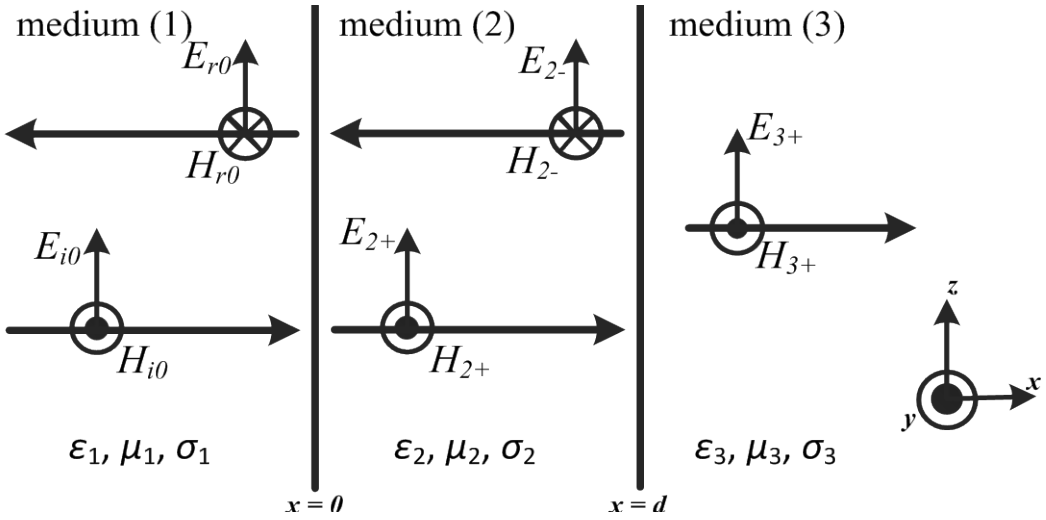

Figure 3.3: Reflection and transmission of electric and magnetic fields at the interface(s) of a slab of finite thickness. Note that this image is based on that given in [21].

Since the structures examined in this thesis were materials of finite dimensions, the more complex analysis derived for a TEM plane wave with normal incidence on a slab of finite thickness (bounded by air) as shown in Figure 3.3, was used whose reflection and transmission coefficients are given respectively, by [21]:

$$\Gamma_{slab} = \frac{E_{r0}}{E_{i0}} = \frac{\Gamma_{12} - e^{-j2\beta_2 d}}{1 - \Gamma_{12} e^{-j2\beta_2 d}}; \qquad T_{slab} = \frac{E_3^+}{E_{i0}} = \frac{(1 - \Gamma_{12}^2) e^{-j\beta_2 d} e^{j\beta_1 d}}{1 - \Gamma_{12}^2 e^{-j2\beta_2 d}} \tag{3-1}$$

where Γ_{12} is the reflection coefficient at boundary; β_2 and β_1 are the phase constants in the slab and the bounding media respectively; and d is the thickness of the slab (equation (3-1) assumes lossless dielectrics). These expressions are derived from first principles in [21] by

examining the electric and magnetic fields at the boundaries. From equation (3-1), once the values of the incident, reflected and transmitted fields are known together with the thickness of the test slab, algebraic manipulations can be used to extract the ε and μ of the MUT.

An important point to consider when measuring the properties of dielectric materials using plane wave illumination is the distance between the surfaces of the MUT and the measurement planes/ports and/or source of excitation. For instance, if horn antennas are used for the measurements, as a rule of thumb, a distance of about 10 wavelengths is recommended to make sure that the wave impinging on the material is as 'plane' as possible and that the material is in the farfield region of the antennas, that is, at $2D^2/\lambda$, where D is the largest dimension of the antenna and λ is the shortest wavelength over the frequency range examined [23]. In addition, where coaxial-to-waveguide adapters are used, extra lengths must be allowed between the sample and the adapters to ensure that the "higher order evanescent modes due to the adapters are significantly attenuated prior to reaching the sample" [8]. This extra-distance rule applies also when using numerical simulation tools such as Empire XCcel® for these plane wave simulations. The "Microstrip port" in Empire XCcel® [17] was used to generate the plane waves used in the simulations in this thesis. Note: Empire XCcel® has a plane wave box but using the microstrip port is more advantageous compared to a plane wave excitation as the S-parameter results at the ports are readily available.

3.3.2 Simulated Plane Wave Verification

In order to verify that the plane wave generation source in the simulation tool gave a true TEM wave, an empty port source as shown in Figure 3.4, was simulated first. The PEC and PMC boundary conditions were used in all these plane wave simulations as symmetry planes to replicate the infinite dimensions used in the canonical equations as discussed in Chapter 2, and also to truncate the simulation domain [17]. The PEC and PMC boundaries were at $(z = 0,\ z = z_{max})$ and $(y = 0,\ y = y_{max})$ respectively. The PML boundary conditions were used at each reference plane $(x = 0,\ x = x_{max})$ to minimise reflections from the ports and can be placed in the same position as the ports, giving a higher accuracy in the S-parameter results. Placing the ports in the same location as the PML boundary is possible as it has been built in to Empire XCcel® when the ports are pre-defined as 'Absorbing' ports.

'P1E' and 'P2' are the measurement and reference planes in the simulations. The 'E' in P1E indicates that the port is excited as it is the source. The blue crosses ('X') indicate where these ports are, while the dashed lines (---) indicate the measurement/reference planes and in

this case coincides with the port positions. The 'DumpBox' is used as a storage box in Empire XCcel® to measure and save the values of the E- and H-fields along any path within the box [17]. The electric and magnetic fields along the path of propagation of the waves can also be measured at pre-defined frequencies.

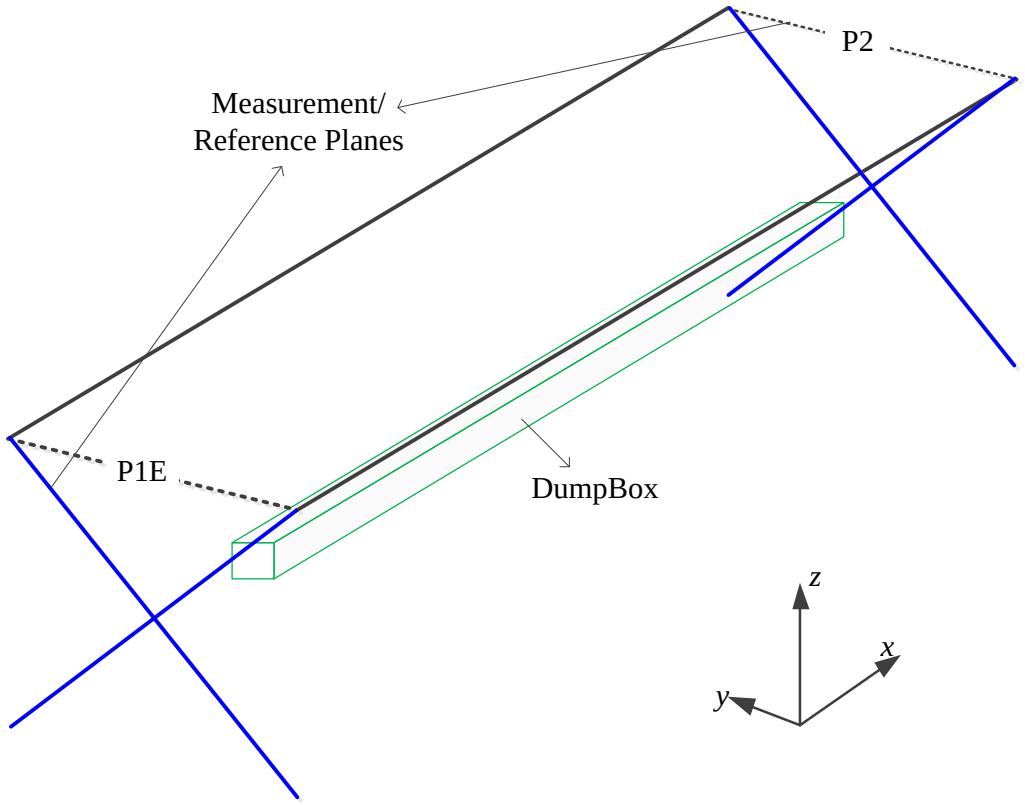

Figure 3.4: The plane wave source – using a "Microstrip port", in Empire XCcel®

Figure 3.5 shows the amplitudes of the three Cartesian components (x, y, z) of each of the fields at 10 GHz. For a plane wave, the E and H fields are in phase and are perpendicular to each other and to the direction of propagation. The wave impedance, η in these regions can be readily obtained by dividing the value of the E-field by that of the H-field, that is, $\eta = E/H$. This gives the well-known wave impedance of free space (or vacuum), 120π Ω (= 376.99 Ω), approximately. From Figure 3.5 (a), E_x and E_y are close to zero while $E_z \cong 14.1$, and from Figure 3.5 (b), H_x and H_z are zero while $H_y \cong 37.4$, all normalised to the incident fields. Using the results of E_z and H_y given in Figure 3.5, the wave impedance, $\eta \approx 377.01$ Ω, which is equal to that of free space. Similar results were obtained at 1 and 15 GHz. These values show that the wave generated by the port is a true TEM plane wave and therefore, this is a computationally efficient method of creating a plane wave excitation for the simulations.

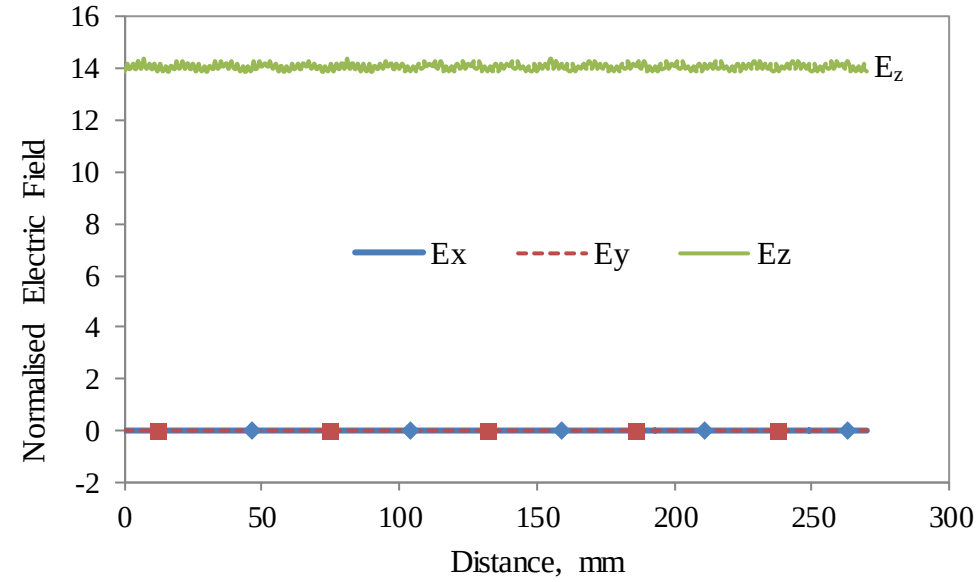

(a)

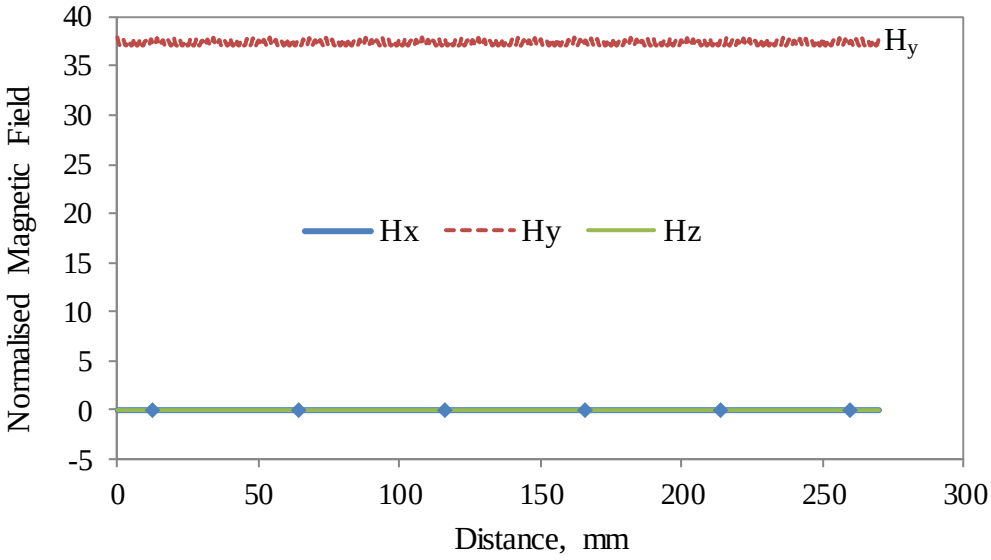

(b)

Figure 3.5: Amplitudes of the (a) electric and (b) magnetic fields along the three Cartesian axes: *x* (—♦—), *y* (--■--), *z* (▬)

3.3.3 Simulation Geometry with Homogenous Slabs

A dielectric slab of finite thickness, see Figure 3.6, was simulated using Empire XCcel® and the electric and magnetic fields were extracted. Sufficient distances had to be placed between the slab and the measurement (reference) planes to ensure that any "higher order evanescent modes" that may be present are significantly attenuated before reaching the slab [8], [24]. This principle is analogous to ensuring the material under test (MUT) is exposed to a plane wave from an antenna by placing it in the far-field of the antenna. The positions of the PEC

and PMC boundary conditions as used in all of the plane wave simulations are as shown in Figure 3.7.

The regions between the measurement planes and the interfaces of the structure along the wave propagation direction can be taken in the simulation domain to be the same as free space, without loss of accuracy. The slab's reflection and transmission coefficients are functions of its EM properties (ε, μ), which can be derived from the amplitudes of the E- and H-fields in these regions. Therefore, for a slab of known thickness, *d*, the field values can be used to obtain its EM properties, ε and μ. However, because these EM properties are intricately woven into the equations in (3-1), inverse scattering methods that use the known values of the scattering parameters and the slab dimensions, were used instead to derive the EM properties of the heterogeneous media.

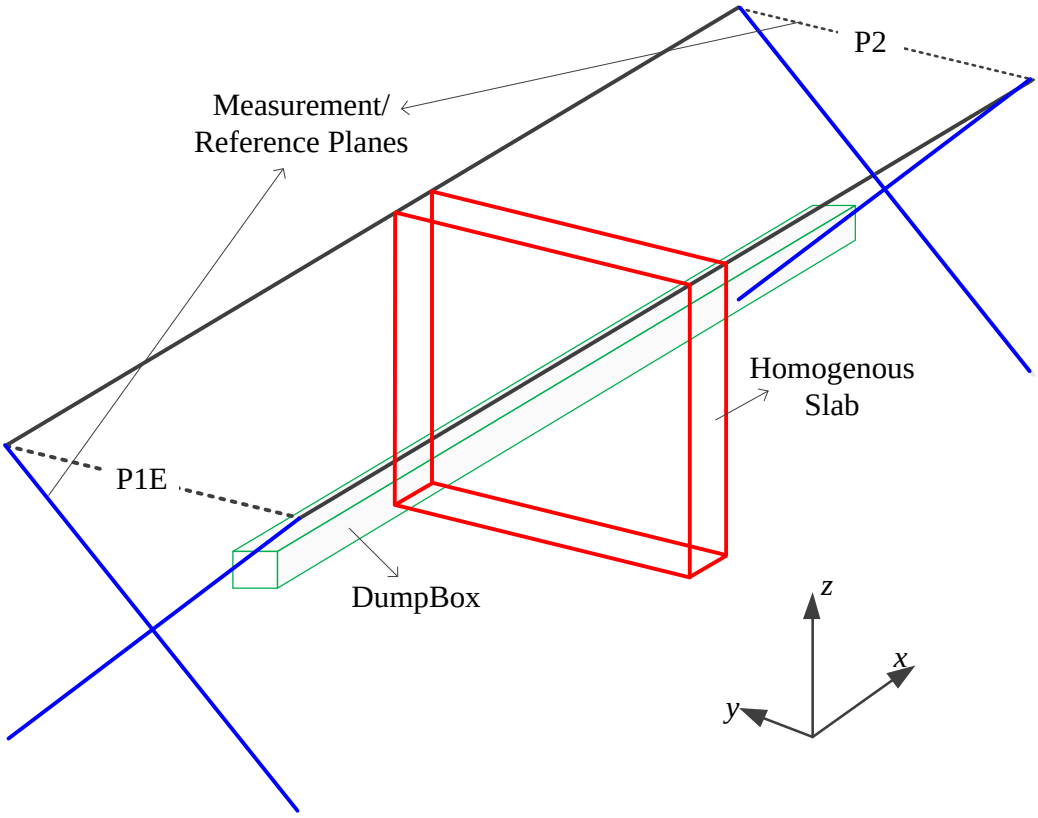

Figure 3.6: Simple 3-D simulation set up of a homogenous dielectric slab under plane wave illumination, with DumpBox for field recording.

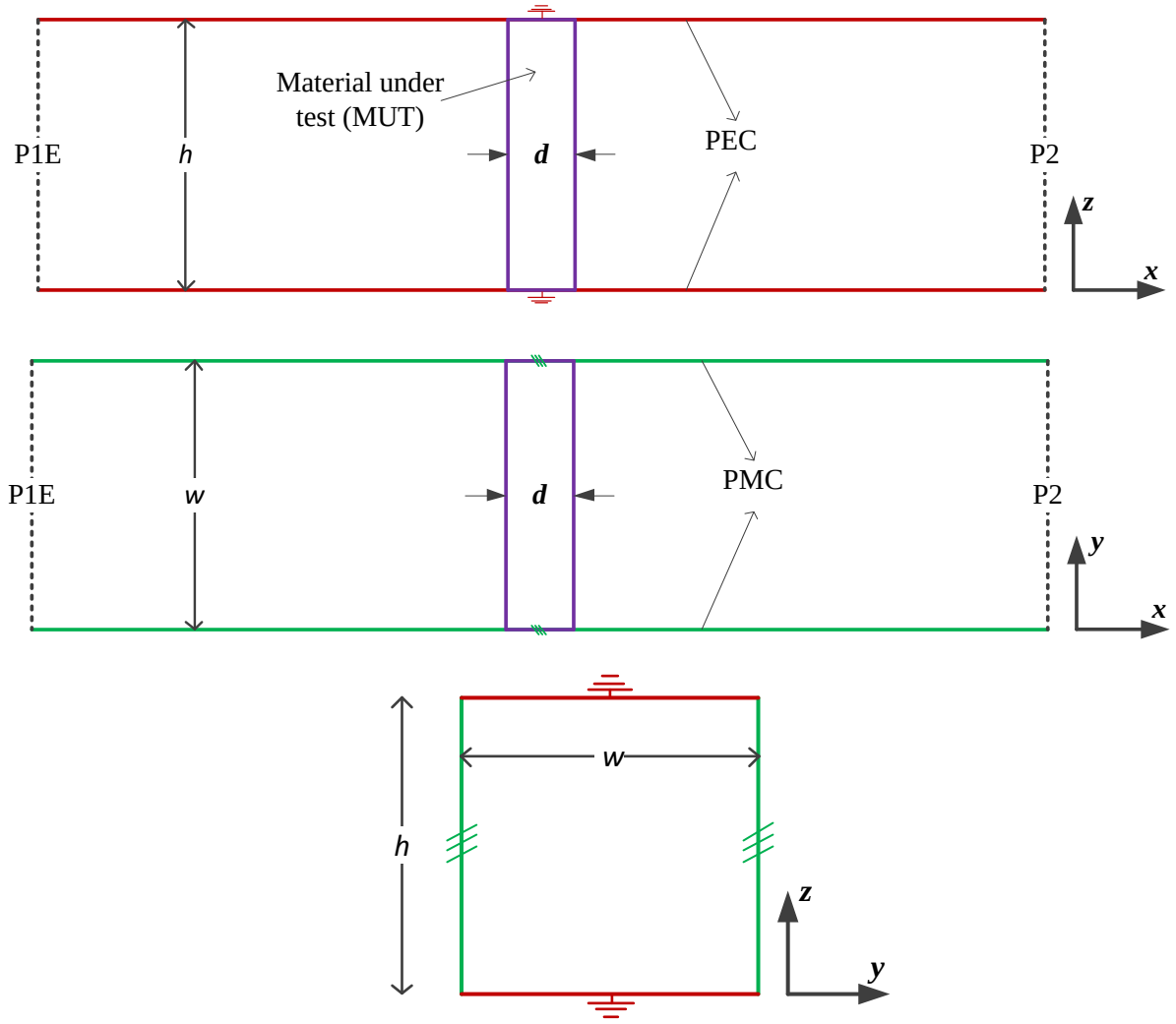

Figure 3.7: 2-D representation of simulation setup to show PEC and PMC boundaries. The dashed lines indicate the PML boundaries and reference planes.

Depending on the maximum width, w or height, h of the Microstrip line (MSL), whichever is greater, a cut-off frequency point is reached after which spurious resonances occur and any results after this point are not fit for use in the extraction calculations or at worst, completely inaccurate. This frequency is given by: $f_c = c/\max(w \text{ or } h)$, where c is the speed of light in free space, $\approx 3 \times 10^8$ m/s. However, due to the fact that the PEC and PMC boundaries on the z- and y-axes providing a symmetry (mirror) plane reproducing an infinite structure, the cross-section of the MSL can be made as small as necessary to increase the cut-off frequency and so that accurate higher frequency results are possible.

3.4 The Inversion Algorithm

The Inverse Scattering Algorithm is a method of taking measured or numerically computed S_{11} and S_{21} parameters of a medium subjected to an incident plane wave and algebraically manipulating them to obtain the EM properties of that medium. These properties are the effective wave impedance and refractive index which can be used to obtain the effective permittivity and permeability of the medium [8], [9], [12]. The complexity of equation (3-1) creates the need for an alternative method compatible with the simulation tool and the results it produces. Empire XCcel® provides the total E- and H- fields within the simulation domain, but it does not break down the E-field in the region between the exciting port and the MUT into the incident and reflected fields. Therefore, this eliminates the use of equation (3-1) in extracting the EM properties of the MUT. Empire XCcel® gives the S-parameters (S_{11} and S_{21}) and reciprocity is assumed for the S_{12} and S_{22} values.

As stated in Section 3.1, there are several inversion techniques [8–10], [13], [25–29] that can be used to extract the ε and μ of the MUT. The S-parameter results from the simulations are used as inputs into these formulations to obtain the effective ε and μ. The inversion technique chosen and used extensively for this thesis is the "Resonant Inverse Scattering" formulations given in [9] and the effective ε and μ extracted from the published S-parameters were reproduced using the equations given in it. It requires a plane wave excitation as shown in Figure 3.4. It was straightforward to implement in MATLAB and robust as it allowed flexibility in the geometries – homogenous and heterogeneous materials, and also showed good agreement with the results from the canonical equations in Chapter 2. Although these formulations apply primarily to homogenous media, they can be applied to heterogeneous structures with good levels of accuracy as heterogeneous media can be viewed as being macroscopically continuous [9], [10], within the boundaries where the effective medium theory applies.

As the EM properties are related to the reflection and transmission coefficients as given in equation (3-1), the relationship between the S-parameters and these coefficients is important and is given by [8], [9], [30]:

$$\Gamma = \mathrm{V} \pm \sqrt{V^2 - 1}; \qquad T = \frac{S_{11} + S_{21} - \Gamma}{1 - (S_{11} + S_{21})\Gamma} \tag{3-2}$$

where $V = \frac{S_{11}^2 - S_{21}^2 + 1}{2S_{11}}$; and Γ and T are the reflection and transmission coefficients respectively.

A direct relationship between the S_{11} and S_{21} and the EM properties is given by [9]:

$$S_{11} = \frac{\eta - 1}{\eta + 1} \frac{1 - x^2}{1 - \left(\frac{\eta - 1}{\eta + 1}\right)^2 x^2}; \qquad S_{21} = \frac{4\eta x}{(\eta + 1)^2} \frac{1 - x^2}{1 - \left(\frac{\eta - 1}{\eta + 1}\right)^2 x^2} \tag{3-3}$$

where η is the wave impedance; $x = e^{jk_0 dn}$; k_0 is the wave number; d is the thickness; and n the refractive index of the sample. The two unknowns here are η and n.

By algebraically inverting these equations, the exact solution to the effective parameters of the medium is given in equations (3-4) – (3-6) [9]:

$$\eta = \frac{1 + A}{1 - A} = \pm\sqrt{\frac{V + 1}{V - 1}}; \quad A = V \pm \sqrt{V^2 - 1} \tag{3-4}$$

$$Re\{n\} = \frac{\cos^{-1}(Re\{x\}/|x|)}{k_0 d}; \qquad Im\{n\} = -\frac{\ln|x|}{k_0 d} \tag{3-5}$$

where

$$V = \frac{1 + S_{11}^2 - S_{21}^2}{2S_{11}}; \quad x = \frac{S}{1 + R - ASR}; \quad S = S_{11} + S_{21}; \quad R = \frac{S_{11}}{S_{21}} \tag{3-6}$$

The decision on which sign to use ($\pm$) in equation (3-4) is dealt with by ensuring that for each frequency point, Re$\{\eta\} > 0$, or $|A| \leq 1$, where $A \equiv \Gamma_\infty$ is the "reflection coefficient for a planar semi-infinite medium". Another issue is the "multivaluedness of the inverse trigonometric function and analytic continuation of phase" in equation (3-5) [9]. Due to the nature of inverse cosine functions, the numerator of $Re\{n\}$ can have several values which are all correct. For example, $\cos^{-1}(1) = 0, 2\pi, 4\pi, ...$ As with frequency, the phase, φ_d of the medium keeps returning to the "first Reimann sheet" [31], [32] because of the inverse cosine function in the equations, whereas physically the phase should be a continuous (analytic) function as should the resulting refractive index, over frequency. The Reimann sheet describes the region over which the phase of a complex number gives the definition/validity of the complex number [33], [34]. In this case, the phase oscillates strictly between 0 and 2π

or $-\pi$ and $+\pi$, whereas it should go above this range, and so the first Reimann sheet is defined by $0 < \varphi_d < 2\pi$, and maps unto the upper half of the complex plane. This oscillation is handled by using a rectification algorithm on the phase which is described in Section 3.4.1.

3.4.1 Rectification Algorithm

Due to the restriction of the phase of the medium to the first Reimann sheet as described above, a rectification process is required to make the phase continuous over the frequency range. The rectification process ensures that if the phase reaches a peak, say, $+\pi$, instead of returning to $-\pi$ for the next frequency point, the phase goes to $+3\pi$. This process is explained in more detail below.

Phase Transfer

As the ports, P1E and P2 serve as the measurement planes and are not at the edges of the structure, the values of the phases of the S-parameters measured are not the same as the phases at the edges of the MUT as the waves have travelled over these distances. The first step in the rectification process is to transfer the phases of the S-parameters. Let the distance from Port 1 to the slab be d_1, the distance from the other end of the slab to Port 2 be d_2, as shown in Figure 3.8, and the phase of the S_{11} from the simulations be φ_1 while the phase of the S_{21} be φ_2. d_1 and d_2 are typically at least five times the thickness of the sample and longer especially where the simulation domain size allows it such that the simulation time is hugely prolonged, especially for the homogeneous slabs presented in Section 3.5.2. $d_{1,2} \gg d$.

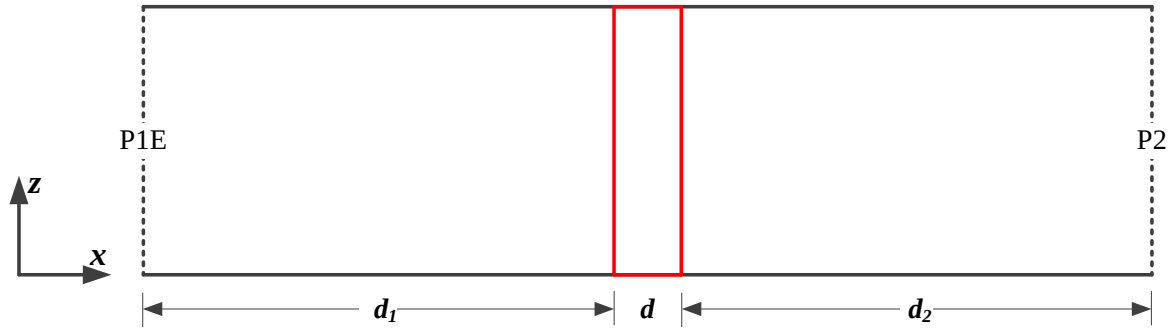

Figure 3.8: 2-D view of simulation set-up with homogenous slab. (not drawn to scale)

Thus, the first stage of the rectification process is to shift these measured or simulated phases to these edges as these are the correct phases to be used in the inversion process [8], [21]. These corrected phases are given in equations (3-7) and (3-8):

$$\varphi_{1c} = \varphi_1 + 2k_0 d_1 \text{ for the } S_{11} \tag{3-7}$$

and

$$\varphi_{2c} = \varphi_2 + k_0 d_2 + k_0 d_1 \text{ for the } S_{21} \tag{3-8}$$

where $k_0 = 2\pi/\lambda$ and λ is the free space wavelength. If the medium surrounding the slab is not free space or vacuum, the value of λ is modified by $\sqrt{\mu_x \varepsilon_x}$, such that λ becomes $\lambda/\sqrt{\mu_x \varepsilon_x}$ where (ε_x, μ_x) is the relative ε and μ of the surrounding medium. The effect of this transfer of phase is shown in Figure 3.9. There are fewer oscillations in the transferred phase than the original phase as the wave has effectively travelled a shorter distance.

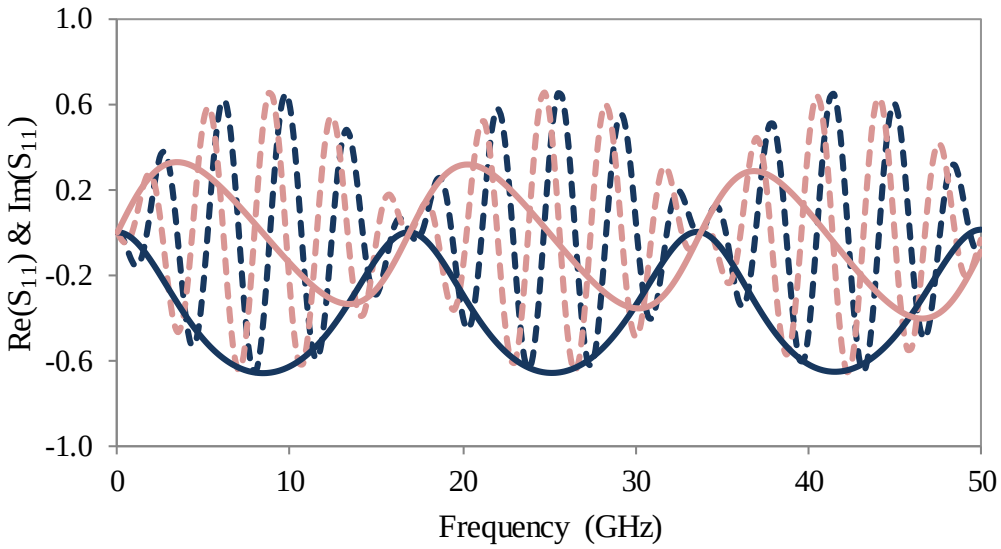

Figure 3.9: An example of $\mathrm{Re}(S_{11})$ (blue) and $\mathrm{Im}(S_{11})$ (red) before (dashed) and after (continuous) transfer of phase to the edge of the structure

Phase Rectification

After transferring the phase of the S-parameters to the edge of the MUT, the phase of the MUT has to be rectified. The phase change for a wave travelling in a (dielectric) medium of finite thickness, d, as shown in Figure 3.8 is given in equation (3-9) [9]:

$$\Delta\phi_d = k_0 d Re\{n\} \tag{3-9}$$

As shown in Figure 3.10, when semi-logarithmic (log scale on *y*-axis only) graphs of $\Delta\phi_d$ and $\pi - \Delta\phi_d$ against frequency are plotted, sharp discontinuities occur at certain frequencies due to the inverse cosine function in equation (3-5). The line labelled $(\pi - \varphi_d)$

has been included to highlight these discontinuities. Without rectification of this phase, the refractive index, n follows these discontinuities falling to zero at the frequencies of the phase minima and peaking at the frequencies of the phase maxima [35], and the phase is therefore only accurate at frequencies below the first discontinuity without the rectification algorithm.

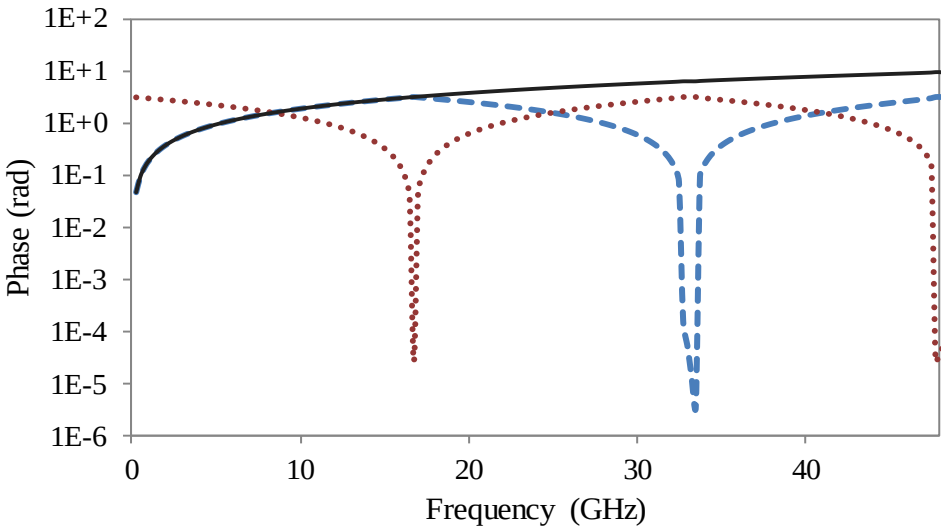

Figure 3.10: Example of the discontinuous phases, $\Delta\varphi_d$ (— — —), $\pi - \Delta\varphi_d$ (••••) and the rectified phase, $\Delta\varphi_r$ (▬▬) of a medium

The rectification process is explained below. Combining equation (3-9) with (3-5) implies that the phase of the medium can also be expressed and calculated as:

$$\Delta\phi_d = \cos^{-1}(Re\{x\}/|x|) \tag{3-10}$$

Depending on the range of frequencies selected, the thickness of the MUT and the EM properties of the medium, there may not be a discontinuity throughout the frequency range. If this is the case, $\Delta\phi_d = \Delta\phi_r$, where $\Delta\phi_r$ is the rectified phase. If discontinuities occur, then it is initially assumed that the rectified phase, $\Delta\phi_r$ is equal to either $\Delta\phi_d$ or $\{(\pi - \Delta\phi_d)\}$, depending on which is increasing, that is, has an initial positive gradient. These two functions are complementary to each other. This continues till the point where the first discontinuity occurs, say at frequency, f_1. This can be written as:

$$\Delta\phi_r(1{:}f_1) = \Delta\phi_d(1{:}f_1) \text{ or } \{(\pi - \Delta\phi_d)(1{:}f_1)\} \tag{3-11}$$

On reaching the first discontinuity, the second function is now increasing and is added to the value of $\Delta\phi_r$ from the point at which the first discontinuity occurs, that is, at the point

$\Delta\phi_r(f_1) = \Delta\phi_d(f_1)$ or $\{(\pi - \Delta\phi_d)(f_1)\}$. Thus, from f_1 to the next discontinuity, say at frequency, f_2, the value of $\Delta\phi_r$ is given as:

$$\Delta\phi_r(f_1{:}\, f_2) = \Delta\phi_d(f_1) + (\pi - \Delta\phi_d)(f_1{:}\, f_2) \text{ or } (\pi - \Delta\phi_d)(f_1) + \Delta\phi_d(f_1{:}\, f_2) \tag{3-12}$$

At f_2, when the second function starts decreasing, the first function which should now be increasing is added from this point of discontinuity. That is, from f_2 to the next discontinuity, say f_3, the value of $\Delta\phi_r$ is given as:

$$\Delta\phi_r(f_2{:}\, f_3) = \Delta\phi_d(f_1) + (\pi - \Delta\phi_d)(f_2) + \Delta\phi_d(f_2{:}\, f_3)$$

$$\text{or } (\pi - \Delta\phi_d)(f_1) + \Delta\phi_d(f_2) + (\pi - \Delta\phi_d)(f_2{:}\, f_3) \tag{3-13}$$

This process is repeated until the end of the operating frequency range. The new 'rectified phase' is now a continuous increasing function of frequency without discontinuities, as shown by the black continuous line in Figure 3.10.

The rectified phase, $\Delta\phi_r$ is then used to re-compute $Re\{n\}$ in equation (3-5), that is,

$$Re\{n\} = \frac{\Delta\phi_r}{k_0 d} \tag{3-14}$$

Thus, the correct values of refractive index, n and wave impedance, η are then obtained and are related to the EM properties ε and μ by:

$$\varepsilon(f) = n(f)/\eta(f)$$

$$\mu(f) = n(f) \cdot \eta(f) \tag{3-15}$$

This rectification process is important as the refractive index of the medium, which varies as a function of frequency, is directly determined from this phase. The whole inversion process including the rectification algorithm was implemented in MATLAB to automatically handle the rectification process using *for* loops, and correctly deal with the sign ambiguity. The imaginary parts of the S-parameters have to be negated due to the difference in sign convention when travelling waves are represented by Physicists ($e^{i(kx-\omega t)}$), as used in [9], or by Engineers ($e^{-j(kx-\omega t)}$). To further illustrate the need for the rectification process in order to improve the accuracy and continuity of the ε_{eff} and μ_{eff}, an example of the extracted ε_{eff} with and without the phase rectification is plotted in Figure 3.11. Note: detailed comparisons with the empirical equations will be discussed in Chapter 4.

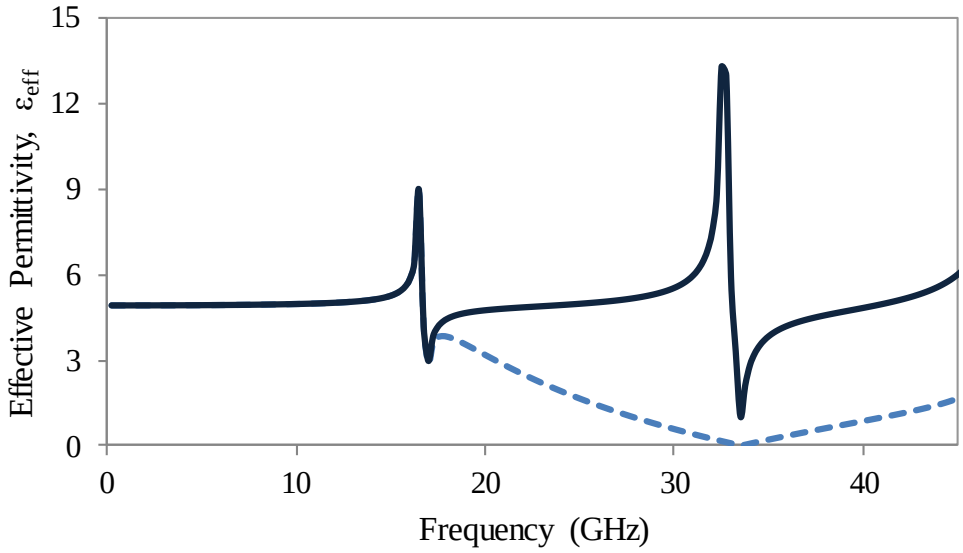

Figure 3.11: An example of the extracted ε_{eff} with (continuous) and without (dashed) the rectification process

Since n is subject to the rectification process, a relatively continuous plot of n can be achieved. However, as the wave impedance, η is still a function of the un-rectified values of the S-parameters (after the phase transfer), its behaviour still shows the discontinuities that have been removed from n. Hence the "spikes" (from the thickness resonance of the structure) as a result of these discontinuities left in its plots will appear in the ε_{eff} and μ_{eff} graphs. Figure 3.12 shows a typical graph to illustrate this point.

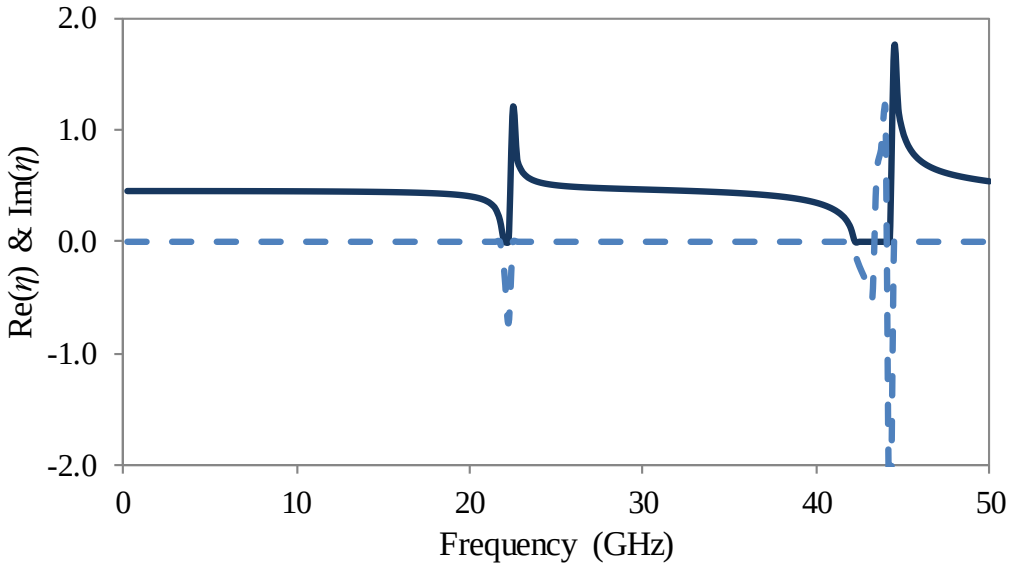

Figure 3.12: An example of the real (——) and imaginary (– – –) parts of the extracted wave impedance, η_{eff}, from the inversion process (including the rectification process)

As shown in Figure 3.11 and Figure 3.12, "spikes" occur at certain frequencies. At these frequencies, which are related to the thickness of the dielectric slab and its EM properties by $d = n\lambda_g/2$ where λ_g is the guided wavelength given by $\lambda_g = \lambda_o/\sqrt{\mu_r \varepsilon_r}$; and n is an integer, = 1, 2, 3 . . ., the slab is transparent to the incident plane wave [21] and so total transmission occurs. Thus at these frequencies, the values of the S_{11} are close to zero [$\mathrm{Re}(S_{11})$, $\mathrm{Im}(S_{11}) \cong 0$], while $|S_{21}| \cong 1$ [$\mathrm{Re}(S_{21}) \cong \pm 1$, $\mathrm{Im}(S_{21}) \cong 0$]. This explains these "spike" points (shown in Figure 3.10 to Figure 3.12 and other subsequent ε_{eff} and μ_{eff} plots), also known as the half-wavelength impedance matching frequencies [21], [26] or thickness resonance points [28]. These "spikes" are also called the Fabry-Perot resonance points [9].

3.4.2 Rectification Verification by Group Delay

It is worth noting that information from the original simulation results is not lost by using the rectification process. The group delay of the medium before and after the inversion process (including rectification) can be used to verify this as shown in Figure 3.13. The group delay of a medium can be defined as the negative derivative of the phase response of that medium with respect to frequency. This phase response is the phase of the S_{21}, ϕ_{S21} [36], [37] and can be in radians or degrees.

Group delay, τ_g is given as:

$$\tau_g = -\frac{1}{2\pi}\frac{\partial \phi_{S21}}{\partial f} \tag{3-16}$$

where ϕ_{S21} is the phase of the S_{21}.

Equation (3-16) was calculated using numerical differentiation which is suitable as the values of the phase response are discrete. Numerical differentiation is a form of differentiation that finds the derivative of a function at a specific point [38], [39] and for the derivative in equation (3-16) can be written as:

$$\frac{\partial \phi_{S_{21}}}{\partial f} = \frac{\phi_{S_{21}}(n+1) - \phi_{S_{21}}(n)}{f(n+1) - f(n)} \tag{3-17}$$

The initial equations for the S-parameters used to obtaining the inversion equations in [9] were used in the reconstruction of the S_{21} from the extracted values of ε_{eff} and μ_{eff}, and the slab thickness, d. The group delay remains the same as shown in Figure 3.13. The slight shift

in the two plots is likely due to the method of differentiation employed as effectively a point is ‘lost’.

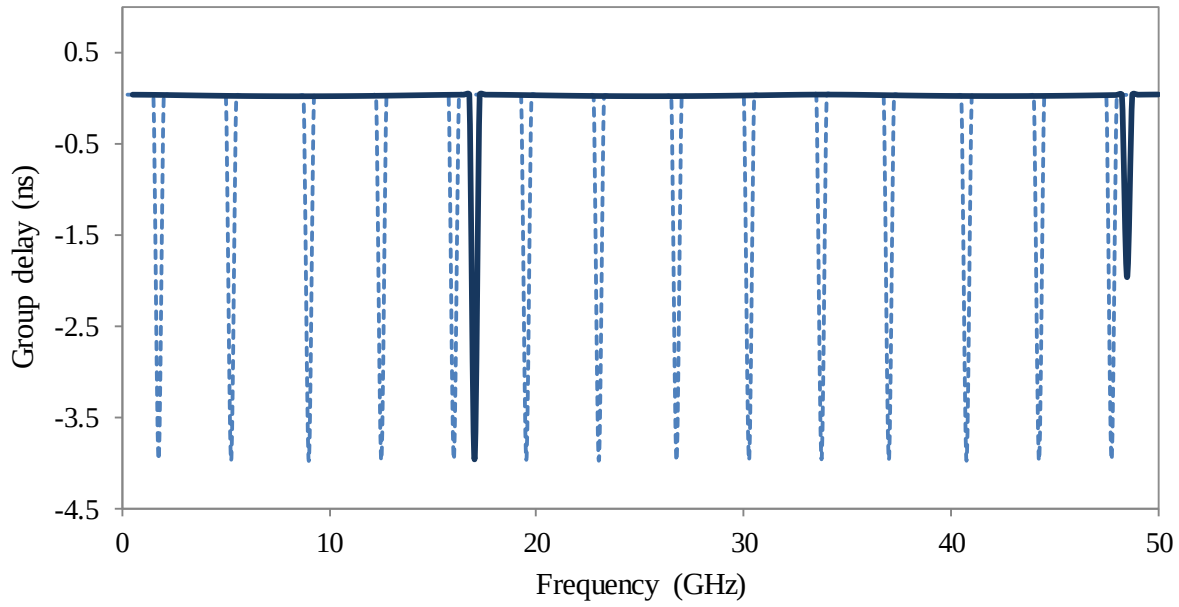

Figure 3.13 An example of the variation of group delay with frequency, before (— — —) and after (▬) phase rectification. ($d = 4$ mm, $\varepsilon_r = 4.9$)

3.5 Implementation of the Inversion Technique

After the inversion process was written in MATLAB, it was tested on the S-parameters estimated from the graphs [9] to make sure it gave similar plots to those published. Once this was achieved, the first structure (Figure 1(a)) in [9] was reproduced and tested. The inversion process was also tested on homogenous MUT's of known EM properties.

3.5.1 Verification of Implementation of Inversion Technique

In order to test the implementation of the resonant inverse scattering method in MATLAB, the exact 4-by-3-by-2 disc lattice presented in [9] was simulated in Empire XCcel®, as shown in Figure 3.14. The simulation domain is similar to that in Figure 3.6 except with a heterogeneous medium replacing the homogenous one. Here, the heterogeneous structure consisted of a 3-D array of thin metallic discs in a dielectric medium used to verify the inversion technique to determine the increased ε_{eff} of the structure. In the paper, the technique was then applied to more complicated structures, some with negative real permittivity [9]. The size of the cross-section of the MSL used in this simulation was 5.25 mm by 7 mm (which was also the size of the structure). Therefore, the cut-off frequency was ~ 42.86GHz. Data used: disc radius, $r = 0.45a$, $a = b = 1.75$ mm, host thickness, $d = 3c = 3 \times 1.7$ mm (a, b and c are as labelled in Figure 3.14), $\varepsilon_{host} = 11.1$ (tan $\delta = 0.0028$), $f = 0$ – 40 GHz. Discs were simulated metallic and 10 μm thick. $d_1 = 13.75$ mm, $d_2 = 17.16$ mm.

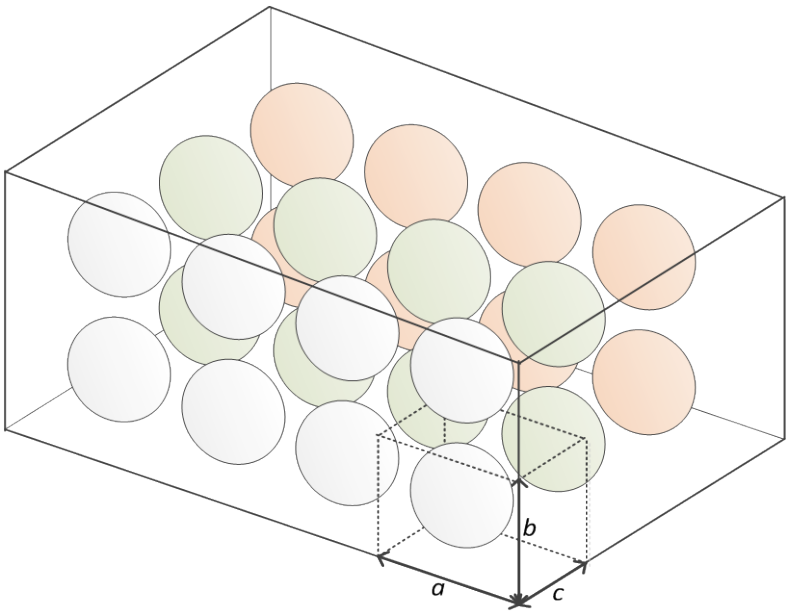

Figure 3.14: Metallic disc medium reproduced from [9]. Different colours are used for the discs even though they are of the same material to aid viewing in 3D.

Initial simulations gave similar S-parameter magnitudes to those in [9], albeit at slightly different resonant frequencies, but the real and imaginary values were different from the paper. After extensive investigation and consultation with the authors of the paper, it was realised that this was due to the S-parameters not being measured on the surface of the MUT and the sign conventions. Therefore, it is important to consider the distances between the surface of the MUT and the reference planes and the sign conventions used for the incident field as discussed in Section 3.4.1, or else the real and imaginary parts of the S-parameters will be incorrect.

As in the process described in Section 3.4, the S-parameters of the structure were simulated and are shown in Figure 3.15. Then the inversion and rectification processes were used to find the phases: $\Delta\phi_d, (\pi - \Delta\phi_d)$ and $\Delta\phi_r$ and are as plotted in Figure 3.16 (a). The rectified phase is continuous over the frequency range. The extracted results (η, n) and $(\varepsilon_{eff}, \mu_{eff})$ from the inversion process are given in Figure 3.16 (b). The resonant points in Figure 3.15 from the S_{11} and S_{21} graphs are the "spikes" explained in Section 3.4.1. These are points where the peaks of large transmission occur.

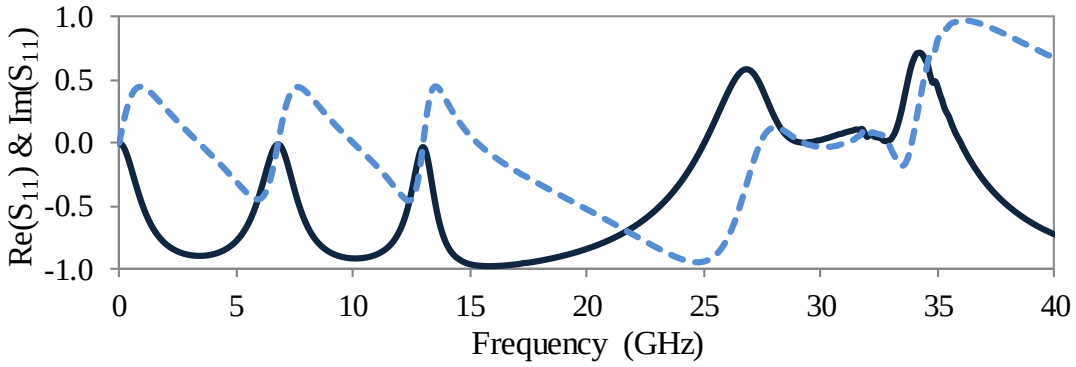

(a)

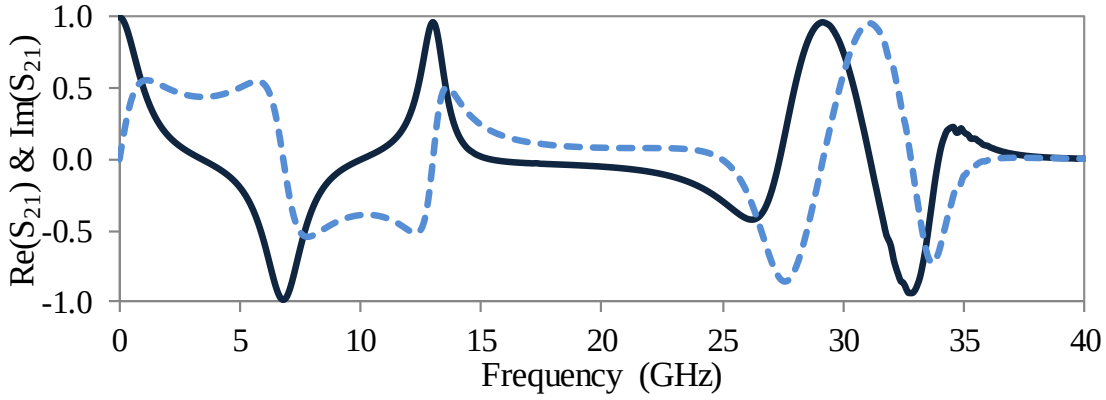

(b)

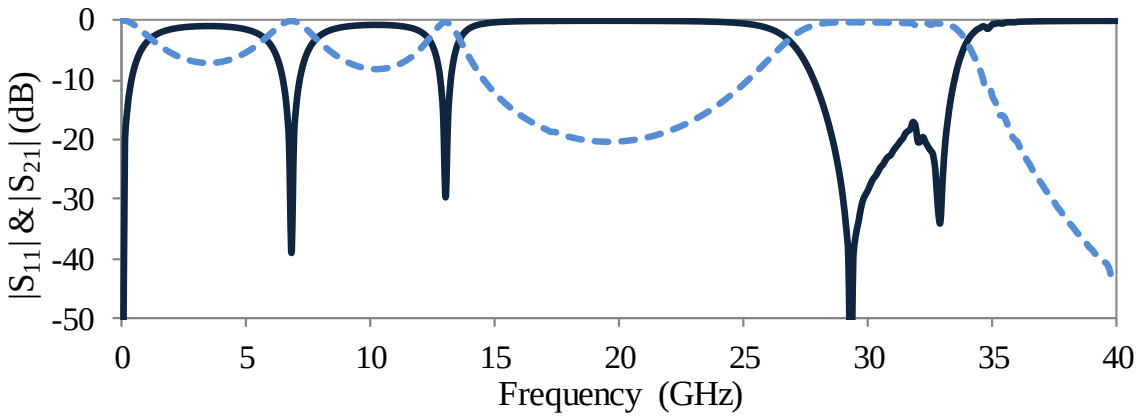

(c)

Figure 3.15: (a), (b) Real (continuous) and imaginary (dashed) and (c) absolute values of S_{11} (continuous) and S_{21} (dashed) results in dB from Empire XCcel®.

Common between the results shown in Figure 3.16 (a) and (b) and those given in [9] are the phase discontinuities that occur over the frequency range for numerically obtained results. These discontinuities have been attributed to the fact that for numerical computations of the S-parameters, $\mathrm{Re}(S_{21})$ is not exactly 1, nor are the other three curves exactly 0 when the MUT is transparent to the wave. Therefore, the real and imaginary parts of S_{11} and S_{21} "are detuned and their phases are slightly inaccurate" resulting in the effective parameters carrying "spurious narrowband resonances which could be identified and subtracted" by forcing the four S-parameter curves to their exact values in order to get a smoother curve [9]. These resonances are the smaller ripples in the S-parameter plots. In this case, these spurious resonances are left in the figures for comparison with the results obtained in [9]. The 'oscillations' towards the end of the frequency range may be due to the fact that these frequencies now approach the cut-off frequency (42.86 GHz). This may be avoided by reducing the maximum dimension of the MSL as its cross-section already represents an infinitely periodic structure. These results showed good agreement with those in [9] giving confidence that the inversion algorithm was correctly implemented.

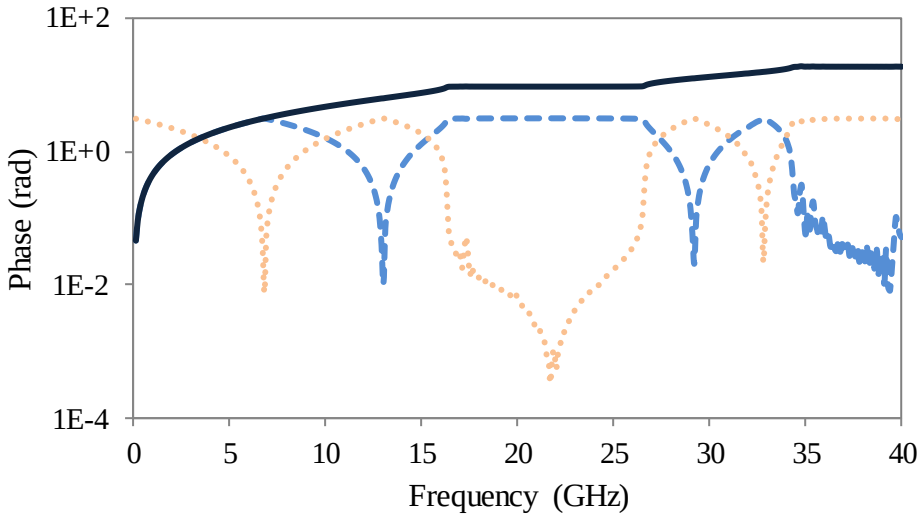

(a)

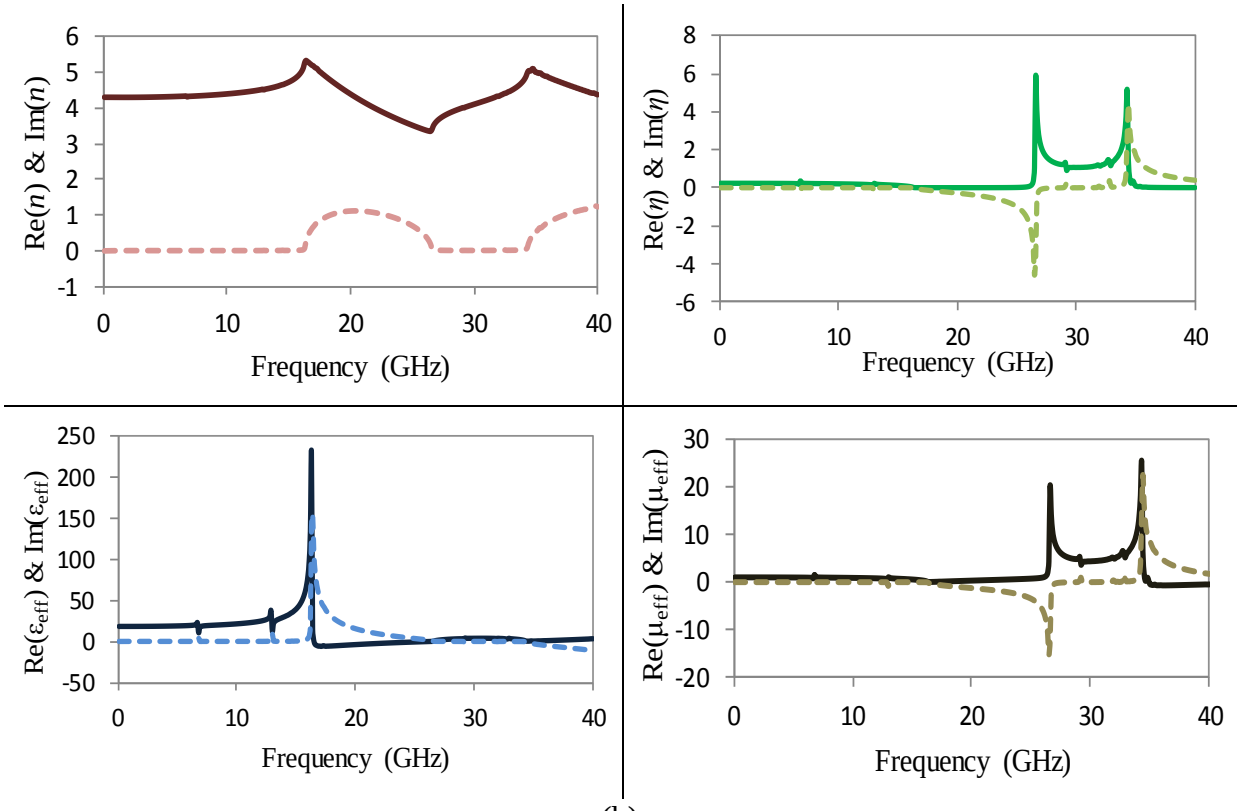

(b)

Figure 3.16: (a) Non-rectified phase $\Delta\phi_d$ (– – –) and rectified phase $\Delta\phi_r$ (——), from the S-parameters. (b) Real (continuous) and imaginary (dashed) parts of the refractive index, n, wave impedance, η, effective permittivity, ε_{eff} and permeability μ_{eff} of the disk medium (viewing left to right)

3.5.2 Validation of Inversion Technique with Homogenous Slabs of Known EM properties

In order to further validate the inversion technique, several homogenous dielectric materials of known ε and μ, and of different thicknesses were considered. The simulation set up is the same as that in Figure 3.6. The real and the imaginary parts of the S-parameters of a 4 mm thick slab (one of the geometries tested) are shown in Figure 3.17. Data used: $d = 4$ mm, $d_1 = d_2 = 38$ mm, $\varepsilon_{slab} = 4.9$, $\tan\delta = 0.025$.

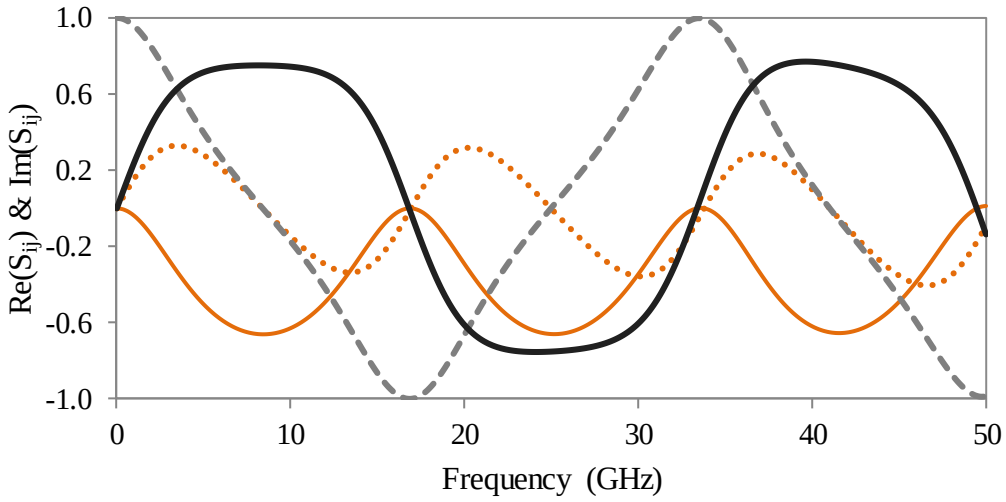

Figure 3.17: Real (continuous) and imaginary (dashed/dotted) parts of (a) S_{11} (orange) and (b) S_{21} (black).

Effect of Slab Thickness

Next, homogenous slabs of the same known permittivity but with different thicknesses were simulated and the extracted results of the EM properties are shown in Figure 3.18. The first thickness resonance occurs at the following frequencies for different dielectric thicknesses: 2 mm at 31.50 GHz, 3 mm at 21.80 GHz, 4mm at 16.50 GHz, 6 mm at 11 GHz, 8 mm at 8.25 GHz and 10 mm at 6.50 GHz – see Figure 3.18. Note: the first thickness resonance for the 1 mm slab occurs above 50 GHz. Below this resonance, the extracted permittivity shows good agreement with the known value. As shown in Figure 3.18, the extracted value of the permittivity decreases from 4.96 for the 1 mm slab to 4.90 for the 10 mm slab – a 1.22% change. Thus, an appropriate slab thickness proportionate to the guided wavelength needs to be used for simulations in order to avoid uncertainties in the extracted results [26] due to thin samples and obtain accurate results from the inversion process. Generally, the extracted results are stable below the first resonant frequency.

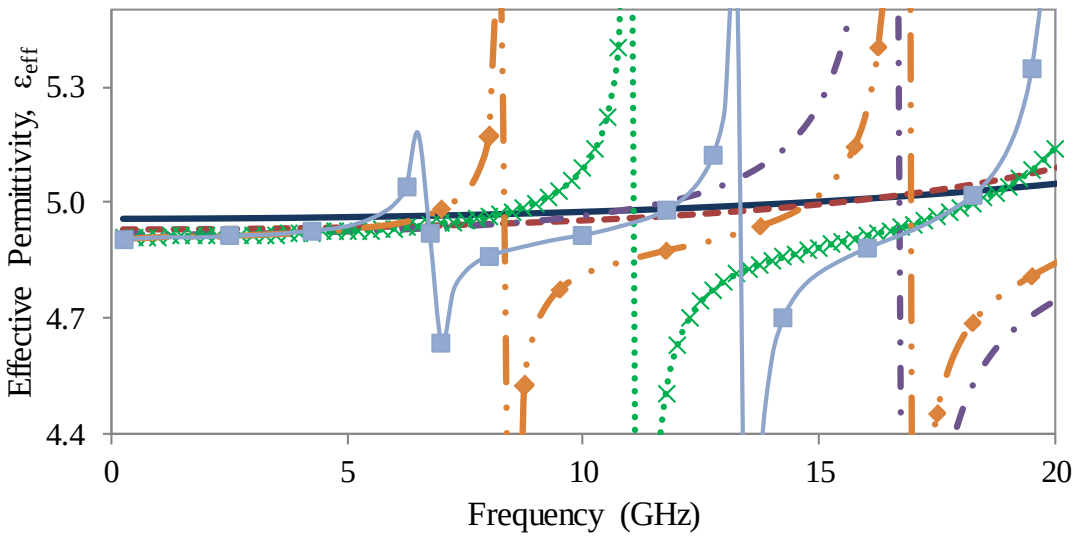

Figure 3.18: Variation with frequency of ε_{eff} derived via the inversion process for different homogenous slab thicknesses: 1- (—), 2- (----), 4- (— • —), 6- (••x••), 8- (—•♦•—), and 10-mm (—■—) $\varepsilon_r = 4.9$, tan $\delta = 0.025$

Effect of Slab Permittivity, ε_r

The ε_{eff} and μ_{eff} of a homogenous slab of fixed thickness, 4 mm, and with varying ε_r is shown plotted in Figure 3.19. In this case, the loss tangent of the material is kept constant at tan $\delta = 0.001$. As the permittivity increases, the number of thickness resonances ("spikes") over the frequency range increases, with the first one for each ε_r occurring earlier on the frequency scale. Also, the gradient of the ε_{eff} between two consecutive resonant frequencies, increases over the frequency range as ε_r increases, reducing the range over which the effective EM properties obtained from this inversion technique are stable. Capping the dB magnitude values of either or both of the S-parameters to -30, -20 or even up to -10 dB to take care of these 'spikes' did not eliminate them from the extracted results, but produced inaccurate results. Figure 3.19 also implies that for materials with higher permittivity values, thinner samples move the first thickness resonance to higher frequencies, thereby making the ε_{eff} more stable. In both plots - Figure 3.18 and Figure 3.19, the increasing $\Delta\phi_r$ (for example, as shown in Figure 3.16 (a)) is reflected in the increasing ε_{eff} and μ_{eff}, as $\Delta\phi_r$ increases above π. However, good agreement is obtained with the known values of permittivity especially below the first (thickness) resonant frequency.

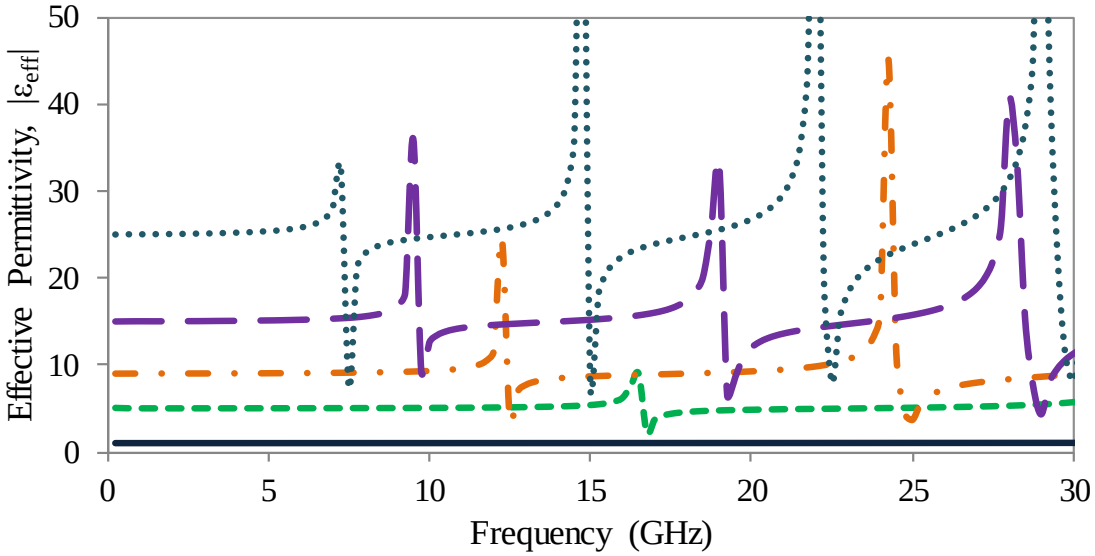

Figure 3.19: Variation of ε_{eff} with frequency of a 4 mm slab with $\varepsilon_r = 1$ (—), 5 (----), 9 (—•—), 15 (═) and 25 (••••)

Over regularly-spaced frequency bands, the real part of the refractive index decreases with increasing frequency, as shown in Figure 3.20 which may be due to anomalous dispersion [40], because the inversion solution is not well-behaved over these frequencies or may be due to the thickness resonance effect explained earlier. The last reason is most likely as it coincides with where the un-rectified phase of the medium is discontinuous. Note: these are not magnetic resonances. These regions are shown circled in Figure 3.20.

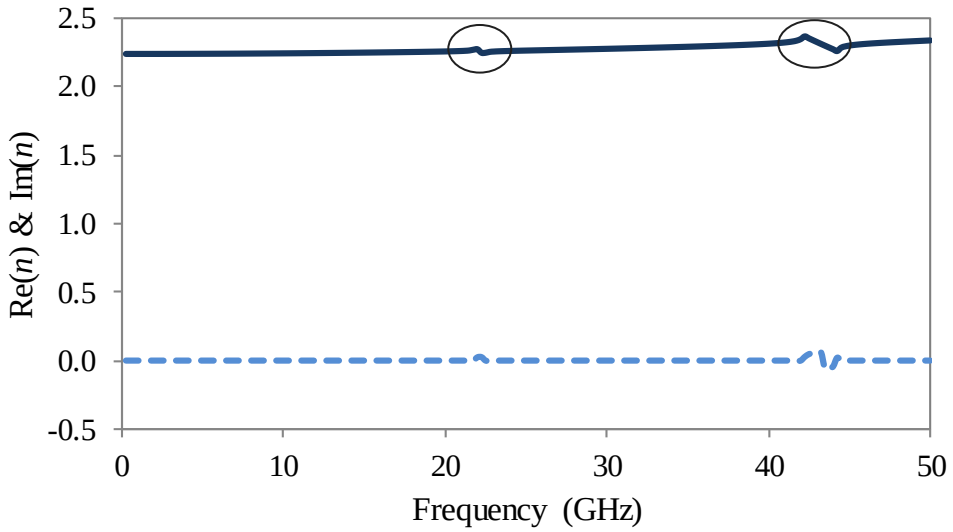

Figure 3.20: Example of the real (——) and imaginary (-----) parts of the extracted refractive index, n_{eff}, to highlight the decrease in Re(n) with increasing frequency (shown circled). $d = 3$ mm, $\varepsilon_r = 4.9$, $\tan\delta = 0.025$

Effect of the d_1 and d_2

A crucial part of the inversion process is the distances between the surfaces of the MUT and the measurement/reference planes (see Figure 3.8). These distances have been varied and the extracted ε_{eff} and μ_{eff} are shown in Figure 3.21. Data used: $d = 1$ mm, $\varepsilon_r = 2.2$ (tan $\delta = 0.0009$). In these simulations, $d_1 = d_2$. As shown, as far as the ports are over 5 times the thickness of the slab away from the surface of the MUT, the results are reliable and accurate. There is very slight increase in the ε_{eff} and μ_{eff} as these distances increase.

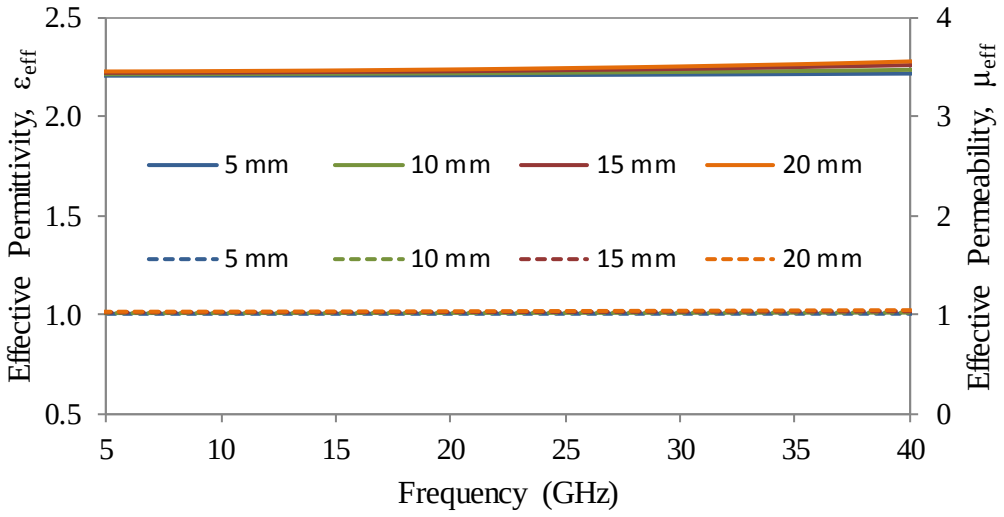

Figure 3.21: Variation of ε_{eff} (continuous) and μ_{eff} (dashed) with frequency for varying port-to-slab distances. $d_1 = d_2$.

Effect of the Number of Layers

As the canonical equations used in deriving most of the structures examined in most of the reviewed literature were of infinite extent in all three dimensions, it was important to understand how the number of layers of the heterogeneous structure used along the direction of propagation, or the axis of finite thickness affects the accuracy of the extracted ε_{eff} and μ_{eff} from the inversion technique. In order to do this, several simulations were run with different number of layers. Data used: sphere size, $a = 125$ μm, spacing, $s = 250$ μm, host permittivity, $\varepsilon_1 = 3.55$ (tan $\delta = 0.0027$), inclusion permittivity, $\varepsilon_2 = 11.9$ (tan $\delta = 0.01$), $\mu_1 = \mu_2 = 1$. The extracted ε_{eff} and μ_{eff} from different number of layers at different frequencies are shown in Figure 3.21. Generally, as the number of layers increase, the value of ε_{eff} and μ_{eff} converges. The deviation from this convergence is due to the proximity of the thickness resonance in the S-parameters (that is, where the structure becomes transparent, see Section 3.4.1). It can also be seen that the extracted results are within less than 0.2 of each

other. The highest value of ε_{eff} is just ~ 2.4% higher than its lowest value, while the highest value of μ_{eff} is ~6% higher than its lowest value, over the whole frequency range and number of layers examined here. This gives confidence that although the number of layers has an impact on the ε_{eff} and μ_{eff} results, it is not significant enough to reduce the accuracy of the results. It should also be noted that the number of layers used also has an effect on how early on the frequency scale, the thickness resonance of the structures comes into play.

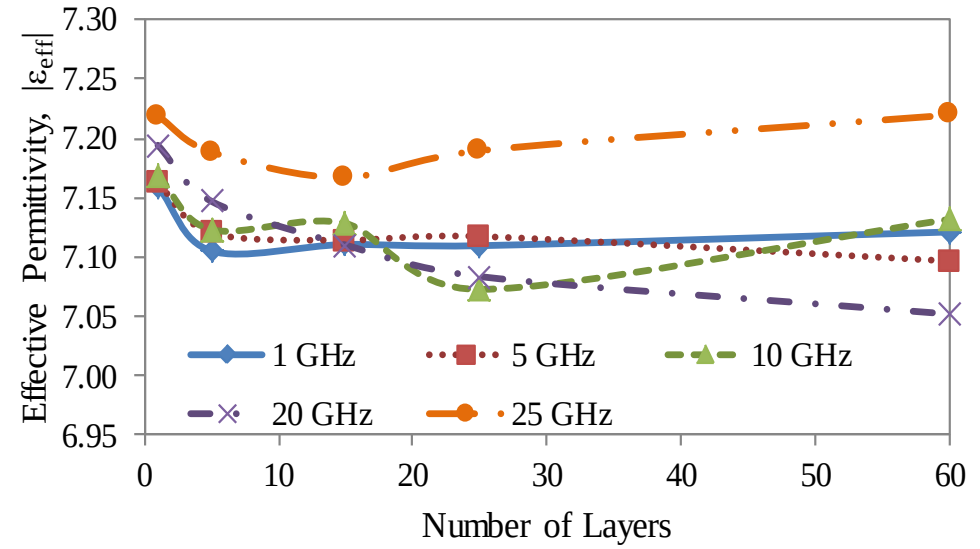

(a)

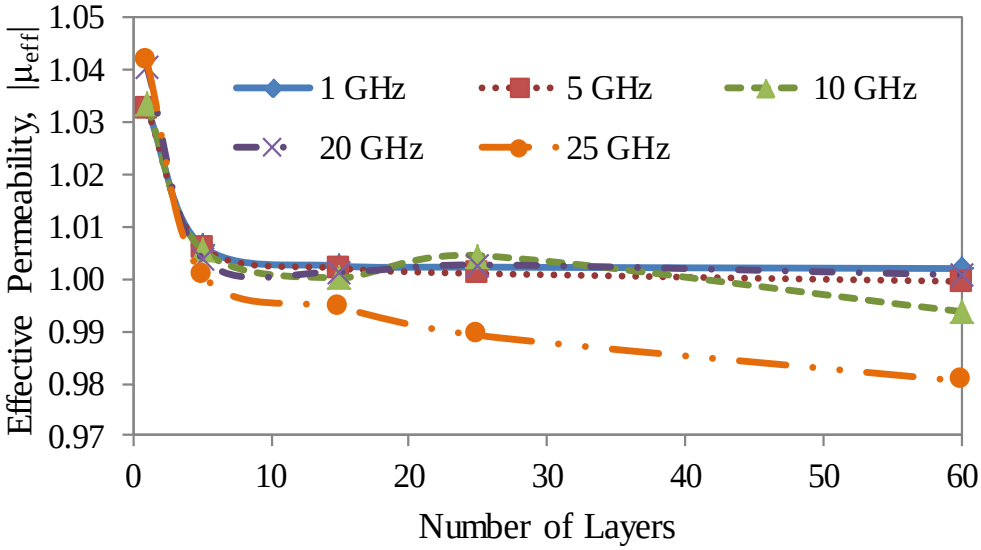

(b)

Figure 3.22: Variation of effective (a) permittivity, ε_{eff} and (b) permeability, μ_{eff} with the number of layers in a heterogeneous medium

3.6 Conclusions

This chapter introduced the simulation and inversion process used for the rest of this thesis. This was done to see how well the results from the simulations of the heterogeneous media agreed with the results from the canonical equations discussed in Chapter 2. The inversion process involved a rectification algorithm to the phase of the medium in order to make it continuous over the frequency range, which was important in order to produce accurate results. The group delay of the medium before and after the phase rectification have been compared and shown to have good agreement with each other, implying that the rectification algorithm does not adversely affect the accuracy of the results. The inversion process was used to extract the effective permittivity and permeability of homogenous and heterogeneous media from the simulated S-parameters results when the medium under test was exposed to a plane wave. This has been introduced and analysed, with graphical results shown. MATLAB was used to implement the inversion process and has been validated with homogenous slabs and the first heterogeneous structure presented in [9]. Other parameters that may affect the accuracy of the inverted results have been investigated. This chapter has demonstrated that the inversion process works very well for these homogenous slabs for different thicknesses and permittivities.

Since the primary structures being investigated in this thesis are heterogeneous, the effect of the number of layers used in the direction of wave propagation has been examined. It can be concluded that although the number of layers has an effect, it is not pronounced nor does it significantly detract from the accuracy of the extracted effective EM properties. For the subsequent chapters, the inversion process will be applied to the S-parameter results in order to extract the ε_{eff} and μ_{eff} of various media being tested.

3.7 References

[1] W. T. Doyle, “Optical properties of a suspension of metal spheres,” *Physical Review B*, vol. 39, no. 14, pp. 9852–9858, 1989.

[2] W. T. Doyle, “The Clausius-Mossotti problem for cubic arrays of spheres,” *Journal of Applied Physics*, vol. 49, no. 2, pp. 795–797, 1978.

[3] X. Cai, R. Zhu, and G. Hu, “Experimental study for metamaterials based on dielectric resonators and wire frame,” *Metamaterials*, vol. 2, no. 4, pp. 220–226, 2008.

[4] A. Sihvola, *Electromagnetic Mixing Formulas and Applications*. London: IET, 1999.

[5] I. A. Kolmakov, L. Jylha, S. A. Tretyakov, and S. Maslovki, “Lattice of dielectric particles with double negative response,” in *28th Gen. Ass. Int. Union Radio Sci. (URSI)*, 2005.

[6] L. Lewin, “The electrical constants of a material loaded with spherical particles,” *IEE-Part III: Radio Comm. Eng.*, vol. 94, no. 27, pp. 65–68, 1947.

[7] A. M. Nicolson and G. F. Ross, “Measurement of the intrinsic properties of materials by time-domain techniques,” *Instrumentation and Measurement, IEEE Transactions on*, vol. 19, no. 4, pp. 377–382, 1970.

[8] W. B. Weir, “Automatic measurement of complex dielectric constant and permeability at microwave frequencies,” *Proceedings of the IEEE*, vol. 62, no. 1, pp. 33–36, 1974.

[9] N. G. Alexopoulos, C. A. Kyriazidou, and H. F. Contopanagos, “Effective parameters for metamorphic materials and metamaterials through a resonant inverse scattering approach,” *IEEE Transactions on Microwave Theory and Techniques*, vol. 55, no. 2, pp. 254–267, 2007.

[10] D. R. Smith, D. C. Vier, T. Koschny, and C. M. Soukoulis, “Electromagnetic parameter retrieval from inhomogeneous metamaterials,” *Physical Review E*, vol. 71, pp. 036617–1 – 11, 2005.

[11] B.-K. Chung, “Dielectric constant measurement for thin material at microwave frequencies,” *Progress In Electromagnetics Research*, vol. 75, pp. 239–252, 2007.

[12] M. N. Afsar, A. M. Ayala, N. Al-Moayed, and M. Obol, “Microwave permittivity and permeability properties and microwave reflections of ferrite powders,” in *IEEE Instrumentation and Measurement Technology Conference*, 2009, pp. 274–278.

[13] K. K. Karkkainen, A. H. Sihvola, and K. I. Nikoskinen, “Effective permittivity of mixtures: numerical validation by the FDTD method,” *IEEE Transactions on Geoscience and Remote Sensing*, vol. 38, no. 3, pp. 1303–1308, May 2000.

[14] J.-M. Lerat, N. Malléjac, and O. Acher, “Determination of the effective parameters of a metamaterial by field summation method,” *Journal of Applied Physics*, vol. 100, no. 8, pp. 084908–1 – 9, 2006.

[15] W. G. Whittow, “Specific absorption rate perturbations in the eyes and head by metallic spectacles at personal radio communication frequencies,” PhD Thesis, University of Sheffield, UK, 2004.

[16] K. Yee, “Numerical solution of initial boundary value problems involving Maxwell’s equations in isotropic media,” *IEEE Transactions on Antennas and Propagation*, vol. 14, no. 3, pp. 302–307, May 1966.

[17] IMST GmbH, “EMPIRE XCcel Manual,” 2011.

[18] J.-P. Berenger, “A perfectly matched layer for the absorption of electromagnetic waves,” *Journal of Computational Physics*, vol. 114, pp. 185–200, 1994.

[19] K. S. Kunz and R. J. Luebbers, *The finite-difference time-domain method in electromagnetics*. CRC Press, 1993.

[20] A. Taflove and S. C. Hagness, *Computational electrodynamics: the finite-difference time-domain method*, 2nd ed. London: Artech House, 2000.

[21] N. Ida, *Engineering Electromagnetics*, 2nd ed., vol. ch. 13. New York: Springer Verlag, 2004.

[22] C. A. Balanis, *Advanced Engineering Electromagnetics*, 2nd ed. New York: Chichester: Wiley, 1989.

[23] C. A. Balanis, *Antenna theory: analysis and design*, 3rd ed. Chichester: Wiley, 1997.

[24] G. Antonini, C. A. Scogna, and A. Orlandi, “De-embedding procedure based on computed/measured data set for PCB structures characterization,” *IEEE Transactions on Advanced Packaging*, vol. 27, no. 4, pp. 597–602, Nov. 2004.

[25] I. Awai, Y. Maegawa, and T. Ishizaki, “Measurement of effective material constants of artificial dielectrics made of spherical metal particles,” in *Asia Pacific Microwave Conference*, 2009, pp. 1655–1658.

[26] J. Baker-Jarvis, E. J. Vanzura, and W. A. Kissick, “Improved technique for determining complex permittivity with the transmission/reflection method,” *IEEE Transactions on Microwave Theory and Techniques*, vol. 38, no. 8, pp. 1096–1103, Aug. 1990.

[27] W. Barry, “A Broad-Band, Automated, Stripline Technique for the Simultaneous Measurement of Complex Permittivity and Permeability,” *IEEE Transactions on Microwave Theory and Techniques*, vol. 34, no. 1, pp. 80–84, Jan. 1986.

[28] A.-H. Boughriet, C. Legrand, and A. Chapoton, “Noniterative stable transmission/reflection method for low-loss material complex permittivity

determination," *Microwave Theory and Techniques, IEEE Transactions on*, vol. 45, no. 1, pp. 52–57, 1997.

[29] T. Galek, K. Porath, E. Burkel, and U. van Rienen, "Extraction of effective permittivity and permeability of metallic powders in the microwave range," *Modelling and Simulation in Materials Science and Engineering*, vol. 18, no. 2, pp. 1–13, Mar. 2010.

[30] H. Zhou, G. Lu, Y. Li, S. Wang, and Y. Wang, "An improved method of determining permittivity and permeability by S-parameters," in *Progress In Electromagnetics Research*, 2009, vol. 11, no. 1, pp. 768–773.

[31] H. M. Farkas and I. Kra, *Riemann Surfaces*, 2nd ed. New York: Springer Verlag, 1992.

[32] G. A. Baker, "Approximate analytic continuation beyond the first Riemann sheet." Los Alamos, pp. 285–294, 2006.

[33] U. Gerlach, "Review: Branches, Branch Cuts, and Riemann Sheets," 2010. [Online]. Available: http://www.math.osu.edu/~gerlach.1/math/BVtypset/node106.html. [Accessed: 09-Oct-2012].

[34] E. W. Weisstein, "Analytic Continuation," *From MathWorld-A Wolfram Web Resource*, 2012. [Online]. Available: http://mathworld.wolfram.com/AnalyticContinuation.html. [Accessed: 09-Oct-2012].

[35] C. C. Njoku, W. G. Whittow, and Y. C. Vardaxoglou, "Simulation methodology for synthesis of antenna substrates with micro-scale inclusions," *IEEE Transactions on Antennas and Propagation*, vol. 60, no. 5, pp. 2194–2202, 2012.

[36] C. J. Struck, "Calculation of Group Delay from Phase Data," 2007. [Online]. Available: http://www.cjs-labs.com/sitebuildercontent/sitebuilderfiles/GroupDelay.pdf. [Accessed: 30-Jun-2011].

[37] O. F. Siddiqui, S. J. Erickson, G. V. Eleftheriades, and M. Mojahedi, "Time-domain measurement of negative group delay in negative-refractive-index transmission-line metamaterials," *IEEE Transactions on Microwave Theory and Techniques*, vol. 52, no. 5, pp. 1449–1454, May 2004.

[38] E. W. Weisstein, "Numerical Differentiation," *From MathWorld-A Wolfram Web Resource*, 2012. [Online]. Available: http://mathworld.wolfram.com/NumericalDifferentiation.html. [Accessed: 11-Oct-2012].

[39] R. Butt, *Introduction to Numerical Analysis using MATLAB*. Massachusetts: Jones & Bartlett Publishers, 2009.

[40] W. West, "Absorption of electromagnetic radiation," *AccessScience*. McGraw-Hill Book Inc, 2008.

Chapter 4. Comparison of the Effective Electromagnetic Properties via Canonical Equations and Simulations

4.1 Introduction

This chapter examines how the results from the inversion and simulation processes of heterogeneous media discussed in Chapter 3 compare with those from the canonical equations from Chapter 2. The effective electromagnetic (EM) properties of heterogeneous mixtures with dielectric and metallic spherical and cubic inclusions have been examined and are presented in this chapter. In addition, the general process involved in deriving the appropriate parameters for the host and inclusions in order to create a heterogeneous medium with pre-determined EM properties have been explained.

It was important to investigate how the canonical analysis agreed with the simulation analysis of these media as it establishes a higher level of confidence for measurements and future work on using these heterogeneous media with probably more complex geometries.

Section 4.2 compares the ε_{eff} and μ_{eff} from theory and simulations-inversions for different geometries having dielectric spherical and cubic inclusions in a simple cubic (SC) lattice in a dielectric host. For the simulations, a plane wave incidence, as described in Chapter 3, was used. Section 4.3 examines and compares mixtures with metallic spherical and cubic inclusions while Section 4.4 looks at the losses (using the loss tangents) of the mixtures. Section 4.5 examines the general process and deciding factors needed to be taken into account for creating a heterogeneous mixture with a pre-determined ε_{eff} using dielectric and/or metallic inclusions and compares these two inclusion types. The conclusions are given in Section 4.6.

4.2 Heterogeneous Media with Dielectric Inclusions

As the simulation and inversion processes have been validated with the disk medium from [1] and with different thicknesses of homogenous dielectric slabs of known permittivities in Section 3.5, heterogeneous media with 3D arrays of spheres and cubes as shown in Figure 4.1 and Figure 4.2 were simulated. As explained in Chapter 3, the S-parameter calculation planes had to be placed away from the structure to avoid higher order mode interference. The effective EM properties from dielectric spherical and cubic inclusions are discussed in this section. The microstrip line (MSL) is modelled as infinitely periodic along the polarisations of the E- and H-fields and the inclusions are arranged in a simple cubic lattice. Thus, the size of the array parallel to the plane of incidence is irrelevant due to the PEC and PMC boundaries (that is, a 1-by-1 array is equivalent to a 6–by-6 array) as they are both infinite. 6 layers of inclusions in the direction of wave propagation, that is, along the x-axis, were used in the simulations in order to allow for uniformity in all three dimensions and to ensure that the MUT was not too thin – as shown in Figure 4.1 and Figure 4.2 (a) and (b).

By using more layers in the simulations, the values of the extracted results from the inversion process tends to converge towards those obtained from the canonical equations as the structure is closer to the semi-infinite structure assumed by the equations. However, this increased the simulation time and as has been shown in Section 3.5.2, fewer layers produce reasonably accurate results. Therefore a compromise was found between the accuracy and the simulation time and 6 layers were used.

As the simulation technique uses FDTD, a possible source of error would be from the curved surfaces of the spherical inclusions. However, this was minimised by meshing the structures very finely – at least 34 cells per wavelength at the smallest wavelength, to more accurately approximate these curved surfaces.

The results from the simulation of these heterogeneous mixtures with dielectric inclusions were put through the inversion process (as described in Chapter 3, Section 3.4). The absolute relative values of the permittivity and permeability are used here. The *spacing* is the inclusions' centre-to-centre or edge-to-edge distance – see Figure 2.2. Common data used in Sections 4.2.1 to 4.4: frequency, $f = 1$ – 30 GHz, $\mu_1 = \mu_2 = 1$. For the spherical inclusions, $d_1 = 9.85$ mm, $d_2 = 8.35$ mm, $d = 1.8$ mm; for the cubic inclusions, $d_1 = d_2 = 6.96$ mm and $d = 1.08$ mm for the 180-µm inclusion spacing and $d_1 = d_2 = 5.5$ mm and $d = 1.5$ mm for the 250-µm spacing.

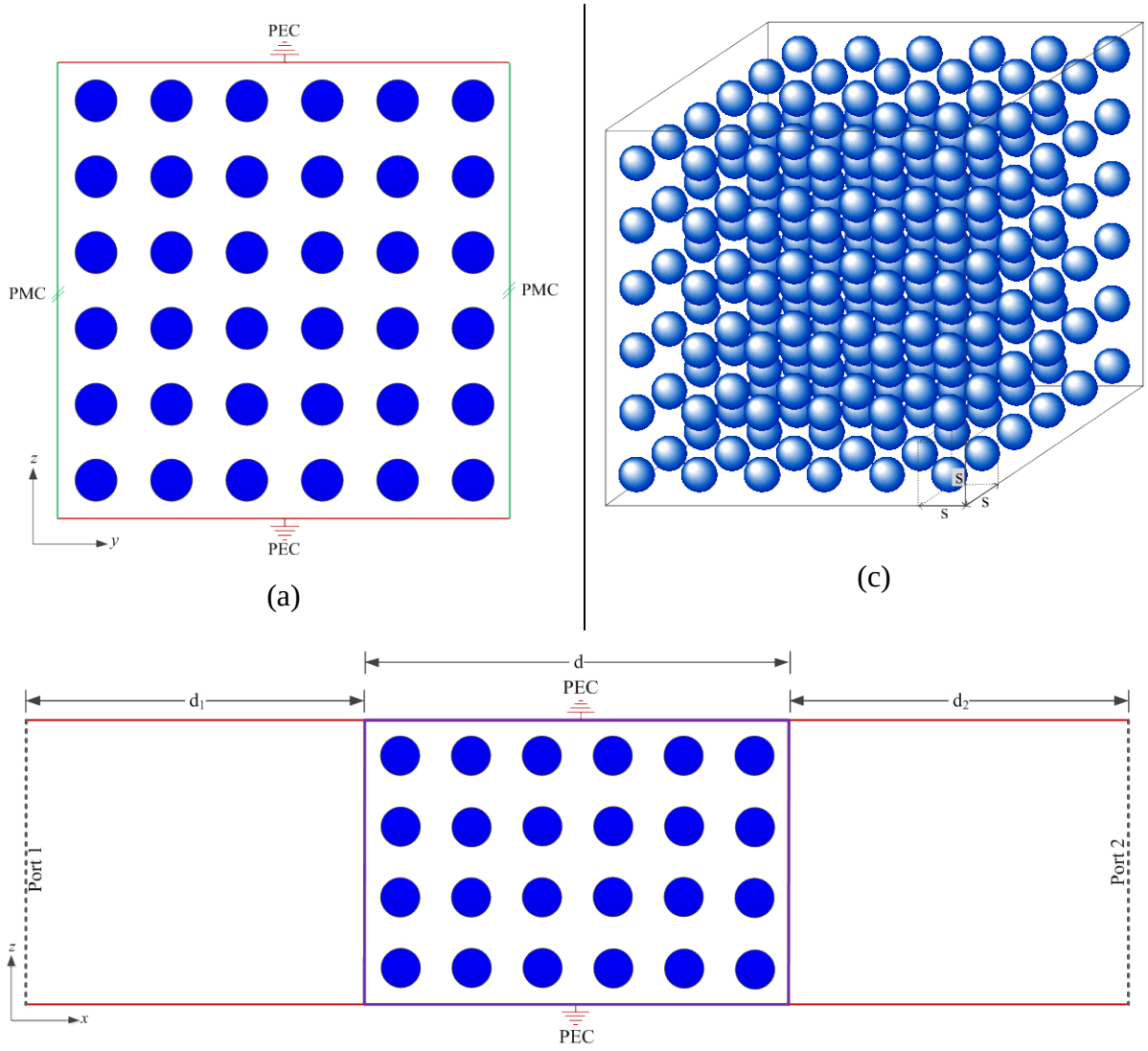

Figure 4.1: (a), (b) 2D cross-sections of the simulation domain and (c) 3D view of dielectric spheres in a dielectric host.

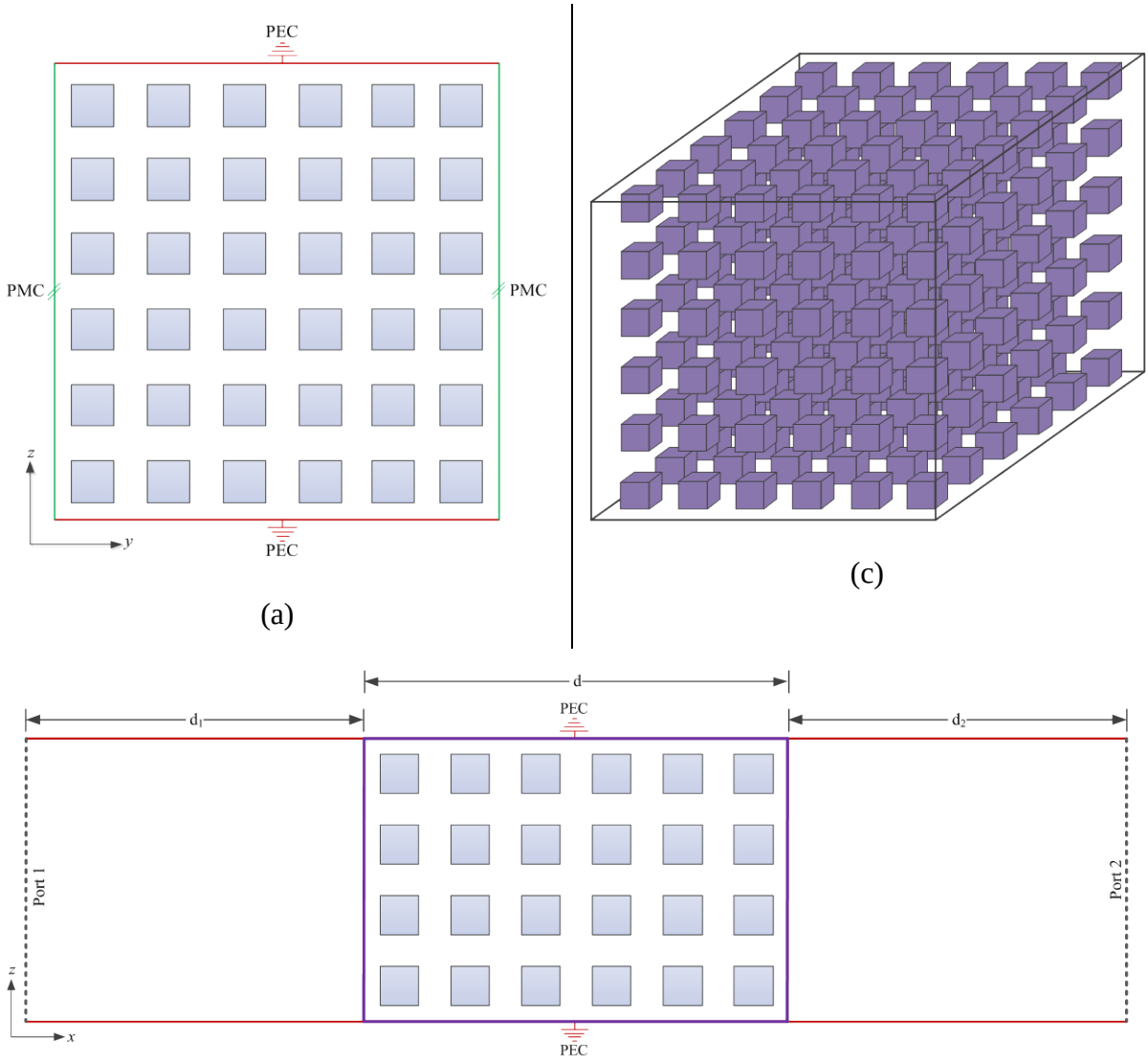

Figure 4.2: (a), (b) 2D cross-sections of simulation domain and (c) 3D view of dielectric cubes in a dielectric host

4.2.1 Dielectric Spherical Inclusions

Dielectric spheres were used initially to allow an accurate comparison with the canonical equations which were primarily based on having spherical inclusions [2–4]. Data used: radius of sphere, $a = 100$ μm, spacing, $s = 300$ μm (see Figure 4.3), $\varepsilon_1 = 2.25$ (tan $\delta = 0.001$), $\varepsilon_2 = 10.2$ (tan $\delta = 0.0023$). The physical dimensions were chosen such that they were less than a tenth of the minimum wavelength over the frequency range examined, while the EM properties of the host and inclusions were selected from readily available materials.

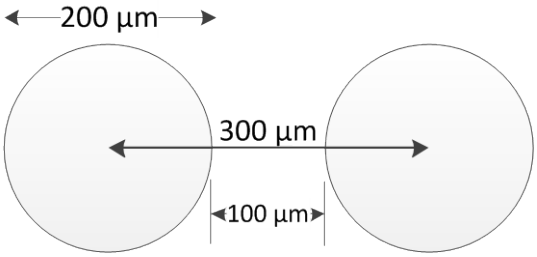

Figure 4.3: Diagram showing dimensions for the heterogeneous mixture with spherical inclusions

The ε_{eff} and μ_{eff} from the simulation and equations from [2] are shown in Figure 4.4. As shown, there is very good agreement between the two results. The average values of $(\varepsilon_{eff}, \mu_{eff})$ over the frequency range examined, from the simulation-inversion process and the canonical equations are (2.89, 1.01) and (2.87, 1.0) respectively. Due to the small values of the loss tangents, it did not have a noticeable impact on the extracted ε_{eff} and μ_{eff}. The slight different between the ε_{eff} from the equations and simulations are numeric and is not significant enough to detract from the accuracy of the results.

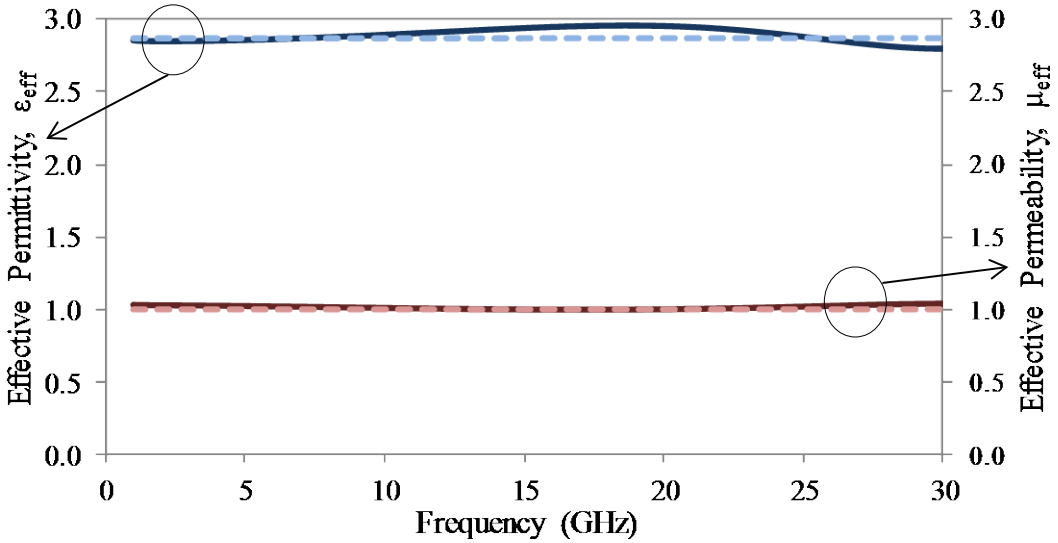

Figure 4.4: Variation with frequency of ε_{eff} and μ_{eff} from simulations (continuous) and canonical equations from Lewin [2] (dashed) for a heterogeneous mixture of 100 µm (radius) spheres uniformly spaced 300 µm apart. $\varepsilon_1 = 2.25$ (tan $\delta = 0.001$), $\varepsilon_2 = 10.2$ (tan $\delta = 0.0023$)

It should be noted from the μ_{eff} plot, that the magnetic resonance does not occur within the frequency range examined, but further up the frequency scale at 459 GHz using Lewin's

equation [2]. As the size or the permittivity, ε_2 of the inclusions increases, this magnetic resonance occurs earlier on the frequency scale. Thus, with metallic inclusions of this same size and spacing, the magnetic resonance will occur earlier on but still not as low as 30 GHz. In this case, the electric resonance occurs at 549 GHz using Lewin's equations. However, below the electric and magnetic resonant frequencies, the ε_{eff} and μ_{eff} are quite stable. It should also be noted that the electric resonance occurs at a higher frequency than that of the magnetic resonance. This explains the 'flat' nature of μ_{eff} in the other graphs.

4.2.2 Dielectric Cubic Inclusions

Cubes (see Figure 4.2) were also investigated using simulations as they had less demand for computing resources and avoided the stair-casing effect that curved structures are subject to when meshed in the FDTD space. The cubes are therefore quicker to simulate, and in practise, may be more common to find or create than spheres. For these cubic inclusions, data used: length of cube, $l = 100$ μm, spacing, $s = 180$ and 250 μm (see Figure 4.5), $\varepsilon_1 = 2.50$ (tan $\delta = 0.002$), $\varepsilon_2 = 11.9$ (tan $\delta = 0.01$). The simulation results were put through the inversion process.

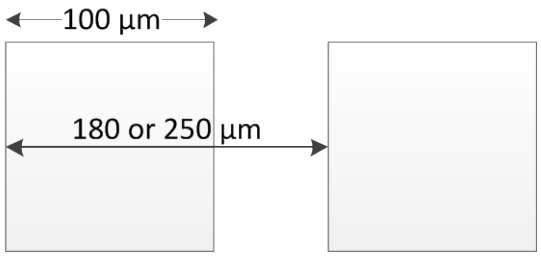

Figure 4.5: Diagram showing dimensions for the heterogeneous mixture with cubic inclusions

The absolute values from the inversion process of the ε_{eff} and μ_{eff} for the heterogeneous media with the 180 and 250 μm inclusions' spacings are shown in Figure 4.6. The average values of ε_{eff} over the frequency range examined are (3.29, 2.78) from the simulation-inversion process and (3.39, 2.82) for the canonical equations for the (180, 250) μm spaced inclusions. As the EM properties of the materials used are not frequency dependent, the ε_{eff} and μ_{eff} results are flat over the frequency range examined. Also, the FDTD is able to generate the S-parameters at lower frequencies as shown.

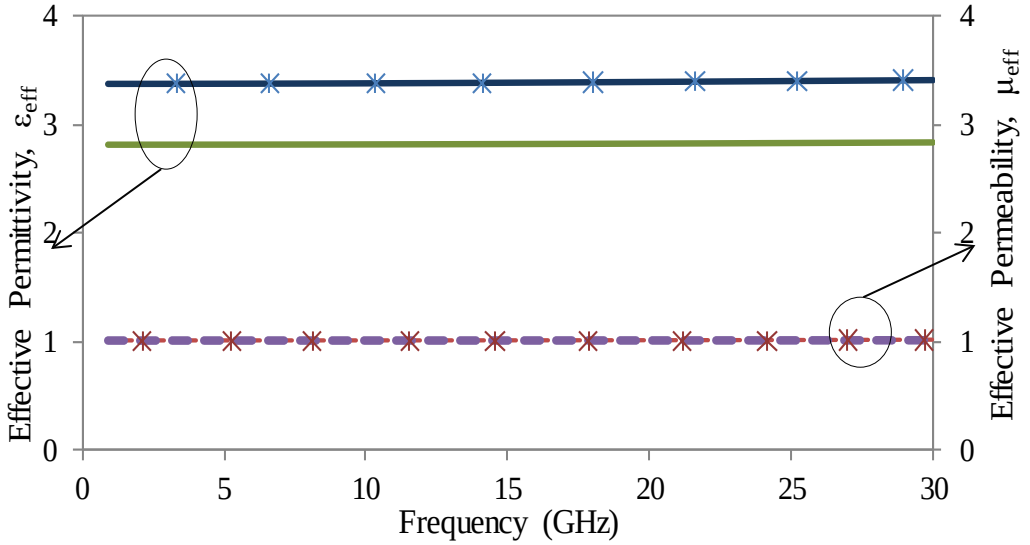

Figure 4.6: Variation with frequency of ε_{eff} (continuous) and μ_{eff} (dashed) for a heterogeneous mixture of 100 μm cubes with 180 μm (starred) and 250 μm (unmarked) spacing from simulations.

The theoretical equations for heterogeneous mixtures examined in Chapter 2 all assumed semi-infinite arrays of spherical inclusions in an SC lattice in a homogeneous medium [2], [3], [5–7]. Note: it has been shown previously in Chapter 2 that the effective EM values from [2], [5], [7] give very similar results. Therefore to get an approximation for the simulated cubic inclusions, an equivalent process was used to arrive at a suitable approximation for the radius of the spheres to be used for the canonical equations. Both the equivalent volume and equivalent surface area of the cubes were considered.

This equivalent volume process is represented as:

$$4\pi r^3/3 = l^3 \tag{4-1}$$

An equivalent surface area process carried out by equating the surface area of the cube to that of a sphere is given as:

$$4\pi r^2 = 6l^2 \tag{4-2}$$

where r is the radius of the sphere and l is the length of the cube.

Using equation (4-1), a 100 μm cube has the same volume as a 62.04 μm radius sphere, and the same surface area as a 69.10 μm radius sphere from equation (4-2). In carrying out the

canonical analysis using these equivalent radius values, the inclusions' spacing, and the host's and inclusions' EM properties remained the same.

Figure 4.7 compares the ε_{eff} from the simulations and the canonical equations by using the equivalent volume and the equivalent surface area processes. As shown, the values from the simulations are slightly higher than those from the canonical equations (using the equivalent volume process) by about 2.5% and 1.3% for the 180 μm and 250 μm spacings respectively. This discrepancy is due to the spheres being used instead of cubes in the equations. If the surface area equivalence is used here instead, a higher difference is seen with the results from the canonical equations being higher than those from the simulations – 7.9% and 2.7% for the 180 and 250 μm spacings, see Figure 4.7 (b). In both cases, the higher the inclusion spacing, the smaller the difference is between the results from the simulations and equations. This is because there is inherently less interactions between the inclusions. As the difference between the results from the simulations and the results from the canonical equations using the equivalent volume process is lower, it can be concluded that the equivalent volume process is a more accurate approach than the equivalent surface area process. In these two plots, the ε_{eff} and μ_{eff} are non-dispersive as the EM properties of the host and inclusions are also non-dispersive.

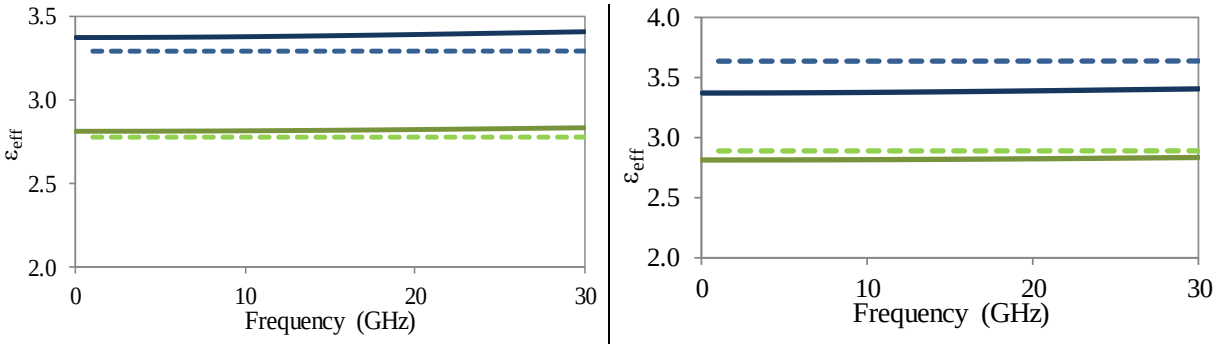

Figure 4.7: Comparison of ε_{eff} from the simulations (continuous) of 100 μm dielectric cubes with the ε_{eff} using (a) 62.04 μm (volume equivalence) and (b) 69.10 μm (surface area equivalence) radius spheres in the equations (dashed) with 180 μm (blue) and 250 μm (green) spacing

The equation from [8] for the ε_{eff} of heterogeneous mixtures with cubic inclusions uses the exact equations for the polarisability of a cube in its Clausius-Mossotti (C-M) formulations. From this, the ε_{eff} for the same geometries and EM properties is 3.35 and 2.80 for the 180

μm and 250 μm spacings respectively. These values agree more closely with those from the simulations-inversions. As the equation in [8] uses the C-M equation which does not have a frequency term, it cannot be compared over the frequency range used in Figure 4.7, but does not matter as there is little variation with frequency as shown. However, as will be seen in Section 4.5.1, the equations do not give accurate results for heterogeneous media with high inclusions' volume fraction as the equations are restricted to "quite dilute mixtures" [8].

Cubic inclusions are advantageous over spheres as larger Yee cells could be used to mesh the volume which would then reduce the simulation times. Another advantage is that the volume fraction of the inclusions when using cubes could approach 100% whereas spherical inclusions are limited. This advantage is further highlighted in Section 4.3 when metallic inclusions are used giving rise to much higher values of ε_{eff}.

4.3 Heterogeneous Media with Metallic Inclusions

In Chapter 3, the numerical analysis of a heterogeneous mixture with metallic discs from [1] was replicated. In this section, the effect of having metallic cubes and spheres as inclusions will be examined. The Drude Model [9–11] can be used to obtain the permittivity of metallic materials and has been discussed in Chapter 2. From this model, the relative permittivity of Copper was (1.27 + j107.93) × 10^6, which is far greater than that of a typical dielectric, and as such can be used to further increase the ε_{eff} of these heterogeneous media over those with dielectric inclusions. Common data used in this section: for simulations, the inclusion material was Copper, $\sigma = 5.80\times10^7$ S/m, and for the equations: $\varepsilon_2 = (1.27 + j107.93) \times 10^6$.

4.3.1 Metallic Spherical Inclusions

The same geometry shown in Figure 4.1 applies here and Figure 4.8 shows the extracted ε_{eff} and μ_{eff} from equations and simulations. Data used: radius of sphere, $a = 100$ μm, spacing, $s = 300$ μm, $\varepsilon_1 = 2.25$ (tan $\delta = 0.001$). Over the frequency range examined, the average (ε_{eff}, μ_{eff}) are (3.49, 0.79) and (3.48, 0.81) from the equations and simulations respectively, which show good agreement. This is because the equations use spheres in their analyses and so more accurately predict what the simulation-inversion process should give. From these results of the μ_{eff}, diamagnetism is seen. This diamagnetism may have been brought about by the use of Copper, which is a diamagnetic material with a relative permeability, $\mu_r = 0.999991$ [12] as the inclusion material, and the diamagnetic effect been accentuated by clustering these Copper inclusions in close proximity. This is because as the spacing between the inclusions is reduced, the diamagnetic effect is further increased, that is, μ_{eff} is further reduced. Theoretically, it may be possible to create a material with $\mu_{eff} \approx 0$, by increasing the volume fraction of the Copper inclusions. Diamagnetism may be included in materials whose wave numbers may want to be reduced as required by the applications in which they are to be used for. As discussed in Section 4.2.1, the magnetic resonance of this structure occurs at a much higher frequency than the upper frequency limit used here, as the size of the inclusions are much lower the wavelengths of operation.

As a reference, Figure 2.6 in Chapter 2 shows the change in ε_{eff} up to the limit that the spherical inclusions in an SC lattice were in contact (“touching”) and was obtained using the canonical equations which have a faster computational time than the simulations.

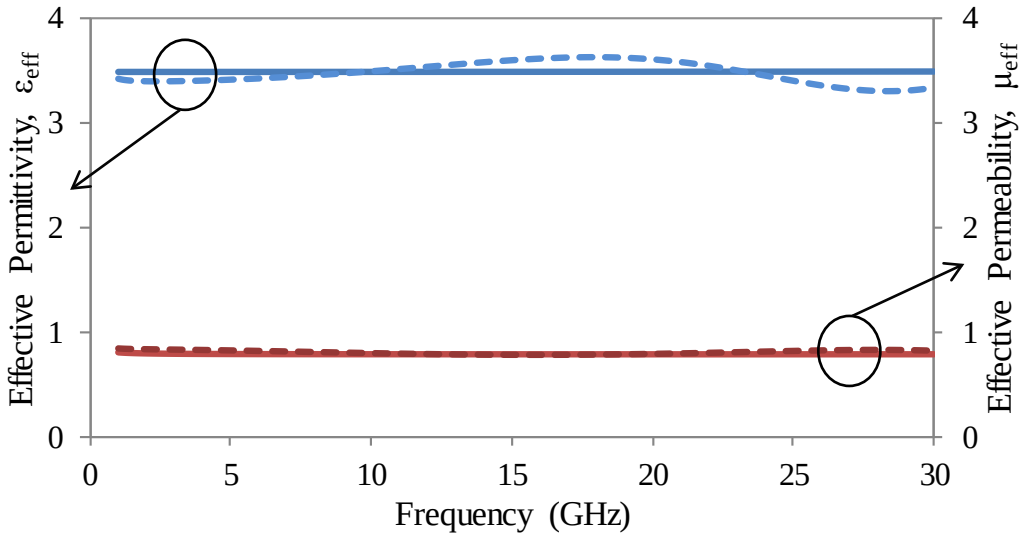

Figure 4.8: Variation of ε_{eff} (blue) and μ_{eff} (red) with frequency of a heterogeneous medium with 100 μm radius spherical metallic inclusions from simulations (continuous) and equations (dashed) with 300 μm spacing

4.3.2 Metallic Cubic Inclusions

For spheres in an SC lattice, the maximum volume density is ~50% and goes up to ~68% for the BCC lattice and ~74% for the FCC lattice of spherical inclusions [13–15]. This limit can be increased towards 100% with cubic inclusions. With metallic spheres, the highest ε_{eff} theoretically possible is about four times that of the host [2]. The same geometry shown in Figure 4.2 is used here. Figure 4.9 shows the extracted ε_{eff} and μ_{eff} from equations and simulations. Data used: length of cube, $l = 100$ μm (in simulations) and equivalent radius, $a = 62.04$ μm (in equations), spacing, $s = 180$ and 250 μm, $\varepsilon_1 = 2.50$ (tan $\delta = 0.002$).

Figure 4.9 also gives a comparison between the effective values from the equations and simulations for the same volume fractions. Over the frequency range examined, $(\varepsilon_{eff}, \mu_{eff})$ is (4.58, 0.75) from the simulation-inversion and (4.05, 0.78) from the canonical methods for the 180 μm spacing, and (3.01, 0.91) from the simulation-inversion and (3.22, 0.90) from the canonical methods for the 250 μm spacing. As in the case of the dielectric cubes, the results of the ε_{eff} from the simulation-inversion process are higher than those of the canonical equations by 13% and 6.7% for the 180 μm and 250 μm spacing respectively. This differences are higher than those from the dielectric cubes in Section 4.2.2 and can be interpreted to mean that for the same volume fraction, the cubes give a higher ε_{eff} than the

spheres. The difference is more significant for the higher inclusion volume fraction. For the μ_{eff}, the results from the equations are slightly higher than those from the simulations but the difference is smaller for the lower volume fraction. From the analysis in [8] which uses the appropriate equations for the polarisability of a cube, the ε_{eff} is 4.47 and 3.13 for the 180 and 250 μm spacings, which is closer to the values obtained from the simulation-inversion process. Here again, the ε_{eff} and μ_{eff} are non-dispersive.

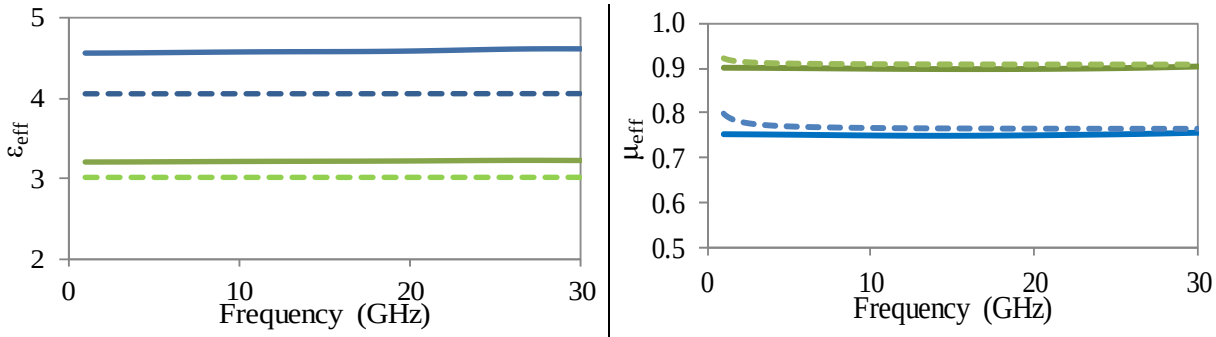

(a) (b)

Figure 4.9: Variation of (a) ε_{eff} and (b) μ_{eff} with frequency from the 100 μm metallic cubes simulations (continuous) and the 62.04 μm (volume equivalence) radius spheres in the equations (dashed) with 180 μm (blue) and 250 μm (green) spacing.

From Figure 4.8 and Figure 4.9 (b), it can be seen that although the host's and inclusion's permeabilities were modelled as $\mu_{1,2} = 1$, the extracted μ_{eff} is less than 1, which has also been reported in [13].

Figure 4.10 shows the effect of increasing the volume fraction of the metallic cubic inclusions to an almost-touching situation. Data used: $l = 100$ μm, $s = 105$–250 μm, $\varepsilon_1 = 2.25$ (tan $\delta = 0.001$), inclusion material was Silver, $\sigma = 6.1\times10^6$ S/m (this was chosen to see if there were any significant difference in the effective EM properties obtained for the heterogeneous medium – it is expected that the equivalent ε_2 for Silver will be as high as that of Copper and so will not produce any difference in the ε_{eff} if ε_2 of Copper is used in the canonical equations). As shown, when the cubes are 5 μm apart (adjacent edge-to-edge), an ε_{eff} of 46.7 is obtained—an increase of 21.2 times that of the host. It is expected that an even higher ε_{eff} could be obtained by further reducing this spacing. However, in the limit where the metallic cubes are touching, it can be expected that the heterogeneous medium will behave like a continuous metal structure. Metallic cubic inclusions produce a significantly

larger ε_{eff} than either metallic spherical inclusions or dielectric cubic inclusions considered in Sections 4.2 and 4.3.1 [16].

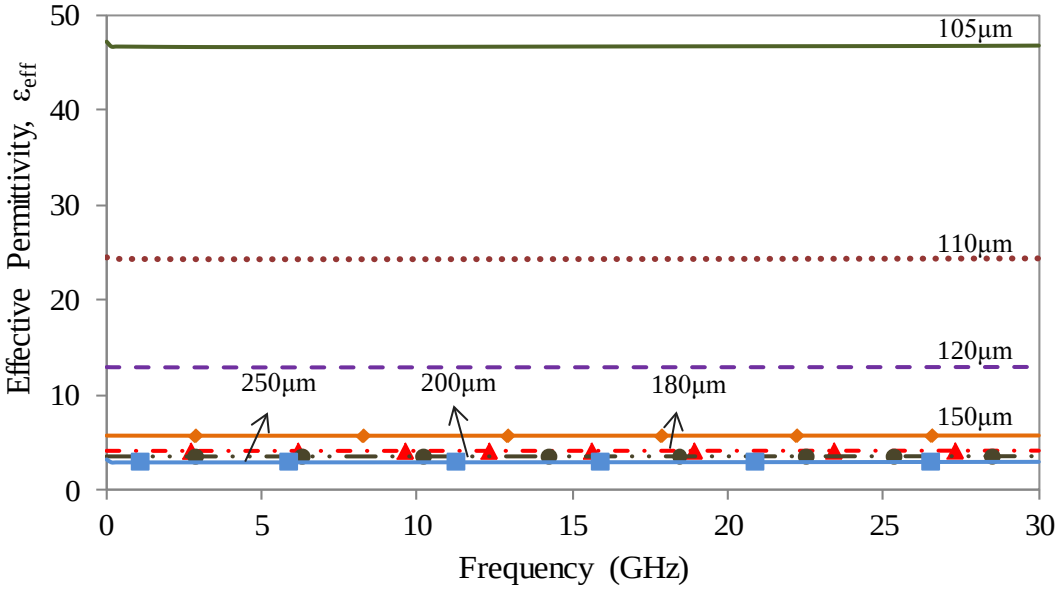

Figure 4.10: Variation of ε_{eff} with frequency for 100 µm metallic cubes spaced 105 µm (—), 110 µm (•••••), 120 µm (– – –), 150 µm (—♦—), 180 µm (—●▲●—), 200 µm (—●●●—) and 250 µm (—■—) apart.

Further simulations were carried out for three lengths of cubic inclusion – 100, 75, and 40 µm using the same volume fractions (equivalent to spacing-to-size ratios) for each length. Figure 4.11 shows the variation of ε_{eff} for each cube size with volume fraction. As shown, the canonical results for spheres using [2], [5], [7] (which all give very similar results) with the volume equivalence method show very good agreement with the results from the simulated cubes. The equations in [8] were not used as these were mixtures with high inclusions' volume fractions. Note that [2], [5], [7] are mainly for spheres and only allow a 0.52 volume fraction for an SC lattice. It can be deduced that, as with spherical inclusions, the volume fraction of the inclusions plays a dominant role in determining the ε_{eff} of the mixture. However, the size of the cubes itself for a fixed volume fraction, plays a lesser role in determining the overall permittivity of the structure. This suggests that as long as the frequency of operation is well below the resonant frequency of the inclusions (or that the inclusion size is less than a tenth of the wavelength), the same ε_{eff} can be predicted even when the inclusions' size is reduced while keeping the volume fraction constant. This does not take into account any quantum and molecular effects.

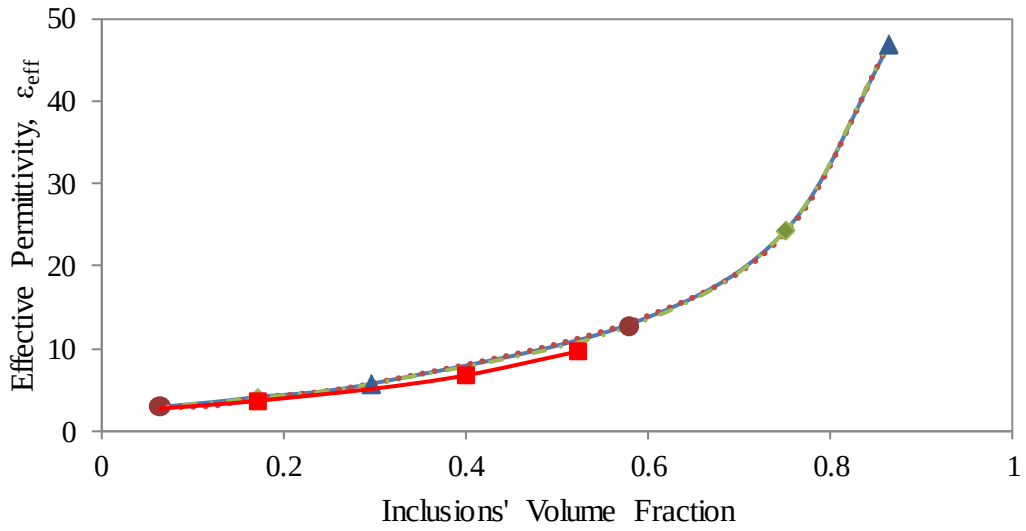

Figure 4.11: Variation of ε_{eff} with inclusions' volume fraction for 100 µm (—▲—), 75 µm (••●••) and 40 µm (—•♦•—) cubes at 10 GHz and from the equations (—■—) in [2], [5], [7]

From this section, it can be concluded that the choice of the shape and material of the inclusion plays a key role in determining the EM properties of the heterogeneous medium. For the same volume fraction of the spheres, the metallic inclusions increase the ε_{eff} from (3.39, 2.82) which was obtained using dielectric inclusions to (4.58, 3.22) for the (180, 250) µm spacings.

4.4 Loss Tangent

An important property of a dielectric medium in addition to its real permittivity value is its loss tangent. It is also called the *dissipation factor* and can be described as the amount of the field energy lost via dissipation in a dielectric material when subjected to an alternating electric field as the dipoles formed within the material when exposed try to align themselves with the alternating polarity of the electric field [12]. It is the tangent of the angle, δ, of the complex dielectric constant [17] and can be mathematically represented as:

$$\tan\delta = \frac{imag(\varepsilon_r)}{real(\varepsilon_r)} = \frac{\varepsilon''}{\varepsilon'} \tag{4-3}$$

where ε_r is the complex permittivity of the medium, given by $\varepsilon_r = \varepsilon' - j\varepsilon'' = |\varepsilon_r|e^{-j\delta}$; δ is the angle between the real and absolute values of the permittivity.

So far, only the absolute values of the ε_{eff} and μ_{eff} of the heterogeneous mixtures have been given. In this section, the loss tangents of the different heterogeneous mixtures examined previously are calculated using equation (4-3). A plot of the loss tangent with frequency for the dielectric cubic inclusions in a dielectric host is shown in Figure 4.12.

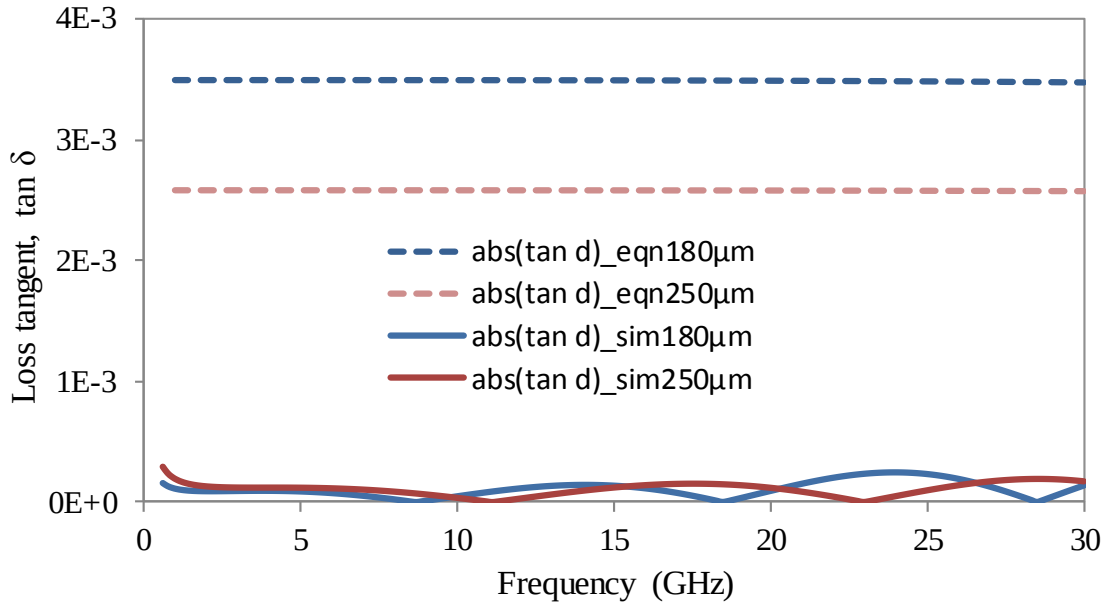

Figure 4.12: Variation of tan δ with frequency for 100 µm dielectric cubes spaced 180 µm (blue) and 250 µm (red) apart from simulations (continuous) and canonical equations (dashed)

The values of the loss tangents shown in the highlighted columns of Table 4-1 are the average values over the frequency range examined (1–30 GHz). The simulated and analytical results Table 4-1 show good agreement for the case of the metallic cubic inclusions. However, they significantly differ from each other in the other cases. This may be due to the imaginary values being small, thus, numerical errors are possible making it more difficult to obtain the tan delta values. Also, in the simulations, a Debye model is applied to the loss tangents and resistivity of the dielectrics and conducting materials, creating a slight variation in these values over the frequency range [18] during simulations. However, with the canonical equations, these values are fixed over the frequency range. It can be assumed that the simulated results give a truer indication of the lossy-ness of these heterogeneous medium. The results indicate that the structures are not inherently lossy and thus could be used for low loss substrates.

Table 4-1: Table of the simulated loss tangents for different heterogeneous media

Inclusion Shape	Host Permittivity, ε_1	Inclusion Permittivity, ε_2	Size (µm)	Spacing (µm)	Loss tangent, tan δ	
					Simulations	Equations
Spheres	2.25 (tan $\delta = 0.001$)	10.2 (tan $\delta = 0.0023$)	100	300	0.013	0.001
		Copper, σ =5.8e7 S/m			0.025	0.001
Cubes	2.50 (tan $\delta = 0.002$)	11.90 (tan $\delta = 0.01$)	100	180	0.0002	0.003
				250	0.0002	0.003
		Copper, σ =5.8e7 S/m	100	180	0.0022	0.002
				250	0.0021	0.002

4.5 Design of a Heterogeneous Medium with Specified Permittivity

So far the effective permittivity, ε_{eff} has been calculated for arbitrary geometries and EM properties primarily to prove that the canonical equations and the simulation results agree. In this section, the possibility of designing a heterogeneous mixture with a pre-determined ε_{eff} has been considered. The different parameters affecting the effective EM properties of the heterogeneous mixtures are ε_1, ε_2, μ_1, μ_2, the volume fraction and shape of the inclusions. It has been shown in the previous sections and chapters that the dominant criterion of these parameters is the volume fraction. Given that the properties of the host and inclusion material can be decided on prior to creating the heterogeneous medium, the volume fraction has to be calculated in order to obtain the desired ε_{eff}. Using Lewin's equation in [2] for ε_{eff} given as

$$\varepsilon_{eff} = \varepsilon_1 \left(1 + \frac{3p}{\frac{\varepsilon_p + 2\varepsilon_1}{\varepsilon_p - \varepsilon_1} - p} \right) \tag{4-4}$$

and rearranging equation (4-4) such that the volume fraction, p is on the left side of the equation gives equation (4-5):

$$p = \frac{X(\varepsilon_{eff} - \varepsilon_1)}{2\varepsilon_1 - \varepsilon_{eff}} \tag{4-5}$$

where $X = (\varepsilon_p + 2\varepsilon_1)/(\varepsilon_p - \varepsilon_1)$.

Lewin's equation is used here because of its algebraic simplicity. Assuming the design is for a heterogeneous mixture with $\varepsilon_{eff} = 10$, and that the host permittivity, ε_1 has been chosen as 1.04 with a loss tangent, $\tan\delta = 0.0017$ (Rohacell® [19]) and the inclusions are made from Copper ($\sigma = 5.80\times10^7$ S/m), in an SC lattice, the next decision to be made is on the size and spacing of the inclusions, that is, the inclusions' volume fraction. Thus, it is very important to understand the effect of the choice of the scale of the particle size, vis-à-vis, its volume fraction, on the effective EM properties of the mixtures.

4.5.1 Choice of Inclusion Size

In this section, different analytical equations to find the desired volume fractions have been compared. The choice of inclusion size involves deciding on whether to use smaller particles in the nano-scale (nm) range (ignoring other quantum effects) or larger particles in the micro-scale (μm) range. In Chapter 2, the effect of the volume ratio of the particles on the effective permittivity has been examined using canonical equations while Figure 4.11 shows the same effect but with the use of the simulation-inversion process.

Spherical Inclusions

Since the volume fraction is dependent on the size of the inclusions, it is rather complex to write an explicit expression for p directly from equation (4-5) as the effective permittivity of the inclusion, ε_p is computed from $\theta = (2\pi/\lambda)a\sqrt{\varepsilon_2\mu_2}$. Reference [2] shows that for metallic inclusions, because ε_2 is much greater than ε_1 as given by the Drude model (see Section 2.4), the ε_{eff} can be approximated as:

$$\varepsilon_{eff} = \varepsilon_1(1 + 3p/(1 - p)) \tag{4-6}$$

Therefore, the volume fraction, p can be written as:

$$p = \left(\varepsilon_{eff} - \varepsilon_1\right)/\left(2\varepsilon_1 + \varepsilon_{eff}\right) \tag{4-7}$$

which is much easier to compute than equation (4-5).

Substituting $\varepsilon_2 = (1.27 + j107.93) \times 10^6$ and $\varepsilon_1 = 1.04$ ($\tan\delta = 0.0017$) into equation (4-7), gives $p = 0.74$. For dielectric inclusions, it is more complicated to write an explicit solution for the size of inclusions to use as it is intricately embedded in the calculation of ε_p for ε_{eff} using Lewin's equations [2]. However, rearranging the Maxwell-Garnett (M-G) equation in [4], the inclusions' volume fraction for known ε_{eff}, ε_1 and ε_2 is given by

$$p = \left(\frac{\varepsilon_{eff} - \varepsilon_1}{\varepsilon_{eff} + 2\varepsilon_1}\right)\left(\frac{\varepsilon_2 + 2\varepsilon_1}{\varepsilon_2 - \varepsilon_1}\right) \tag{4-8}$$

Using this equation gives $p = 0.74$, same as from equation (4-7) and is applicable to both dielectric and metallic inclusions. From this value of p, it can be seen that there is effectively

an infinite number of suitable values of inclusion size and spacing pairs that will give this same volume fraction in any given lattice. This suggests the need to decide on a suitable inclusion size for the specific application. In addition, this p value limits the type of lattice arrangement that can be used for this ε_{eff} value. For example, spherical inclusions in an SC lattice have a maximum p value of 0.524 (using $p = (4\pi/3)a^3/s^3$) which is less than the required p value here. Thus a different lattice arrangement such as the FCC with a maximum volume fraction of 0.74 [15] is better suited if spherical inclusions are to be used. However, the preceding canonical equations have been derived based on the SC lattice, although work has been done for the BCC and FCC lattices via numerical methods (simulations) in [13]. This restraint on using the SC lattice may be dealt with by increasing the value of the host permittivity, ε_1 to say, 2.25 (tan $\delta = 0.001$). This reduces the value of p to 0.53 which is closer to the maximum p for an SC lattice and so equation (4-7) and (4-4) can be used in the preliminary studies on the EM properties of the heterogeneous mixture to be designed.

Cubic Inclusions

The second option is the use of equally spaced cubes as a maximum p value of 1 is theoretically possible for an SC lattice. Rearranging the C-M equation in [8] for the ε_{eff} of cubic inclusions, the volume fraction of the inclusions is given as

$$p = \frac{X3\varepsilon_1}{1 + X\alpha_c} \tag{4-9}$$

where $\alpha_c = \alpha/V_l$; α is the polarisability of the cube; V_l is the volume of the cube; and $X = \left(\varepsilon_{eff} - \varepsilon_1\right)/3\alpha_c\varepsilon_1$. Using equation (4-9) with the same values given in the previous section, gives $p = 0.61$ corresponding to a size-to-spacing ratio, $l/s = 0.85$ using $p = l^3/s^3$; again an infinite number of possible cube sizes and their spacings, theoretically. The p value is different here because the ε_{eff} equation and polarisability expression is different.

Simulation Verification

After these calculations, simulations are used to check that these p values really give an ε_{eff} of 10. For the model with metallic inclusions in a host with $\varepsilon_1 = 1.04$, $p = 0.61$ is obtained. Due to the cost of computational resources, three different cube sizes were chosen for simplicity and ease: 100, 500 and 1000 µm for volume fraction of 0.61. Figure 4.13 shows the inaccuracy of [8] in predicting the ε_{eff} for a closely-packed structure as the results it

gives are close to double the values obtained from inversion of the simulation results. The authors in [8] gave the limit of the accuracy of their equations as for "quite dilute mixtures" with no specific number, which could explain the reason for the over-estimation of ε_{eff} here. (Note: the spikes in Figure 4.13 from the 1000 µm case are from the thickness resonance of the sample simulated.) At 1 GHz, $\varepsilon_{eff} = 6.45$, 6.71, and 6.57 for the 100, 500 and 1000 µm cubic inclusions cases respectively, from simulations. Using $p = 0.61$ in [4] also gives $\varepsilon_{eff} \cong 6$. Even though $p = 0.61$ is not possible using spheres in an SC lattice, it has been shown in [20] that the value of $p > 0.52$ represent the case where the spheres theoretically overlap/intersect each other and the ε_{eff} calculated still produces relatively accurate results. Thus, by using this value of p in the equations in [2] and an equivalent sphere size for the inclusions, ε_{eff} is obtained as 6. If the original value of $p = 0.74$ is used in the equations in [8], an even higher value of $\varepsilon_{eff} = 29.34$ is obtained. It can be concluded from here that even though the equations in [8] give a simple expression p, when used to determine the design volume fraction, inaccurate ε_{eff} results are possible. Thus, care must be taken if using this equation in its limits.

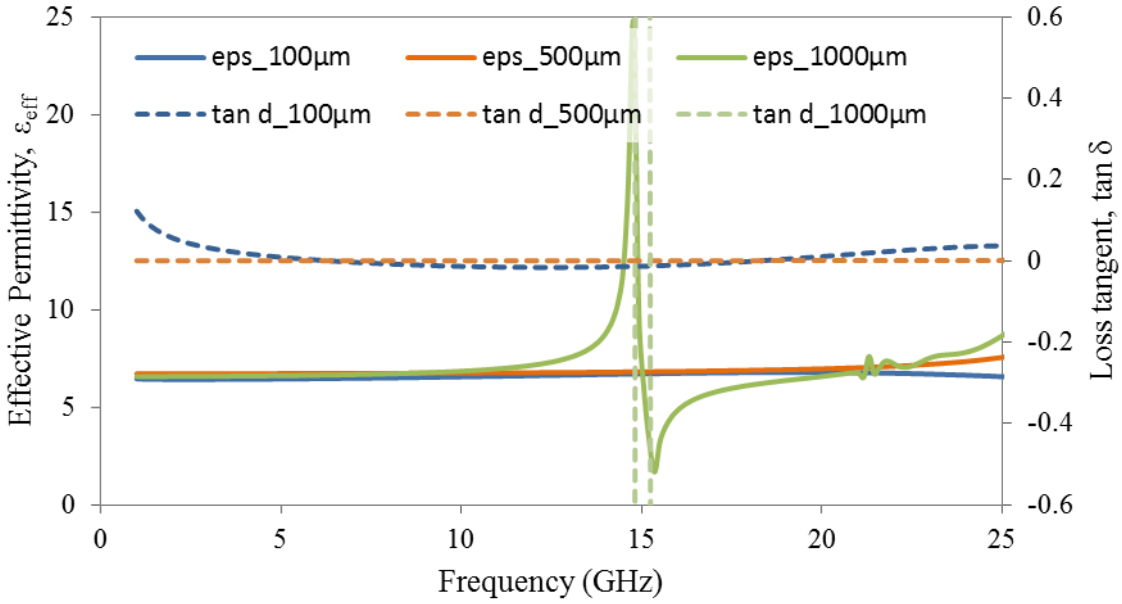

Figure 4.13: Simulated variation of ε_{eff} (continuous) and tan δ (dashed) with frequency of a heterogeneous mixture with 100 (red), 500 (black) and 1000 µm (blue) metallic cubic inclusions with $p = 0.61$

$p = 0.74$ corresponds to $l/s = 0.91$; using this in the simulations for the same cube sizes gives the results shown in Figure 4.14. At 1 GHz, $\varepsilon_{eff} = 10.86$, 10.89 and 10.90 for the 100,

500 and 1000 µm cubic inclusions cases respectively. Although these values are about 10% higher than the design value, they show much better agreement with each other than what was obtained using $p = 0.61$. Therefore, it can be concluded that equations (4-7) and (4-8) give a more accurate prediction of the volume fraction than equation (4-9). This increase in ε_{eff} does not detract from the accuracy of the parameters chosen but can be seen to give room for variation if this structure is to be made, as the exact, well-arranged SC lattice might prove difficult to realise in practise.

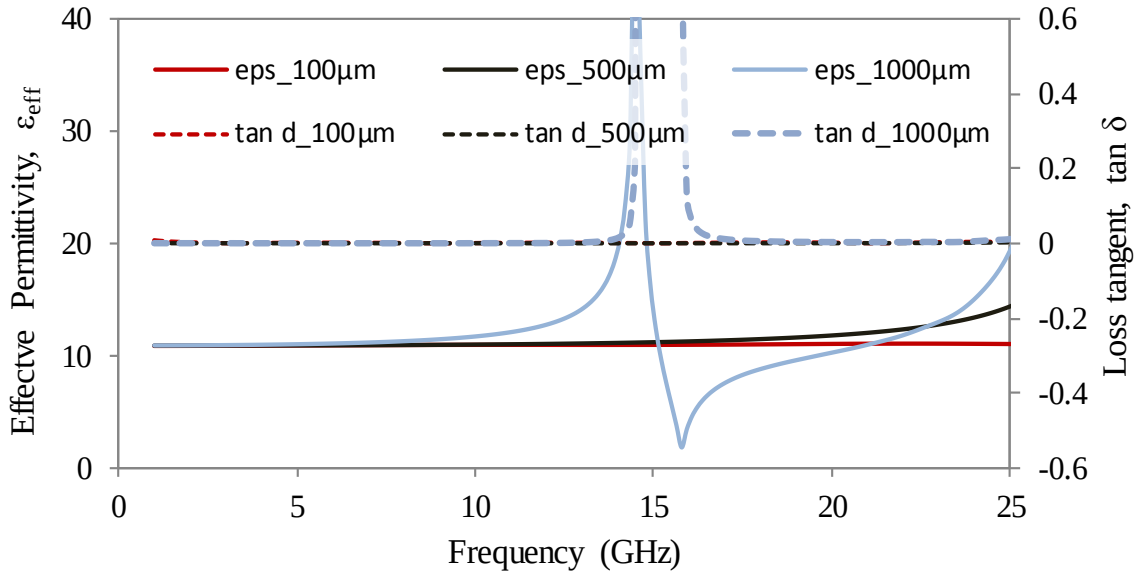

Figure 4.14: Simulated variation of ε_{eff} (continuous) and tan δ (dashed) with frequency of a heterogeneous mixture with 100 (red), 500 (black) and 1000 µm (blue) metallic cubic inclusions with $p = 0.74$

Design with Dielectric Inclusions

Here, the use of dielectric inclusions in creating the heterogeneous mixture with $\varepsilon_{eff} = 10$ will be examined. So far metallic inclusions have been used; if the inclusions were to be made out of a material, say, Silicon with $\varepsilon_2 = 11.9$, tan $\delta = 0.01$ [18], with the same host, $\varepsilon_1 = 1.04$ (tan $\delta = 0.0017$) as above, to get an $\varepsilon_{eff} = 10$ from equation (4-8), the volume fraction, $p = 0.95$ is required with $l/s = 0.98$. This implies that a higher density of the cubic inclusions, about 30% higher, is required to produce the same ε_{eff} than when metallic inclusions are used. Again, this value of volume fraction cannot be achieved using spheres in any of the cubic lattices, so cubes are used here. For these non-metallic inclusions, the $\varepsilon_{eff} = 10$ and tan $\delta = 0.01$, using the equations in [2]. This also buttresses the point that the ε_{eff}

cannot exceed the permittivity values of the host or inclusion material but lies somewhere between ε_1 and ε_2 and that the ε_{eff} is not simplify a direct ratio of the contributing permittivities of the host and the inclusions [4].

Simulation Verification of Design

Figure 4.15 shows the plot of the absolute values of the ε_{eff} and tan δ for a heterogeneous mixture with 500 µm Silicon cubes in an SC lattice, from simulations and the inversion process. As shown, the ε_{eff} shows good agreement with the initial design value of 10. It can be concluded that the equations (4-7) and (4-8) give a consistent and accurate value of the volume fraction independent of the design materials' chosen and the required ε_{eff} as the simulation results from using these p values agree very closely with the design ε_{eff}. It should be noted that the resonance shown by the spike in Figure 4.15 is the thickness resonance effect (see Chapter 3) due to the choice of the overall thickness of the sample in the direction of propagation, which occurs earlier on the frequency scale as this thickness is increased. It is primarily a numeric effect. Please note: it is not a resonance due to the scale of the inclusions or the spacing between them, as these come into play further up the frequency scale (see Section 2.2.6), where the size or spacing approaches the wavelength.

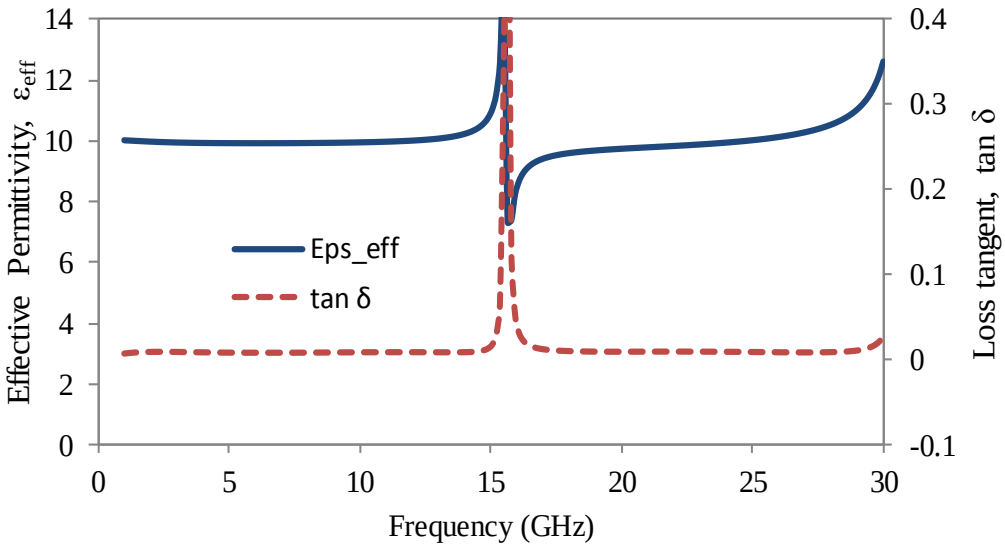

Figure 4.15: Variation of ε_{eff} (continuous) and tan δ (dashed) of a heterogeneous mixture with 500 µm non-metallic cubic inclusions from simulation-inversion process

It should be noted that with software such as MathCAD or MATLAB, a simple sweep of the parameter space can be used to obtain the parameters for the heterogeneous medium with a desired ε_{eff}, but this can be a repetitive process as both the spacing and the size need to be

changed simultaneously to maintain the calculated volume fraction of the medium. However, it presents a quick option when the inclusion size is fixed and different spacing values tested to realise the desired ε_{eff}. As discussed, different equations for p give different accuracy levels when compared with simulation results. Therefore, the correct equations have to be used to accurately predict the p value, or else an over-estimation of the desired ε_{eff} may result as with [8]. Once this has been done, simulations can then be carried out to further confirm the expected results, and the sample built and tested.

4.6 Conclusions

With the foundation for the canonical equations and electromagnetic simulations of heterogeneous media laid in Chapters 2 and 3 respectively, this chapter set out to compare the ε_{eff} and μ_{eff} results from these two techniques for different heterogeneous mixtures. These mixtures composed of dielectric and metallic spheres or cubes in a dielectric host have been investigated. The results from the simulations have been shown to agree well with those from the canonical equations especially when appropriate equations are used, as seen in the design scenario in Section 4.5.1.

Cubes with the same volume as spheres can be used for faster simulations and to increase the volume fraction of the inclusions. The loss tangent of these mixtures from the equations and the simulations have been given and compared. The predicted losses have been found to be comparable to conventional low loss substrates. However, further research may be required to understand why the loss tangents from the simulations do not exactly agree always with those from the canonical equations.

The design process of calculating the parameters of a heterogeneous mixture for a pre-determined ε_{eff} value has been shown, using metallic and non-metallic inclusions in an SC lattice in a very low dielectric host. Two main expressions, equations (4-8) and (4-9), have been used in determining the volume fraction of the designed heterogeneous medium with cubic inclusions. Equation (4-8) showed much better agreement with the simulation results and the canonical equations than (4-9), especially in the case of high inclusions' volume fractions.

This chapter has proven that the canonical equations can be used directly to predict what the effective permittivity and permeability values of a to-be-manufactured heterogeneous medium will be. This provides a good starting point in the design process of the geometric and electromagnetic properties of the host and inclusion materials. It also lays the foundation for the measurements to be made and these are presented in the next two chapters – Chapters 5 and 6.

4.7 References

[1] N. G. Alexopoulos, C. A. Kyriazidou, and H. F. Contopanagos, “Effective parameters for metamorphic materials and metamaterials through a resonant inverse scattering approach,” *IEEE Transactions on Microwave Theory and Techniques*, vol. 55, no. 2, pp. 254–267, 2007.

[2] L. Lewin, “The electrical constants of a material loaded with spherical particles,” *IEE-Part III: Radio Comm. Eng.*, vol. 94, no. 27, pp. 65–68, 1947.

[3] X. Cai, R. Zhu, and G. Hu, “Experimental study for metamaterials based on dielectric resonators and wire frame,” *Metamaterials*, vol. 2, no. 4, pp. 220–226, 2008.

[4] A. Sihvola, *Electromagnetic Mixing Formulas and Applications*. London: IET, 1999.

[5] I. A. Kolmakov, L. Jylha, S. A. Tretyakov, and S. Maslovki, “Lattice of dielectric particles with double negative response,” in *28th Gen. Ass. Int. Union Radio Sci. (URSI)*, 2005.

[6] W. T. Doyle, “The Clausius-Mossotti problem for cubic arrays of spheres,” *Journal of Applied Physics*, vol. 49, no. 2, pp. 795–797, 1978.

[7] W. T. Doyle, “Optical properties of a suspension of metal spheres,” *Physical Review B*, vol. 39, no. 14, pp. 9852–9858, 1989.

[8] J. Avelin, A. Sihvola, R. Sharma, and I. Hanninen, “Modelling of dielectric materials with cubic inclusion shapes,” in *29th European Microwave Conference*, 1999, pp. 36–39.

[9] M. A. Ordal, L. L. Long, R. J. Bell, S. E. Bell, R. R. Bell, R. W. Alexander, and C. a Ward, “Optical properties of the metals Al, Co, Cu, Au, Fe, Pb, Ni, Pd, Pt, Ag, Ti, and W in the infrared and far infrared,” *Applied Optics*, vol. 22, no. 7, pp. 1099–1120, Apr. 1983.

[10] J. C. Vardaxoglou, “Optical switching of frequency selective surface bandpass response,” *Electronics Letters*, vol. 32, no. 25, pp. 2345–2346, 1996.

[11] K. L. Kelly, E. Coronado, L. L. Zhao, and G. C. Schatz, “The optical properties of metal nanoparticles: the influence of size, shape, and dielectric environment,” *Journal of Physics Chemistry B*, vol. 107, pp. 668–677, 2003.

[12] C. A. Balanis, *Advanced Engineering Electromagnetics*, 2nd ed. New York: Chichester: Wiley, 1989.

[13] I. Awai, O. Mizue, and A. K. Saha, “Artificial dielectric resonator made of spherical metal particles,” *IEICE Transactions on Electronics*, vol. E92–C, no. 1, pp. 72–76, 2009.

[14] I. Awai, Y. Maegawa, and T. Ishizaki, “Measurement of effective material constants of artificial dielectrics made of spherical metal particles,” in *Asia Pacific Microwave Conference*, 2009, pp. 1655–1658.

[15] B. Van Zeghbroeck, *Principles of Semiconductor Devices*. Boulder: ECEE, University of Colorado, 2004.

[16] C. C. Njoku, W. G. Whittow, and Y. C. Vardaxoglou, “Effective permittivity of heterogeneous substrates with cubes in a 3-D Lattice,” *IEEE Antennas and Wireless Propagation Letters (Special Issue on Metamaterials)*, vol. 10, pp. 1480–1483, 2011.

[17] H. A. Haus and J. R. Melcher, *Electromagnetic Fields and Energy*. Massachusetts: MIT Press, 1998.

[18] IMST GmbH, “EMPIRE XCcel Manual,” 2011.

[19] Evonik-Industries, “Rohacell HF,” 2011. [Online]. Available: http://www.rohasell-online.com/products.html. [Accessed: 05-Nov-2012].

[20] B. Sareni, L. Krahenbuhl, A. Beroual, and A. Nicolas, “A boundary integral equation method for the calculation of the effective permittivity of periodic composites,” *IEEE Transactions on Magnetics*, vol. 3, no. 2, pp. 1580–1583, 1997.

Chapter 5. Dielectric Measurement Techniques for Heterogeneous Mixtures and Results

5.1 Introduction

The long term aim of this research is to create heterogeneous materials using nano-fabrication techniques which will allow antenna systems to be manufactured in one integrated process. Some of these techniques were briefly described in Chapter 1 and the specific ones used during this project have been explained here. The different measurement techniques used for characterising the electromagnetic (EM) properties of the fabricated samples are also explained with the merits and demerits highlighted and discussed. The three measurement techniques examined are with the split-post dielectric resonator, the rectangular waveguide, and the microstrip ring resonator. The results from the canonical equations and the plane wave simulations of the created samples are compared with the measured results. The challenges associated with these methods have also been mentioned.

So far the work has been carried out using the canonical equations [1] and S-parameter inversion processes from simulations described in [2], to determine the EM properties of heterogeneous mixtures with inclusions. In this chapter, a brief description of the fabrication techniques used in this research are given in Section 5.2 along with the materials used in making the specific samples. It also outlines the samples created and presents the extracted ε_{eff} and μ_{eff} using plane wave simulations. Section 5.3 demonstrates the split-post dielectric resonator measurement technique with the results from homogenous samples presented. Section 5.4 examines the waveguide measurement method with results from simulations and measurements. In Section 5.5, the method of dielectric characterisation using a microstrip ring resonator has been discussed and simulated and measured results of various samples have been presented. The conclusions are given in Sections 5.6.

5.2 Fabrication Techniques for Samples

As the emphasis of this thesis is on the electromagnetic behaviour of artificial dielectrics, it is envisaged that emerging nanofabrication techniques will enable such structures. Possible nanofabrication techniques have been summarised in Chapter 1, however, these were beyond the scope of this thesis. In this section, the manual arrangement of the inclusions and the etching technique are briefly described.

5.2.1 Array of Metal Balls

One of the methods used in creating the heterogeneous substrates measured in this project was simply by drilling 10 mm diameter holes with a 13 mm spacing in a 10 mm thick Rohacell® substrate and filling these holes up with 10 mm diameter chrome steel balls. Three layers of this structure were made and separated by a continuous 3 mm Rohacell® layer to provide the necessary insulation between the spheres and closely approximate a simple cubic lattice-type structure with 13 mm spacing in all three directions. Rohacell® was assumed to have the electrical properties of air. This arrangement is shown in Figure 5.1. This structure acted as a scaled-up measurement of the heterogeneous mixtures and was used to further validate the analytical and simulated results. One of the challenges faced in this sample construction method was the effect of the weight on the structural integrity of the Rohacell®, especially when trying to fit it in the sample holder of the waveguide.

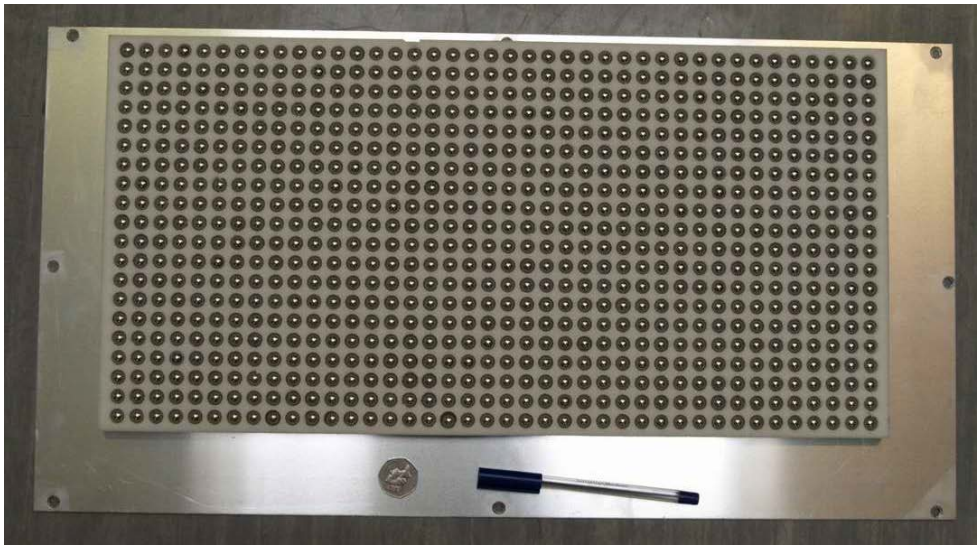

Figure 5.1: 10 mm chrome steel balls in a Rohacell® layer with 13 mm uniformly spaced holes

5.2.2 Etching:

Etching is a top-down technique whereby unwanted sections of metals, typically Copper (Cu) are removed from a laminate structure, by coating the substrate with a ultra-violet (UV) photoresist material and exposing the unwanted areas to UV light. Once this has been done, the laminate is then placed in an acid bath to allow the exposed areas to be etched away with the remaining photoresist removed by using acetone. Etching has a number of variants such as (deep) reactive ion plasma etching [3], [4], plasma etching [5], and beam-induced etching [6].

Etched Samples

The etching process has been used in this project to create the initial heterogeneous test samples as determined by the resources available within the School. This created smaller sized inclusions than the metal balls above. The initial material was a thin dielectric laminate with Cu covering both sides. One side of the final etched layer is shown in Figure 5.2. The structure shown here is double-sided, that is, the same pattern is etched directly opposite on the other side such that the Cu squares are aligned. Two scales were considered: (i) 2 mm squares with 500 µm gaps and (ii) 500 µm squares with 250 µm gaps between adjacent squares. The thickness of the Cu layer was ~ 35 µm. The dielectric material of the laminate was GTS® with a permittivity of 3 and a thickness of 110 µm. Thus, the volume fractions, p, of the Cu, air and dielectric material for the 2 mm squares are 0.25, 0.14 and 0.61 respectively while those for the 500 µm squares are 0.17, 0.22 and 0.61 respectively (see calculations for the 500 µm squares below).

<u>For the 500 µm squares case:</u>

Volume of unit cell, $V = (750 \times 750 \times 180)$ µm^3

Volume of Copper per unit cell, $V_{Cu} = (500 \times 500 \times 70)$ µm^3

Volume of air per unit cell, $V_{air} = [(250 \times 750) + (250 \times 500)] \times 70$ µm^3

Volume of GTS® material per unit cell, $V_{GTS} = (750 \times 750 \times 110)$ µm^3

Total volume of unit cell, $V = V_{Cu} + V_{air} + V_{GTS} = 101.25 \times 10^6$ µm^3

Therefore, the volume fraction of Copper, $p_{Cu} = V_{Cu}/V = 0.17$.

Similarly, $p_{air} = V_{air}/V = 0.22$, and $p_{GTS} = V_{GTS}/V = 0.61$

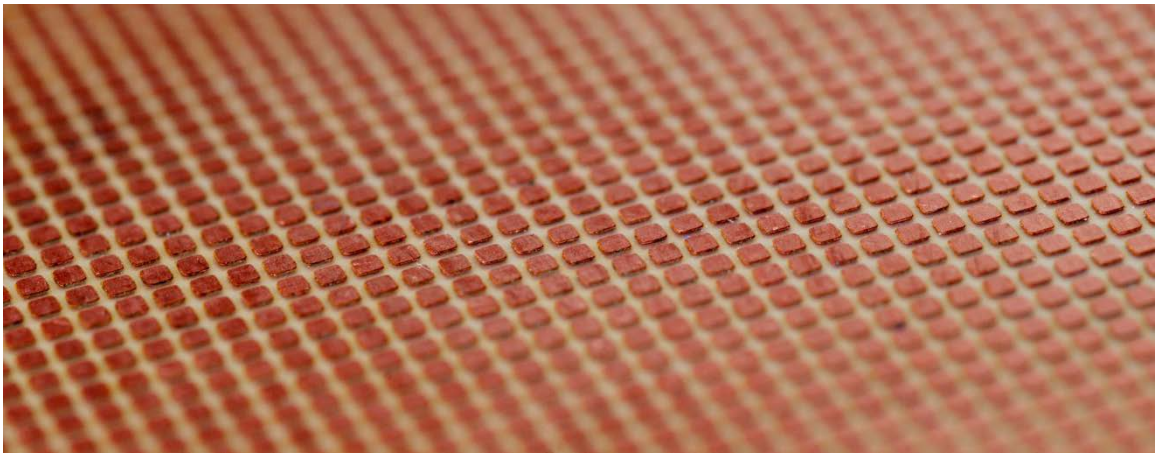

Figure 5.2: Etched heterogeneous sample of 500 µm Cu squares with 250 µm gaps on GTS® material

In order to create a suitable heterogeneous sample with significant thickness, (to allow measurement of ε_r) several layers of this structure were stacked on top of each other. Given that the thickness of one layer was ~ 180 µm, to get a thickness of ~ 1.5 mm (in the region of those of readily available substrates to allow a fair comparison), 9 layers were used. A major drawback of this process of manually layering the sample is that it is very difficult to align more than two layers to give exact back-to-back alignment. The 2D plots of the layered structure are given in Figure 5.3.

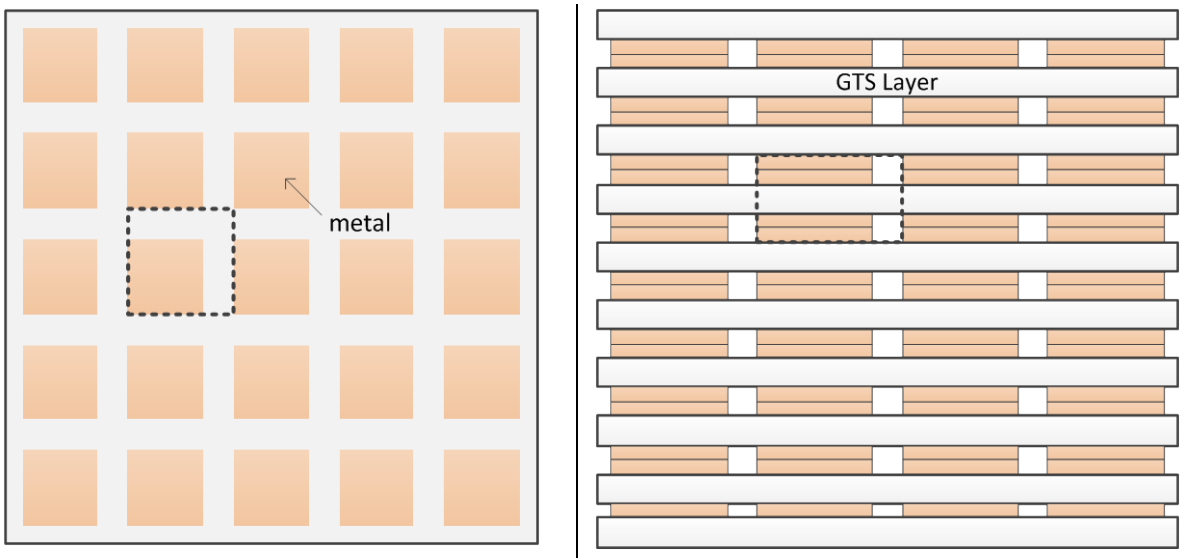

(a) (b)

Figure 5.3: Small section of the (a) top view and (b) side view (not to scale) of the GTS® 9-layered structure with Cu squares. The dashed boxes show the unit cells in both planes. Note: (b) is stretched vertically to clearly show the inclusions

5.2.3 Plane Wave Simulations of Constructed Sample

Array of chrome steel balls in Rohacell®

The extracted ε_{eff} and μ_{eff} results of the simulation of the structure shown in Figure 5.1 for different number of layers of the sample are shown in Figure 5.4 and Figure 5.5 respectively using two different waveguide sizes. It can be seen that as the number of layers increase the values of ε_{eff} and μ_{eff} converges. Using the results of the 10-layer structure which should have the most accurate EM results as they are closer to the infinite structure used in the canonical equations, this gives $\varepsilon_{eff} = 2.31$ and 2.37 at 400 MHz and 1 GHz respectively, and $\mu_{eff} = 0.67$ and 0.68 (a diamagnetic property) at 400 MHz and 1 GHz respectively.

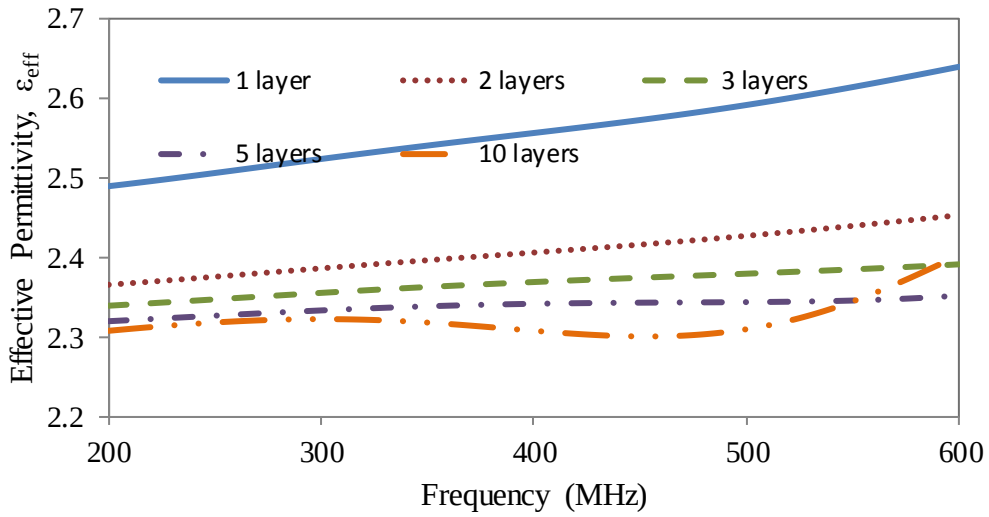

(a)

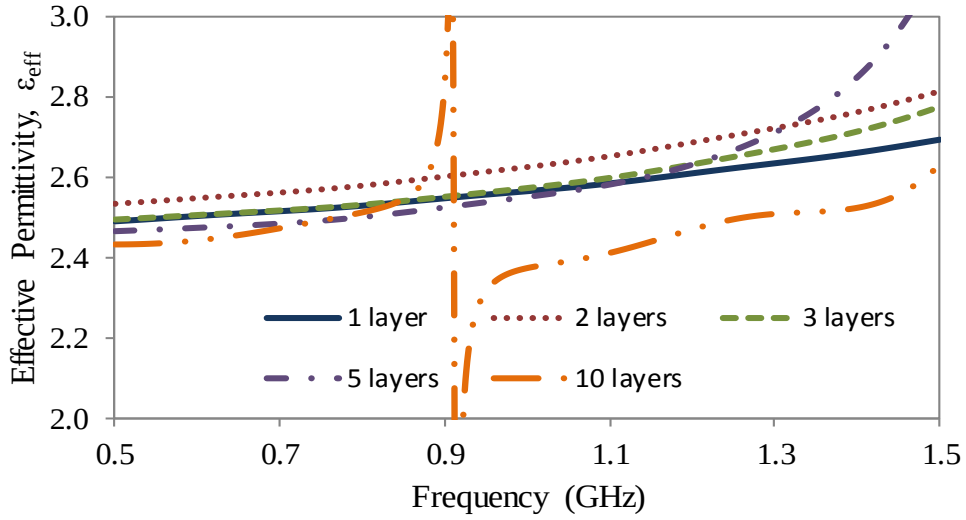

(b)

Figure 5.4: Simulated variation of ε_{eff} with frequency for increasing layers of the structure shown in Figure 5.1 with the (a) 400 MHz and (b) 1 GHz waveguides

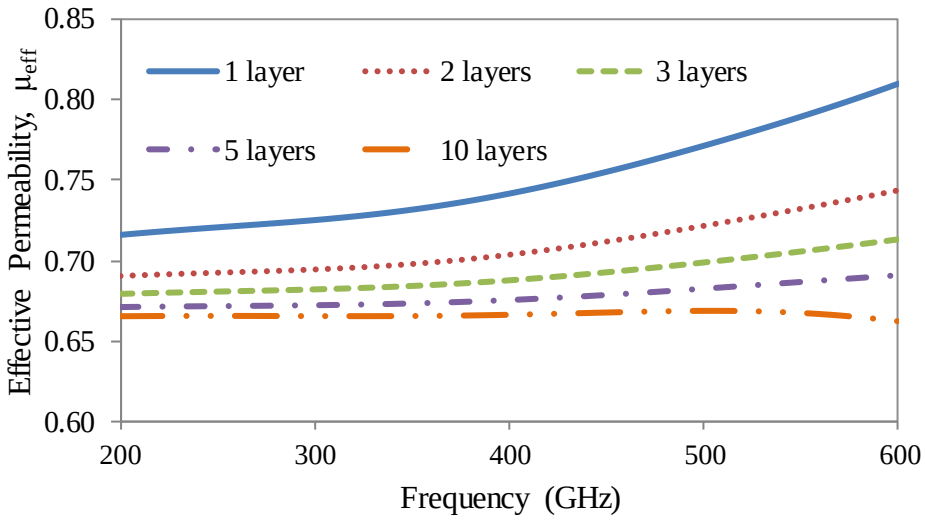

(a)

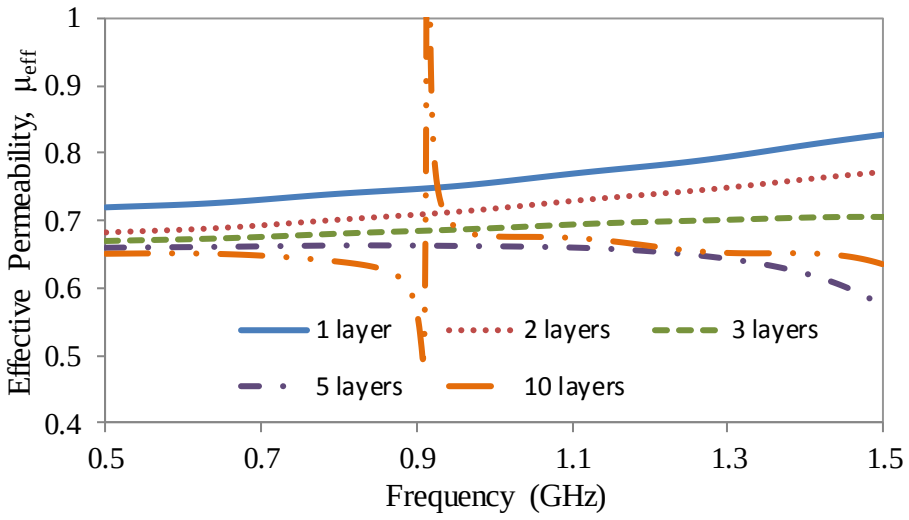

(b)

Figure 5.5: Simulated variation of μ_{eff} with frequency for increasing layers of the structure shown in Figure 5.1 with the (a) 400 MHz and (b) 1 GHz waveguides

Figure 5.4 and Figure 5.5 also show that depending on the size of the inclusions, the spacing between them and the frequency of operation, it is important to get the number of layers (in the direction of the wave propagation) right in order to obtain accurate results. This has been further discussed in Chapter 3.

Layered-up Structure

As a first step, the sample shown in Figure 5.3 was simulated with the setup discussed in Chapter 3. The ε_{eff} and μ_{eff} were extracted from the S-parameters and are shown in

Figure 5.6. Due to the metallic inclusions and as shown from the simulated results of heterogeneous media with metallic inclusions in Chapter 4, the μ_{eff} was less than 1.0 (a diamagnetic behaviour), in this case 0.81. The average $(\varepsilon_{eff}, \mu_{eff})$ from Figure 5.6 over the frequency range was (6.01, 0.81). The rise of ε_{eff} shown in Figure 5.6 indicates the thickness resonant point of the sample is approaching where it becomes transparent to the incoming plane wave – please see Section 3.4 for more details.

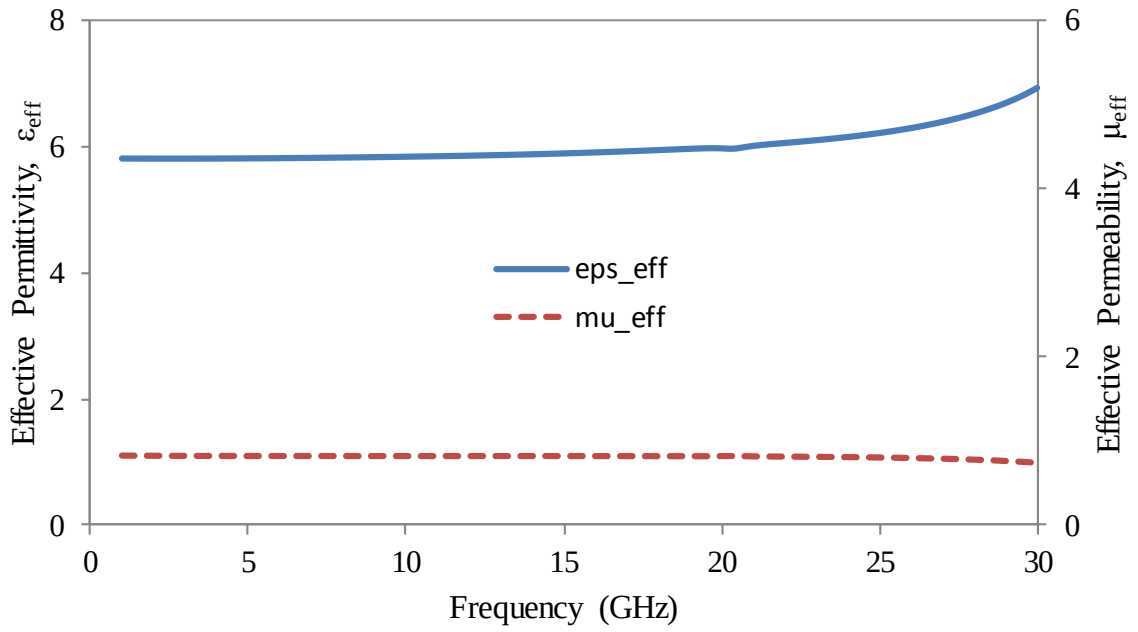

Figure 5.6: Simulated variation of ε_{eff} (continuous) and μ_{eff} (dashed) with frequency for a 9-layered GTS® structure when the electric field is parallel to the plane of the copper metal squares

It should be noted that for the plane wave simulations of this sample, the electric field was polarised in the same direction as the plane of the metallic cuboids as shown in Figure 5.7 (a). This is important because the structure is not uniform in all three directions and as such exhibits anisotropy. The extracted ε_{eff} and μ_{eff} values when the electric field is perpendicular to the thickness of the metallic layer for the same structure (see Figure 5.7 (b)) is shown in Figure 5.8 with the average $(\varepsilon_{eff}, \mu_{eff})$ over the frequency range is (4.43, 0.69) below 15 GHz. This shows that the effective permittivity and permeability for this sample are tensors and can be written as $\varepsilon_{eff} =$ (6.01, 6.01, 4.43) and $\mu_{eff} =$ (0.81, 0.81, 0.69).

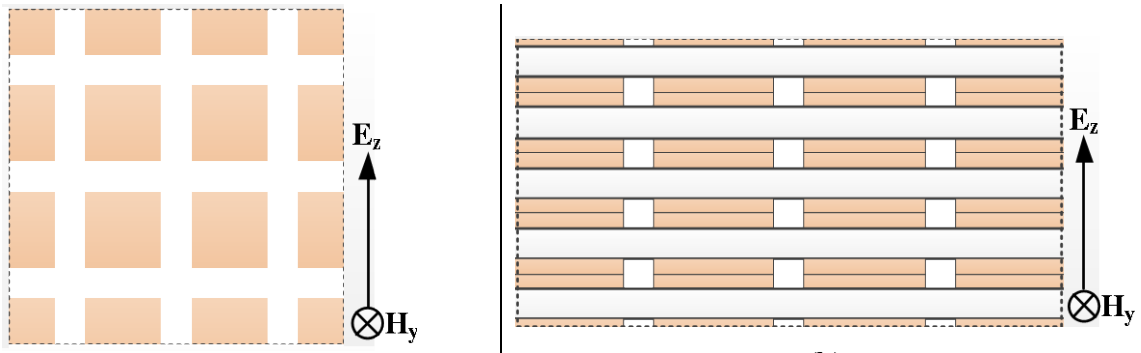

(a) (b)

Figure 5.7: Diagram showing two polarisations of the electric field with respect to the simulated structure, when the electric field is (a) in the plane of and (b) perpendicular to the area of the copper squares

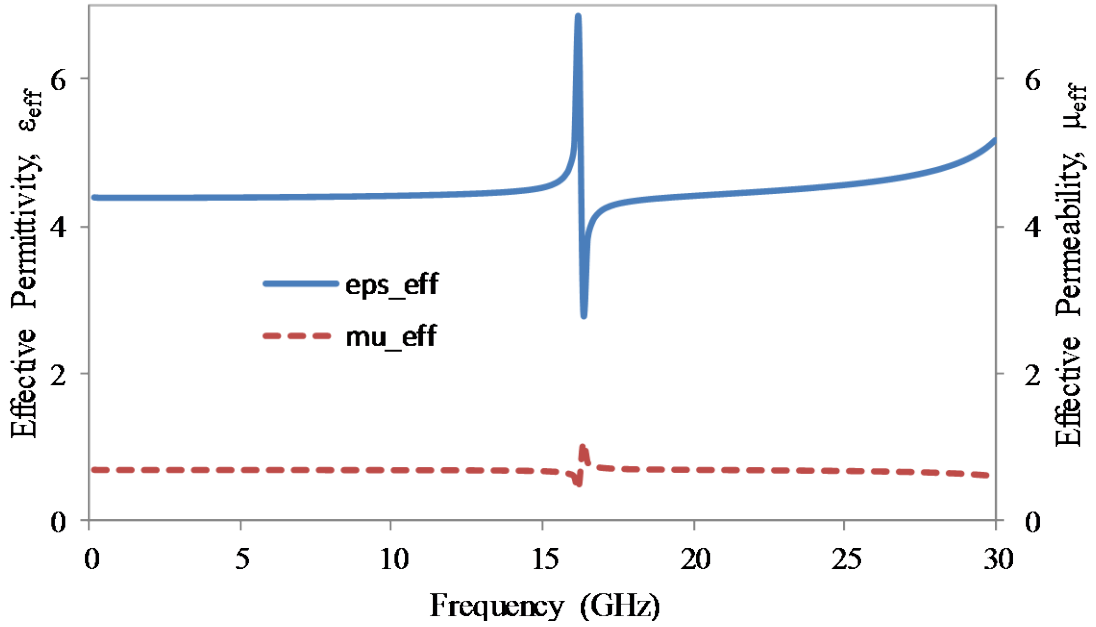

Figure 5.8: Simulated variation of ε_{eff} and μ_{eff} with frequency for an 8-layered structure when the electric field is perpendicular to the plane of the copper squares

Given that the simulation-inversion process was rigorously verified both with homogenous and heterogeneous samples in Chapter 4 and shows good agreement with the canonical results over a wide range of geometries, the values of the ε_{eff} and μ_{eff} obtained for the sample shown in Figure 5.6 and Figure 5.8, were assumed to be accurate for this sample structure. This was also verified by using equation (5-1) from [7] for multiphase mixtures, that is, mixtures having more than one inclusion type. The sample here can be thought of as a

GTS® host material with copper and air cuboid inclusions with volume fractions of 0.17 and 0.22 respectively.

$$\varepsilon_{eff} = \varepsilon_1 + 3\varepsilon_1 \frac{\sum_{k=2}^{K} p_k \frac{\varepsilon_k - \varepsilon_1}{\varepsilon_k + 2\varepsilon_1}}{1 - \sum_{k=2}^{K} p_k \frac{\varepsilon_k - \varepsilon_1}{\varepsilon_k + 2\varepsilon_1}} \quad (5\text{-}1)$$

This equation gives an ε_{eff} of 4.13 which is close to the value of ε_{eff} from the simulations using the polarisation shown in Figure 5.7 (b). Note: equation (5-1) does not take into account the polarisation of the electric field with respect to the inclusions.

Beyond the use of the canonical equations and the simulation analyses in designing and/or analysing a heterogeneous structure, a very important part of this project was deciding on suitable and repeatable measurement methods for the different structures. The next sections discuss the various techniques examined during this research and compare the results with those from simulations. The permittivity of the materials relative to free space is examined.

Plane wave measurements were considered but were not implemented because of the difficulty in creating the heterogeneous samples shown in Figure 5.3 with the present etching facilities in the School, on a large scale and with high level of resolution, alignment and accuracy. A large size would be required as the sample should be in the far field of the measurement (horn) antenna and at least 10 wavelengths long and wide to minimise diffraction at the edges.

Metallic Nano-films

In addition to these two categories of samples made, collaborators on this research at the University of Patras, Greece, made some samples to be measured but they were too fragile to be handled continuously without breaking. They were thin metallic nano-films as shown in Figure 5.9. These samples were porous oxides – Al_2O_3-Ag-Au, with 200 nm diameter cylindrical Silver inclusions, see Figure 5.10, which shows the dimensions of the sample. Sturdier substrates such as Rohacell® had to be used to handle the sample during measurements as they were very brittle making it impossible to fill the waveguide with the sample without damaging them. The Rohacell®-Sample-Rohacell® structure was placed between the flanges of the RWG without trying to fit it in the waveguide slot. Cellotape was

used to bind this structure together to ensure fit. The measurements did not give sensible results for the ε_{eff} and μ_{eff} when the S-parameters were put through the NRW algorithm, probably due to the extremely thin nature of the sample.

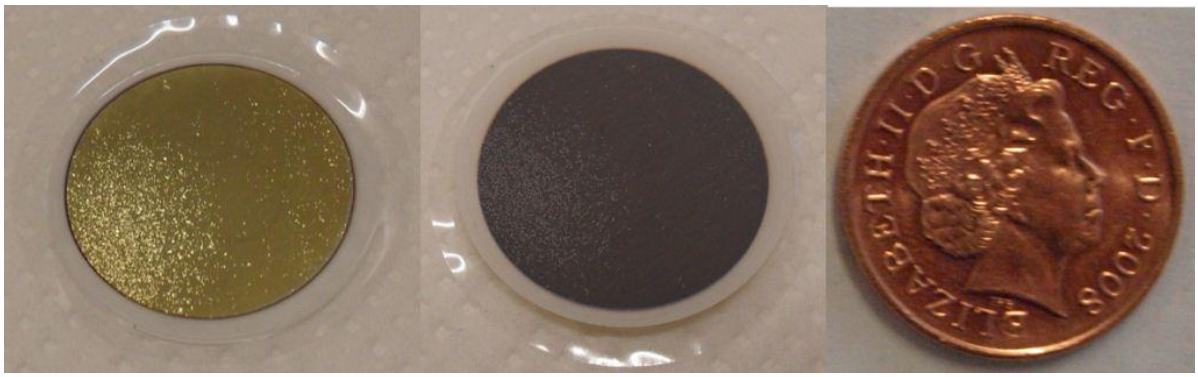

Figure 5.9: Front and back views of thin samples

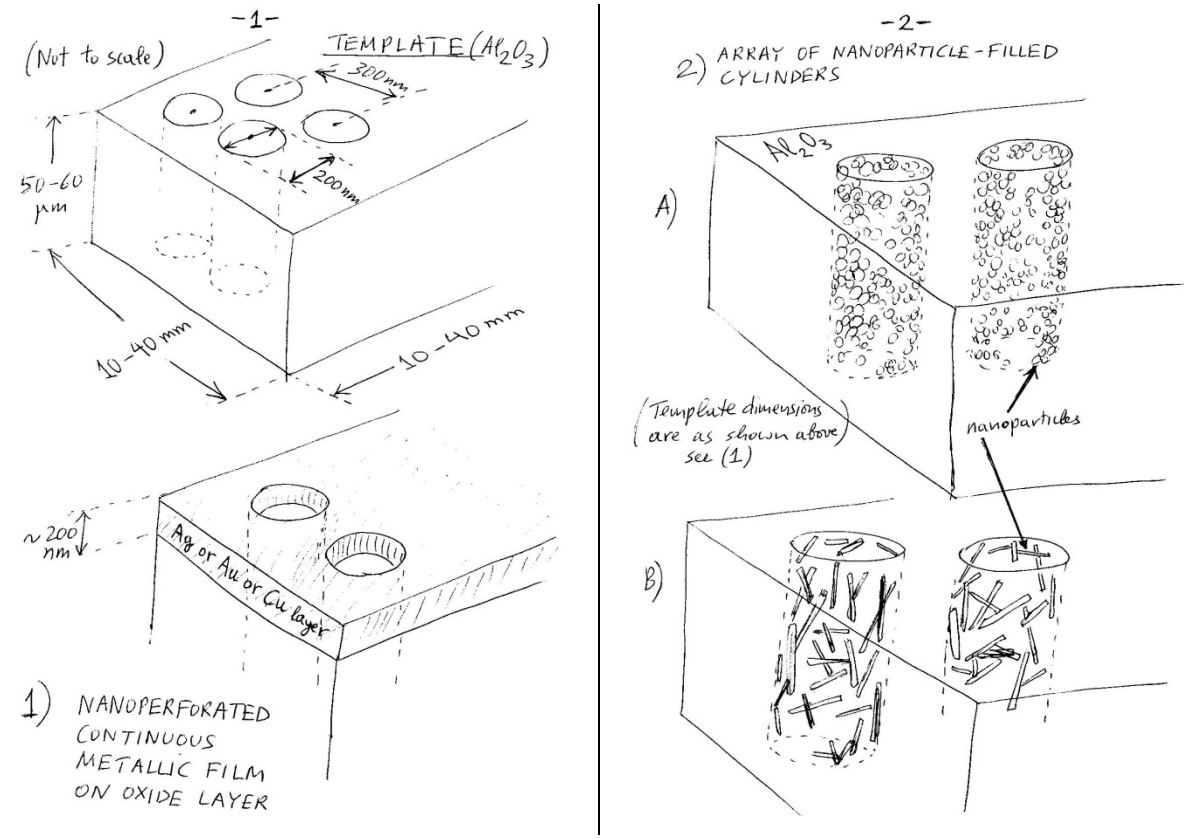

Figure 5.10: Schematic diagrams of thin samples in Figure 5.9

5.3 Split Post Dielectric Resonators

The split post dielectric resonators (SPDR) were initially used for measurements of the etched samples as the technique was quick to implement without additional constraints of lare scale samples as previously required for the horns and did not require a complex pre-measurement setup.

5.3.1 Theory

The split-post dielectric resonator was introduced approximately 17 years ago [8] and is now routinely used in the measurement of the complex permittivity of planar dielectric materials with reasonable accuracy [9]. The SPDR is shown in Figure 5.11 and uses the sample's thickness, and the Q-factors and resonant frequencies with and without the test sample to determine the permittivity and loss tangent of the sample. In this project, it was used first to measure substrates of known dielectric properties to validate the method.

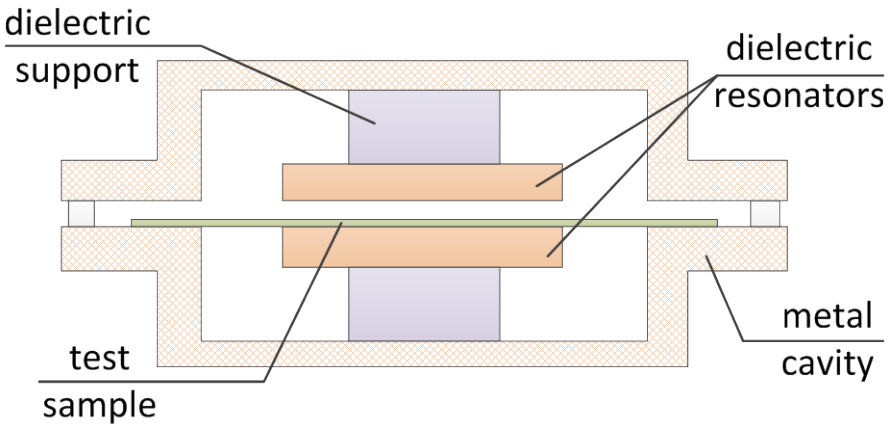

Figure 5.11: Cross-section of an SPDR containing a material sample placed on a dielectric substrate

The steps involved in this measurement technique are given as:

1. Measure the thickness of the test sample in mm (required by executable file for the SPDR software)
2. Calibrate the Vector Network Analyser (VNA) to the ends of the cables that connect directly to the SPDR, making sure there are enough points selected around the estimated resonant frequency of the SPDR to accurately determine the 3-dB points below the resonant frequencies of the SPDR with and without the sample. Multiple calibrations may be required to obtain a higher level of accuracy

3. Connect the empty SPDR to the Network Analyser and measure the resonant frequency, f_{r1} and the 3-dB frequency points below f_{r1}
4. Insert the test sample into the cavity of the SPDR to completely cover the resonator
5. Measure the new resonant frequency, f_{r2} of the SPDR and the 3-dB bandwidth
6. Calculate the Q-factors with and without the sample using

$$Q = \frac{f_r}{3\ dB\ bandwidth} \tag{5-2}$$

7. Using the equations in [10] or the executable file that comes with the SPDR software, calculate the relative permittivity and loss tangent of the test sample, using its thickness, f_r's and Q-factors

5.3.2 Measured Results

This method was used to measure the permittivities of substrates such as Perspex and FR4 and the results showed good agreements with known values. Measured Perspex permittivity = 2.67, tan $\delta = 0.0044$; permittivity of Perspex from literature = 2.68 [11]. Typically, $f_{r1} > f_{r2}$ due to the effect of the dielectric property of the test sample. However, when the heterogeneous sample shown in Figure 5.2 was placed in the cavity of the SPDR, the opposite reaction was obtained, that is, the resonant frequency increased. This was explained by the manufacturers of the SPDR as either being due to the diamagnetic behaviour of the material or the frequencies at higher modes being displaced to lower frequencies when a high permittivity material is inserted. For the latter option, the manufacturers advised that a different analysis would be required to correctly interpret the results. A similar increase in frequency has been reported for the SPDR used in measurements of metamaterials in [12] and thin films [13], however, an explanation on the validity of the ε_{eff} results obtained using this frequency increase was not given.

5.4 Waveguides

Rectangular waveguides (RWG) are commonly used tools for measuring the complex permittivity and complex permeability of different materials [14–18]. This method has been used in this thesis and the theory and results are explained below.

5.4.1 Theory

Rectangular waveguides are generally defined by their dimensions and cut-off frequencies below which waves do not propagate within the waveguide. The dimensions of these waveguides are related to their frequency range of operation within which various field modes can propagate that all satisfy the boundary conditions of the waveguide [19]. In this section, only the Transverse Electric (TE) mode is considered.

The waveguide is first calibrated to its port ends using for example, the TRL (Through-Reflect-Line) [20] calibration. The sample under test is generally loaded at the centre of the waveguide or as was the case in these measurements, flushed to one end of a quarter-wavelength long sample holder. The latter is done in order to know the exact position of the sample so that accurate values of the phase of the scattering (S-) parameters, S_{11} and S_{21} can be obtained. As the measurements are made at the ends of the waveguide, the correct phases of these parameters can be easily calculated given that the exact distances of the edges of the samples to the ports of the waveguide are known. From these S-parameters, the reflection (Γ) and transmission (T) coefficients can readily be calculated, along with knowledge of the thickness of the sample. Using these coefficients, the complex permittivity and permeability can be readily obtained as given in [14], [16].

5.4.2 Measured Results

The simulated results of the sample in Figure 5.1 were inverted and the ε_{eff} and μ_{eff} results shown in Figure 5.4 and Figure 5.5. Waveguides were used in this research to extract the ε_{eff} and μ_{eff} of the heterogeneous media, the first of which was that carried out at Sheffield University, UK using their 0.35 – 0.53 GHz (or 400 MHz) and 0.75 – 1.12 GHz (or 1 GHz) waveguides, with the former shown in Figure 5.12 and its quarter-wavelength sample holder with the sample shown in Figure 5.13. Note: the use of low frequency waveguides was convenient to measure the structure in Figure 5.1, and also to minimise the errors due to positional uncertainties. The length of each half-section of the 400 MHz RWG = 2215 mm,

length of sample holder = 221 mm $= \lambda/4$ at the lower frequency. The cross-sectional dimensions of these waveguides were the same as the standard ones. The dielectric properties can be obtained from the S-parameters, the thickness of the sample and the distances between the ports and the sample by using the equations in [14]. These waveguides were used to measure the permittivity, ε_r and permeability, μ_r of Perspex to validate the measurement process. The ε_r from the 1 GHz and 400 MHz waveguides were obtained as 2.7 and 2.3 respectively. This difference might be due to the different measurement setup and environment.

For the sample shown in Figure 5.1, these measurements with 10 mm diameter chrome steel ball bearings spaced 13 mm apart and placed in a Rohacell® host, were used to represent scaled-up samples compared to micro-sized inclusions and spacings. A 3 mm thick Rohacell® layer was placed on either side of the structure to ensure the 13 mm unit cell size along each axis. Spray glue was also used in holding the structure together which was necessary given that the samples were vertically mounted. Figure 5.14 shows the simulated and measured S-parameter results which show very good agreement. Simulating this structure at 1 GHz gave an $\varepsilon_{eff} = 2.37$ and $\mu_{eff} = 0.68$, while the measurements gave an $\varepsilon_{eff} = 1.83$ and $\mu_{eff} = 0.76$ from the 400 MHz waveguide and $\varepsilon_{eff} = 1.80$ and $\mu_{eff} = 0.80$ from the 1 GHz waveguide, extracted using the Nicholson-Ross-Weir (NRW) method from the S_{11} and S_{21}. These values show good agreement and corroborate our canonical and simulation analysis.

Figure 5.12: 0.35-0.53 GHz waveguide measurement facility at Sheffield University, UK

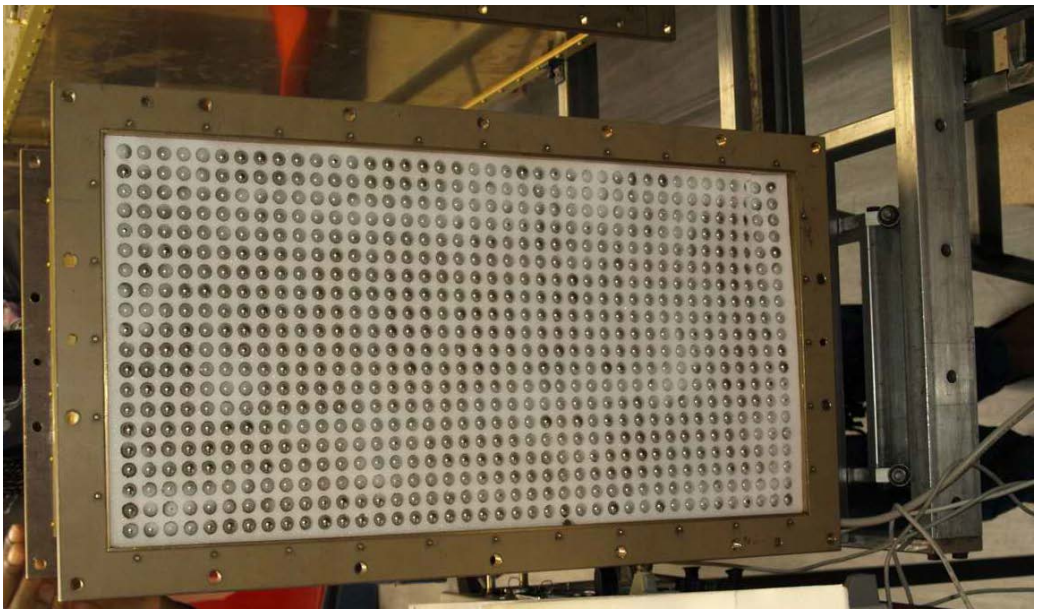

Figure 5.13: One-quarter wavelength sample holder for the 0.35-0.53 GHz waveguide at Sheffield University, UK

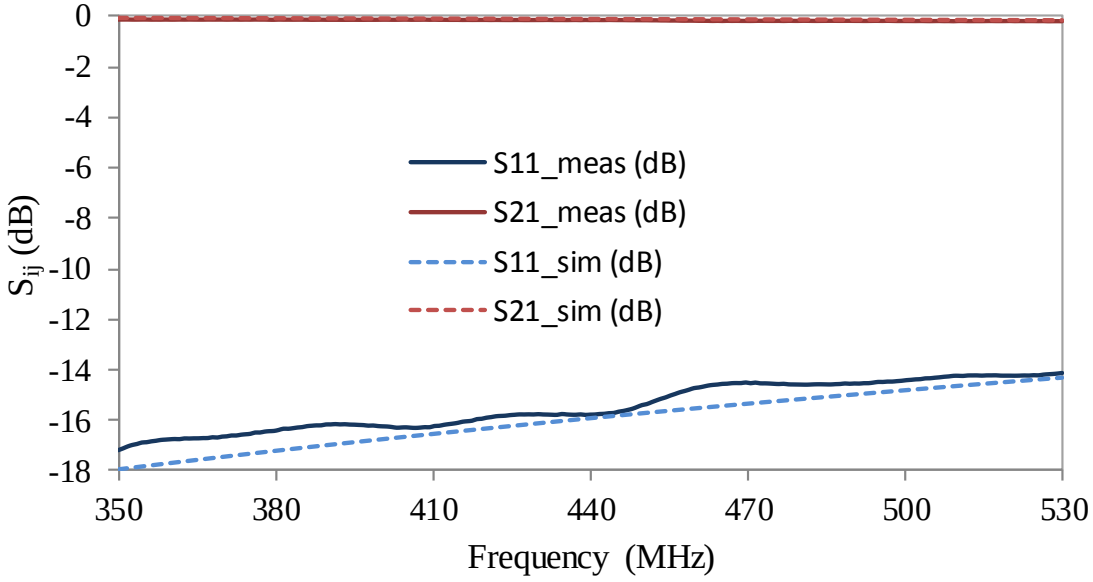

(a)

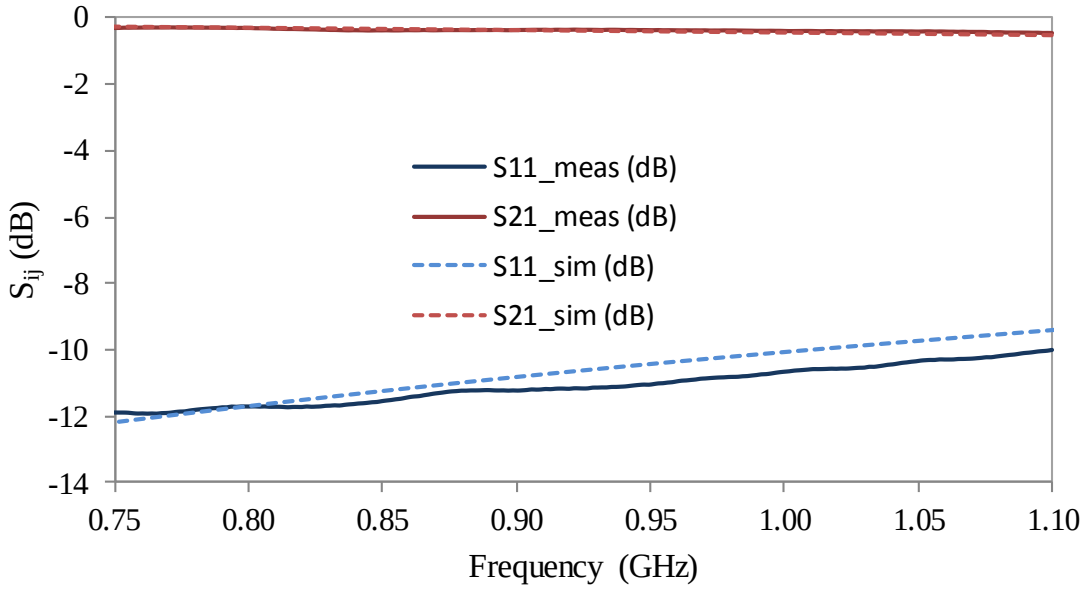

(b)

Figure 5.14: Simulated (dashed) and measured (continuous) S-parameters of 2 layers of balls-in-Rohacell® sample in a (a) 400 GHz waveguide and (b) 1 GHz waveguide

Measured results may be lower as the spheres were not exactly aligned or because of the gap between the outer metal balls and the edge of the waveguide. The delicate nature of the samples used in these waveguide measurements was not easy to manipulate to allow accurate measurements. Additional possible sources of error were:

- The top and bottom covering 3 mm layers were not directly glued to the rest of the structure because the glue was not sticky enough for the weight it has to bear; Sellotape had to be used for the bigger sample
- The bottom corner of the heterogeneous medium cracked due to the weight of the steel balls and so some balls fell off into the waveguide
- The sample holder was not aligned with the transition sections
- The measurement kit was slanting due to support mechanism/method
- The distances between the edges of the balls at one end and the wall of the waveguide were not equal along all four edges
- There was a non-perfect fit of the sample holder to the rest of the waveguide structure.

5.5 Microstrip Ring Resonators

The frequency response of microstrip resonators is partly dependent on the EM properties of the substrates underneath or on top of it. The ring resonator was originally introduced by Troughton for the measurement of dispersion and wavelengths in microstrip transmission lines [21]. This concept is explored in this section using the line capacitances of the resonator elements to determine the effective permittivity of various materials.

5.5.1 Theory

Based on the work reported in [22–25], the effective permittivity of a material under test (MUT) can be determined from the ratio of the capacitances between an unloaded and loaded microstrip line. This concept is based on the "Variational Method for the analysis of microstrip lines" initially discussed in [25] for a microstrip line on a single layer and was extended to when the microstrip line had multiple dielectric layers under or on top of it. With the complete equations governing this multi-layered microstrip line developed in [24], the authors of [22], [26] applied the principles to a microstrip ring resonator, see Figure 5.15 with multi-layered substrates as shown in Figure 5.16. The width of the ring is the same as the width of the transmission line.

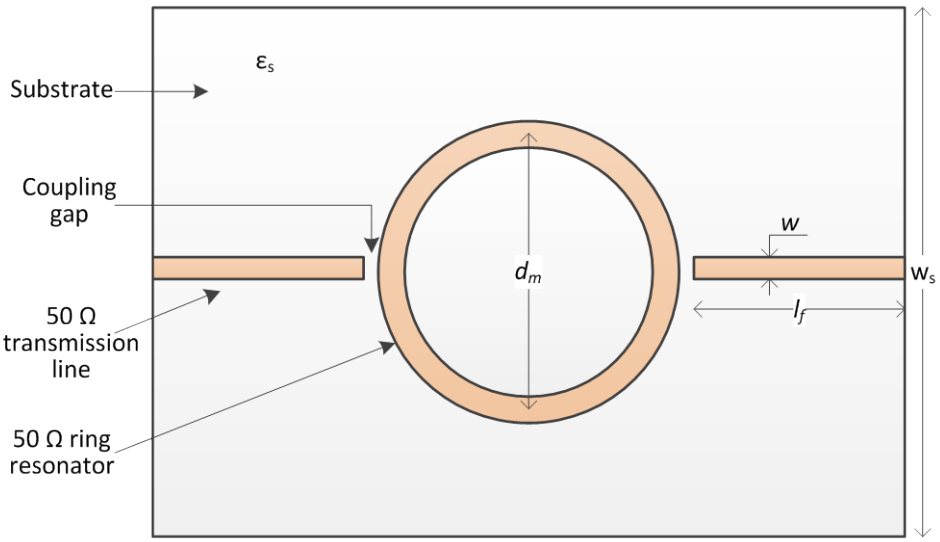

Figure 5.15: Top view of a microstrip ring resonator on substrate of permittivity, ε_s

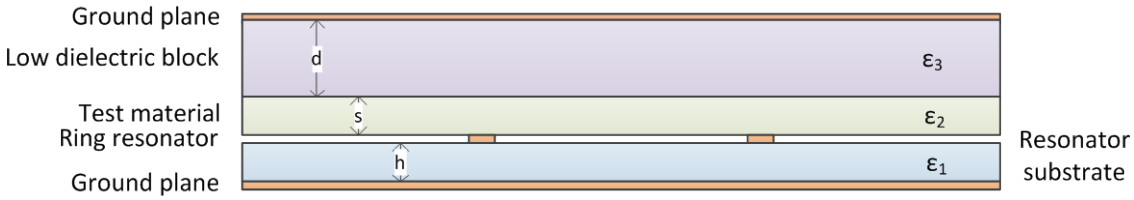

Figure 5.16: Side view of multi-layered microstrip ring resonator (not drawn to scale). h, s and d are the thicknesses of the resonator substrate, test material and support (low) dielectric layers respectively; ε_1, ε_2 and ε_3 are their respective relative (real) permittivities.

The Variational Method of calculating the line capacitances of a multi-layered microstrip ring were used to compute the effective permittivity of the structure, and hence the resonant frequencies using known dielectrics. It is well known that the dielectric loading and the length of a microstrip line affects its resonant frequency. With measurements, the thicknesses of the dielectric layers, the dimensions of the ring and the resonant frequencies can easily be measured and from there, the permittivity of the dielectric layer with unknown permittivity can be calculated. The steps involved in this process are as listed below:

1. The resonant frequency of the ring resonator alone (without the top layers) can be calculated using:

$$\pi d_m = n\lambda_g = \frac{n\lambda_0}{\sqrt{\varepsilon_{ef}}} \tag{5-3}$$

   where n = 1, 2, 3, …; d_m = mean diameter of the ring; λ_0 and λ_g are the free space and guided wavelengths and ε_{ef} is the effective permittivity of the substrate seen by the resonator. It is necessary for the width of the ring to be thin such that the ratio of the inner radius to the outer radius to be approximately unity for equation (5-3) to apply as is, otherwise it has to be modified as in [27]. The calculated resonant frequency with known dielectrics can be compared with the measured or simulated values. Measured or simulated frequencies can therefore be used to calculate ε_{ef}.
2. The Variational Method for expressing the capacitance of the line, ignoring the line thickness for very thin strips, in the Fourier-transformed coordinates, referred to as the β coordinates [22], [24], [25] is given in equation (5-4):

$$\frac{1}{C} = \frac{1}{\pi Q^2 \varepsilon_0} \int_0^\infty [f(\beta)]^2 g(\beta) d\beta \tag{5-4}$$

where ε_0 is the permittivity of free space. For a 3-layer microstrip line,

$$g(\beta) = \frac{\varepsilon_3 D + \varepsilon_2 S}{|\beta|[\varepsilon_3 D(\varepsilon_1 H + \varepsilon_2 S) + \varepsilon_2(\varepsilon_2 + \varepsilon_1 HS)]} \tag{5-5}$$

where $H = \coth(|\beta|h)$, $D = \coth(|\beta|d)$, $S = \coth(|\beta|s)$, and

$$\frac{f(\beta)}{Q} = \frac{8}{5}\left\{\frac{\sin(\beta w/2)}{\beta w/2}\right\} + \frac{12}{5(\beta w/2)^2}\cdot\left\{\cos(\beta w/2) - 2\frac{\sin(\beta w/2)}{\beta w/2} + \frac{\sin^2(\beta w/4)}{(\beta w/4)^2}\right\}$$

where $f(\beta)$, the charge density, is the Fourier transform of

$$f(x) = \begin{cases} 1 + \left|\frac{2x}{w}\right|^3, & -\frac{w}{2} \le x \le \frac{w}{2} \\ 0, & \text{otherwise} \end{cases}$$

such that $Q \equiv \int_{-\infty}^{+\infty} f(x)dx$, is the total charge over the line and w is the width of the line. If the line thickness is significant, the integral in equation (5-4) includes a third term given by equation (5-6) as

$$\tilde{h}(\beta) = \frac{1}{2}\left\{1 + \frac{\sin d(|\beta|h - |\beta|t)}{\sin d(|\beta|h)}\right\} \tag{5-6}$$

where t is the thickness of the line.

3. Since the thicknesses of all three layers are known, the line capacitance of the unloaded line, C_0 can be calculated from equation (5-4) using $\varepsilon_1 = \varepsilon_2 = \varepsilon_3 = 1$.
4. A range of values for ε_{ef} is generated for different values of ε_2 by calculating the line capacitances of the loaded line, C for each ε_2 with the known values of ε_1, ε_3, h, s and d. These can be used to plot a graph of ε_{ef} against ε_2, an example of which is shown in Figure 5.17. Data used: $h = 1.27$ mm, $s = 0.83$ mm, $d = 6$ mm, $w = 1.24$ mm, $d_m = 30.16$ mm, $\varepsilon_1 = 9.2$ (tan $\delta = 0.0022$), $\varepsilon_3 = 1.04$ (tan $\delta = 0.00017$). ε_{ef} is calculated using $\varepsilon_{ef} = C/C_0$, given that the free space and guided wavelengths, effective permittivities and line capacitances of a loaded and unloaded line for non-magnetic materials are related by equation (5-7)

$$\frac{\lambda}{\lambda_0} = \left(\frac{C_0}{C}\right)^{1/2} = \left(\frac{1}{\varepsilon_{ef}}\right)^{1/2} \tag{5-7}$$

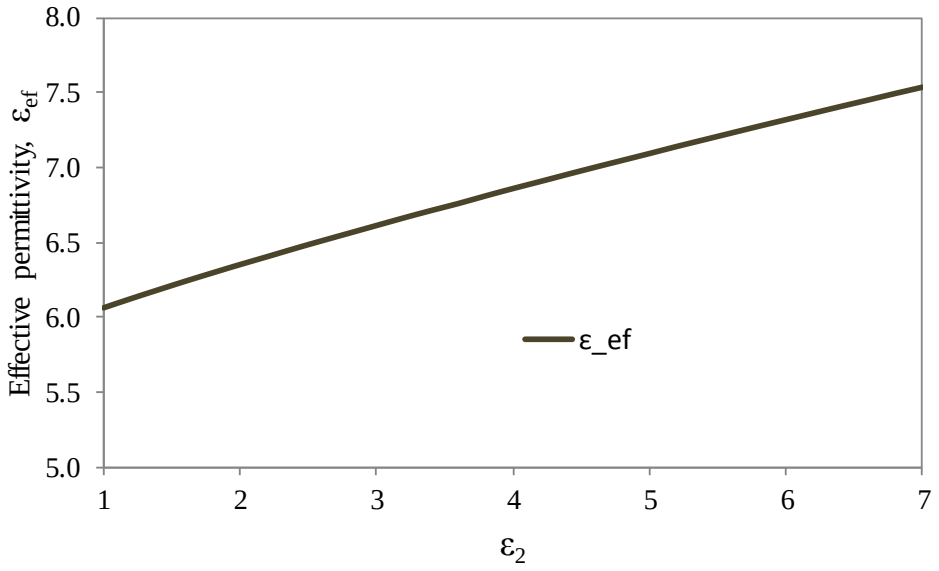

Figure 5.17: Plot of effective permittivity, ε_{ef} against ε_2 using equations (5-4) – (5-7)

5. The effective permittivity, ε_{ef0} of the resonator without the test material is calculated using $\varepsilon_2 = \varepsilon_3 = 1$ and $d, s \to \infty$.
6. The resonator is connected to the network analyser and the resonant frequency without the test material, f_{r0}, and with the test material, f_{r1} are measured. By using equation (5-8):

$$\pi d_m = n\lambda_g = \frac{n\lambda_0}{\sqrt{\varepsilon_{ef}}} = \frac{nc_0}{f_{r0}\sqrt{\varepsilon_{ef0}}} = \frac{nc_0}{f_{r1}\sqrt{\varepsilon_{ef1}}} \tag{5-8}$$

   the effective permittivity with the test material, ε_{ef1}, can be calculated from (5-9):

$$\varepsilon_{ef1} = \varepsilon_{ef0}\left(\frac{f_{r0}}{f_{r1}}\right)^2 \tag{5-9}$$

7. By searching the plot of ε_{ef} against ε_2 for this calculated value of ε_{ef1}, the unknown value of ε_2 can be found. The calculations here were carried out using Mathcad.

The complete derivation of these expressions are given in [24] and were obtained by taking the Fourier transform of the Poisson's equation relating the potential distribution across the cross-sectional area of a microstrip line to its charge density distribution and the permittivity of the line. It should be noted that the Variational Method is based on the static field theory and so it may be necessary to extrapolate the results obtained to zero frequency as shown in

[28]. However, the method has been shown to have high levels of accuracy comparing calculated and measured values for frequencies as high as 4 GHz [24].

The main factors that determine the characterisation accuracy of the ring resonator method are the coupling gap, the substrate width, w_s, the feed line lengths, l_f and the dielectric constant, ε_s of the material on which the ring is etched. Reference [28] presents an extensive analysis on these factors, concluding that a relatively wide coupling gap and a short substrate width causes an unstable resonator; that the extracted effective permittivity tends to increase slightly as the feed line length increases; and that a high permittivity substrate, also used in [22], is needed to cover a wider range of frequencies. These studies were used to design the ring resonator used in this research – see Figure 5.19. The grooves (shown labelled 2 in the inset) below the connectors to the resonator were to allow the vertical movement of the resonator in order to carry out measurements of the samples placed under the resonator substrate.

5.5.2 Simulated Ring Resonator Results

The ring resonator (see Figure 5.15) was simulated to validate the extraction of ε_r. Data used: the mean diameter, $d_m = 30.16$ mm; $\varepsilon_1 = 9.2$ (tan $\delta = 0.0022$); width of transmission line and ring; $w = 1.24$ mm; coupling gap = 0.2 mm, substrate height; $h = 1.27$ mm and width, $w_s = 62$ mm. Using equation (5-4), the unloaded line (when $\varepsilon_1 = \varepsilon_2 = \varepsilon_3 = 0$ and $d, s = \infty$) capacitance, $C_0 = 2.95\varepsilon_0$. The resonant frequency, $f_{r0} = 1.18$ MHz, which gives $\varepsilon_{ef0} = 7.45$ using equation (5-8). Next, the resonator was set up as in Figure 5.16, with $\varepsilon_2 = 4.4$ (tan $\delta = 0.02$), $\varepsilon_3 = 1.04$ (tan $\delta = 0.00017$), $s = 0.83$ mm, $d = 6$ mm. The simulation results of the ring resonator alone and in the 3-layered configuration with the above parameters are shown in Figure 5.18 and Figure 5.19, which also shows the different harmonic resonant frequencies at $n = 1, 2, 3, \ldots$, of the ring resonator. The first resonant frequency (with $n = 1$), is used for the calculations.

With the 3-layered structure (as in Figure 5.16), the simulated resonant frequency, $f_{r1} = 1.11$ GHz which implies $\varepsilon_{ef1} = 7.48$ using equation (5-9) – the equation for the method examined here. By calculating C/C_0 with the known constant values of ε_1 and ε_3, such that $C/C_0 = \varepsilon_{ef1} = 7.40$, ε_2 was obtained as 3.99. This value of ε_2 is ~10.25% lower than the simulated value of 4.4 which was deemed less accurate than ideal.

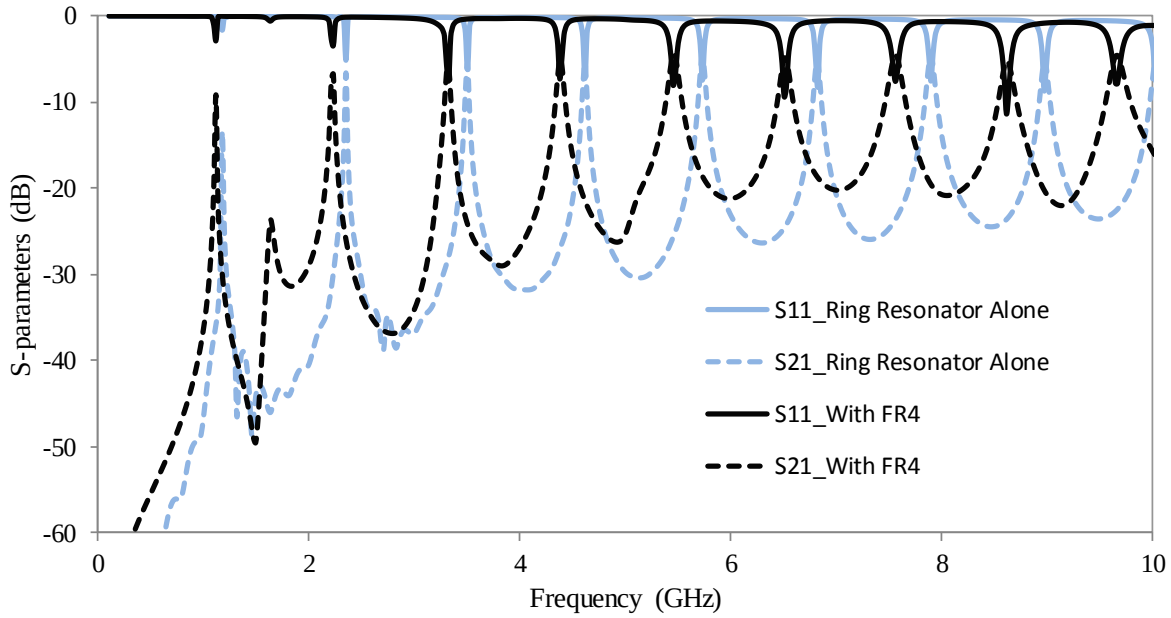

Figure 5.18: S_{11} (continuous) and S_{21} (dashed) of the 30.16 mm ring resonator alone (thin lines) and with 3 layers (thick lines) from simulations

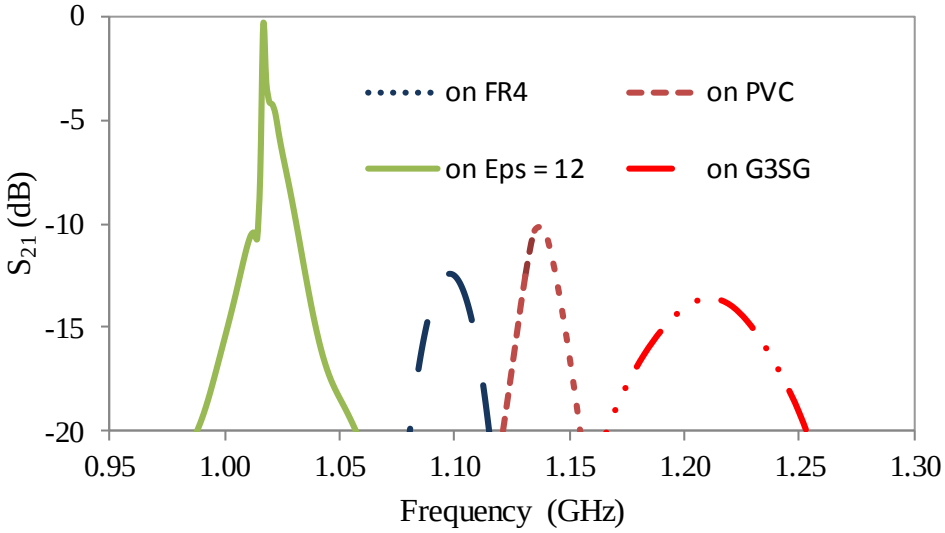

Figure 5.19: Simulated S_{21} of the ring resonator with different test samples on top as in Figure 5.16

In order to test the accuracy of the results obtained using the Variational Method in [24], the calculated effective permittivity of a stand-alone resonator, also referred to as a 1-layer structure in Table 5.1 (that is, without the upper layers nor the ground plane) and a 3-layered ring resonator was compared with that obtained using the well-known conformal mapping method [29–31], the well-known equation for effective permittivity of a microstrip line in [32] and equations (5-3) and (5-9). The conformal mapping method is based on static field theory

and can be used to obtain the effective permittivity of a microstrip line with multi-layered substrate. The results are listed in Table 5.1 which shows significant variation between methods, with the results from [29] and [32] showing good agreement and are well-established methods used in the literature. Although the geometry in [24] and [29] differ by the top ground plane, it has been shown in [24] that the effect of shielding is negligible for $d/h > 5$, as the radiation from the ring attenuates with distance.

Table 5.1: Effective permittivity values of a simulated microstrip line using different methods

Type of Structure	Variational Method [24]	Conformal Mapping [29]	Effective Permittivity [32]	Equation (5-3) [22]	Equation (5-9) [24]
1 layer	6.64	6.85	6.80	7.45	-
3 layers	7.58	7.49	-	8.11	7.48

Table 5.1 shows disparity between the different methods for calculating the effective permittivity seen by a microstrip line. Therefore, an option of rectifying this may be by multiplying ε_{ef1} by the ratio of the ε_{eff} from [32] to that from [24] for the single layer case, say k_e, that is, by $k_e = 6.80/6.64 = 1.02$, to give a new $\varepsilon_{ef1} = 7.64$, which inverts to give $\varepsilon_2 = 4.72$, a closer value to that simulated (although 7.27% higher). In order to test the accuracy/consistency of this hypothesis, other test materials were simulated: (i) $\varepsilon_2 = 2.91$ ($\tan\delta = 0.025$) which gave an $f_{r1} = 1.14$ GHz and (ii) $\varepsilon_2 = 12$ ($\tan\delta = 0.001$) which gave an $f_{r1} = 1.02$ GHz. The modified extraction process gave $\varepsilon_2 = 3.21$ and 11.77 respectively. These extracted values were closer to the known values – 4.40 and 12.0 respectively, than those obtained using the exact method in [22].

5.5.3 Measurements with Ring Resonator

The ring resonator was constructed and measured as in the configuration in Figure 5.16 and Figure 5.20 with different dielectrics in order to compare with the simulation results. The same dimensions as in Section 5.5.2 were used here. Pressure was applied over the sustrates by pressing down manually over the structure to minimise any air gaps that may be present between the different layers.

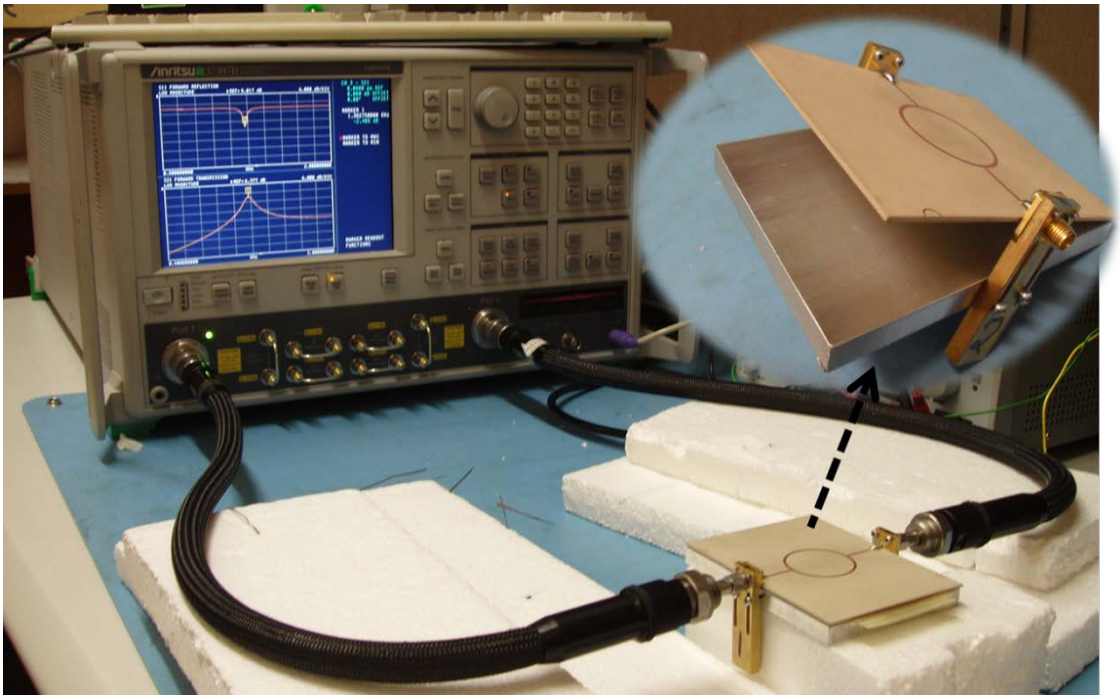

Figure 5.20: Measurement setup showing ring resonator. Inset: ring resonator on adjustable ground plane. No top layers shown as in Figure 5.13.

For the measurements, $f_{r0} = 1.15$ GHz, the mean diameter, $d_m = 30.18$ mm, substrate permittivity, $\varepsilon_1 = 10.2$, and line width, $w = 1.29$ mm, substrate length $\cong 80$ mm, see Figure 5.15. For the calculations, the thickness of the top low dielectric material, d was taken as 50 mm although it was much greater, > 10 cm. Figure 5.21 shows the measured S_{21} for various combinations of materials with known permittivities – see note below. The scale of the S_{21} axis was restricted to -18dB in order to emphasize the resonant positions of the different materials. The materials represented by the various suffixes in Figure 5.21, replaced the middle material with thickness, s and permittivity, ε_2 in Figure 5.16.

Note:

- Suffix 'Rgrs' represents the Rogers 3210 material with $\varepsilon_{Rgrs} = 10.143 - 10.361$, tan $\delta = 0.0025 - 0.0029$ (from data sheet),
- 'FR4'represents the FR4 epoxy glass laminate with $\varepsilon_{FR4} \approx 4.4$,
- '3GTS' represents 3 GTS® metal-free layers stacked with $\varepsilon_{GTS} \approx 3$,
- 'Poly' represents thin polystyrene with $\varepsilon_{Poly} = 1 - 2.55$ (from literature [33]),
- 'Rhcl' represents Rohacell® with $\varepsilon_r \approx 1.04 - 1.10$, tan $\delta = 0.0002 - 0.0041$ (from data sheet),

- 'G*n*SG' represents the multi-layered sample shown in Figure 5.3 where 'G' represents the 110 µm thick GTS® material, 'S' is the 180 µm thick double-sided etched layer, that is, with Copper etched on both sides of the GTS® material and '*n*' the number of these double-sided ('S') layers. 'G1SG' represents one double-sided layer insulated on either side by the GTS® material.

From the resonant frequencies in Figure 5.21, it can be inferred that the ε_{eff} for the G*n*SG samples seen by the resonator is less than that for the FR4 sample ($\varepsilon_r \approx 4.4$) but greater than that of Polystyrene, ($\varepsilon_r \approx$ 1-2.5). A summary of the results from the simulations are given in Table 5.2. It can also be seen that the insertion loss for the heterogeneous samples, G*n*SG were comparable to that of the homogenous samples measured. The rather low insertion loss for the Rgrs sample may be due to ring resonator having been designed for and etched on the same substrate. Using equations (5-4) to (5-9), the unloaded line capacitance, $C_0 = 2.94\varepsilon_0$, while the effective permittivity with the top layers, $\varepsilon_{ef0} = 7.53$. Following the steps outlined earlier, the extracted values of ε_2 have been calculated and are also shown in Table 5.2. It can be seen from the table that only 3 of the materials (FR4, Polystyrene and Rohacell®) tested were within the range of their values given in their data sheets or from literature.

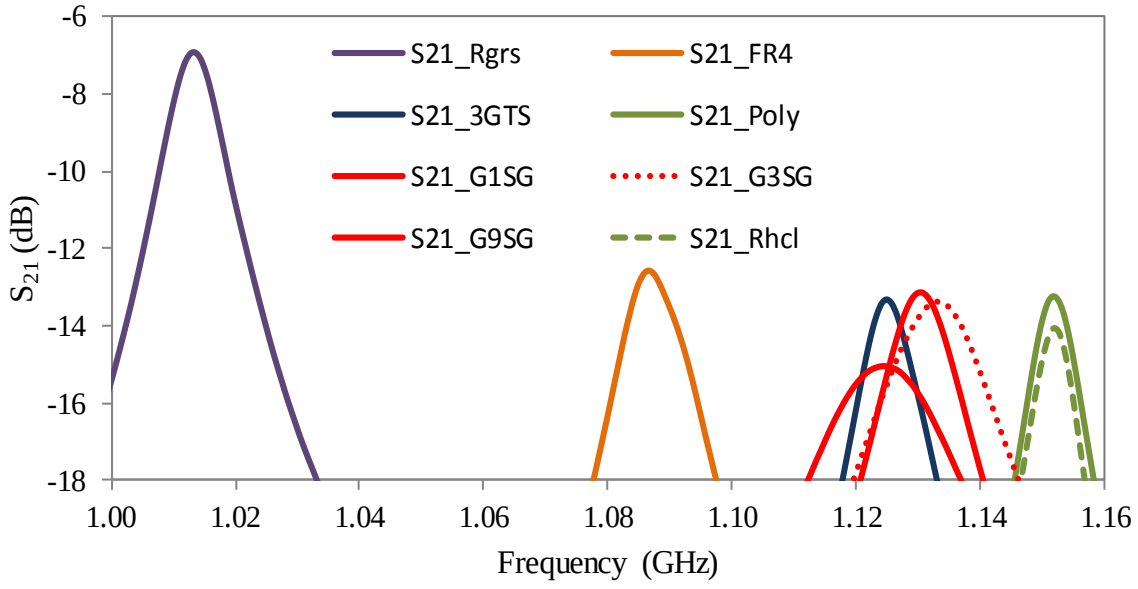

Figure 5.21: S_{21} of the ring resonator with different test samples placed on it and a top layer of a thick slab of expanded Polystyrene

Table 5.2: Summary of measured and extracted results for the ring resonator measurements with different dielectric materials

Material	Known ε_2	Thickness, s (mm)	Measured resonant frequency, f_{r1} (GHz)	C/C_0 ($\times \varepsilon_0$) equation (5-7)	Extracted ε_2
Rgrs	10.2	1.27	1.02	8.80	8.11
FR4	~ 4.4	1.50	1.08	7.84	4.30
3GTS	~ 3.0	0.33	1.12	7.23	3.73
Poly	1.0-2.5	1.74	1.15	6.89	1.32
Rhcl	1.04-1.10	2.74	1.15	6.89	1.30
G1SG	-	0.40	1.13	7.15	2.93
G3SG	-	0.76	1.13	7.12	2.22
G9SG	-	1.85	1.12	7.24	2.30

In terms of the polarisation of the E-field, the closest geometry of the plane wave simulations to these measurements is that shown in Figure 5.7 (b) which gave an $\varepsilon_{eff} = 4.43$. The low values of the heterogeneous samples, G*n*SG, may be due to the diamagnetic nature of the samples as shown in Figure 5.6 and Figure 5.8. With the main reason for exploring this method being for extracting the ε_{eff} of the heterogeneous layered samples, it can be concluded that this ring resonator method may not have been a suitable solution for the heterogeneous samples, G*n*SG as the extracted values were significantly below 4.43 as obtained from the plane wave simulations stated in Section 5.2.3.

The difference in the extracted ε_2 from the Variational Method and the actual simulated value may be due to "mutual inductance" given that the length of the ring is not at least 5 times the operating wavelength [21]. However, when this was the case in simulations, the increased size of the ring did not provide better results. Another possible reason for the discrepancy between the known and extracted values may be that the samples were not thin enough and/or may not have a low enough dielectric constant to ensure little variations in the resonant frequencies of the ring with and without the samples under test [22], [34]. Some of the published work bypassed the use of the Variational Methods by etching the ring resonator directly on the sample [26], [28], [35], which would not be practical in this case as the surface of the sample has copper squares etched on both sides and it would not be possible to

measure the resonant frequency for such a thin 'one layer' sample of GTS® material placed directly on a ground plane.

In order to understand why the extracted ε_{eff} of the G*n*SG sample did not agree with its value in Section 5.2.3, further simulations were carried out. These led to the understanding that because the sizes of the coupling gap between the resonator and the feed line and the width of the ring and transmission lines were comparable to those of the etched squares, the positioning of these squares were crucial in deciding the f_{r1} and thus the ε_{eff}. This was because these lines were not 'seeing' an effectively homogenous material underneath. Different geometries were simulated to check if more accurate values of ε_{eff} could be obtained such as placing all the 3 layers ($\varepsilon_1, \varepsilon_2, \varepsilon_3$) under the resonator; removing the top ground plane and using a 2-layer structure under the resonator without a top dielectric, but these modifications showed no advantage.

Other measurement techniques include the microstrip line methods [36], [37], open-end coplanar waveguide method [38]. Different methods can be combined to form another one such as the waveguide dielectric resonator [39], and the complementary frequency selective surface (CFSS) resonator [40], [41].

5.6 Conclusions

In this chapter, the fabrication techniques used in the construction of the samples used in this thesis have been explained. Three samples have been created in this research; one of these was an array of metallic spheres arranged uniformly within a low dielectric material, Rohacell®. One and two layers of this structure were measured with a 0.35-0.53 GHz and 0.75-1.12 GHz rectangular waveguide. The second structure was a 110-µm thick low permittivity laminate material, GTS® with 35-µm thick Copper squares etched on either side and stacked to create a composite with thickness in the 1–2 mm range, depending on the number of layers. Two metal-free layers of the laminate were placed on either side of the layered structure to ensure that the metal cuboids were not touching the resonator. The third structure was a very thin sample of metallic nano-film made from porous oxides. The fabricational resources available within the School have limited the range of samples that can be made. Plane wave simulations have been used to estimate the ε_{eff} and μ_{eff} of the first two samples. As the simulations have been shown to have good agreement with the canonical equations, this served as a basis for the results to be obtained from the measurement techniques examined. The G*n*SG sample was shown to have anisotropic and diamagnetic properties due to the non-symmetric nature of the metallic cuboids and the Copper inclusions respectively, thus yielding permittivity and permeability tensors.

Various methods of measuring the dielectric properties of the heterogeneous structures have been considered – the SPDR, the Rectangular Waveguide (RWG) and the Microstrip Ring Resonator (MRR). The results from these measurement methods have been presented and compared with the results from simulations for the RWG and MRR measurement techniques. The challenges involved with these techniques have also been highlighted. These methods were chosen as they are commonly used and were readily available at the School.

The SPDR gave good results for homogenous substrates – Perspex; however, when used to measure the G*n*SG sample, negative ε_{eff} values were obtained as the frequency shift from an empty resonator was upward after loading the resonator with the sample. It was concluded that this was not a suitable method for the samples created here especially those with metallic inclusions.

Thus far, the analytical and simulation based research has been verified with waveguide measurements for the sample with the array of metallic balls in a Rohacell® host. Waveguides

become harder to use accurately as the frequency increases as the positional errors become proportionately larger. It was also beyond the capabilities of this project to fabricate a physically durable sample to be placed in a smaller waveguide as discussed in Section 5.2.3. Further work is required for measuring the G*n*SG sample.

The ring resonator was investigated and was a reasonable measurement method; however, the extracted results did not agree well with the known ε_r values of the homogeneous and G*n*SG samples, both from the simulated and measured results. For the G*n*SG sample, it can be concluded that with the size of the inclusions and the spacing being comparable to the ring width and the coupling gap (between the ring and the transmission line), if the size of the inclusions were further reduced, this may present a suitable method. Increasing the ring width makes the extraction process more complex.

It can thus be concluded that although other measurement methods need to explored, the waveguide measurement technique was the best of the three for measuring the samples created for this thesis. It is expected that the dielectric properties will be easier to measure if the metallic inclusions are reduced in size – which will be investigated in future work. The simulated and measured performances of a rectangular patch antenna with the heterogeneous sample (G*n*SG) as substrates are presented in Chapter 6.

5.7 References

[1] C. C. Njoku, W. G. Whittow, and J. C. Vardaxoglou, "Comparative study of nanomaterials' effective properties using canonical formations," in *Loughborough Antennas & Propagation Conference (LAPC)*, 2010, pp. 413–416.

[2] C. C. Njoku, W. G. Whittow, and Y. C. Vardaxoglou, "Simulation methodology for synthesis of antenna substrates with micro-scale inclusions," *IEEE Transactions on Antennas and Propagation*, vol. 60, no. 5, pp. 2194–2202, 2012.

[3] M. S. Schmidt, A. Boisen, and J. Hubner, "Towards easily reproducible nano-structured SERS substrates," in *IEEE Sensors*, 2009, pp. 1763–1767.

[4] J. Rao, H. Zou, R. R. A. Syms, E. Cheng, and C. Liu, "Fabrication of 2D silicon nano-mold based on sidewall transfer," *Micro & Nano Letters*, vol. 6, no. 1, pp. 29–33, 2011.

[5] U. Cvelbar, M. Mozetic, and M. Klanjsek-Gunde, "Selective oxygen plasma etching of coatings," *IEEE Transactions on Plasma Science*, vol. 33, no. 2, pp. 236–237, 2005.

[6] A. Botman, J. J. L. Mulders, and C. W. Hagen, "Creating pure nanostructures from electron-beam-induced deposition using purification techniques: a technology perspective," *Nanotechnology*, vol. 20, no. 37, Sep. 2009.

[7] A. Sihvola, *Electromagnetic Mixing Formulas and Applications*. London: IET, 1999.

[8] J. Krupka, R. G. Geyer, J. Baker-Jarvis, and C. J., "Measurements of the complex permittivity of microwave circuit board substrates using split dielectric resonator and reentrant cavity techniques," in *Seventh International Conference on Dielectric Materials, Measurements and Applications*, 1996, vol. 1996, pp. 21–24.

[9] J. Krupka, A. P. Gregory, O. C. Rochard, R. N. Clarke, B. Riddle, and J. Baker-Jarvis, "Uncertainty of complex permittivity measurements by split-post dielectric resonator technique," *Journal of the European Ceramic Society*, vol. 21, pp. 2673–2676, 2001.

[10] J. Krupka, K. Derzakowski, and J. G. Hartnett, "Measurements of the complex permittivity and the complex permeability of low and medium loss isotropic and uniaxially anisotropic metamaterials at microwave frequencies," *Measurement Science and Technology*, vol. 20, Oct. 2009.

[11] F. Thompson, "Permittivity measurements in solids, powders, and liquids," *American Journal of Physics*, vol. 73, no. 8, pp. 787–789, 2005.

[12] J. Krupka, W. Gwarek, N. Kwietniewski, and J. G. Hartnett, "Measurements of planar metal – dielectric structures using split-post dielectric resonators," *IEEE Transactions on Microwave Theory and Techniques*, vol. 58, no. 12, pp. 3511–3518, 2010.

[13] J. Krupka, "Measurement of the complex permittivity of metal nanoislands and the surface resistance of thin conducting films at microwave frequencies," *Measurement Science and Technology*, vol. 19, pp. 1–8, Jun. 2008.

[14] W. B. Weir, “Automatic measurement of complex dielectric constant and permeability at microwave frequencies,” *Proceedings of the IEEE*, vol. 62, no. 1, pp. 33–36, 1974.

[15] A. M. Nicolson and G. F. Ross, “Measurement of the intrinsic properties of materials by time-domain techniques,” *Instrumentation and Measurement, IEEE Transactions on*, vol. 19, no. 4, pp. 377–382, 1970.

[16] J. Baker-Jarvis, E. J. Vanzura, and W. A. Kissick, “Improved technique for determining complex permittivity with the transmission/reflection method,” *IEEE Transactions on Microwave Theory and Techniques*, vol. 38, no. 8, pp. 1096–1103, Aug. 1990.

[17] M. N. Afsar, A. M. Ayala, N. Al-Moayed, and M. Obol, “Microwave permittivity and permeability properties and microwave reflections of ferrite powders,” in *IEEE Instrumentation and Measurement Technology Conference*, 2009, pp. 274–278.

[18] U. C. Hasar and C. R. Westgate, “A broadband and stable method for unique complex permittivity determination of low-loss materials,” *IEEE Transactions on Microwave Theory and Techniques*, vol. 57, no. 2, pp. 471–477, Feb. 2009.

[19] C. A. Balanis, *Advanced Engineering Electromagnetics*, 2nd ed. New York: Chichester: Wiley, 1989.

[20] B.-K. Chung, “Dielectric constant measurement for thin material at microwave frequencies,” *Progress In Electromagnetics Research*, vol. 75, pp. 239–252, 2007.

[21] P. Troughton, “Measurement techniques in microstrip,” *Electronics Letters*, vol. 5, no. 2, pp. 25–26, 1969.

[22] P. A. Bernard and J. M. Gautray, “Measurement of dielectric constant using a microstrip ring resonator,” *IEEE Transactions on Microwave Theory and Techniques*, vol. 39, no. 3, pp. 592–595, 1991.

[23] H. Suzuki and T. Hotchi, “Microwave measurement of complex permittivity of a sheet material under test sandwiched between sheet metal and a calibrated stripline resonator,” in *IEEE International Instrumentation and Measurement Technology Conference*, 2008.

[24] E. Yamashita, “Variational method for the analysis of microstrip-like transmission lines,” *IEEE Transactions on Microwave Theory and Techniques*, vol. MTT-16, no. 8, pp. 529–535, 1968.

[25] E. Yamashita and R. Mittra, “Variational method for the analysis of microstrip lines,” *IEEE Transactions on Microwave Theory and Techniques*, vol. MTT-16, no. 4, pp. 251–256, 1968.

[26] R. Hopkins, “The Microstrip Ring Resonator for Characterising Microwave Materials: MPhil to PhD,” University of Surrey, UK, 2006.

[27] M. W. Hosking, B. A. Tonkin, Y. G. Proykova, A. Hewitt, N. M. Alford, T. W. Button, and S. J. Penn, “Measurements of material and circuit properties using a microstrip ring-resonator circuit on zirconia at 77K,” in *23rd European Microwave Conference*, 1993, pp. 558–561.

[28] D. Thompson, M. Falah, X. Fang, and D. Linton, “Dielectric characterization using the microstrip resonator method,” in *High Frequency Postgraduate Student Colloquium*, 2003, pp. 23–26.

[29] J. Svacina, “A simple quasi-static determination of basic parameters of multilayer microstrip and coplanar waveguide,” *IEEE Microwave and Guided Wave Letters*, vol. 2, no. 10, pp. 385–387, 1992.

[30] Y. Wu, Z. Tang, Y. Xu, B. Zhang, and X. He, “Measuring complex permeability of ferromagnetic thin film up to 10GHz,” *Progress In Electromagnetics Research Letters*, vol. 9, pp. 139–145, 2009.

[31] H. A. Wheeler, “Transmission-line properties of parallel wide strips by a conformal-mapping approximation,” *IEEE Transactions on Microwave Theory and Techniques*, no. 3, pp. 280–289, 1964.

[32] T. C. Edwards, *Foundations of Microstrip Circuit Design*, 2nd ed. 1981.

[33] I. Waldron, S. N. Makarov, S. Biederman, and R. Ludwig, “Suspended ring resonator for dielectric constant measurement of foams,” *IEEE Microwave and Wireless Components Letters*, vol. 16, no. 9, pp. 496–498, 2006.

[34] K. Sarabandi and E. S. Li, “Microstrip ring resonator for soil moisture measurements,” *IEEE Transactions on Geoscience and Remote Sensing*, vol. 35, no. 5, pp. 1223–1231, 1997.

[35] J.-M. Heinola, P. Silventoinen, K. Latti, M. Kettunen, and J.-P. Strom, “Determination of dielectric constant and dissipation factor of a printed circuit board material using a microstrip ring resonator structure,” in *15th International Conference on Microwaves, Radar and Wireless Communications*, 2004, pp. 202–205.

[36] A. M. El-Bakly, “Optimization Study of the Stripline Resonator Technique for Dielectric Characterization,” PhD Thesis, Virginia Polytechnic Institute and State University, USA, 1999.

[37] W. Barry, “A Broad-Band, Automated, Stripline Technique for the Simultaneous Measurement of Complex Permittivity and Permeability,” *IEEE Transactions on Microwave Theory and Techniques*, vol. 34, no. 1, pp. 80–84, Jan. 1986.

[38] J. Hinojosa, “Dielectric permittivity measuring technique of film-shaped materials at low microwave frequencies from open-end coplanar waveguide,” *Progress In Electromagnetics Research C*, vol. 5, pp. 57–70, 2008.

[39] J. Sheen, “Microwave dielectric properties measurements using the waveguide reflection dielectric resonator,” in *IEEE Instrumentation & Measurement Technology Conference (IMTC)*, 2007, pp. 1–4.

[40] D. S. Lockyer, J. C. Vardaxoglou, and R. A. Simpkin, “Complementary frequency selective surfaces,” *IEE Proceedings - Microwaves, Antennas and Propagation*, vol. 147, no. 6, pp. 501–507, 2000.

[41] C. C. Njoku, Y. C. Vardaxoglou, and W. G. Whittow, “Complementary frequency selective surfaces in a waveguide simulator,” in *European Conference on Antennas and Propagation (EuCAP)*, 2013.

Chapter 6. Heterogeneous Materials as Substrates for Patch Antennas

6.1 Introduction

Extensive research [1–4] has been considered on moving away from using standard substrates in different antenna systems to using more user-defined substrates for advanced applications. These includes the use of magnetic metamaterials in order to miniaturise and improve the performance of the antenna [1], [5], [6]; using textured dielectrics to broaden the bandwidth of the antenna [2], [3], [7–9]; and creating dual resonances in the antenna [10]. The antenna itself, such as a patch antenna can be made from an array of small patterned metal patches in order to achieve the required antenna performance such as broad bandwidth and high gain [11], [12]. These studies show that examining the behaviour of antennas when placed on artificial dielectrics, especially those containing metallic inclusions, is important in order to understand how the antenna performance can be improved.

For further confirmation of the effective permittivity results obtained from the canonical equations (in Chapter 2), the simulation-inversion process (in Chapters 3 and 4) and the measurements (in Chapter 5), a patch antenna was used in this chapter. This also extends the results from an infinite medium to a finite medium and places the material in close proximity to the source. Here, an important part of a typical antenna system – the substrate (on which the radiating part of the antenna is etched or printed) is altered by replacing the homogenous substrate with a heterogeneous one in order to understand how this heterogeneity may influence the performance of the antenna. This also introduces the concept of how a heterogeneous material can be used in microwave applications to verify the effective permittivity, ε_{eff}.

The patch antenna was used here for its simplicity, low cost of manufacture and the readily available standardised design equations in the literature [13–15]. The key parameters affecting the operation of the rectangular microstrip patch are its length, width, substrate height, permittivity and the feed mechanism. Therefore, if the other parameters are known, patch antenna measurements can be used to calculate the effective permittivity of heterogeneous substrates. The resonant frequency of the same sized patch is dependent on the permittivity below the patch [14] and so as this permittivity is altered, the resonant frequency

is altered. The microstrip line feed method was selected over the probe feed for ease of fabrication, modelling and to allow the sample holder to be mounted on the positioner in the anechoic chamber during measurements. The matching of the patch is affected by the changing permittivity but this chapter will focus on the resonant frequency.

In this chapter, the results from simulations and measurements of a standard rectangular patch antenna on the heterogeneous material described in Section 5.2.2 (see Figures 5.2 and 5.3) are presented. The simulations were carried out using Empire XCcel® while the measurements were carried out in the anechoic chamber at Loughborough University. The Anritsu Vector Network Analyser (VNA) has also been used to carry out S-parameter measurements. Two forms of the microstrip line feed mechanisms were used: the offset feed and the recessed/inset feed. More emphasis has been placed on the inset-fed patch because the offset feed may present further variables in the results, one of which is that the current distribution is not symmetric about the feed line.

Section 6.2 describes the simulations of the patch antenna used in this chapter on a heterogeneous substrate with dielectric and metallic cubic inclusions in a simple cubic (SC) lattice and compares the performance with that when the patch is on a homogenous substrate of equivalent effective permittivity. It also compares and discusses the simulated and measured results of the patch antenna on homogenous substrates. Section 6.3 gives a comprehensive analysis via simulations of the designed patch on the multi-layered sample introduced in Section 5.2 in order to fully understand the different variables that may affect the results. Section 6.4 compares the results from the simulations and measurements of the designed patch antenna on the multi-layered sample substrate to other materials of known permittivity. Also, other performance parameters of the patch antennas, such as the radiated efficiency, 10dB bandwidth and gain, using both feed mechanisms from simulations and measurements are compared. The conclusions to this chapter are given in Section 6.5.

6.2 Patch Antennas on Heterogeneous Substrates with Dielectric and Metallic Inclusions in a Simple Cubic (SC) Lattice

The inclusion material in the heterogeneous medium can be dielectric or metallic. In this section, the effect of both inclusion types are analysed and compared for the same-sized patch antenna. An analysis of the patch antenna on a heterogeneous medium with spherical inclusions was compared with its homogenous equivalent in [16]. Due to the isotropic nature of heterogeneous mixtures configured in an SC lattice and the accuracy and/or speed of simulations, cubic inclusions were used as an initial study of how the behaviour of a patch antenna is affected by these inclusions.

6.2.1 Antenna Design

The design equations for a rectangular patch antenna are given by [14], [17], [18]:

$$W_p = \frac{c}{2f_r}\sqrt{\frac{2}{\varepsilon_r + 1}} \tag{6-1}$$

$$\varepsilon_{reff} = \frac{\varepsilon_r + 1}{2} + \frac{\varepsilon_r - 1}{2}\left[1 + 12\frac{h}{W_p}\right]^{-1/2} \tag{6-2}$$

$$\frac{\Delta L}{h} = 0.412\frac{\left(\varepsilon_{reff} + 0.3\right)\left(\frac{W}{h} + 0.264\right)}{\left(\varepsilon_{reff} - 0.258\right)\left(\frac{W}{h} + 0.8\right)} \tag{6-3}$$

$$L_p = \frac{\lambda}{2\sqrt{\varepsilon_{reff}}} - 2\Delta L \tag{6-4}$$

where W_p is the patch's width; f_r is the resonant frequency; ε_r is the permittivity of the substrate on which the patch is printed; ε_{reff} is the effective dielectric constant of the patch (to account for fringing effects as some of the waves travel in air too [14]); h is the substrate thickness; L_p is the resonant length of the patch; ε_r is the permittivity of the substrate on which the patch is printed; and λ is the free space wavelength at the resonant frequency.

Using equations (6-1) to (6-4) with a design frequency, $f_r = 4$ GHz, the dimensions of the patch were obtained as $L_p = 14.77$ mm and $W_p = 20.02$ mm when $\varepsilon_r = 6.01$, and $L_p = 17.21$

mm and $W_p = 22.74$ mm when $\varepsilon_r = 4.43$. The value of f_r was chosen such that it fell within the frequency range of the anechoic chamber used in carrying out these measurements, while the ε_r values are the effective permittivity values of the multi-layered sample (in Section 5.2.3) for the two electric field orientations shown in Figure 5.5. These values of ε_r were chosen as they were the values of ε_{eff} extracted from the plane wave (PW) simulations of the sample (as in Section 5.2) and were relatively close to the values of the homogenous substrates used as references for the patch antenna measurements. The width of the feed line, w_o should be such that its characteristic impedance, Z_{cf} matches that of the patch and the source. In this work, 50-Ω impedance was used for the source. Z_{cf} is calculated from equation (6-5) [19]:

$$Z_{cf} = \begin{cases} \dfrac{60}{\sqrt{\varepsilon_{reff}}} ln\left(\dfrac{8h}{w_o} + \dfrac{w_o}{4h}\right), & \dfrac{w_o}{h} \leq 1 \\ \dfrac{120\pi}{\sqrt{\varepsilon_{reff}}\left[\dfrac{w_o}{h} + 1.393 + 0.667\ln\left(\dfrac{w_o}{h} + 1.444\right)\right]}, & \dfrac{w_o}{h} \geq 1 \end{cases} \tag{6-5}$$

As stated in Section 6.1, two feed methods – offset and recessed feed, as shown in Figure 6.1, were simulated and measured. For the offset-feed (see Figure 6.1 (b)), $W_1 < W_2$.

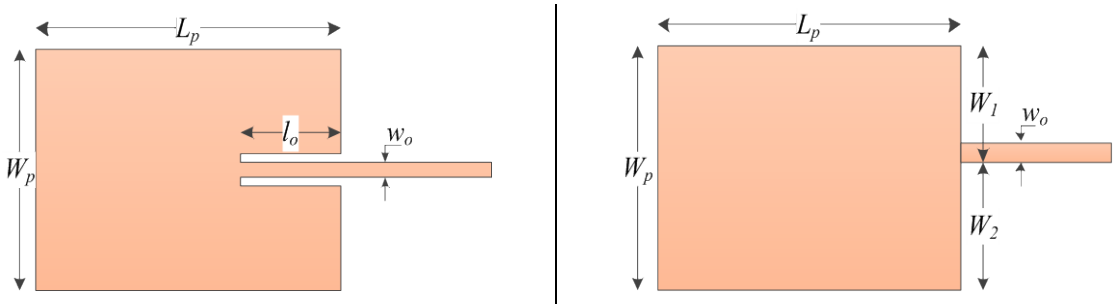

Figure 6.1: Generic schematic diagram of rectangular patch with (a) recessed/inset and (b) offset feeds (not drawn to scale)

For the recessed feed, the depth of recess is important in determining how well the patch is matched to the input impedance. This depth, l_o can be calculated from [15], [20]:

$$l_o = \frac{L_p}{\pi}\left[\cos^{-1}\left(\frac{Z}{R_{in}}\right)^{1/2}\right] \tag{6-6}$$

where Z is the required input impedance and R_{in} is the impedance at the leading radiating edge. Typically, l_o is about third of the length, L_p of the patch.

Parametric studies of these relevant dimensions of the patch and its feed were then carried out using simulations with homogenous substrates of different permittivity values and different number of layers in order to determine which particular dimension gave an acceptable impedance match across all. This resulted in a final patch size of $L_p = 24$ mm and $W_p = 27.76$ mm; feed line inset, $l_o = 9.50$ mm and width, $w_o = 3.12$ mm for f_r between 2 and 4 GHz in order to, as much as possible, give an acceptable match for each measurement.

6.2.2 Dielectric Inclusions

In [16], it has been shown via simulations, that the patch antenna on a substrate with dielectric spherical inclusions has similar performance to its homogenous equivalent substrate with the same effective permittivity. In this section, cubic inclusions are used to check this agreement between the heterogeneous and homogenous substrates. Data used: cube length, $l = 500$ µm, centre-to-centre spacing, $s = 750$ µm, $\varepsilon_1 = 2.25$ (tan $\delta = 0.001$), $\varepsilon_2 = 11.9$ (tan $\delta = 0.01$), thickness of the substrate, $d_s = 1500$ µm. Therefore, the substrate had 2 layers of cubes as shown in Figure 6.2 (b). Here, the inset feed depth, $l_o = 8$ mm.

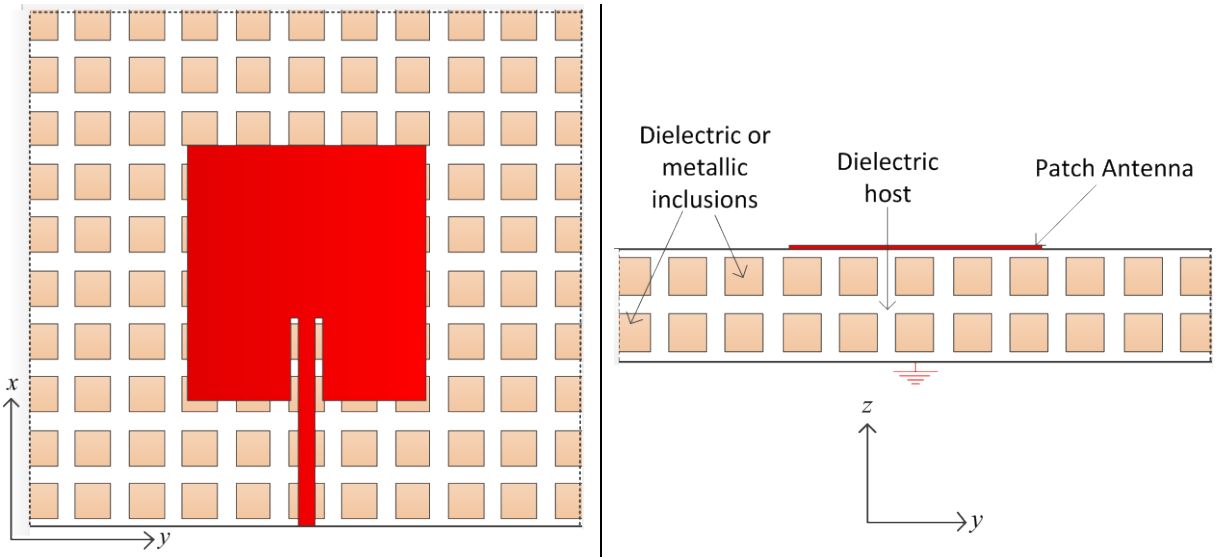

(a) (b)

Figure 6.2: (a) Top view and (b) side view of inset-fed patch on heterogeneous substrate (not drawn to scale)

As established in prior chapters, the ε_{eff} of a heterogeneous medium can be quickly determined from the canonical equations by Lewin and Sihvola [21], [22] and applying the equivalent volume process. Using these equations, the ε_{eff} for this medium is 3.69 (tan $\delta =$ 0.0016) which is used as the permittivity value in the simulation of the patch with the homogenous substrate, keeping the same substrate thickness. The return loss, that is, the S_{11} of these two scenarios are shown in Figure 6.3, which show very good agreement with the resonant frequency of the heterogeneous medium slightly higher than that of its homogenous equivalent. The radiation efficiencies on the heterogeneous and homogenous are 88.1% and 93.1% respectively. The 3D and 2D radiation patterns for both cases are shown in Figure 6.4, which again show good agreement. The main difference is that the nulls at 0° for E_ϕ and E_θ at ϕ =0° and ϕ = 90° respectively are more pronounced for the heterogeneous substrate than for the homogeneous equivalent. In addition, the electric field is more distributed over the surface area captured by the 'animation box' (see Figure 6.4 (a), (b)) for the heterogeneous substrate than for the homogenous. The close agreement between the homogenous and heterogeneous plots provides further confidence that the inversion process is accurate and that these heterogeneous materials can be adequately used in finite antenna designs.

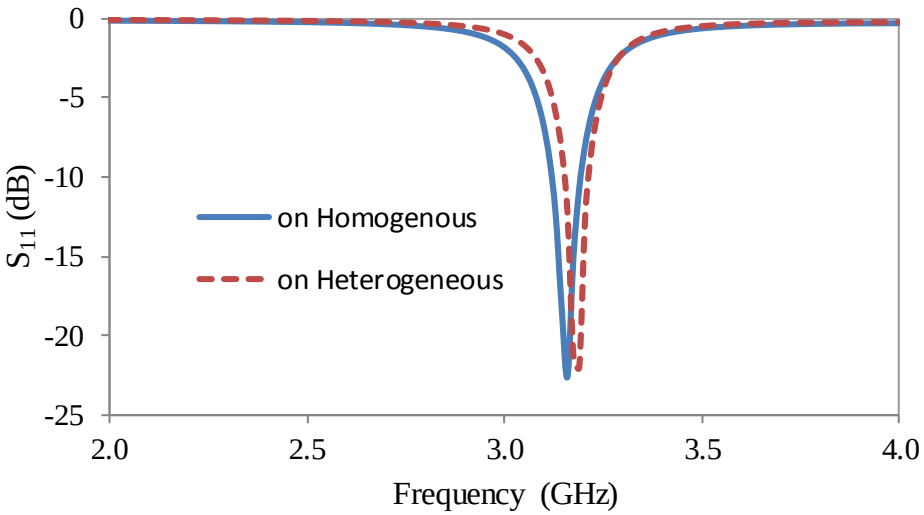

Figure 6.3: Simulated S_{11} of same sized patch on a homogenous (continuous) and heterogeneous (dashed) substrates with dielectric cubic inclusions

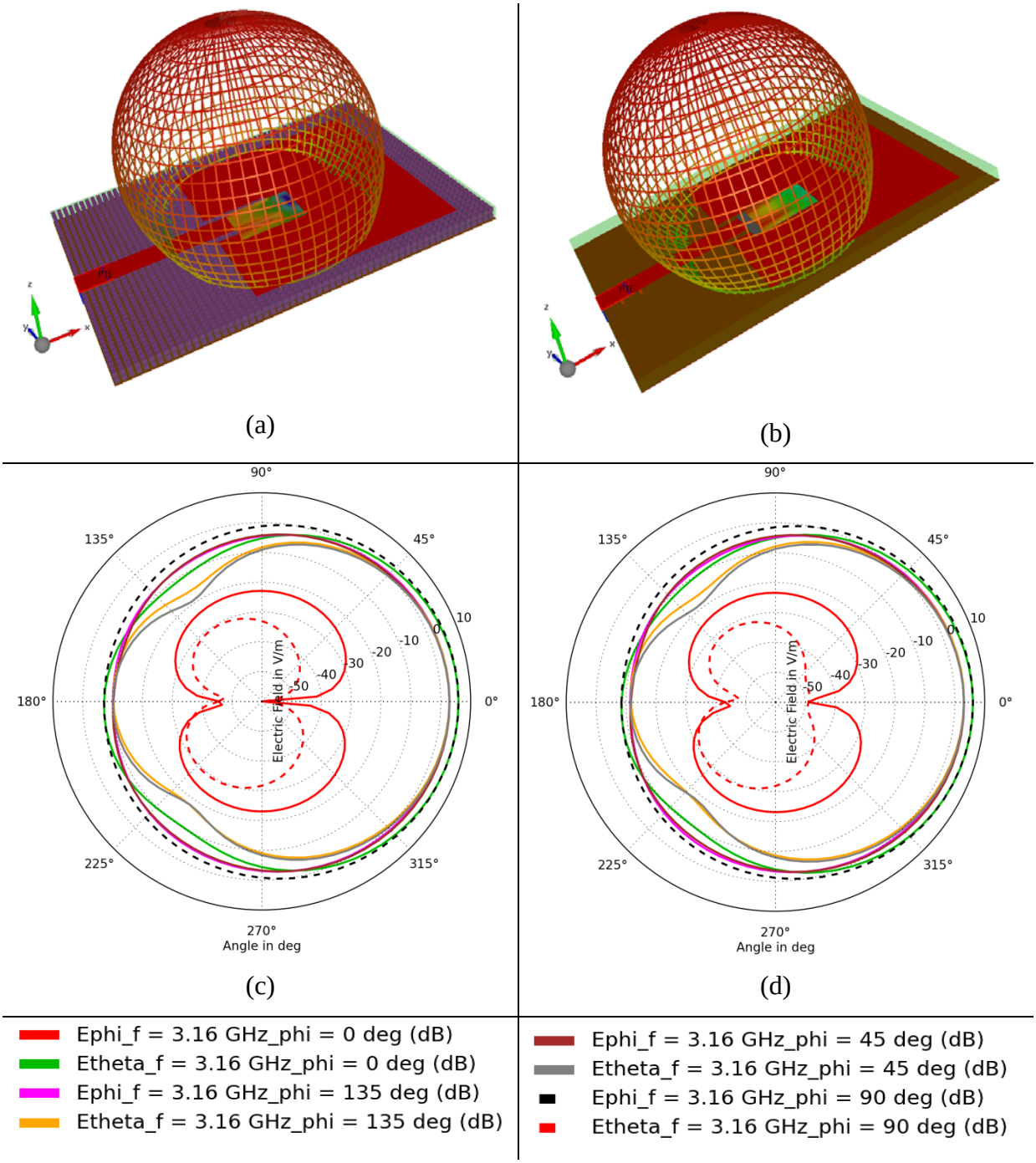

Figure 6.4: (a), (b) 3D and (c), (d) 2D simulated radiation patterns of an inset-fed patch antenna on (a), (c) heterogeneous (with dielectric cubes) and (b), (d) homogenous substrates obtained

6.2.3 Metallic Inclusions

Metallic (copper) inclusions in an SC lattice in a dielectric host were also examined here. The same inclusion length, spacing, substrate thickness (2 layers of inclusions) and host permittivity as in Section 6.2.2 was used here, but with inclusion material was Copper ($\sigma =$

5.8×10^7 S/m). In order to obtain the ε_{eff} from the canonical equations, $\varepsilon_2 = (12.7 + j103.93) \times 10^6$ was used as the equivalent permittivity of copper (calculated using the Drude model [23], [24]). From these equations, $\varepsilon_{eff} = 5.09$ (tan $\delta = 0.001$) and was used as the value of ε_r for the homogenous equivalent case. The simulated S_{11} results are shown in Figure 6.5. As shown, the agreement is less accurate when patch antennas have heterogeneous substrates containing metallic cubes, that is, the frequency response did not agree with the equivalent homogeneous case. This is thought to be due to the patch coupling to the metal cubes and the surface waves along the heterogeneous substrate. The heterogeneous patch was not as well matched as the homogenous case as if the ε_r has changed at the inset feed point, the 50 Ω point will change. The match can be improved by changing the dimensions of the patch. However, this was not done here as like comparisons with the exact same patch antenna was the main objective. As will be further discussed in Section 6.4, the value of the effective permeability, $\mu_{eff} = 0.62$ from the canonical equations (see equation (2-1)), and would have reduced the effective refractive index seen by the patch, thereby increasing its resonant frequency. A parametric study on the μ_{eff} of the homogenous equivalent was carried out via simulations in order to match its f_r to the f_r of the heterogeneous substrate suggested that the heterogeneous medium had an μ_{eff} between 0.7 and 0.8. The 3D and 2D radiation patterns from simulations are shown in Figure 6.6. The radiation efficiencies of the patch on the heterogeneous and homogenous substrates are 73.7% and 93.2% at their resonant frequencies. The differences between the radiation patterns of the homogenous and heterogeneous cases are more pronounced in this case. Deeper nulls are present in the radiation patterns of the homogenous compared to those of the heterogeneous. This may be due to the presence of diamagnetism 'seen' by the patch antenna. In addition, the electric field distributions are quite similar to each other.

The upward shift in the resonant frequency can be as a result of the initial antenna design process not taking into account the permeability of the medium. If the permeability can be accounted for, the wave number is effectively reduced, thereby increasing the required patch antenna size and thus reducing the resonant frequency. This may be done by substituting ε_r in equations (6-1) and (6-2) with $\varepsilon_r \mu_r$, where μ_r has been assumed to be 1 in these equations, and the diamagnetic value of $\mu_r < 1$ used instead. However, this is not done here, as the frequency and performance differences introduced by the use of different dielectrics and the GnSG sample were of more importance and the focus here.

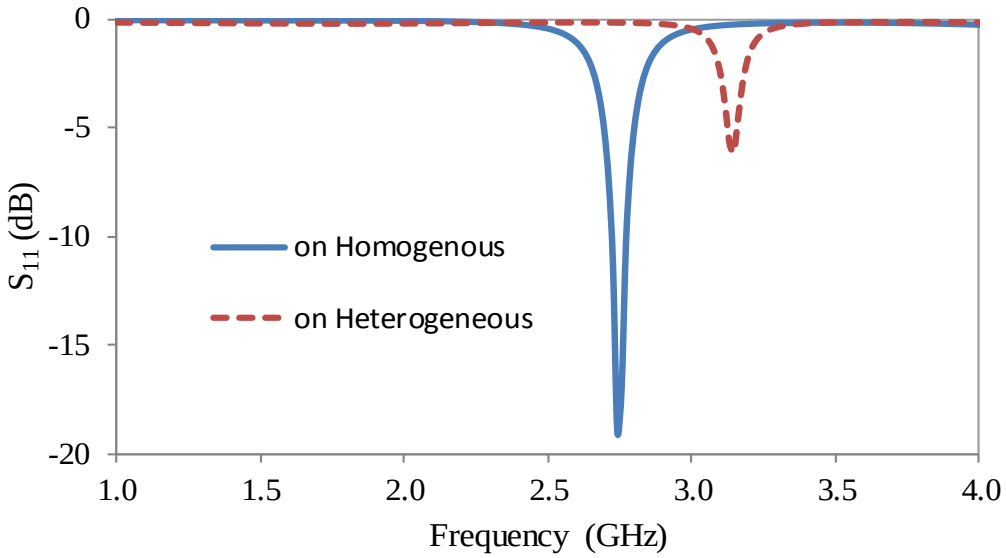

Figure 6.5: Simulated S_{11} of same sized patch on a homogenous (continuous) and heterogeneous (dashed) substrate with metallic cubic inclusions

Using a 1.5-mm thick substrate meant that two layers of the inclusions in the direction normal to the patch were used. It has been shown in [25] that the number of layers of the heterogeneous substrate did not cause a significant variation in its effective permittivity. The patch on the heterogeneous medium can take up to 3 hours to run as there are many Yee cells in both the X and Y directions. This simulation time goes up to 20 hours for spherical inclusions due to their shape and the meshing algorithm used in the Empire XCcel® [16]. A summary of the results using both dielectric and metallic inclusions is given in Table 6.1. The loss as captured by the values of the radiation efficiencies would be due to the impedance mismatch, the loss tangents of the materials used and the conduction losses which were taken into account by the simulation tool by its 'wide band lossy' option.

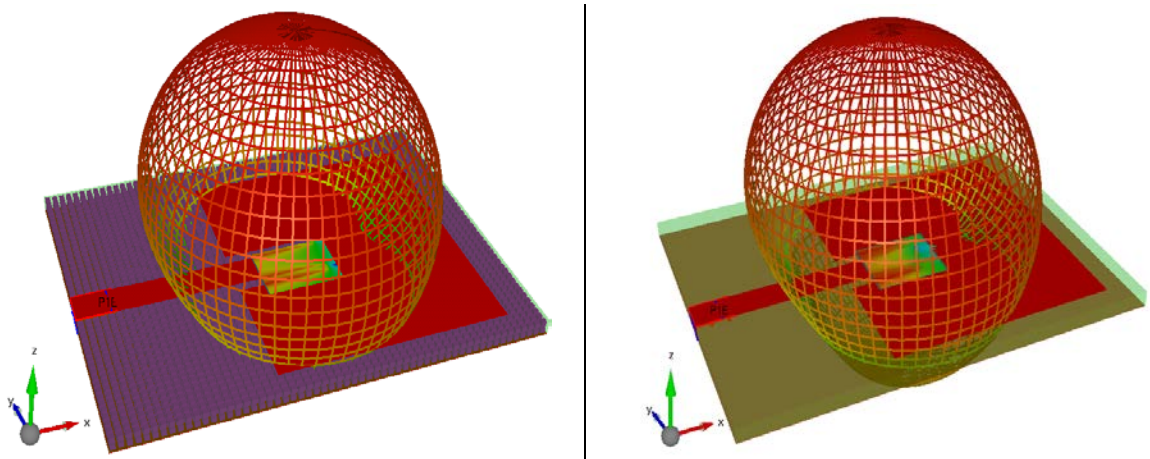

(a) (b)

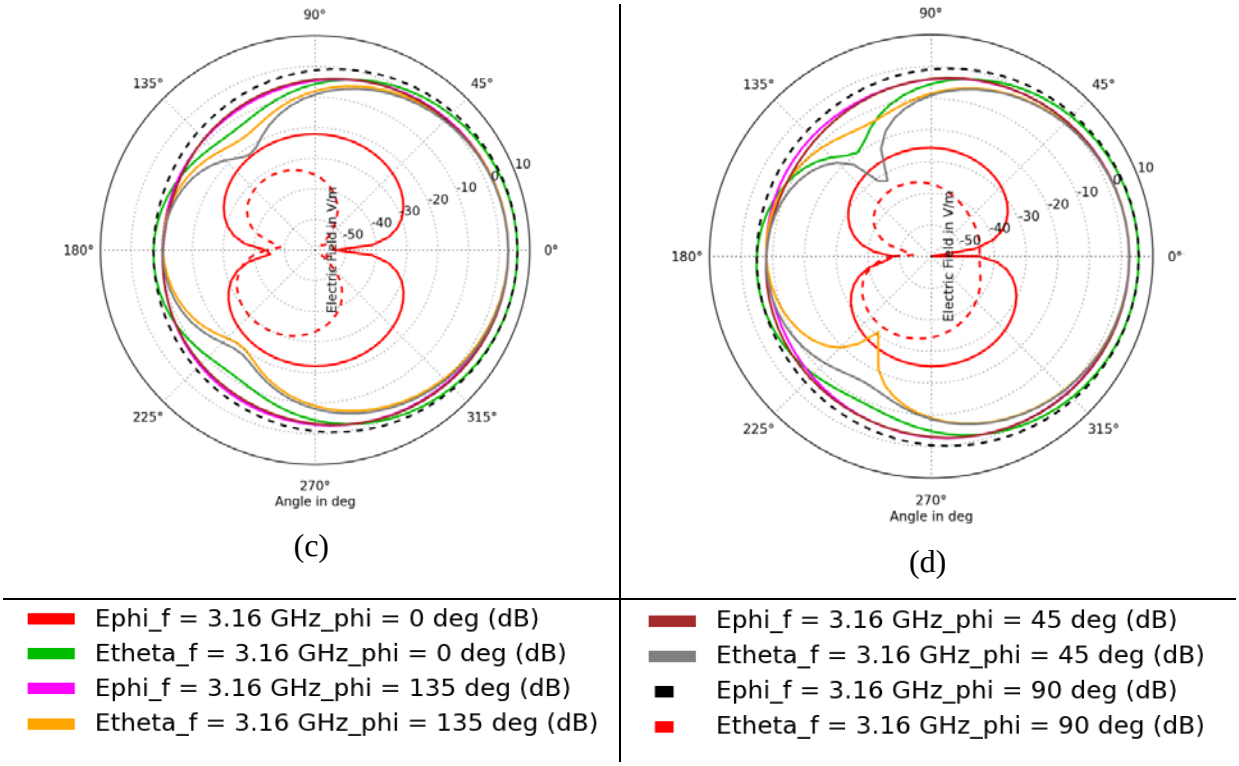

Figure 6.6: 3D (top row) and 2D (bottom row) simulated radiation patterns of an inset-fed patch antenna on (a), (c) heterogeneous (with metallic cubes) and (b), (d) homogenous substrates

Table 6.1: Summary of simulated results of patch antenna on substrates with cubic inclusions

	Dielectric Inclusions		**Metallic Inclusions**	
	Heterogeneous substrate	Homogenous equivalent	Heterogeneous substrate	Homogenous equivalent
ε_{eff}	3.69 (tan $\delta = 0.0016$)		5.09 (tan $\delta = 0.001$)	
S_{11} (not optimised)	-22.6 dB	-22.0 dB	-6.1 dB	-19.0 dB
Resonant frequency, f_r	3.16 GHz	3.19 GHz	3.15 GHz	2.74 GHz
10 dB bandwidth	74.3 MHz	61.8 MHz	-	52.3 MHz
Radiated efficiency at f_r	88.1%	93.1%	73.7%	93.2 %

6.2.4 Comparison of the Simulated and Measured Performance of the Patch Antenna on a Homogenous Substrate

In this section, the measurement results of the patch on known permittivity substrates are presented. The patch was measured using a recessed and offset feed as shown in Figure 6.1 and the results are discussed here. In both cases, the patch was printed on a lossy FR4 substrate ($\varepsilon_r = 4.4$, $\tan\delta = 0.02$, thickness = 1.5 mm) as shown in Figure 6.7. The patch dimensions in Section 6.2.3 are used here. The S_{11} results for the inset fed and offset-fed patch are as shown in Figure 6.8 (a) and (b) respectively. For the offset feed, the return loss shows different matching levels which could be improved. These results were acceptable for the primary purpose of the investigation which was to investigate the ε_{eff} and losses. These simulated and measured results have been summarised in Table 6.2.

Note: the 'Lossy FR4' substrate refers to the FR4-Epoxy substrate which tends to be lossy.

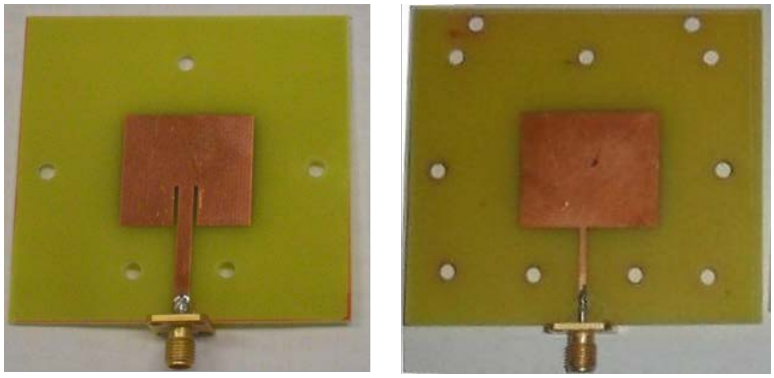

Figure 6.7: The inset-fed and offset-fed patch antennas on lossy FR4

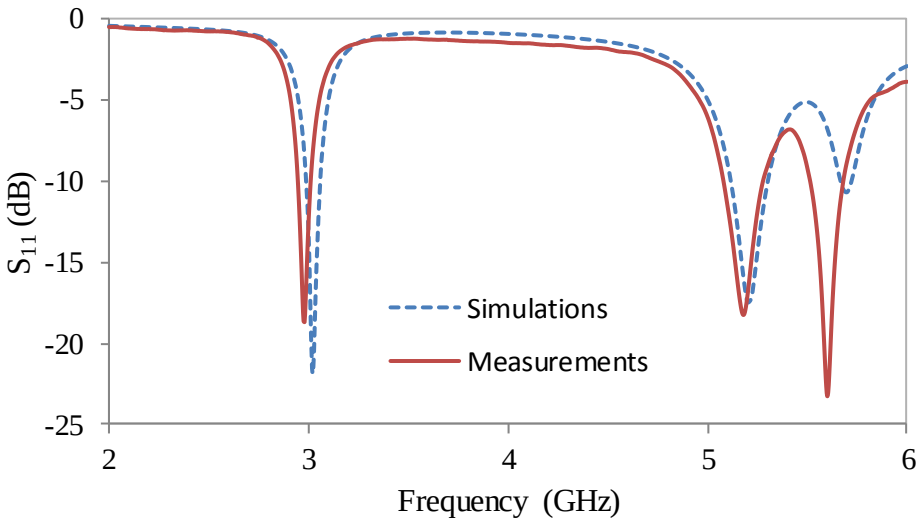

(a)

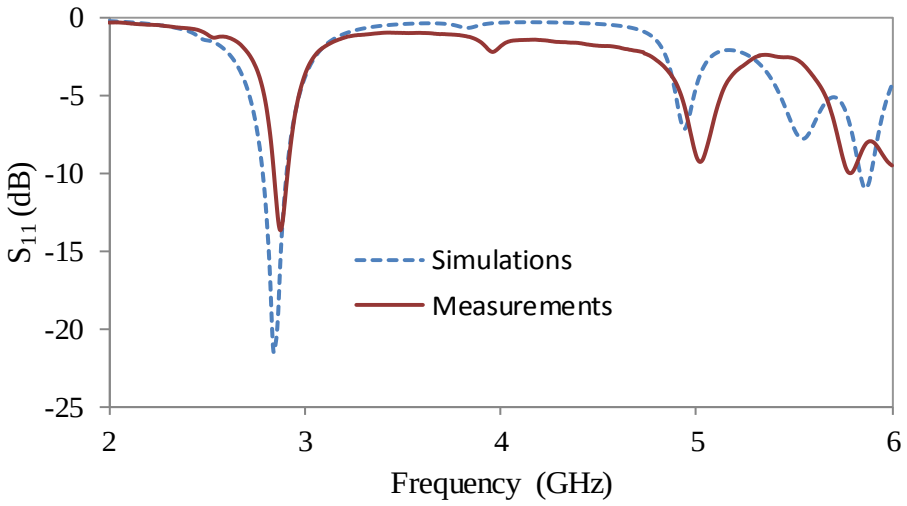

(b)

Figure 6.8: Simulated and measured S_{11} of (a) inset-fed and (b) offset-fed patch on lossy FR4

Table 6.2: Summary of performance attributes of patch antenna on lossy FR4 substrate

	SIMULATIONS		MEASUREMENTS	
	Inset-fed patch	Offset-fed patch	Inset-fed patch	Offset-fed patch
S_{11}	-21.9 dB	-22.3 dB	-18.7 dB	-13.7 dB
Resonant frequency, f_r	3.02 GHz	2.85 GHz	2.99 GHz	2.88 GHz
10 dB bandwidth	71.7 MHz	119.5 MHz	65.0 MHz	70.0 MHz
Radiated efficiency at f_r	91.3 %	57.2 %	39.9 %	52.5 %
Peak Gain	-	-	2.34 dBi	3.81 dBi

The frequency changes with the feed type, however this does not present a problem as the resonant frequencies and performance per antenna type is what is being compared here. The simulated and measured resonant frequencies for each feed type show reasonable agreement.

Radiation Patterns of Patch on Homogenous Substrates

The 2D radiation patterns at $\phi = 0°$ and 90°, from the simulations and measurements for the inset-fed and the offset-fed patches with homogenous substrates are shown in Figure 6.9. As shown, the radiation patterns are in general agreement with each other. Disparities between the simulated and measured patterns can be due to different issues such as cable and connector losses, instrument variations, positioning and the environment in which the

measurements take place. E_ϕ at $\phi = 0°$ is very small and so does not appear in the Figure 6.9 (a). The effects of the positioner are also reflected in the measured patterns from the reduced radiation at 180°.

Please note that due to the inherent configuration of the simulation tool, Empire XCcel® used here, the radiation patterns from the simulation are rotated 90° to the right relative to those from the measurements.

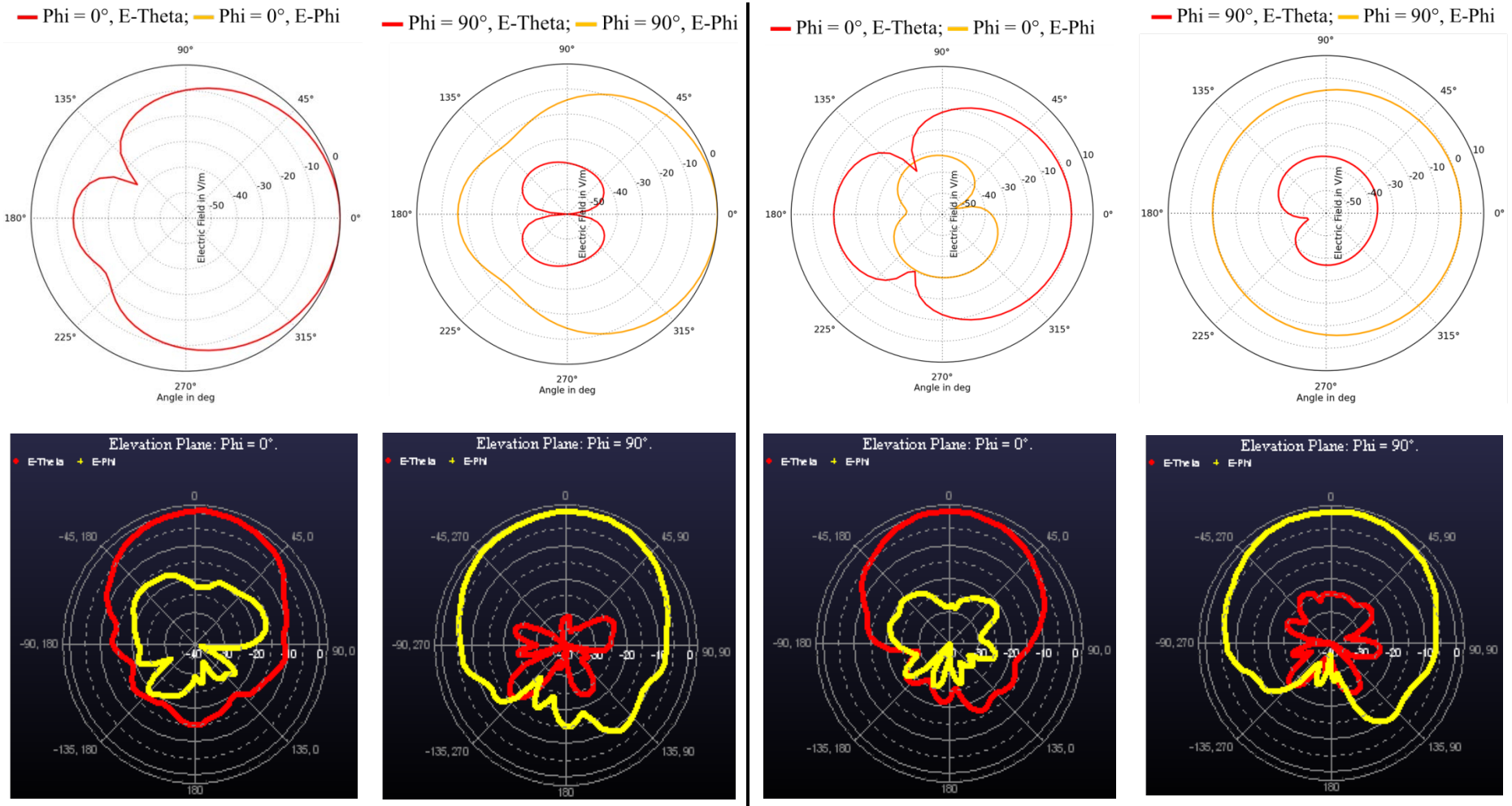

Figure 6.9: Simulated (top row) and measured (bottom row) 2D radiation patterns of (a) **inset**-fed (left) and (b) **offset**-fed (right) patches on the homogenous lossy FR4 substrates

6.3 Simulation Analysis of Rectangular Patch Antennas on the Multi-layered Sample Substrate

The dimensions of the patch used in the previous sections have been used here to analyse the multi-layered sample described in Section 5.2 (see Figure 5.3), which has a thickness of 1.84 mm when 9 double-sided layers are stacked with plain GTS® insulating either side. For simplicity, this structure is referred to as 'G9SG' in the rest of this chapter. From the PW simulation results presented in Section 5.2.3, the ε_{eff} of the sample was obtained as a permittivity tensor (6.01, 6.01, 4.43) where the lower value of ε_{eff} was obtained from a different orientation of the sample to the impinging EM wave. This characteristic has been determined as an *anisotropic* behaviour as the dimensions of the inclusions of the sample are not equal in all three axes. Figure 6.10 shows a patch antenna on the heterogeneous medium.

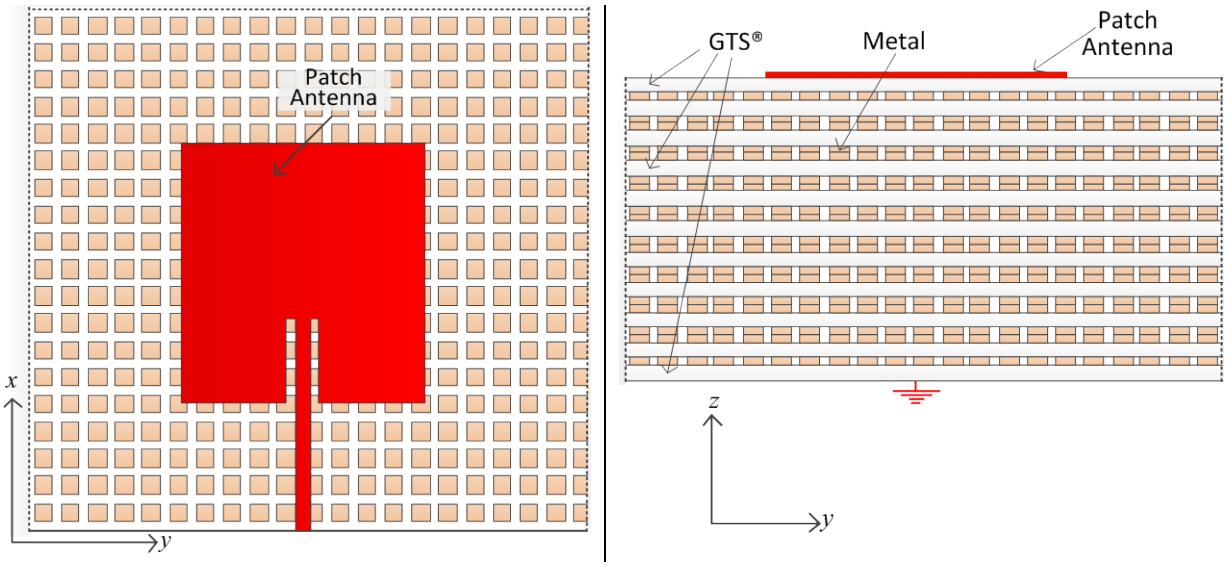

(a) (b)

Figure 6.10: (a) Top and (b) side views of patch antenna on heterogeneous G9SG substrate (not drawn to scale). Metal cuboid size = 500 × 500 × 70 µm, spaced 750 µm along the *x*- and *y*-axes, and 110 µm along the *z*-axis.

6.3.1 Inset-fed Patch Simulation Results

The simulated S-parameter, S_{11} of the inset-fed patch antenna on a standard low loss FR4 substrate with $\varepsilon_r = 4.5$, is shown in Figure 6.11, which shows a good impedance match. This value of ε_r was chosen because it was close to lower value of ε_{eff} tensor (4.43) obtained for the G9SG sample. The same patch was then simulated with the sample, G9SG directly below

and the simulated S_{11} is also shown. It is expected that should parametric studies be done on the feed for this patch using the G9SG as substrate, a much better match would be achieved. However, due to the computational cost of each simulation of this kind, ~ 6 hours, this was not done. The resonant frequency for the patch on the sample increased to 3.38 GHz from its 2.96 GHz value when it was on the homogenous substrate, a 14% increase. This in itself suggests that the effective permittivity seen by the patch is higher for the homogenous than the G9SG sample, implying that $\varepsilon_{eff} < 4.5$.

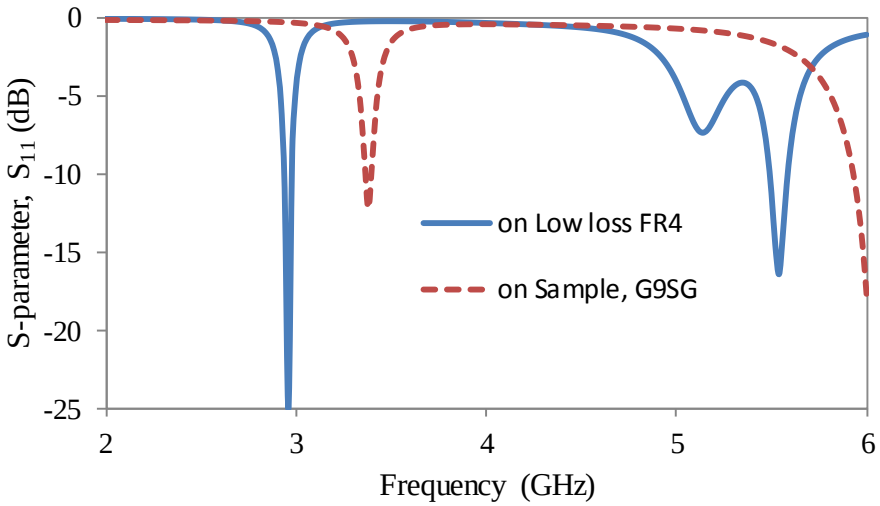

Figure 6.11: Simulated S_{11} of same sized patch on a homogenous FR4 substrate (continuous) and heterogeneous G9SG substrate (dashed)

In order to determine what the ε_{eff} of the G9SG sample might be, the ε_r of the homogenous substrate with the same thickness was varied from 2 to 5. The S_{11} from these simulations are shown in Figure 6.12. As shown, the resonant frequency of the sample falls between $\varepsilon_r = 3$ and 3.5, instead of 6.01 or 4.43 as from the PW simulations. This suggested that the lower ε_r could be due to the anisotropy of the sample and/or that the μ_{eff} of the sample was less than 1 (diamagnetism), as determined in Section 5.2.3, hence, taking the resonant frequency up by reducing the wave number.

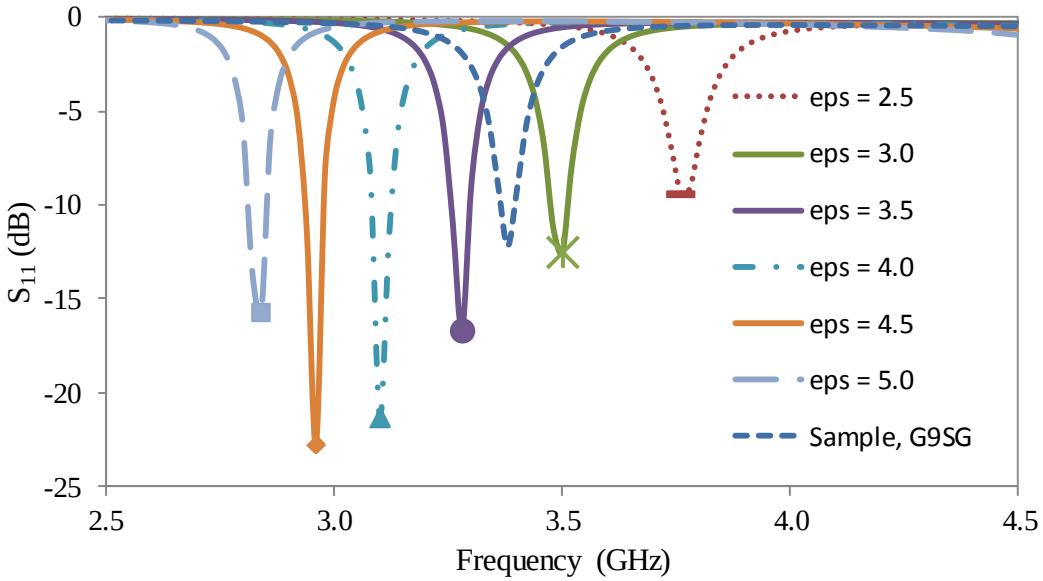

Figure 6.12: Simulated S_{11} of same sized patch on a homogenous substrates of equal thickness but different permittivities for comparison with S_{11} of heterogeneous G9SG sample

6.3.2 Anisotropy and Diamagnetism of Sample

Anisotropic Behaviour

Another simulation of the patch was run with the copper cuboids rotated by 90° with respect to the patch surface, in order to check how the anisotropic nature of the sample was playing a role on the patch antenna performance. In this geometry, the flat surface area of the copper squares was perpendicular to the plane of the patch and parallel to its width, see Figure 6.13; the substrate thickness was 1.5 mm here. The results are shown in Figure 6.14. The resonant frequency, $f_r = 3.0$ GHz, is now closer to that of the homogenous substrate with $\varepsilon_r = 4.5$, confirming that the structure is indeed anisotropic. As in Section 6.2.3, the patch antenna simulations indicate a lower ε_{eff} than that obtained with PW simulations without the diamagnetic effect.

The resonant frequency implied that the orientation of the squares relative to the patch is important as the polarisation of the electric fields within the substrate of a patch are generally pointing in the direction from the patch to its ground plane and so are 'disturbed' differently from one orientation to another. It may also be that when these copper cuboids are parallel to the length of the patch, a different coupling response might be seen. These last two orientations of these small squares are difficult to make using etching techniques as it is

difficult to create a stacked layer of thin strips fixed together and sufficiently long and wide to surround the patch. As such these analyses were limited to simulations.

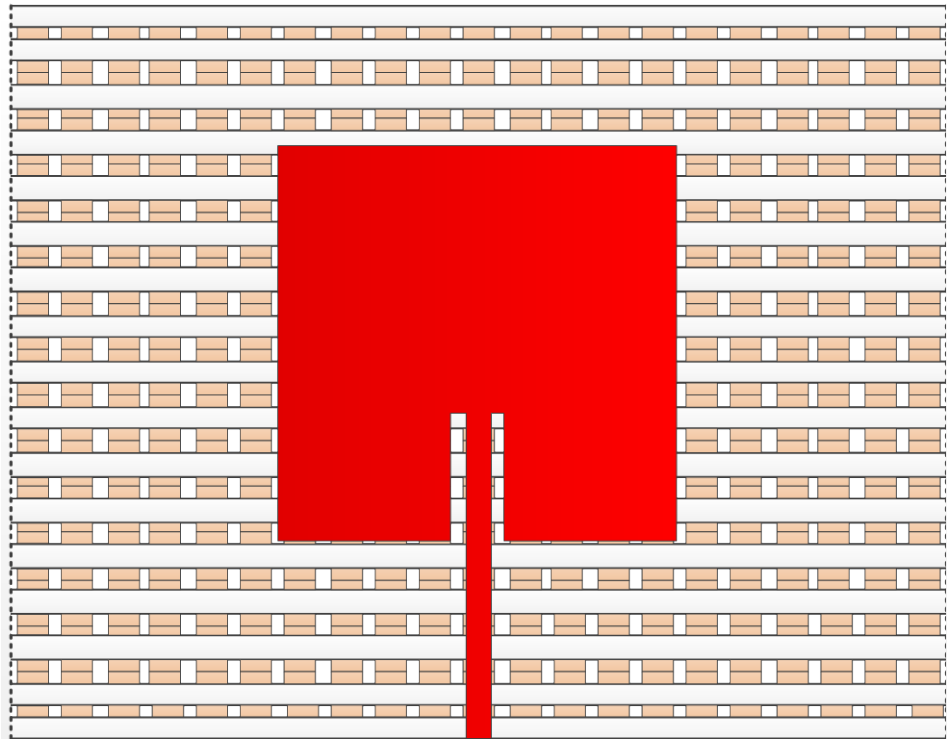

Figure 6.13: Alternative orientation of copper cuboids under inset-fed patch (not drawn to scale in order to visualise the structure)

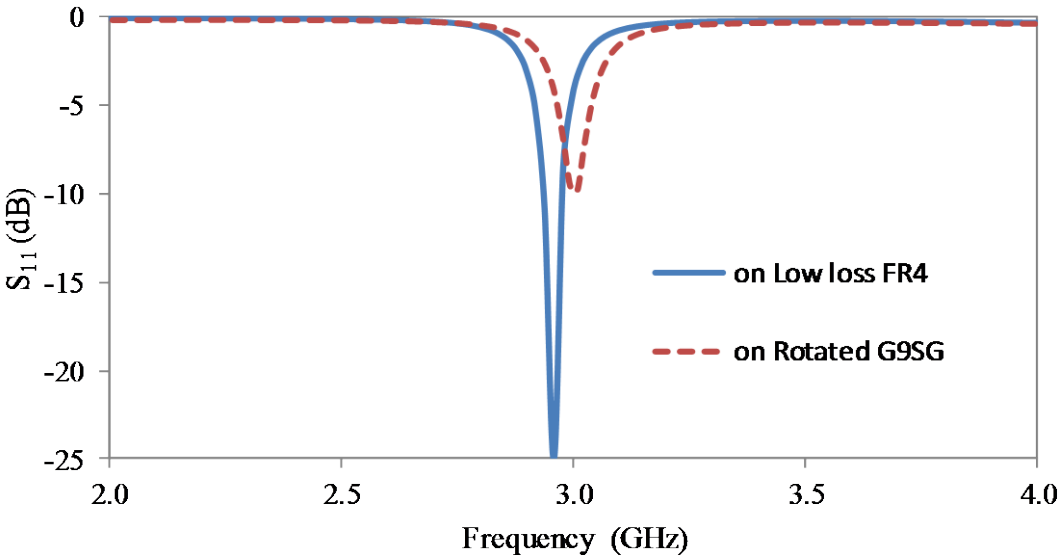

Figure 6.14: Simulated S_{11} of same sized patch on a homogenous (continuous) and heterogeneous (dashed) substrate with rotated copper cuboids as in Figure 6.13

Diamagnetic Behaviour

To test the effect of the diamagnetism on the resonant frequency of a patch antenna, a parametric sweep of varying μ_r from 0.1 to 1 with fixed value of ε_r was carried out via simulations and the results shown in Figure 6.15. From this, it can be seen that the resonant frequency increases for decreasing permeability and so confirms the point that the diamagnetic nature of the sample could be contributing to the upward shift in the resonant frequency and reducing the impedance match of the patch. In Section 5.2.3, it was determined from the simulation-inversion process that the sample had an average $\mu_{eff} = 0.82$. Comparing this with the plot for $\mu_r = 0.8$ in Figure 6.15 which represents a 14% drop in f_r as seen in Figure 6.11 between the f_r of the G9SG sample and the homogenous $\varepsilon_r = 4.5$ substrate, it can be concluded that the G9SG sample actually has an ε_r around 4.5, a value quite close to the one of values in its permittivity tensor.

The above analysis has given a reasonable explanation for the upward shift in the resonant frequency of the patch antenna compared to the homogenous equivalent; therefore it is more reasonable to compare the performance of the patch on the sample with that of the homogenous substrate with $\mu_r = 0.8$. The S_{11} values are shown in Figure 6.16. Having accounted for the permeability of the medium, the resonant frequencies and the impedance match of both geometries are now closer than they were in Figure 6.11 but still different. It also indicates that μ_{eff} for the G9SG sample falls between 0.9 and 1.

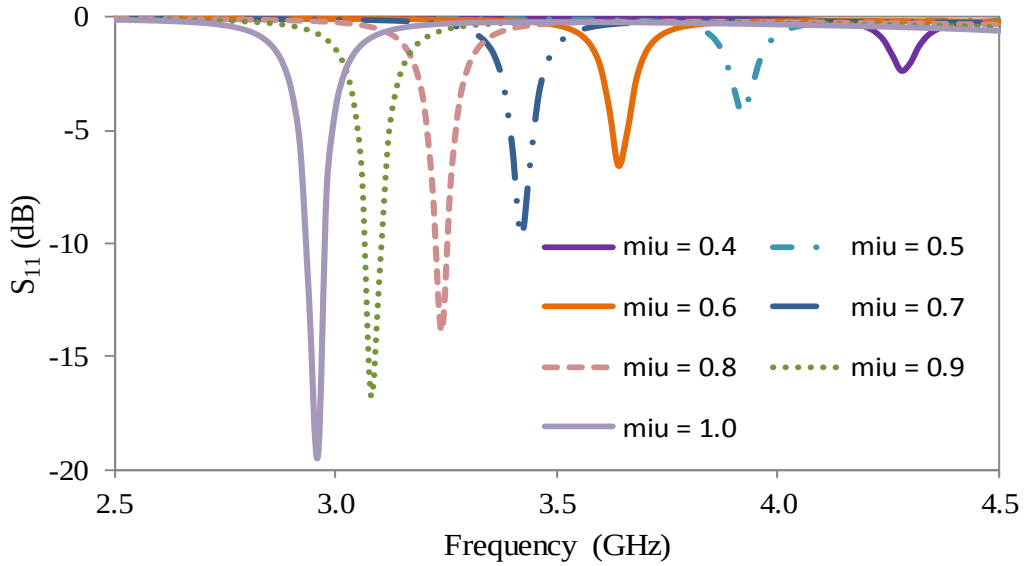

Figure 6.15: S_{11} of same sized patch on a homogenous substrates of equal thickness and permittivity, but with decreasing permeability, for comparison with S_{11} of heterogeneous sample (G9SG) orientated as in Figure 6.10.

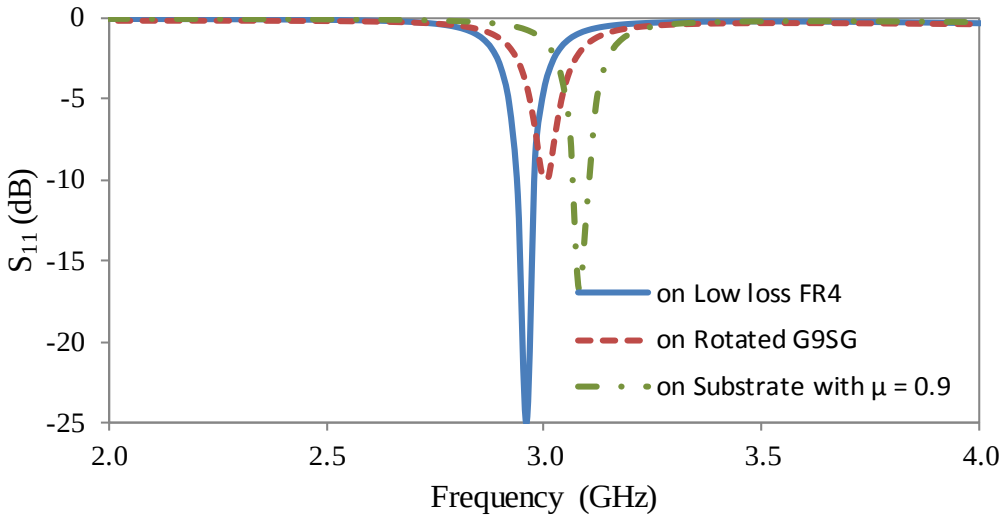

Figure 6.16: S_{11} of same sized patch on a homogenous substrate with $\varepsilon_r = 4.5$, $\mu_r = 1.0$ (continuous), and with $\varepsilon_r = 4.5$, $\mu_r = 0.9$ (dash-dot) and heterogeneous (dashed) substrate

6.3.3 Offset-fed Patch Simulation Results

Simulated results for the offset-fed patch are given in this section as measured results using this patch are also presented in this chapter. The dimensions of the patch are the same as the inset fed patch and the microstrip line feed was offset 1.12 mm ($= W_2 - W_1$) from the centre line of the patch as shown in Figure 6.1 (b). The S_{11} results are shown in Figure 6.17, for the patch on the homogenous equivalent and the heterogeneous substrate. From the S_{11} results, it can also be seen that the resonant frequency for the G9SG sample is higher than that of its homogenous substrate with permeability, $\mu_r = 1$ and $\mu_r = 0.8$. The same explanation given in the Sections 6.3.1 and 6.3.2 applies to this set of results also. Further results using the offset-fed patch antenna are given in Section 6.4.3.

It can be concluded that the inclusion of $\mu_{eff} < 1$ in the EM properties of the homogenous medium reduces the difference between the resonant frequencies of a heterogeneous medium with metallic inclusions and its homogenous equivalent. However, this does not completely provide the full explanation for the variation in f_r.

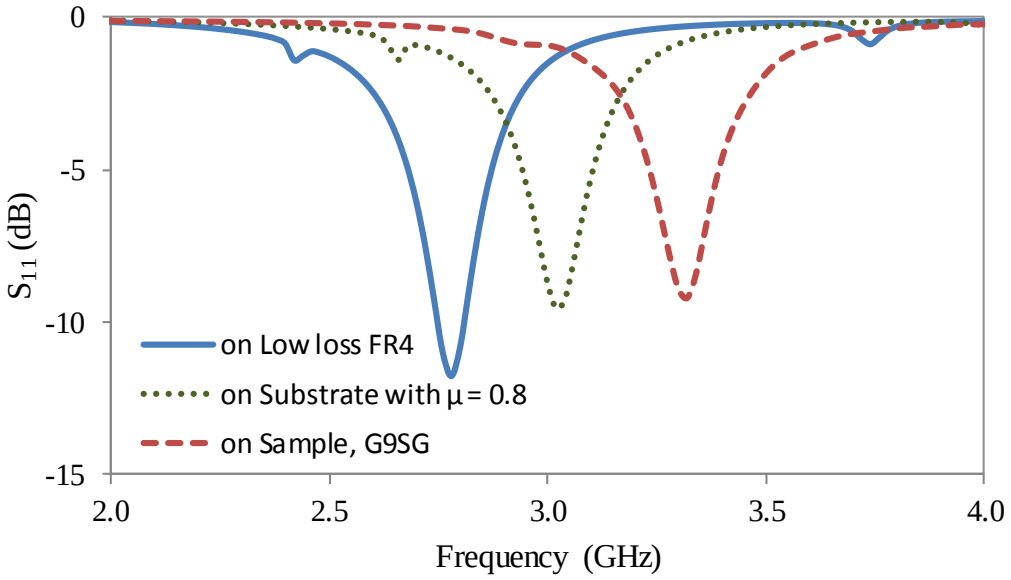

Figure 6.17: Simulated S_{11} of same sized offset-fed patch on a homogenous $\varepsilon_r = 4.5$ (continuous), homogenous $\varepsilon_r = 4.5$, $\mu_r = 0.8$ (dotted) and heterogeneous (dashed) substrate

The differences in the ε_{eff} and the μ_{eff} results between that obtained by the plane wave and the patch antenna simulations are very likely due to the fact that the plane wave simulations are set up such that the sample is in the far field of the port, whereas with the patch antenna simulations, the sample is in the near field of the source. Therefore, it can be expected that the frequency response from both cases will differ from each other.

6.4 Measurement of Patch Antennas on Dual Substrates

In this section, patch antennas with either inset or offset feeds on multi-layer substrates were fabricated and measured in order to (a) validate the ε_{eff} from the resonant frequencies and (b) investigate and compare the radiation patterns and efficiencies of the patch in this configuration. Patch size: $L_p = 24$ mm, $W_p = 27.76$ mm, $l_o = 9.50$ mm, $w_o = 3.12$ mm. A two-layer substrate was used as shown in Figure 6.18 as another method of comparing the performance of a patch antenna on homogenous and heterogeneous substrates. The patch is printed directly on the 'homogenous substrate' and the 'standard or test substrate' is sandwiched between the 'homogenous substrate' and ground. These two substrates were varied in the measurements. The two-layer geometry was used here in order to compare the performance of a patch antenna with the G9SG and other homogenous substrates. The nature of the G9SG sample did not allow direct etching of the patch antenna on its metallic surface.

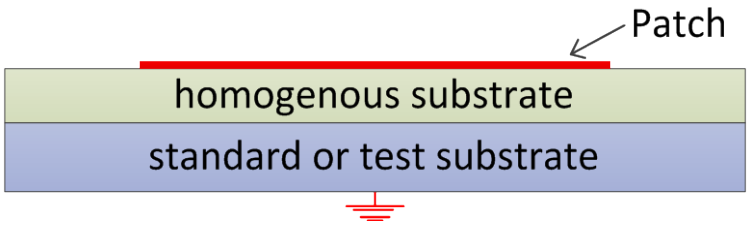

Figure 6.18: Side view of patch antenna on dual substrates.

6.4.1. Measurement Summary

Due to the fact that the patch was to be placed on several different dielectrics and measured in the full wave anechoic chamber, a support mechanism was designed to hold the test sample in place. This consisted of a solid metal block, sample holder and plastic screws. The metal block acted as the ground plane for the patch antenna system and had holes drilled on either side as shown in Figure 6.19. The plastic screws were used to hold everything in the right place and minimise the air gaps between layers. The in-chamber arrangement is shown in Figure 6.20. In order to mount these substrate layers on the sample holder, holes had to be drilled through all the substrates at the exact same points to ensure alignment. Examples of these holed materials are shown in Figure 6.21. The properties of these materials and the measured and simulated results are given in Table 6.3.

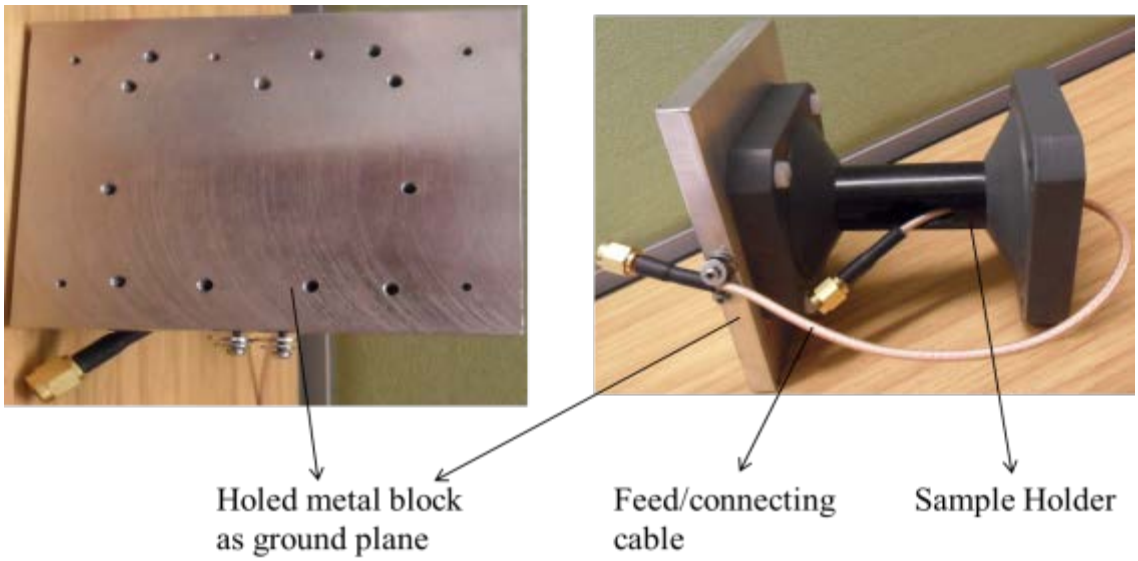

Figure 6.19: Top and side views of support structure for the anechoic chamber measurement

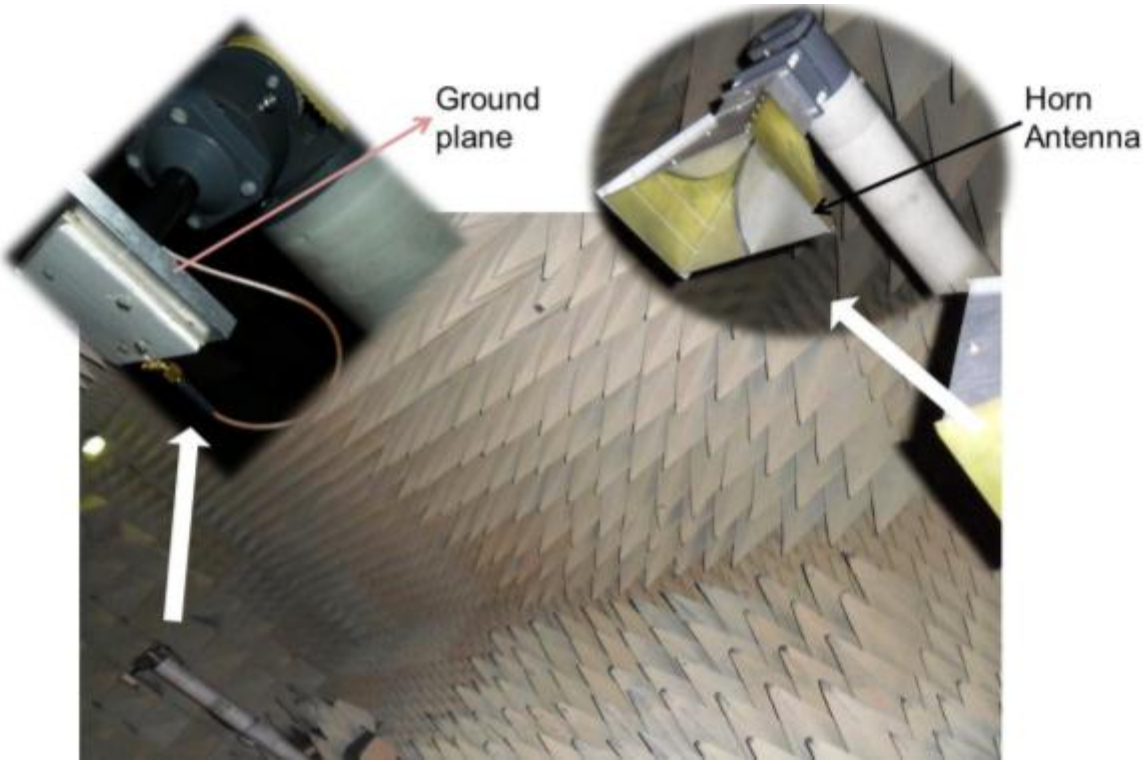

Figure 6.20: Anechoic chamber antenna measurement setup showing the reference horn antenna and the sample holder with the materials being measured

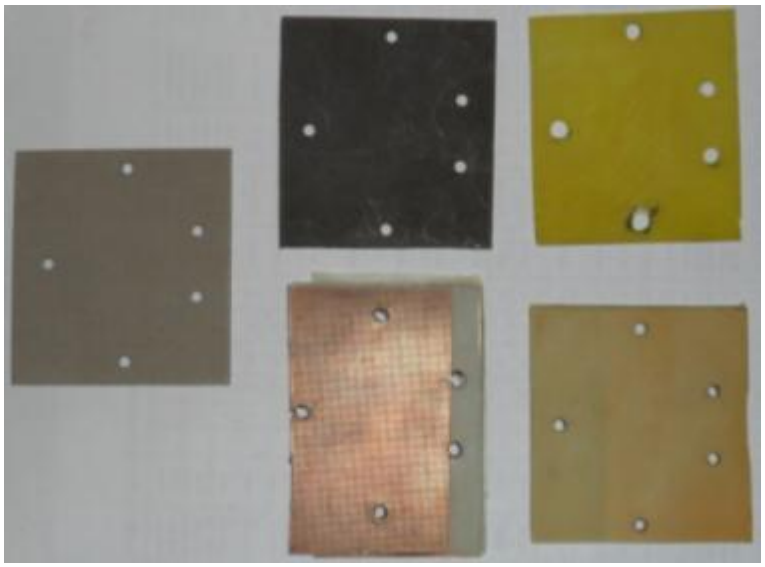

Figure 6.21: Holed samples: Taconic, low loss FR4, lossy FR4, GTS Layers and G9SG (clockwise from left)

For the measurements with the patch printed on the thin GTS® materials, an additional layer of Rohacell® (see the white top layer in the left inset of Figure 6.20) was necessary to apply the required pressure to the measured material in order to eliminate air gaps. As Rohacell® has a permittivity close to that of air, this has negligible effect on the results, and can be ignored as the relative frequency changes are of interest here.

Note: the 'GTS Layers' substrate was a stack of 14 thin GTS® material (total height = 1.53 mm) used in this work, with the copper etched away from either side and stacked to create the required thickness; the 'Low loss FR4' refers to a high quality RF-45 substrate.

6.4.2. Inset-fed Patch

The inset-fed patch was etched on two substrates – the 1.5-mm lossy FR4 and 0.11-mm GTS® substrate. The simulated and measured results from these two samples are shown and compared here. The S_{11} result from the GTS® patch antenna with the 1.84-mm G9SG sample below it (see Figure 6.10) is shown in Figure 6.22, which gives a very good impedance match with $|S_{11}|$ = -28.98 dB at f_r = 3.71 GHz.

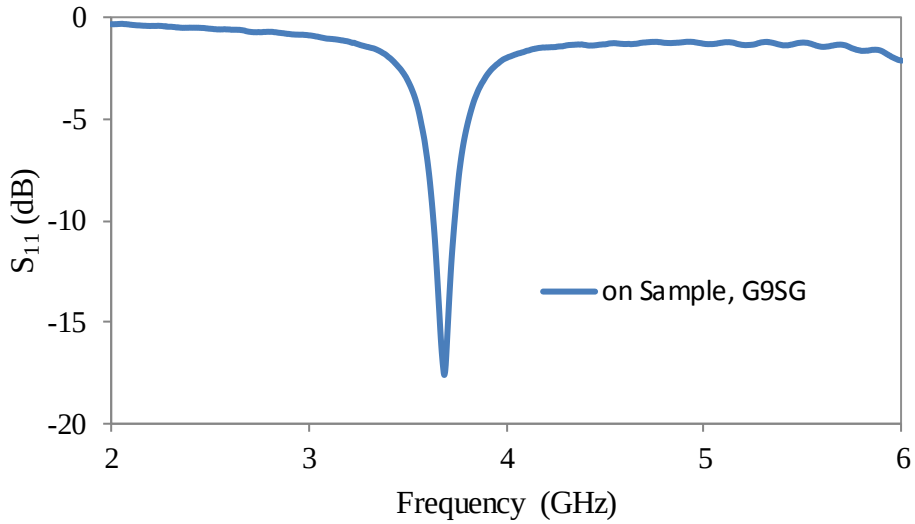

Figure 6.22: Measured S_{11} of GTS® printed inset-fed patch on the G9SG sample

Further comparisons were done when these 2 inset-fed patches – on FR4 and GTS®, were placed above other dielectric substrates as in the arrangement of Figure 6.18. The S_{11} plots are shown in Figure 6.23. Bearing in mind that the resonant frequency is partly a function of the permittivity of the substrate beneath the patch, it can be concluded that the permittivity of the G9SG lies between that of the known permittivity values of FR4, $\varepsilon_r = 4.5$ and Taconic, $\varepsilon_r = 2.2$. Although the ε_{eff} of the G9SG sample seems to be less than that of the GTS® Layers, it should be recalled that the copper cuboids have been shown to introduce a diamagnetic behaviour to the sample which accounts for this reduction in the effective refractive index. Also, the volume fraction of the air gaps in the sample, which is ~30% more than that of the copper cuboids will also contribute to reducing the ε_{eff} of the G9SG sample. The differences in total substrate height between measurements have an effect on the impedance match, and also affect the resonant frequencies. Note that the identical patch (including the inset dimensions) was used in all cases and hence as the ε_r changes, the impedance of the line also changes.

The radiation patterns from the simulations and measurements of the lossy FR4 substrate and the GTS® substrate with the G9SG sample underneath are shown in Figure 6.24 (a) and (b) respectively. The patterns from the simulations are rotated by 90° with respect to the measured patterns. Radiation patterns from the measurements are similar for both scenarios. From these results, it can be concluded that the simulation results give 'ideal' results and the measurements seem to have more nulls. This could be due to the positioner, the cable and the

asymmetric samples. However, the general distributions and shapes of the patterns from the simulations and measurements show reasonable agreement.

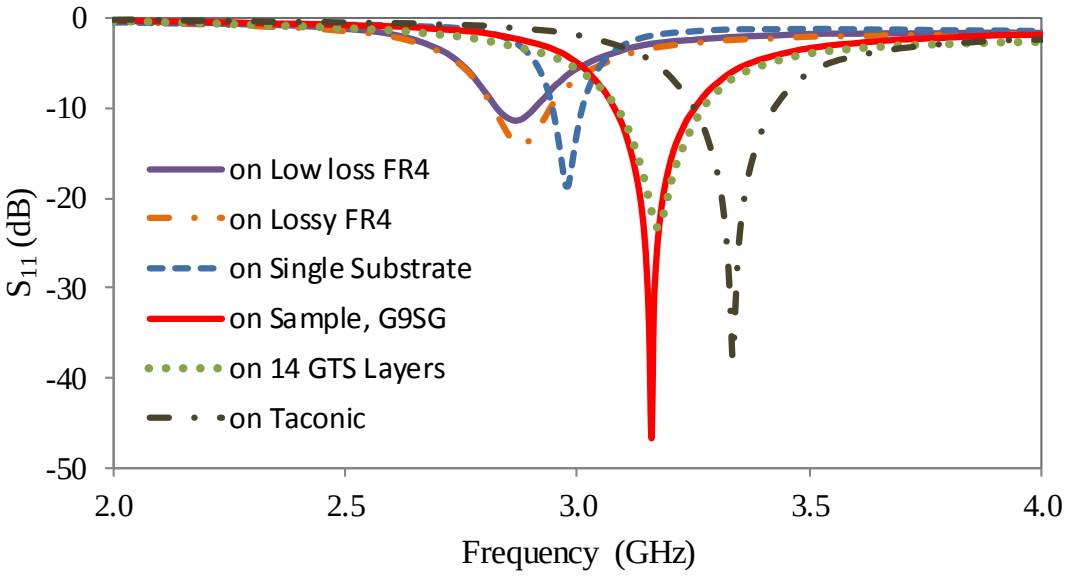

(a)

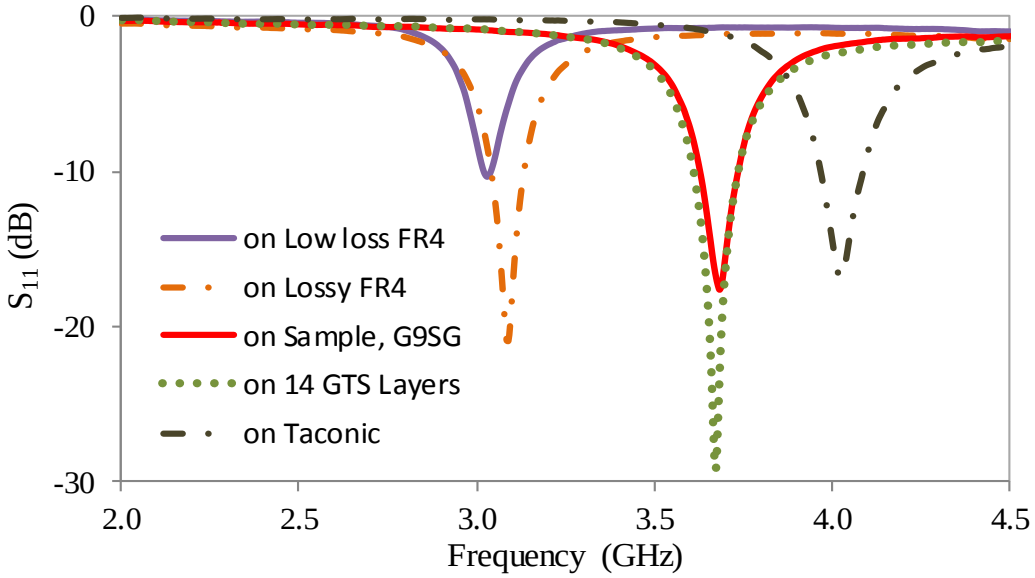

(b)

Figure 6.23: Measured S_{11} of inset-fed patch printed on (a) 1.5 mm lossy FR4 and (b) 110 µm GTS® substrates with different dielectrics (as listed in the legend) underneath as the standard or test substrates – see Figure 6.18.

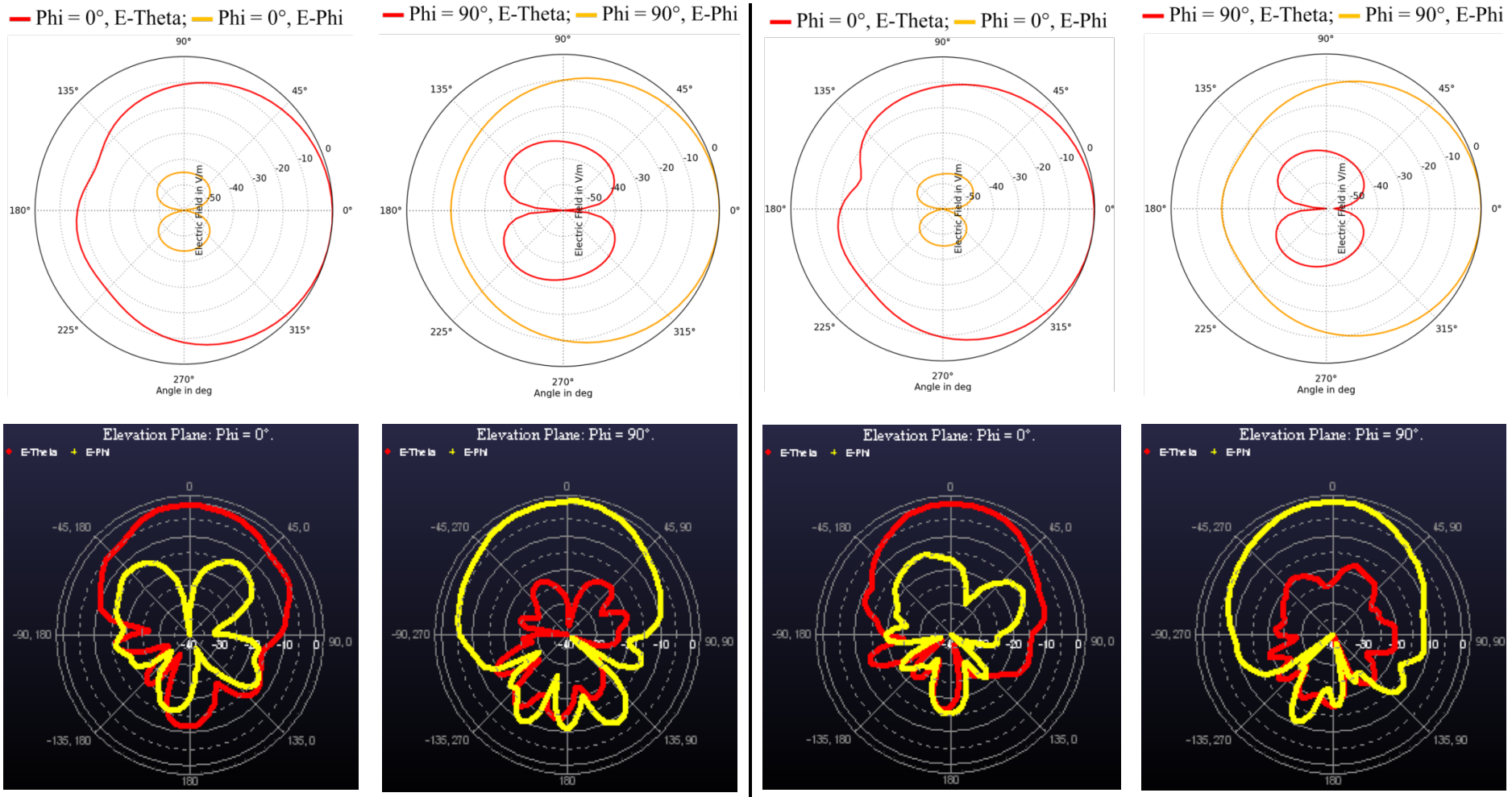

(a) (b)

Figure 6.24: Simulated (top row) and measured (bottom row) 2D radiation pattern of (a) **lossy FR4** inset-fed patch and (b) **GTS®** inset-fed patch antenna on sample, G9SG

A summary of the simulated and measured results along with the other parameters of the patch antenna are given in Table 6.3 and Table 6.4. 'ALONE' in the tables is the case when there is just a single substrate below the patch antenna, that is, no 'standard/test substrate' below the 'patch substrate' as shown in Figure 6.18. This geometry was not measured for the GTS inset-fed patch case as the substrate was 110 µm thick. Both tables show that the resonant frequencies from the simulations show good agreement with those from the measurements for the homogeneous samples. The main disagreements between the simulations and the measurements for the G9SG sample are in their resonant frequencies as the measured f_r are higher than the simulated values. In both cases, the S_{11} at the resonant frequencies from the measurements are higher than those from the simulations; however it can be assumed that the measured results give a truer picture of the antenna performance. The radiated efficiencies from both measurements are above 50% and may be further improved with separately designed patches for each set of measurements. From the results of the lossy FR4 in Table 6.3, the radiated efficiencies and return losses from the simulations and measurements are comparable. Please note that the simulations did not include μ_r in the substrates as identical configurations were being compared and that the transmission line widths were not optimised for the different dielectrics, for example, in the low loss FR4 case which has a lower 10dB bandwidth compared with that of the G9SG sample.

The resonant frequency of a patch antenna can be approximated by:

$$f_r = \frac{c}{2L_p\sqrt{\varepsilon_r\mu_r}} \tag{6-7}$$

Therefore, relationship between the resonant frequency of the patch antenna with and without the diamagnetic effect in its substrate can be written as:

$$f_{r,no\ diamagnetism} = \frac{f_{r,with\ diamagnetism}}{{\mu_r}^{-0.5}} \tag{6-8}$$

Using this relationship on the values in Table 6.3 - Table 6.7 allows the resonant frequencies from the simulations and measurements to show better agreement. The rather high values of the radiation efficiencies from the simulations have been cross-checked with the simulation software support team and found to be as expected even though the materials – conductors and dielectrics were treated as "broad band lossy" [26] which takes into account all the losses in the materials.

Table 6.3: Summary of simulated and measured results of 1.50 mm **lossy FR4** ($\varepsilon_r = 4.4$, $\tan\delta = 0.02$) **INSET** patch antenna on different dielectrics

From Simulations: 1.50 mm lossy FR4 INSET-fed patch antenna on:							
	Thickness of bottom substrate	Material Type	ε_r of substrate	Resonant Frequency, f_r	Return Loss at f_r	10dB Bandwidth	Radiated Efficiency at f_r
ALONE	-	-	-	3.02 GHz	-26.8 dB	75.1 MHz	43.2%
On G9SG	1.74 mm	Sample		3.02 GHz	-15.7 dB	95.9 MHz	71.5%
On Low loss FR4	1.55 mm	Low loss FR4	4.5	2.87 GHz	-14.5 dB	95.6 MHz	68.9%
On GTS Layers	1.53 mm	Layered GTS	3.0	3.12 GHz	-19.9 dB	116.3 MHz	76.3%
On Taconic	1.60 mm	Taconic	2.2	3.35 GHz	-34.0 dB	129.8 MHz	80.8%

From Measurements: 1.50 mm lossy FR4 INSET-fed patch antenna on:							
	Thickness of bottom substrate	Material Type	ε_r of substrate	Resonant Frequency, f_r	Return Loss at f_r	10dB Bandwidth	Radiated Efficiency at f_r
ALONE	-	-	-	2.98 GHz	-18.7 dB	65 MHz	39.9%
On G9SG	1.74 mm	Sample		3.16 GHz	-46.7 dB	175 MHz	62.2%
On Low loss FR4	1.55 mm	Low loss FR4	4.5	2.87 GHz	-11.4 dB	80 MHz	59.5%
On GTS Layers	1.53 mm	Layered GTS	3.0	3.18 GHz	-23.3 dB	185 MHz	54.6%
On Taconic	1.60 mm	Taconic	2.2	3.34 GHz	-37.9 dB	170 MHz	74.7%

Table 6.4: Summary of simulated and measured results of 0.11 mm **GTS®** ($\varepsilon_r = 3$, $\tan\delta = 0.001$) **INSET-fed** patch antenna on different dielectrics

From Simulations: 0.11 mm GTS® INSET-fed patch on:							
	Thickness of bottom substrate	Material Type	ε_r of substrate	Resonant Frequency, f_r	Return Loss at f_r	10dB Bandwidth	Radiated Efficiency at f_r
On G9SG	1.74 mm	Sample		3.38 GHz	-12.2 dB	29.9 MHz	76.4%
On Low loss FR4	1.55 mm	Low loss FR4	4.5	2.98 GHz	-10.0 dB	-	91.4%
On GTS Layers	1.53 mm	Layered GTS	3.0	3.52 GHz	-15.4 dB	62.6 MHz	94.2%
On Taconic	1.60 mm	Taconic	2.2	4.00 GHz	-35.6 dB	95.1 MHz	100%

From Measurements: 0.11 mm GTS® INSET-fed patch on:							
	Thickness of bottom substrate	Material Type	ε_r of substrate	Resonant Frequency, f_r	Return Loss at f_r	10dB Bandwidth	Radiated Efficiency at f_r
On G9SG	1.74 mm	Sample		3.69 GHz	-17.62 dB	95 MHz	54.1%
On Low loss FR4	1.55 mm	Low loss FR4	4.5	3.03 GHz	-10.3 dB	20 MHz	64.7%
On GTS Layers	1.53 mm	Layered GTS	3.0	3.68 GHz	-29.2 dB	120 MHz	55.7%
On Taconic	1.60 mm	Taconic	2.2	4.03 GHz	-16.8 dB	120 MHz	78.9%

6.4.3. Offset-Fed Patch

The offset-fed patch was also examined here to check the repeatability and consistency of the above results on different antenna types, and how or if the feed method affects the performance of the antenna. It should be noted that the modes are more complicated in this case, thus, the measurement parameters were restricted to those used for the inset-fed patch scenario. The patch was etched on three dielectrics: a 110 µm thick GTS®, a 1.55 mm thick low loss FR4 of $\varepsilon_r = 4.5$, $\tan\delta = 0.0037$ and a 1.50 mm thick lossy FR4 of $\varepsilon_r \cong 4.4$, $\tan\delta = 0.02$. The patches were first measured individually and then above other substrates as in Figure 6.18.

The results for the measurements of the offset-fed patch with these three dielectrics as the top substrate are shown in Figure 6.25. The GTS 'ALONE' was not measured due to its 110 µm thickness. From these graphs, it can be seen that there is closer agreement in resonant frequencies between Figure 6.25 (b) and (c) with each other than with (a). This is expected as the low loss FR4 and lossy FR4 has similar ε_r. Both (b) and (c) show that the permittivity of the sample, G9SG lies between the low loss FR4 and Taconic, that is between 4.5 and 2.2. In all cases, the impedance match for the antennas with the G9SG sample under is very good as the transmission line width was designed for an ε_r around 4.5. For the offset patch measurements, the bandwidth of the structure with the G9SG is comparable to that of the low loss Taconic material. The frequency response for the different 'standard/test substrates' occur in the same order moving from one of the FR4's to the Taconic.

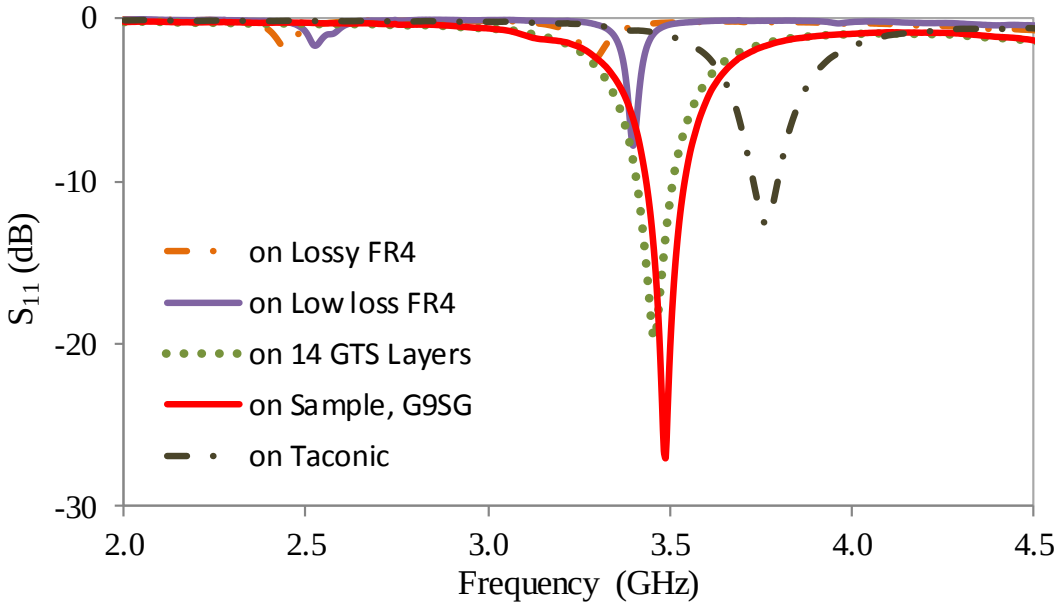

(a)

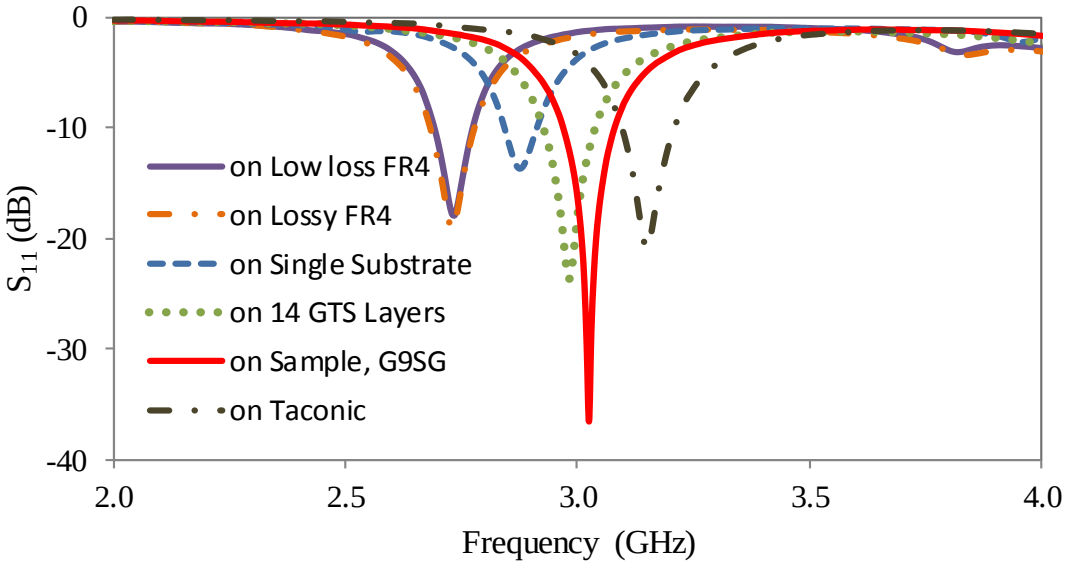

(b)

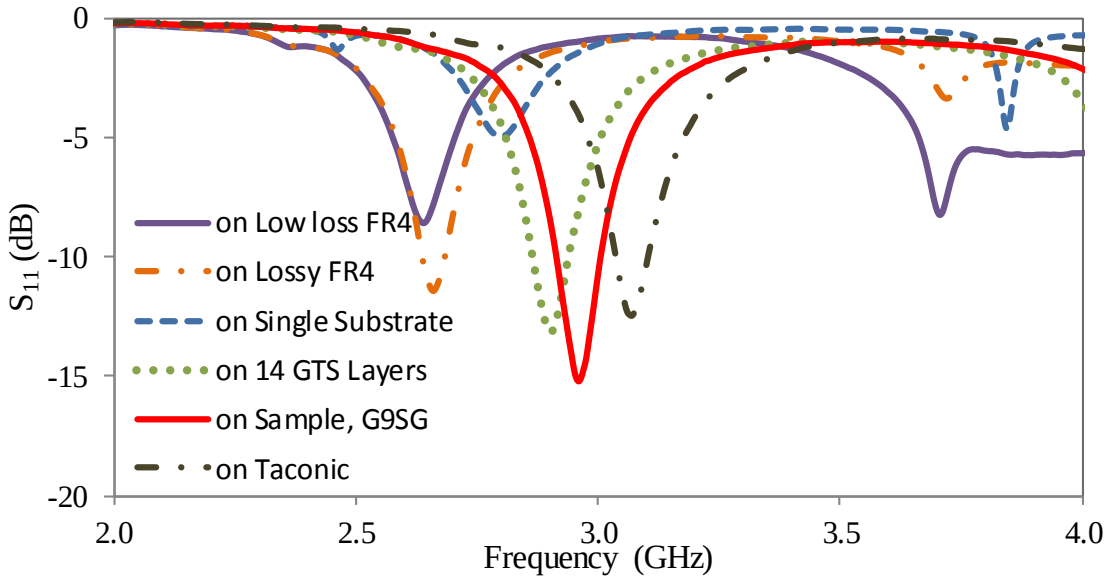

(c)

Figure 6.25: Measured S_{11} results of offset-fed patch printed on (a) GTS®, (b) lossy FR4 and (c) low loss FR4 substrates and placed on five different substrates

The radiation patterns for the offset patch on the lossy FR4 and GTS® substrates on the G9SG sample from simulation and measurements are given in Figure 6.26 (a) and (b) respectively. These patterns are similar except for the multiple nulls in back lobe of the results from the measurements which do not appear in the simulations. The differences in the pattern are due to the measurement environment and may also reflect the influence of the positioner as the antenna moves 180° away from the transmitting horn antenna. Comparing

the measured results with those from the single substrate case as shown in Figure 6.9, the nulls are more pronounced in this case. A summary of the results is given in Table 6.5 to Table 6.7. These measurements give similar results to those from the inset-fed patch antenna measurements with respect to the performance of the antenna on the G9SG sample. The radiated efficiencies with this sample are ~ 50% in these three cases compared with ~60% in the inset-fed measurements. The differences in the values between the measured and simulated results could be due to the difference in measurement/simulation setup for each case. For example, the exact resonant frequency will be affected by how many points are scanned over the frequency range measured/simulated frequency range. The measured resonant frequencies of the patch antenna on dual substrates with the G9SG sample, for each of the patch substrates examined, shows good agreement with the simulated results. This could mean that the effect of the G9SG sample on the patch differs depending on the feed mechanism used and it may be that should a probe feed be used, a different response might be obtained for the same sized patch.

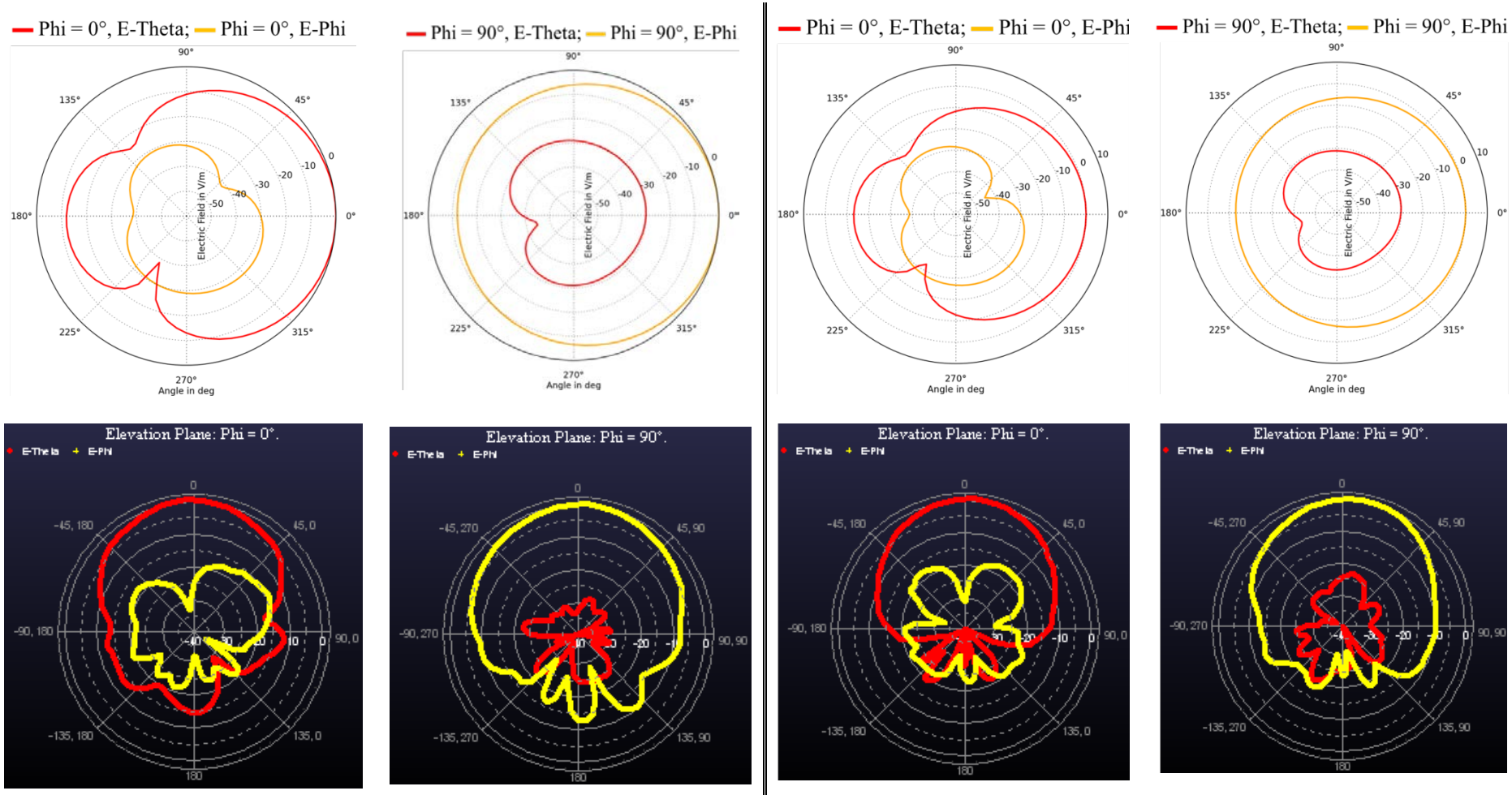

(a) (b)

Figure 6.26: Simulated (top row) and measured (bottom row) 2D radiation pattern of (a) **lossy FR4 offset** and (b) **GTS® offset-fed** patch antenna on sample, G9SG. The simulated patterns are rotated 90° with respect to the measured ones.

Table 6.5: Summary of simulated and measured results of 110 µm **GTS®** ($\varepsilon_r = 3$, $\tan\delta = 0.001$) **OFFSET-fed** patch antenna on different dielectrics

From Simulations: 0.11 mm GTS® OFFSET-fed patch on:							
	Thickness of bottom substrate	Material Type	ε_r of substrate	Resonant Frequency, f_r	Return Loss at f_r	10dB Bandwidth	Radiated Efficiency at f_r
On G9SG	1.74 mm	Sample		3.35 GHz	-16.0 dB	107.2 MHz	84.1%
On Low loss FR4	1.55 mm	Low loss FR4	4.5	2.85 GHz	-13.8 dB	76.4 MHz	93.6%
On Lossy FR4	1.50 mm	Lossy FR4	4.4	2.92 GHz	-34.4 dB	120.0 MHz	63.2%
On GTS Layers	1.53 mm	Layered GTS	3.0	3.39 GHz	-13.8 dB	87.4 MHz	93.6%
On Taconic	1.60 mm	Taconic	2.2	3.88 GHz	-17.7 dB	116.8 MHz	94.6%

From Measurements: 0.11 mm GTS® OFFSET-fed patch on:							
	Thickness of bottom substrate	Material Type	ε_r of substrate	Resonant Frequency, f_r	Return Loss at f_r	10dB Bandwidth	Radiated Efficiency at f_r
On G9SG	1.74 mm	Sample		3.63 GHz	-29.1 dB	142.5 MHz	50.0%
On Low loss FR4	1.55 mm	Low loss FR4	4.5	2.81 GHz	-14.1 dB	67.5 MHz	46.2%
On Lossy FR4	1.50 mm	Lossy FR4	4.4	2.94 GHz	-15.4 dB	87.5 MHz	34.4%
On GTS Layers	1.53 mm	Layered GTS	3.0	3.49 GHz	-20.1 dB	105.0 MHz	56.5%
On Taconic	1.60 mm	Taconic	2.2	3.76 GHz	-18.2 dB	95.0 MHz	79.1%

Table 6.6: Summary of simulated and measured results of 1.55 mm **low loss FR4** ($\varepsilon_r = 4.5$, $\tan\delta = 0.0037$) **OFFSET-fed** patch antenna on different dielectrics

From Simulations: 1.55 mm low loss FR4 OFFSET-fed patch antenna on:							
	Thickness of bottom substrate	Material Type	ε_r of substrate	Resonant Frequency, f_r	Return Loss at f_r	10dB Bandwidth	Radiated Efficiency at f_r
ALONE	-	-	-	2.77 GHz	-10.4 dB	30.8 MHz	95.5%
On G9SG	1.74 mm	Sample		3.02 GHz	-15.7 dB	95.6 MHz	95.1%
On Low loss FR4	1.55 mm	Low loss FR4	4.5	2.73 GHz	-21.2 dB	143.2 MHz	97.8%
On Lossy FR4	1.50 mm	Lossy FR4	4.4	2.77 GHz	-29.9 dB	152.0 MHz	84.4%
On GTS Layers	1.53 mm	Layered GTS	3.0	3.00 GHz	-43.7 dB	140.0 MHz	95.8%
On Taconic	1.60 mm	Taconic	2.2	3.24 GHz	-25.7 dB	150.8 MHz	94.3%

From Measurements: 1.55 mm low loss FR4 OFFSET-fed patch antenna on:							
	Thickness of bottom substrate	Material Type	ε_r of substrate	Resonant Frequency, f_r	Return Loss at f_r	10dB Bandwidth	Radiated Efficiency at f_r
ALONE	-	-	-	2.80 GHz	-4.9 dB	-	52.5%
On G9SG	1.74 mm	Sample		2.96 GHz	-15.2 dB	90 MHz	65.2%
On Low loss FR4	1.55 mm	Low loss FR4	4.5	2.64 GHz	-8.6 dB	-	69.2%
On Lossy FR4	1.50 mm	Lossy FR4	4.4	2.66 GHz	-11.4 dB	45 MHz	60.8%
On GTS Layers	1.53 mm	Layered GTS	3.0	2.90 GHz	-13.2 dB	75 MHz	65.2%
On Taconic	1.60 mm	Taconic	2.2	3.07 GHz	-12.5 dB	65 MHz	78.7%

Table 6.7: Summary of simulated and measured results of 1.50 mm **lossy FR4** ($\varepsilon_r = 4.4$, $\tan\delta = 0.02$) **OFFSET-fed** patch antenna on different dielectrics

From Simulations: 1.50 mm lossy FR4 OFFSET-fed patch antenna on:							
	Thickness of bottom substrate	Material Type	ε_r of substrate	Resonant Frequency, f_r	Return Loss at f_r	10dB Bandwidth	Radiated Efficiency at f_r
ALONE	-	-	-	2.87 GHz	-20.1 dB	116.0 MHz	60.0%
On G9SG	1.74 mm	Sample		3.08 GHz	-17.8 dB	143.6 MHz	78.5%
On Low loss FR4	1.55 mm	Low loss FR4	4.5	2.79 GHz	-43.7 dB	156.8 MHz	81.3%
On Lossy FR4	1.50 mm	Lossy FR4	4.4	2.83 GHz	-18.4 dB	163.6 MHz	73.5%
On GTS Layers	1.53 mm	Layered GTS	3.0	3.05 GHz	-21.9 dB	147.6 MHz	82.6%
On Taconic	1.60 mm	Taconic	2.2	3.30 GHz	-36.9 dB	164.0 MHz	83.5%

From Measurements: 1.50 mm lossy FR4 OFFSET-fed patch antenna on:							
	Thickness of bottom substrate	Material Type	ε_r of substrate	Resonant Frequency, f_r	Return Loss at f_r	10dB Bandwidth	Radiated Efficiency at f_r
ALONE	-	-	-	2.88 GHz	-13.7 dB	70 MHz	27.6 %
On G9SG	1.74 mm	Sample		3.02 GHz	-29.7 dB	110 MHz	49.4 %
On Low loss FR4	1.55 mm	Low loss FR4	4.5	2.74 GHz	-17.9 dB	80 MHz	58.8 %
On Lossy FR4	1.50 mm	Lossy FR4	4.4	2.73 GHz	-19.1 dB	90 MHz	43.6 %
On GTS Layers	1.53 mm	Layered GTS	3.0	2.98 GHz	-23.6 dB	110 MHz	62.9 %
On Taconic	1.60 mm	Taconic	2.2	3.15 GHz	-20.8 dB	115 MHz	70.5 %

These results show that the patch antenna still radiates and gives a reasonable frequency response when placed on the G9SG sample, and not being too adversely affected by the presence of the copper cuboids in such close proximity to it. It also shows that similar conclusions can be obtained using different types of feed mechanisms for the patch antenna as the resonant frequencies with these dual substrates underneath the patch for the two feed methods were similar. Also, the 10dB bandwidth with the G9SG sample was similar in both cases. For the inset-fed case, the simulations show that the ε_{eff} of the G9SG sample lies between the ε_r of the GTS Layers and the low loss FR4 substrates, while the measurements indicate that it lies between the ε_r of the Taconic and GTS Layers substrates. For the offset-fed case, the simulations suggest that the ε_{eff} of the G9SG sample lies between the ε_r of the GTS Layers and the Taconic substrates for both FR4's while the measurements indicate that it lies between the GTS Layers and the lossy FR4 in one and between the Taconic and the lossy FR4 in the low loss FR4 case. It shows that there are little differences between the inset-fed and off-set fed cases. This disparity in the prediction of the ε_{eff} of the G9SG sample could be due to some of the issues highlighted in the following section.

6.4.4. Alignment and Handling Issues with these Measurements

Due to the limited fabrication options available, measurements of this type posed some challenges which could have affected the results presented here as possible sources of error: two of these challenges are briefly discussed here. First, when creating the G9SG sample, there is the issue of aligning more than 2 layers such that they are parallel and aligned with each other. Also, when holes are drilled through the multi-layered substrates, the material is not completely cut out, resulting in bulges which do not make these substrates lie completely flat. As such this could have included an extra proportion of air volume fraction in the sample which would thus lower the effective permittivity of the medium. This issue is also encountered in creating the GTS-Layered sample as after stacking them together, as they were drilled through as one material. When screwing the patch substrate and the measured/test substrate together, it is almost impossible to ensure that these are completely flush with each other and with the ground plane (metal block) as shown in Figure 6.27, and that each test sample is screwed together in the exact same way.

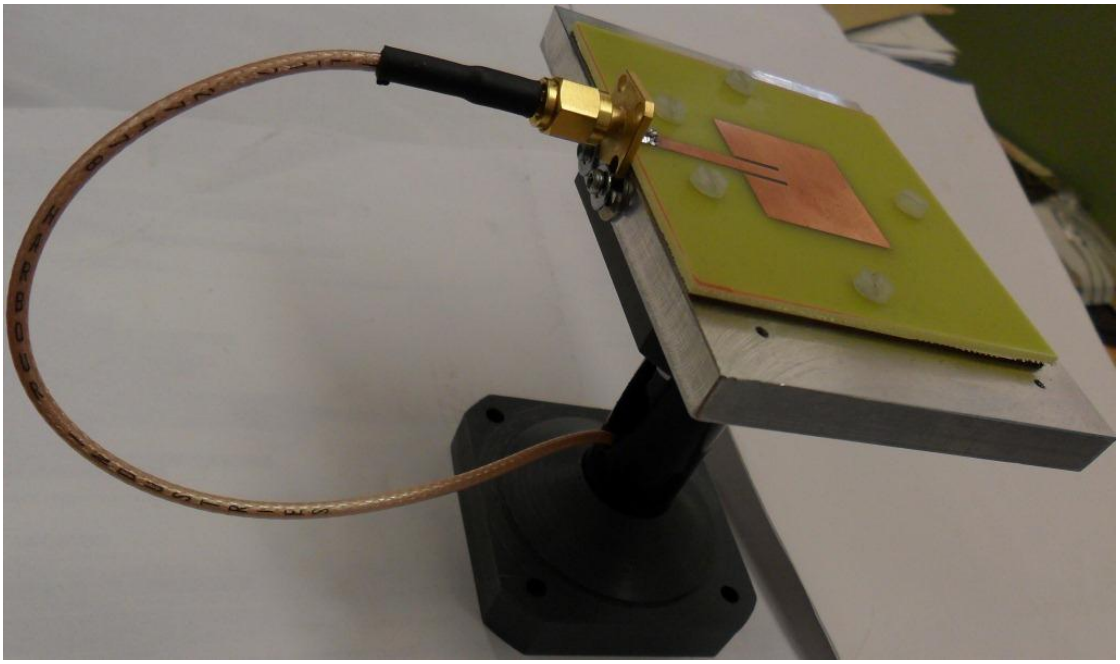

Figure 6.27: Example of patch antenna on dual substrates with plastic screws holding both down to ground plane

Secondly, after each measurement, the connecting cable had to be removed from the connector on the sample holder and the positioner in the chamber. This continuous fixing and removal may have affected the proper application of the calibration file to the measurement.

6.5 Conclusions

It is well known from theory that the resonant frequency and the performance of any antenna are affected by the substrate on which it is printed, and to a smaller degree, the height of the substrate. For a fixed patch size as used in this chapter, it has been shown that this expectation from theory can be used to predict the dielectric properties of the substrate on which the patch antenna was printed. EM simulations have been carried out to compare the EM performance of the patch when on a homogenous substrate and when on a heterogeneous substrate with metallic and spherical cubic inclusions in an SC lattice, and show good agreement when both the ε_{eff} and μ_{eff} are taken into account for the homogenous equivalents. Two forms of feeds to the patch antenna were examined: the inset feed and the offset feed.

Patch antennas on substrates with dielectric cubic inclusions have been shown via simulations to behave like their homogenous equivalents. This further validates the analytical and simulation results and shows the results are valid in patch antenna geometries. However, there is lesser agreement between the performance of the patch on substrates with metallic cubic inclusions and their homogenous equivalent. The agreement is improved by adding a permeability value not equal to unity to the properties of the homogenous equivalent, as $\mu_{eff} < 1$ – a diamagnetic behaviour, for heterogeneous materials with metallic inclusions. This has been shown via simulations in this chapter. For media with cuboid-shaped inclusions, it has been shown that they exhibit anisotropy and are to be treated as having ε_{eff} and μ_{eff} tensors. Thus the two new characteristics of the G9SG heterogeneous sample examined in this chapter were: anisotropy and diamagnetism. These properties were individually examined and it can be deduced that they both combine to alter the performance of the patch from the case where isotropy and uniform magnetism are assumed.

Simulations and measurements of inset-fed and offset-fed patch antennas printed on different substrates with different homogenous dielectrics and the G9SG sample placed underneath have been presented. As the dielectric properties of the Taconic and Low loss FR4 substrates were well known, the S_{11} plots of these patch antennas on the different substrates show that the ε_{eff} and μ_{eff} of the G9SG sample lies between these two. This presents another measurement technique in characterising the permittivity and permeability of the sample. The measured results also show the anisotropic and diamagnetic nature of the G9SG sample. The return loss and 2D radiation patterns of these different structures were compared and

generally showed good agreement, except for the multiple nulls in the back lobe due in part to the positioning. Even though the resonant frequency of these inset-fed patch antennas on the G9SG sample from simulations and measurements did not match up, they showed better agreement in the simulation and measurement results from the offset-fed case. This difference in the inset-fed patch results might be due to the size of the gap between the microstrip feed line and the antenna itself being comparable to that of the metallic cubes directly below; this gap is not present in the offset feed. It should be noted that the S_{11} values at the resonant frequencies were not of significant importance as the main observation here was the frequency shifts for the different substrates for the same size patch. It can be expected that with better matching, the performance should be improved. Other issues that may have affected the measurements have been highlighted in Section 6.4.4.

Worthy of note is that although the G9SG sample with metallic cuboids is quite close to the radiating element – the patch antenna, this does not completely 'kill' the radiation of the patch. The proximity of the heterogeneous G9SG sample with metallic inclusions to the source, that is, in its near field, is quite different from the simulations that placed the sample in the far-field of the source and using a plane wave. This presents another scenario of examining the robustness of the sample in practical use.

Further investigation will be required to understand how the presence of $\mu_{eff} < 1$ affects the patch antenna design so that it can be properly accounted for in the measurements. An alternative expression to account for this has been given in Section 6.4.2. It may be necessary to have two patches of different sizes where the bigger size is used for the cases where the G*n*SG sample is used as a substrate for the patch antenna and the smaller size for other homogenous substrates. This would allow the proper examination of the anisotropy and diamagnetism of this sample. In addition, a standard sample with similar diamagnetic properties as the predicted values (via simulations) of the G9SG sample can be used as a more accurate basis of comparison. Also, the refractive index and/or impedance of these materials can be used instead in the design and comparisons as they both take into account ε_r and μ_r (see Section 3.4.1) in their expressions. It can be hypothesized that as the heterogeneous samples are reduced in size, better agreement between the measured and simulated results will be obtained.

6.6 References

[1] K. Buell, H. Mosallaei, and K. Sarabandi, “Embedded-circuit magnetic metamaterial substrate performance for patch antennas,” in *IEEE Antennas and Propagation Society International Symposium*, 2004, vol. 2, pp. 1415–1418.

[2] C.-C. Chen and J. L. Volakis, “Bandwidth broadening of patch antennas using nonuniform substrates,” *Microwave and Optical Technology Letters*, vol. 47, no. 5, pp. 421–423, Dec. 2005.

[3] G. Kiziltas, D. Psychoudakis, J. L. Volakis, and N. Kikuchi, “Topology design optimization of dielectric substrates for bandwidth improvement of a patch antenna,” *IEEE Transactions on Antennas and Propagation*, vol. 51, no. 10, pp. 2732–2743, Oct. 2003.

[4] D. Psychoudakis, Y.-H. Koh, J. L. Volakis, and J. H. Halloran, “Design method for aperture-coupled microstrip patch antennas on textured dielectric substrates,” *IEEE Transactions on Antennas and Propagation*, vol. 52, no. 10, pp. 2763–2765, Oct. 2004.

[5] K. Buell, H. Mosallaei, and K. Sarabandi, “A substrate for small patch antennas providing tunable miniaturization factors,” *IEEE Transactions on Microwave Theory and Techniques*, vol. 54, no. 1, pp. 135–146, Jan. 2006.

[6] M. I. Kitra, C. J. Panagamuwa, P. McEvoy, J. (Yiannis) C. Vardaxoglou, and J. R. James, “Low SAR ferrite handset antenna design,” *IEEE Transactions on Antennas and Propagation*, vol. 55, no. 4, pp. 1155–1164, Apr. 2007.

[7] L. Xing, Q. Xu, J. Li, Z. Wei, J. Ding, and C. Guo, “Broaden the bandwidth of patch antenna by using inhomogeneous metamaterial substrate,” in *Progress In Electromagnetics Research Symposium*, 2010, vol. 1, pp. 155–159.

[8] Y. Lee and Y. Hao, “Characterization of microstrip patch antennas on metamaterial substrates loaded with complementary split-ring resonators,” *Microwave and Optical Technology Letters*, vol. 50, no. 8, pp. 2131–2135, Aug. 2008.

[9] D. Psychoudakis, J. L. Volakis, Z. N. Wing, S. K. Pillai, and J. W. Halloran, “Enhancing UHF antenna functionality through dielectric inclusions and texturization,” *IEEE Transactions on Antennas and Propagation*, vol. 54, no. 2, pp. 317–329, Feb. 2006.

[10] X. Wang, Y. Hao, and P. S. Hall, “Dual-band resonances of a patch antenna on UC-EBG substrate,” in *Asia-Pacific Microwave Conference Proceedings*, 2005, vol. 1.

[11] L.-W. Li, Y.-N. Li, T. S. Yeo, J. R. Mosig, and O. J. F. Martin, “A broadband and high-gain metamaterial microstrip antenna,” *Applied Physics Letters*, vol. 96, no. 16, pp. 1–3, 2010.

[12] M. A. Antoniades and G. V Eleftheriades, “A compact and broadband NRI-TL metamaterial monopole antenna,” in *13th International Symposium on Antenna*

Technology and Applied Electromagnetics and the Canadian Radio Sciences Meeting, 2009, pp. 13–16.

[13] D. M. Pozar, *Microwave Engineering*, 3rd ed. 2005.

[14] C. A. Balanis, *Antenna theory: analysis and design*, 3rd ed. Chichester: Wiley, 1997.

[15] A. G. Derneryd, "A theoretical investigation of the rectangular microstrip antenna element," *IEEE Transactions on Antennas and Propagation*, vol. AP-26, no. 4, pp. 532–535, 1978.

[16] C. C. Njoku, W. G. Whittow, and Y. C. Vardaxoglou, "Simulation methodology for synthesis of antenna substrates with micro-scale inclusions," *IEEE Transactions on Antennas and Propagation*, vol. 60, no. 5, pp. 2194–2202, 2012.

[17] I. J. Bahl and P. Bhartia, *Microstrip Antennas*, 2nd ed. Artech House, 1980.

[18] E. O. Hammerstad, "Equations for microstrip design," in *5th European Microwave Conference*, 1975, pp. 268–272.

[19] C. A. Balanis, *Advanced Engineering Electromagnetics*, 2nd ed. New York: Chichester: Wiley, 1989.

[20] K. Carver and J. Mink, "Microstrip antenna technology," *IEEE Transactions on Antennas and Propagation*, vol. 29, no. 1, pp. 2–24, Jan. 1981.

[21] L. Lewin, "The electrical constants of a material loaded with spherical particles," *IEE-Part III: Radio Comm. Eng.*, vol. 94, no. 27, pp. 65–68, 1947.

[22] A. Sihvola, *Electromagnetic Mixing Formulas and Applications*. London: IET, 1999.

[23] M. A. Ordal, L. L. Long, R. J. Bell, S. E. Bell, R. R. Bell, R. W. Alexander, and C. a Ward, "Optical properties of the metals Al, Co, Cu, Au, Fe, Pb, Ni, Pd, Pt, Ag, Ti, and W in the infrared and far infrared," *Applied Optics*, vol. 22, no. 7, pp. 1099–1120, Apr. 1983.

[24] D. S. Lockyer, J. C. Vardaxoglou, and M. J. Kearney, "FSS array generation by optical means," *Antennas and Propagation, 1999. IEE National Conference on.*, pp. 132–135.

[25] C. C. Njoku, W. G. Whittow, and Y. C. Vardaxoglou, "Microstrip patch antennas on substrates with metallic inclusions," in *Loughborough Antennas & Propagation Conference (LAPC)*, 2012, pp. 1–4.

[26] IMST GmbH, "EMPIRE XCcel Manual," 2012.

Chapter 7. Conclusions and Future work

7.1 Summary of Research Novelty and Advantages

The main aim of this thesis was to investigate the effective electromagnetic (EM) properties of heterogeneous media with different inclusions; this has so far been accomplished via canonical equations, EM simulations and measurements. As stated in the Chapter 1, the novel contributions were:

- a comprehensive and critical analysis of the various canonical equations used in characterising the ε_{eff} and μ_{eff} of heterogeneous media;
- the introduction of the concept of synthesising microwave antennas using nanomaterials;
- using spherical and cubical inclusions and applying FDTD EM simulations with a suitable algorithm to find the effective permittivity of heterogeneous substrates of finite volumes, on which antennas and other circuit components can be printed;
- using different measurement techniques and to determine the properties of the heterogeneous substrates while ensuring repeatability

These have been accomplished as presented in Chapters 2 – 6.

7.2 Summary of Key Results

In Chapter 2, the canonical equations from published literature describing the effective permittivity, ε_{eff} and effective permeability, μ_{eff} of heterogeneous mixtures have been extensively examined. These equations have been compared to each other in order to understand the differences and similarities where these exist. It has been shown that under certain conditions such as assuming the host is free space and uniform spacing of the inclusions along the *x*, *y* and *z* axes, the equations tend to be similar. Graphical representations of these equations have been presented. Different parameters such as frequency, inclusion size and spacing affects the ε_{eff} and μ_{eff} of heterogeneous structures. These parameters have been individually examined to understand their influence on the effective properties of these media. The equations by Lewin and Doyle have been selected as the most robust of the equations examined and used in the later chapters of this thesis. Heterogeneous mixtures with non-spherical inclusions have been analysed in order to understand how they may influence the properties of these mixtures. As most of the canonical

equations use spherical inclusions, it has been shown that an equivalent volume process can be used to approximate the ε_{eff} and μ_{eff} of these mixtures.

In Chapter 3, detailed explanation of the EM simulation process to obtain a plane wave impinging on a material was given. This was done in order to satisfy the assumptions made in deriving the ε_{eff} and μ_{eff} equations of heterogeneous media. An inversion process was necessary to extract the ε_{eff} and μ_{eff} from the scattering (S-) parameters after simulations. The resonant scattering inversion algorithm was used in this thesis and showed very good agreement with the known values of the homogenous media. This algorithm included a phase rectification stage which was explained in detail. The implementation of the inversion process was validated using the S-parameters from published literature. Parametric studies of the various parameters such as the distance from the measurement planes to the surfaces of the materials under test (MUT), the thickness and the EM properties of the MUT, that contribute to the accuracy of the inversion process have been presented. Graphical results were presented to buttress these points.

Numerically and analytically computed values of ε_{eff} and μ_{eff} of various heterogeneous media containing dielectric or metallic cubic or spherical inclusions were compared in Chapter 4. These values were shown to have good agreement giving the confidence that the equations and the simulation-inversion process were implemented correctly. It was also determined that heterogeneous mixtures with metallic inclusions exhibited a diamagnetic behaviour, that is, had an $\mu_{eff} < 1$. This helped explain the rise in the resonant frequency for the heterogeneous samples, G9SG, examined in Chapters 5 and 6. The loss tangents of these heterogeneous media were calculated from the canonical equations and EM simulations. Their values showed that these structures had low losses comparable to those of conventional low loss substrates used in microwave applications. An example of designing a heterogeneous medium with pre-determined ε_{eff} using different types/shapes of inclusions was also described. This also showed the limit of the equation by Avelin et al. describing a heterogeneous medium with a high volume fraction of cubic inclusions.

In Chapter 5, the fabrication techniques used in creating the samples used in this research were examined. The fabricational resources available within the School have limited the range of samples that were made during this research. Plane wave simulations were used to obtain the expected ε_{eff} and μ_{eff} of the G9SG sample, which was determined to be

anisotropic as the size of the inclusions was not uniform in all 3 axes. Different measurement methods – waveguides, split-post dielectric resonators and ring resonators, used in characterising their EM properties of materials were used for the samples. The theories behind these methods along with the simulated and measured results were presented and compared. The analytical and simulation based research has been verified with waveguide measurements. The ring resonator was investigated as a reasonable measurement method. The challenges faced with these measurement methods were explained including the possible sources of error. It was concluded that the waveguide provided the best measured results of the three, that closely matched the simulated and canonical results.

Patch antennas were used in Chapter 6 to investigate how the performance of an antenna may be affected by heterogeneous media with metallic inclusions. Simulated results of the patch antenna on heterogeneous media with dielectric and metallic cubic inclusions in a simple cubic lattice were presented. It has been shown that the frequency response of the patch antenna on heterogeneous media with dielectric inclusions and on the homogenous equivalent, show very good agreement. This was not the case with metallic inclusions due to the diamagnetic nature of the heterogeneous medium. This property has been tested via simulations by adding an $\mu_{eff} < 1$ to the property of the homogenous equivalent and has been shown to have better agreement with that of the heterogeneous medium. Two feed mechanisms for the patch antenna – the offset and inset feeds, were used in the measurements to test the robustness of the sample and measurement method. The patch antenna still radiated suggesting that its performance was not severely inhibited by the presence of the metallic inclusions in close proximity to its main radiating part. The measurements were carried out by placing different substrates under the patch substrates. The return loss and 2D radiation patterns of these different structures were compared and generally showed good agreement, except for the multiple nulls in the back lobe. The patch antenna measurement also served as a measurement technique by comparing the resonant frequency of the G9SG sample with that of substrates of known permittivities, in order to estimate the sample's ε_{eff}. The thickness of the substrates used in this thesis varied from 1.50 to 1.74 mm. Patch antenna measurements can also be used to characterise the EM properties of bespoke substrates or textured dielectrics.

It can be concluded that the simulated and canonical results showed good agreement while the measurement methods requires further investigation in order to obtain better agreement

with the simulated results. However, there is a very good level of confidence of the extraction process which has been verified with homogenous and heterogeneous samples, thus, leaving the primary focus to be on finding a robust, suitable and repeatable measurement method to match up with the simulations and equations.

7.3 Implications for Industry

Once the effective permittivity is known, the antenna simulation time can be reduced by approximating the heterogeneous structures with the equivalent homogeneous material for some of the simulation runs which take very long times for small-scale inclusions. The canonical equations have been shown to provide accurate values for the ε_{eff} and μ_{eff}.

The process of varying the permittivity of substrates with micro-sized inclusions may not inherently improve the efficiency of the antenna. However, the micro-sized inclusions allow the effective permittivity to be controlled at various locations. Therefore, antennas can be designed in future where the permittivity can be varied smoothly and in step in three dimensions. This variation can be further exploited to improve the bandwidth and efficiency as has been shown with textured dielectrics.

The advantages of producing antenna systems for microwave applications using nano-fabrication methods include improved EM performance and physical durability with fewer variations in the properties of mass produced materials. By using artificial dielectrics, bespoke materials can be created where the permittivity at different parts of the antenna systems, especially the substrates on which the antennas are printed can be varied giving the antenna designer an additional degree of freedom.

7.4 Future Work

Further investigation is required into the rectification of the wave impedance in order to remove the "spikes" from the thickness resonances in the extracted ε_{eff} and μ_{eff} from the simulated results as shown in Chapters 3 and 4. From Table 4-1 in Section 4.4, it has been concluded that more investigation is needed in order to understand and verify the loss mechanism for heterogeneous mixtures with dielectric and/or cubic inclusions.

In order to replicate the plane wave simulations as discussed in Chapters 3 and 4, horn antennas can be used such that the structure to be measured is placed in the far-field of the antenna, that is, at a distance $2D^2/\lambda$, where D is the largest diagonal of the horn and λ is the shortest operating wavelength of the horn. A major challenge with this measurement technique is controlling the environment where the measurement is done, minimising the movement of the cables, aligning the horns to be directly facing each other and accurately measuring the distances between the horn apertures and the surfaces of the material under test as these distances play a major role in determining the phases of the S-parameters and thus the accuracy of the extracted results.

A structure made of complementary frequency selective surfaces (CFSS) on either side of a low permittivity dielectric can be used for dielectric measurements. These FSS structures are arrays of conductors or dipoles and apertures or slots. Each FSS resonates at a much higher frequency than when combined as in the CFSS. Its resonant frequency is affected by the permittivity and thickness of the materials around it and the dimensions of the dipoles and apertures. The resonant frequency of the CFSS is altered by placing the material under test (MUT) directly behind it. This change in resonant frequency can be used to determine the permittivity and loss tangent of the MUT using equations from published literature. Analysis via simulations and measurements constitute part of the recommendations for future work on this project in determining a suitable, repeatable measurement method for the artificial dielectrics especially those with metallic inclusions. It is anticipated that the width of the conductors and apertures may be crucial especially if it is comparable to the size of the inclusions of the heterogeneous medium. Papers on the CFSS method have been submitted and accepted to the 2013 EuCAP and the 2013 IEEE APS/USNC-URSI Meeting.

Further work is needed to fully understand the differences in resonant frequencies between heterogeneous mixtures with metallic inclusions and their homogeneous equivalent using the ε_{eff} and μ_{eff} of the heterogeneous media. The modes, diamagnetism and anisotropy of

heterogeneous samples with metallic inclusions (such as Copper) require further investigation for microwave applications.

The conclusions from the offset-fed and inset-fed patch antenna measurements with dual dielectric substrates allows for further investigation into the use of these heterogeneous structures for different kinds of antennas. Future work will focus on investigating how the reduction in the size of the cubes towards the nano-scale to increase the homogeneity of the structure, may affect the performance of the antenna. It is expected that the dielectric properties will be easier to measure if the metallic inclusions are reduced in size. It may be useful to examine how heterogeneous mixtures affect the performance on other antenna types.

Fabricating these structures is not straightforward and the limited fabrication facilities at the school restricted the possible size of the G9SG sample and other samples that can be made. This creates the need to outsource the manufacture of this sample in order to carry out the plane wave measurements and compare with the simulated results. Discussions are being held with colleagues in other disciplines and with commercial industries to create suitable samples which will then allow measurements.

One of the EM advantages of having artificial dielectrics is the ability to vary the permittivity of different areas of substrates with their local electric field strengths as introduced in Section 1.5, in order to improve the performance of antennas. This presents an area for future research with possible samples and measurements made.

These issues will be considered under ESPRC Grant No. EP/I01490X/1.